Dynamic Control of Rotating Stall in Axial Flow Compressors Using Aeromechanical Feedback

by

Daniel L. Gysling

GTL Report #219 August 1993

GAS TURBINE LABORATORY
MASSACHUSETTS INSTITUTE OF TECHNOLOGY
CAMBRIDGE, MASSACHUSETTS

Dynamic Control of Rotating Stall in Axial Flow Compressors Using Aeromechanical Feedback

by

Daniel L. Gysling

GTL Report #219 August 1993

This work was supported by a grant from the U.S. Air Force Office of Scientific Research, Major Daniel B. Fant, contract monitor, and by the Air Force Research in Aero-Propulsion Technology (AFRAPT) Program.

Dynamic Control of Rotating Stall in Axial Flow Compressors Using Aeromechanical Feedback

by

Daniel L. Gysling

Abstract

Dynamic control of rotating stall in an axial flow compressor has been implemented using aeromechanical feedback. The control strategy developed used an array of wall jets upstream of a single stage compressor which were regulated by locally reacting reed valves. These reed valves responded to pressure perturbations in the flow that were associated with small amplitude perturbations that precede rotating stall. The control strategy was designed such that the combined system of compressor plus the reed valve controller was stable in previously unstable operating conditions. A 10% decrease in the the stalling flow coefficient was achieved using this dynamic feedback control strategy, and the stable flow range was extended with no noticeable change in the steady state performance of the compression system.

The experimental demonstration is the first use of aeromechanical feedback to extend the stable operating range of an axial flow compressor, as well as the first use of locally reacting feedback and dynamic compensation techniques to stabilize rotating stall in an axial flow compressor.

The design of the experiment was based on a two-dimensional model of the rotating stall dynamics which incorporated the effect of aeromechanical feedback. The physical mechanism responsible for rotating stall in axial flow compressors was examined with focus on the role of dynamic feedback in stabilizing compression system instability. The effectiveness of the aeromechanical control strategy was predicted, and experimentally demonstrated, to be a function of a set of non-dimensional control parameters that determine the interaction of the control strategy and the rotating stall dynamics. Predictions based on linear stability analyses and non-linear numerical simulations agreed qualitatively with the steady state and time resolved experimental data.

During the experimental investigations, large amplitude, one-dimensional acoustic oscillations were observed in the compression system with aeromechanical feedback stabilization. Based on these observations, the role of the compression system parameters in the acoustic oscillations was examined analytically and a method was developed to reduce these oscillations. The mechanism responsible for the generation of self-excited acoustic oscillations, and the implications for dynamic control of compression system instabilities was also examined.

Acknowledgments

The author wishes to thank all those who contributed to the completion of this research. Without each of their contributions, this work would have been much more difficult, if not impossible, to complete. In particular, the author wishes to thank:

The members of the thesis committee: Professor Greitzer, Professor Dugundji, Professor Ingard, and Professor Kerrebrock. Their guidance, enthusiasm, and knowledge was invaluable to this research and to the author's experience at MIT.

Professor Epstein, for his interest and support.

Professor Marble, for his interest and suggestions and for his insistence that research should be fun.

Dr. Choon S. Tan, who was always interested in discussing various aspects of the project.

Professor Paduano, whose expertise in control theory was an invaluable resource.

Viktor Dubrowski, Jim Nash, Jim Letendre and Bill Ames for their interest in the project and their efforts in making sure that the mechanical aspects of the project went smoothly.

This work also benefited from many discussions with Jon Simon, Gavin Hendricks, Professor Cumpsty, and Peter Silkowski. Their interest is greatly appreciated.

The author also thanks all the past and present members of the Gas Turbine Lab staff and students for their assistance in the completion of this research.

Special thanks go to my family and friends for their encouragement and support.

This research was conducted under a grant from the U. S. Air Force Office of Scientific Research, under Grant Number AFOSR-93-0032, Major D. B. Fant, Contract Monitor. Their support is gratefully acknowledged. Financial support for the author was also provided by the Air Force Research in Aero-Propulsion Technology Program (AFRAPT), under Grant Number AFOSR-91-0052.

Table of Contents

List of Figures

List of Tables

Nomenclature

A	area
A_n	nth spatial Fourier coefficient for upstream perturbation streamfunction
B_n	nth spatial Fourier coefficient for downstream potential perturbation streamfunction
B	compression system stability parameter, $\left(B \equiv \frac{U_R}{2\,\omega_H\,L_c}\right)$
b	reed valve damping constant
c	speed of sound
c	chord
C	velocity
C_n	nth spatial Fourier coefficient for downstream vortical perturbation streamfunction
$\vec{F}$	perturbation intensity
H	annulus height
i	imaginary number $\sqrt{-1}$
$\vec{i}\,;\vec{j}$	unit vectors
k	acoustic wave number
L	length
$\tilde{L}$	length of reed valve normalized by annulus height
L_c	length of inlet duct to compressor
M	complex compressor pressure rise versus mass flow transfer function
M	Mach number
M	modal mass of reed valves
$\dot{m}$	mass flow
n	spatial Fourier harmonic number
P	pressure
p	non-dimensional pressure, $\left(p \equiv \frac{P}{\frac{1}{2}\rho\,U_R^2}\right)$
PSD	temporal power spectral density

q normalized reed valve opening, $\left(q \equiv \frac{\Delta}{H}\right)$

q_n nth spatial Fourier coefficient of reed valve deflection

Q natural frequency of reed valves normalized by rotor frequency, $\left(Q \equiv \frac{\omega_n}{U_R / R}\right)$

R mid-span radius of compressor

Re Reynolds number

rms root mean square

s complex frequency

SFC spatial Fourier coefficient

T_{ij} acoustic transmission matrix

U velocity

U_R velocity of rotor at mid-span

u, v Cartesian velocity components

W reed mass parameter, $\left(W \equiv \frac{\rho L R^2}{M}\right)$

x axial distance, normalized by rotor radius

z non-dimensional time rate of change of reed valve opening, $\left(z \equiv \frac{\partial q}{\partial \tau}\right)$

Greek Symbols

α ratio of spring constant in visco-elastic dashpot to that of reed valve

α_i normalized momentum of injected fluid, $\left(\alpha_i \equiv \frac{\dot{m}_i C_{x_i}}{\rho A U_R^2 \Phi^2}\right)$

α perturbation in swirl angle in upstream flow field

β acoustic compressor slope, $\left(\beta = \frac{1}{2} M_R \frac{\partial \Psi}{\partial \Phi} + M_x\right)$

β flow angle

δE rate of non-dimensional perturbation energy production across compressor

Δ reed valve opening

χ visco-elastic influence parameter, $\left(\chi \equiv \frac{2\zeta}{Q\alpha}\right)$

ρ ambient density

θ circumferential position

τ non-dimensional time ($\frac{t\,U_R}{R}$)

Ψ pressure coefficient, $\left(\Psi \equiv \frac{\Delta P}{\frac{1}{2}\rho U_R^2}\right)$

Ψ perturbation streamfunction

Φ mean axial flow Coefficient $\left(\Phi \equiv \frac{\dot{m}}{\rho A U_R} = \frac{C_x}{U_R}\right)$

ϕ axial flow coefficient, $(\phi = \Phi + \delta\phi)$

$\tilde{\phi}_n$ n^{th} spatial Fourier component of $\delta\phi$

ν perturbation circumferential flow coefficient

λ inertial parameter for rotating blade rows

λ acoustic wave length

μ inertial parameter for blade rows

$\frac{\partial\Psi}{\partial\Phi}$ slope of inlet total to exit static pressure rise coefficient (Ψ) versus mass flow coefficient (Φ) compressor characteristic

σ complex, temporal eigenvalue

σ area ratio across throttle

κ acoustic throttle slope, $\left(\kappa = \frac{1-\sigma}{\sigma} M_{x_{th}}\right)$

ν kinematic viscosity

ω frequency

ω_H Helmholtz frequency of compression system

ω_n natural frequency of reed valves

ω_{rs} temporal frequency associated with traveling waves observed at fixed circumferential position

ω normal vorticity

Φ_i injection parameter, $\left(\Phi_i \equiv \frac{C_{x_i}}{U_R}\right)$

γ_R stagger angle of rotor

γ_S stagger angle of stator

ξ assumed mode shape for reed deflection

ζ reed damping parameter, $\left(\zeta \equiv \frac{b}{2 M \omega_n}\right)$

Ξ modal forcing function

Subscripts

a axial station of injection

b axial station downstream of injection region, upstream of compressor

c compressor

d downstream flow field

i injection

n harmonic number

p potential component of flow field

r reed valves

R rotor

s static pressure

S stator

t total pressure

th throttle

t s total-to-static characteristic

t t total-to-total characteristic

u upstream flow field

v vortical component of flow field

Operators

∇^2	Laplacian
δ	perturbation quantity
Real	real part of complex quantity
Imag	imaginary part of complex quantity
∂	partial derivative
∇	gradient of scalar
∇	divergence of vector field
$\cdot$	dot product
$\cdot$	derivative with respect to time

Chapter 1: Introduction

1.1 Description of the Problem

The operating range of turbomachinery compression systems is generally limited at low mass flow rates by the onset of fluid dynamic instability. As the flow rate is reduced, the pressure rise across the compressor typically increases monotomically until a performance limiting, fluid dynamic instability is encountered at which the steady, axisymmetric flow through the compression system transitions to an unsteady flow field with large amplitude oscillations. At these operating conditions, the annulus averaged pressure rise and mass flow through the compression system are reduced from the values that occur when the compression system operates with a steady, axisymmetric flow field.

The specific structure of the instability can take many forms [1], depending on the parameters of the compression system, but the instabilities are generally categorized in one of two broad classes of instabilities: surge or rotating stall. Figure 1.1 shows a schematic of the surge and rotating stall in an axial flow compression system. Surge is an essentially one-dimensional instability characterized by oscillations in compressor annulus averaged mass flow and pressure rise that extend through the entire compression system. Rotating stall is a two- or three-dimensional disturbance in which regions of low, or reversed, mass flow (termed stall cells), rotate about the annulus of the compressor. Although the axial extent of the non-axisymmetric disturbances associated with rotating stall is localized to the compressor, the result of operating in rotating stall is usually reduced annulus averaged pressure rise and mass flow.

Once a compression system enters large amplitude rotating stall, the compression system can also exhibit significant hysterisis [4]. If so, the flow coefficient through the compressor has to be increased to well above the flow coefficient at which the rotating

stall developed before axisymmetric flow is reestablished. Figure 1.2 shows a schematic of a pressure rise versus mass flow coefficient performance characteristic for an axial flow compressor (operating at constant rotational speed) showing the axisymmetric flow region and the annulus averaged compressor performance in large amplitude, rotating stall. The compressor performance remains on the axisymmetric characteristic until the flow rate is reduced below the stalling flow coefficient (Point A). At this point, the flow transitions into rotating stall, moving to Point B. Once in rotating stall, the compressor remains in rotating stall until the mass flow is increased to the mass flow coefficient at which the flow field reverts to axisymmetric flow (Point C).

The operating point of the compressor on the pressure rise versus mass flow performance map at which the essentially steady, axisymmetric flow through the compressor transitions into performance limiting, large amplitude, oscillatory flow is denoted by the stall, or surge, line. In practice, the stall, or surge, line for a given compression system must be determined experimentally, but it generally occurs near the peak of the compressor constant speed pressure rise versus mass flow performance characteristic.

Which form the instability takes in the mature state (rotating stall or surge) has been shown to be related to a non-dimensional compression system stability parameter by Greitzer [2,3]. However, both forms of instability can occur concurrently and interact through non-linearities as the general transient evolves to its final state [5].

Both forms of instability degrade compression system performance and durability and are thus to be avoided. To do this, the compression system must be operated at a safe margin from the stall (or surge) line at all times. Since the stall line (or surge line) can be near operating points with the greatest pressure rise and efficiency, this constraint is often observed at the cost of overall compression system efficiency.

The goal of this research is to use aeromechanical feedback to reduce the flow rate at which axisymmetric flow becomes unstable, thereby extending the useful flow range of compression systems.

1.2 Previous Work on Dynamic Feedback Stabilization

Although rotating stall and surge in compression systems have been extensively studied by numerous researchers [1], dynamic feedback stabilization of rotating stall in axial flow compressors is a relatively new field. The review of previous work presented in this thesis is limited to research that has directly lead to the present investigation. For a review of work on rotating stall and surge in compression systems, the reader is referred to review papers on the subject [1, 5].

In 1976, Greitzer [2,3] identified a non-dimensional compression system stability parameter which parameterized the resultant form of instability encountered at low flow rates in axial flow compression systems. This work illuminated the distinct differences between rotating stall and surge, and provided a predictive technique to isolate the two types of instabilities in axial flow compressors. This parameter, known as the B-parameter, was defined as:

$$B \equiv \frac{U_R}{2\,\omega_H\,L_c} \tag{1.1}$$

where: U_R = compressor wheel speed

ω_H = Helmholtz frequency of compression system

L_c = Equivalent length of inlet ducting

Compression systems with low B-parameters were shown to exhibit rotating stall in the absence of surge, while compression systems with large B parameters were subject to

surge. By studying compression systems with low B-parameters, rotating stall could be examined independently from surge.

In 1986, Moore and Greitzer [6,7] published a model for general compression system instabilities. The papers presented the idea that fully developed rotating stall and surge were actually large amplitude, limit cycle oscillations of initially small amplitude, essentially linear, instabilities. A schematic of the rotating stall inception process predicted by the model is shown in Figure 1.3, which presents the axially velocity through the compressor at a fixed circumferential position during stall inception. The flow is predicted to evolve from axisymmetric flow into fully developed rotating stall via smoothly growing, traveling wave disturbances. The stall inception process shown in Figure 1.3 represents the transition from Point A to Point B on the steady state compression system performance map shown in Figure 1.2. A schematic showing the circumferential variations of the small amplitude, essentially linear, traveling disturbances modeled by the Moore-Greitzer model, and a flow field experiencing fully developed, rotating stall is shown in Figure 1.4.

In 1989, Epstein et al [8], proposed that compression system instabilities such as rotating stall and surge could be suppressed using feedback control. The growth rate of the initial disturbances, and hence the stability of the compression system, was viewed as determined by the small amplitude, unsteady dynamics. Since the control of instabilities could be enacted while the perturbations were small, little steady state power would be required to stabilize the compression system (several orders of magnitudes below the steady state power of the compression system). Calculations of rotating stall and surge predicted that substantial stable flow range extension due to feedback control could be achieved.

Under the influence of feedback control as proposed by Epstein et al. [8], the steady state performance of the compression system is determined by the axisymmetric performance of the compression system. By allowing the flow field to remain essentially steady and axisymmetric, dynamic feedback can extend the stable operating range of the compression system as illustrated in Figure 1.5.

Since this concept was first presented, several authors have used feedback control to stabilize the one-dimensional instability, surge, in compression systems [9,10,11], validating the basic concept presented by Epstein et al. [8]. Much less work has been done, however, in applying dynamic feedback stabilization to rotating stall in axial flow compressors.

Stability models of the compression system predict the existence of small amplitude, non-axisymmetric, disturbances to exist prior to large amplitude, performance limiting, rotating stall. The first evidence that small amplitude, traveling waves existed before the onset of large amplitude rotating stall was presented by MacDougal [12] in a single stage compressor. Subsequently, similar waves were also observed in multi-stage compressors by Garnier [13] and by Longley [14]. Analysis of the traveling waves showed that the rotating stall dynamics of the compression systems investigated were adequately modeled by the Moore-Greitzer model.

Although these results gave confidence in the model, several other studies of rotating stall inception demonstrated that there was also a different mechanism that lead to rotating stall [15]. For a number of compressors, rotating stall appeared to emerge from a localized, but finite amplitude, three-dimensional disturbance which contained significant span-wise non-uniformity. The formation of the localized disturbance was not captured

by the two-dimensional stall inception process described in the Moore-Greitzer model [6,7].

At present, the parameters of the compression system which determine the nature of the stall inception process, i.e. two-dimensional or three-dimensional inception, of a given compression system are not known. For a given compression system the process must, therefore, be determined experimentally. The experiments show, however, that there exists a broad class of compressors for which two-dimensional stability models adequately model the stall inception process.

The first successful attempt to extend the stable flow range of an axial flow compressor using feedback was carried out by Day [16] on a low-speed, multi-stage compressor. The control strategy extended the stable flow range by sensing small amplitude perturbations in axial velocity and, when the perturbations reached a pre-determined amplitude, actuating the flow field via an array of injection valves that injected high pressure fluid into the tip region of the rotor. Although the control strategy used by Day does not appear to function by modifying the linearized unsteady dynamics of the compression system, as proposed by Epstein et al. [8], the results gave the first experimental evidence that introducing disturbances linked to the oscillations of the compression system prior to the onset of rotating stall could significantly change the stalling flow coefficient.

In 1993, Paduano et al. [17], working with a single stage compressor which exhibited small amplitude, traveling waves prior to stall, extended the stable flow range of an axial flow compressor using feedback control to modify the linearized, small amplitude rotating stall dynamics of the compression system. A spatial array of twelve movable inlet guide vanes, located around the annulus at the face of the compressor were used to actuate the flow field. The control strategy was based on viewing the flow field as a

summation of spatial Fourier harmonics. The array of movable inlet guide vanes actuated individual spatial harmonics based on the magnitude and spatial phase of the harmonics of the axial velocity perturbation sensed by a spatial array of hot-wires. To implement the feedback, a high-speed digital computer was used to perform real-time, spatial Fourier decomposition of the flow field.

Paduano's experimental results, followed by similar results of Haynes [18] on a multistage compressor, demonstrated that control strategies designed to modified the small amplitude, two-dimensional dynamics could extend the stable flow range, directly validated the concepts presented by Epstein et al.

1.3 Objectives of Present Study

The experiments of Day [16], Paduano [17], and Haynes [18] were successful proof-of-concept demonstrations of active stabilization of rotating stall in axial flow compressors. However, many issues remain unresolved, concerning not only the control, but also the basic fluid dynamic issues of compression system instabilities. This work is directed at developing a better understanding of the role that dynamic feedback plays in the compression system dynamics and developing an alternative approach to implement dynamic feedback.

Previous control strategies have been based on electro-mechanical implementation of feedback. These required extensive real time computation and high bandwidth sensors and actuators. One can also devise control strategies that employ aeromechanical feedback These have several potential advantages, including stabilization without external input, and the elimination of the need for high bandwidth sensors and actuators. The constraints inherent to aeromechanical feedback stabilization, however, require a different approach than the modal based control strategies used by previous researchers.

The primary objective of this research was to develop, and experimentally demonstrate, a strategy to stabilize rotating stall in axial flow compressors using aeromechanical feedback. The research to be described can be classified into two main phases, analytical and experimental. The goals of the analytical phase were:

1) Define the physical mechanism of instability onset in axial flow compressors in sufficient detail to interpret the role of dynamic feedback in enhancing stability.
2) Based on analytic models, develop a strategy to implement aeromechanical feedback stabilization of rotating stall.

The goals of the experimental phase were:

1) Demonstrate aeromechanical feedback stabilization of rotating stall
2) Evaluate the analytical model of the flow field through the compressor

Since aeromechanical feedback is a subset of the general subject of feedback stabilization, the results of this research contribute to the knowledge base in the field of dynamic control of compression system instabilities.

1.4 Scope of Present Research

The scope of this work was limited to the study of the small amplitude, unsteady compression system behavior associated with rotating stall inception in axial flow compressors, and the influence of dynamic feedback on the compression system dynamics and stability. Detailed study of the steady state compression system performance and large amplitude (post stall inception) rotating stall was not performed.

1.5 Overview of Present Study

The thesis is organized in the following manner:

Chapter 1: Introduction - The general problem of rotating stall in axial flow compressors is introduced and the concept of feedback stabilization of rotating stall is developed. Previous work in the field is reviewed and the motivation and objectives of the present study are presented.

Chapter 2: Modeling Rotating Stall Dynamics - The basic model of the rotating stall dynamics is presented and the physical mechanism behind rotating stall is discussed. The role of dynamic feedback in stabilizing the compression system is addressed and the present aeromechanical feedback strategy is motivated. The effect of aeromechanical feedback is modeled and a parameter optimization study is performed to determine a design configuration for the experimental phase of the research.

Chapter 3: Experimental Facility - The experimental facility is described.

Chapter 4: Experimental Results and Comparison with Theory - The results of the experimental investigation are presented and the results are compared with the analytical model.

Chapter 5: One-Dimensional Acoustic Oscillations in Compression Systems - During the experimental phase of the research, large amplitude acoustic oscillations were observed near the stalling flow coefficient for the compression system with aeromechanical feedback. This chapter presents an analysis of the acoustic oscillations in a compression system and discusses the implications of such oscillations on dynamic control of compression system instabilities.

Chapter 6 Discussion - This chapter discusses the experimental results. Attention is given to the implications of the results for the general problem of extending the stable flow range of compression systems.

Chapter 7: Summary, Conclusions and Recommendations - Results and conclusions of this research are summarized. Recommendations for future work on understanding, and enhancing, the stability of compressor flow fields are presented.

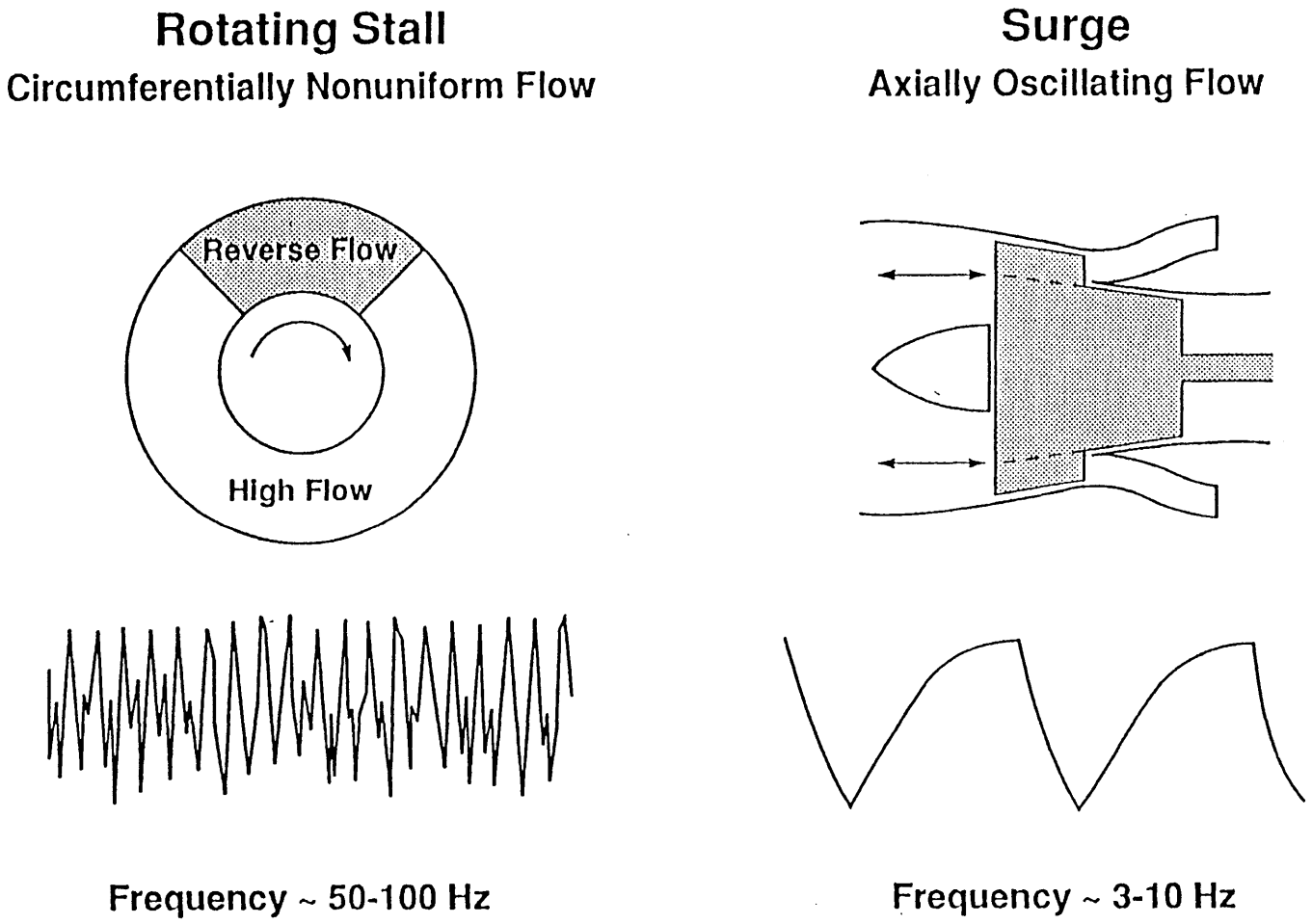

Figure 1.1: Schematic of Rotating Stall and Surge in Axial Flow Compressors

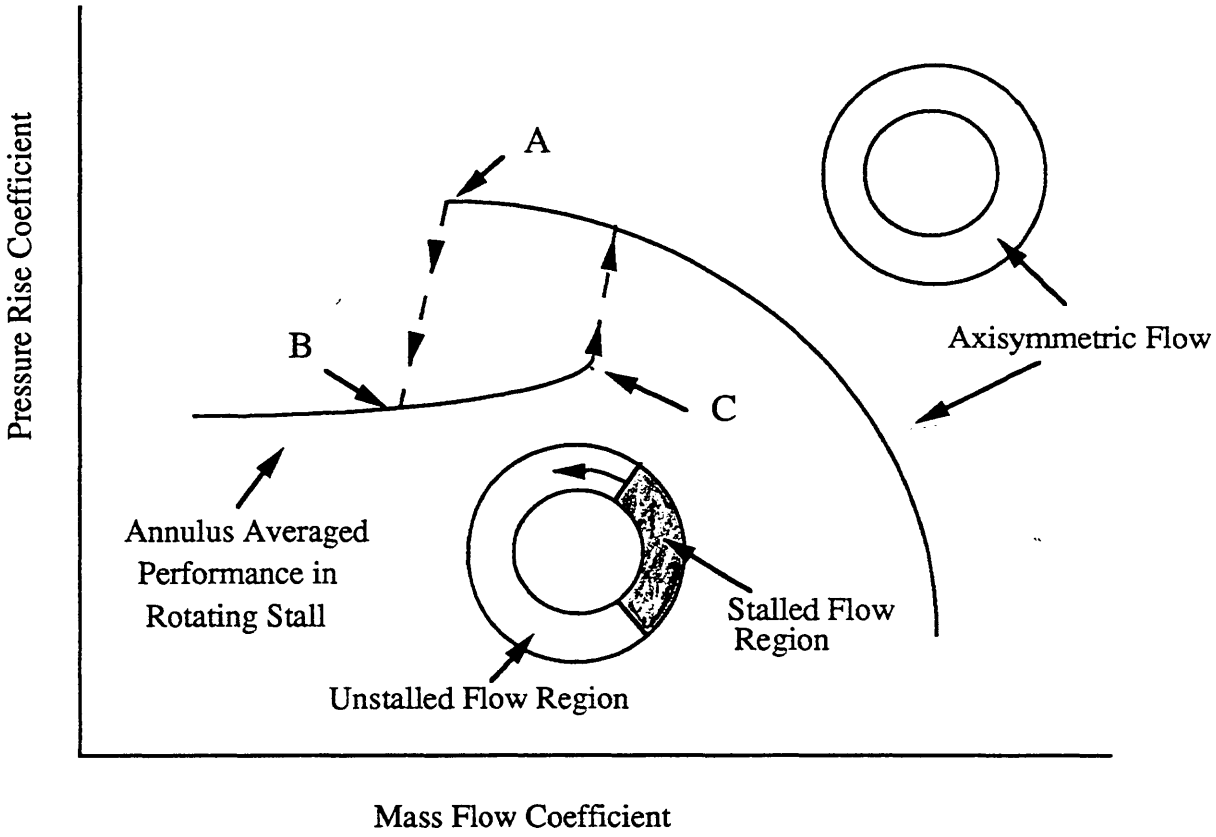

Figure 1.2: Compressor Pressure Rise versus Mass Flow Performance Characteristic, Showing Axisymmetric Performance and Performance in Rotating Stall

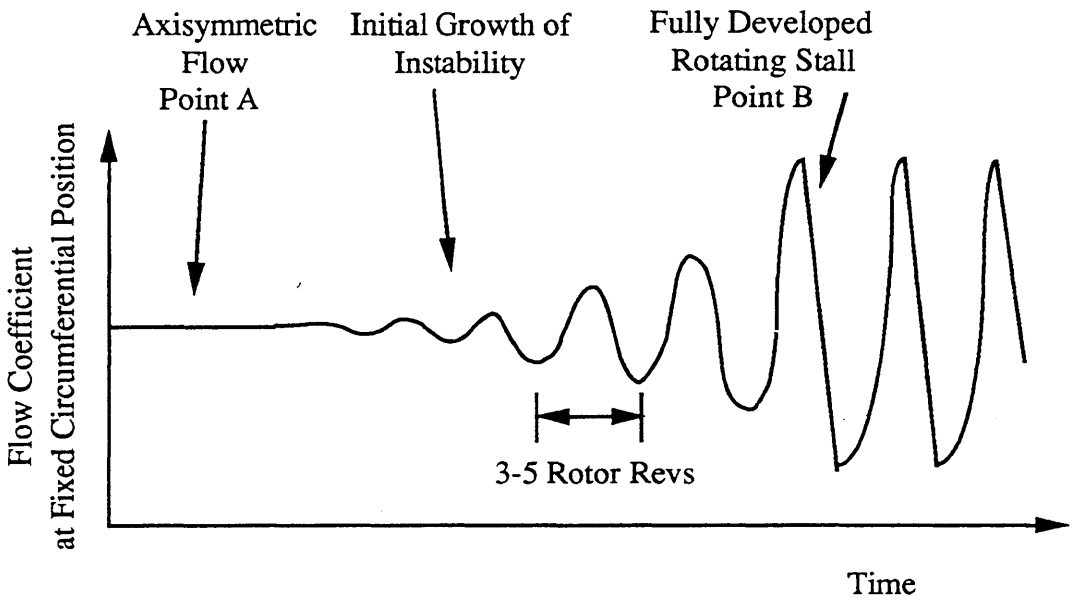

Figure 1.3: Schematic of Axial Velocity through Compressor at a Fixed Circumferential Position During Stall Inception Process

Small amplitude circumferential traveling waves:

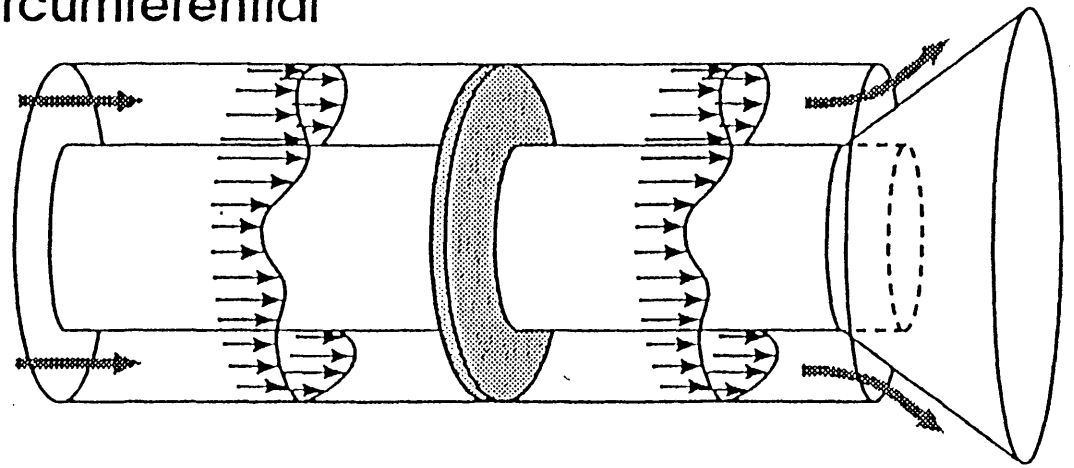

Large amplitude nonlinear 'rotating stall' cell:

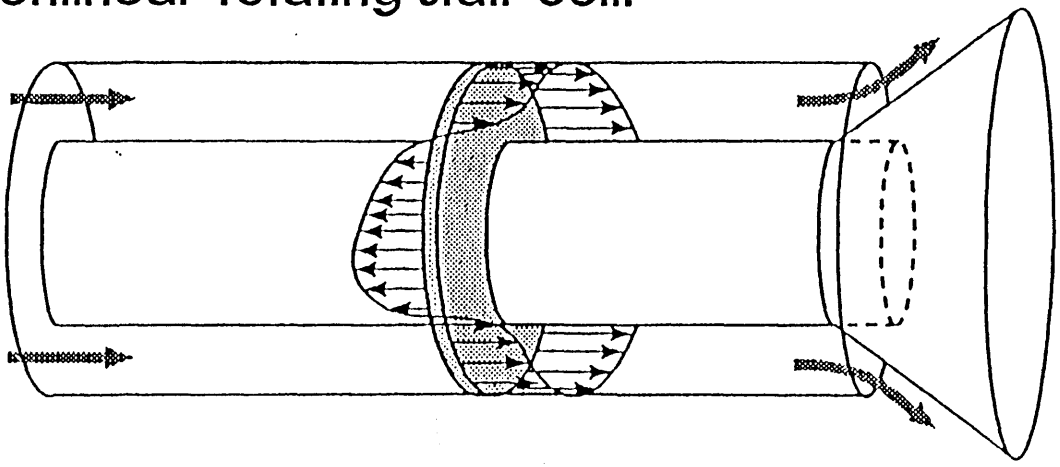

Figure 1.4: Schematic of Small Amplitude, Traveling Wave Disturbances and Large Amplitude, Performance Limiting Rotating Stall

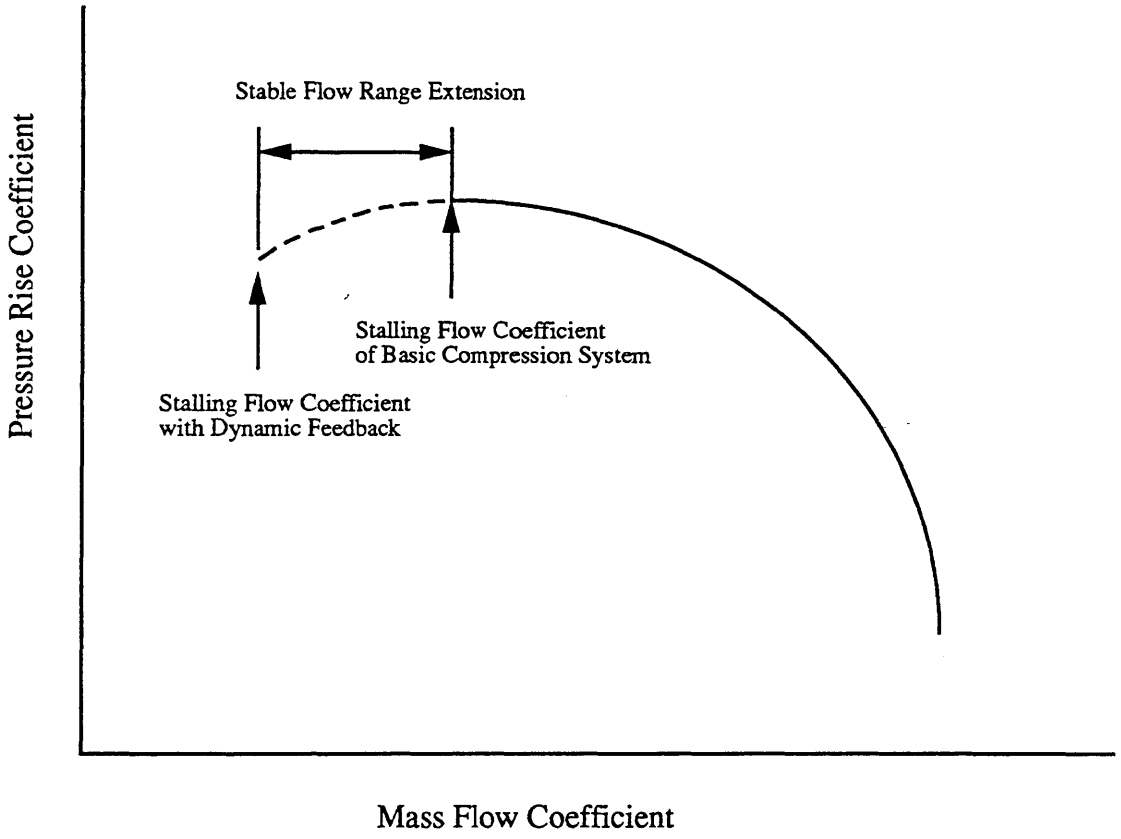

Figure 1.5: Compressor Performance Characteristic Showing Stable Flow Range Extension Due to Dynamic Feedback

Chapter 2: Modeling Rotating Stall Dynamics

In this Chapter, the stability model for the basic compression system is presented and the mechanism responsible for rotating stall is discussed. The present aeromechanical control strategy is proposed and the stability model is modified to incorporate the effect of this control strategy. The effect of aeromechanical feedback on the compression system is assessed using linearized stability analyses and non-linear numerical simulations.

2.1 Introduction to Model

The basic form of the model used to predict the behavior of linearized, small amplitude perturbations about a steady, uniform flow field was first developed by Moore [19] with additional contributions to the model presented by Moore and Greitzer [6,7] and Hynes and Greitzer [20]. The model assumes that fully developed rotating stall is a large amplitude, limit cycle oscillation of an initially linear instability. The stability of the flow field is governed by the linearized compression system dynamics. The model predicts that small disturbances in an unstable flow field will grow (initially exponentially) with time into large amplitude, performance limiting, rotating stall. The model describes the stability of the axisymmetric flow field as well as the structure of the rotating stall inception process.

2.1.1 Assumptions and Limitations of the Model

Before developing the details of the fluid dynamic model, its inherent assumption and limitations will be discussed. The results are intended to be applicable only to compression systems in which the follow assumptions are valid.

1) The flow is incompressible. This assumption is justified since this work focuses on rotating stall in compressors with tip speeds well below Mach 1. Since the effect of compressibility scales with the square of the compressor Mach number, the assumption of incompressible flow is valid throughout the flow field.

2) The flow is inviscid outside of the blade rows. This assumption is justified since Reynolds numbers based on disturbance length scales are large, and the behavior outside the blade rows can be reasonably approximated as inviscid. The Reynolds number for the disturbance flow field based on the length scale of the disturbance is on the order of:

$$Re \approx \frac{10^6}{n}$$

where: n = spatial harmonic number of disturbances

3) The flow field is two-dimensional in the circumferential and axial directions. This assumption limits the applicability of the model to compressors that exhibit little span-wise variation in mean flow and in perturbation quantities, and constrains the analysis to compressors with hub to tip radius ratios approaching unity. It should be pointed out that requiring the compression system to have a near unity hub to tip radius ratio is a necessary but not sufficient condition for determining the applicability of the two-dimensional model to a given compression system. As stated previously, there is substantial evidence that a two-dimensional model of the stall inception process is not adequate for some compressors, independent of hub to tip radius ratio. However, as experimentally demonstrated, there do exist many compressors for which the two-dimensional model is adequate; this research is focused on that class of compressors.

4) Long ducts exist upstream and downstream of the compressor. This assumption requires that constant area, annular ducts extend several compressor radii upstream and downstream from the compressor. This is not, in any sense, a fundamental restriction to the model, but, long ducts are necessary to study the stability of the compressor in isolation from any other flow elements.

5) The compressor can be modeled as a semi-actuator disk. The assumption that the compressor can be modeled as an actuator (or semi-actuator) disk requires that the inter-blade phase angle for the rotating stall disturbances is small, and therefore, the effect of the blade to blade variations within the compression system do not significantly affect the long wave length compression system dynamics. The term semi-actuator disk is used because the model of the compressor accounts for the finite length of the compressor by modeling the inertia of the fluid within the blade rows.

6) The mean flow field is uniform. The uniform flow field assumption implies that there are no circumferential non-uniformities in the annulus averaged quantities entering the compressor. Thus, this analysis is not applicable to compressor operation with inlet distortion.

7) Surge dynamics can be neglected. This model considers only zero-mean non-axisymmetric disturbances. It is thus suitable only for compression systems in which zero order, annulus averaged disturbances can be neglected, i.e. compression systems with a low B parameters.

2.1.2 Perturbation Variables

The model will be presented in non-dimensional form. The steady state and perturbation quantities are non-dimensionalized by the follow quantities specific to each compression system:

R	=	Mid-Span Radius of Compressor
U_R	=	Mid-Span Wheel Speed of Compressor
$\frac{1}{2}\rho U_R^2$	=	Dynamic Head based on wheel speed

The independent variables of the flow field are non-dimensional axial position, circumferential position, and time:

x	=	axial distance / mid-span radius
θ	=	circumferential position around the annulus
τ	=	(time) x (U / R) (non-dimensional time)

The non-dimensional perturbation variables of the disturbance flow fields are functions of non-dimensional temporal and spatial coordinates.

$\delta p_S(x, \theta, \tau)$	=	$(\delta P_s)/(\frac{1}{2}\rho U_R^2)$ = Static pressure perturbations
$\delta p_t(x, \theta, \tau)$	=	$(\delta P_t)/(\frac{1}{2}\rho U_R^2)$ = Total pressure perturbations
$\delta\Psi(x, \theta, \tau)$	=	$(\delta P_{s_d} - \delta P_{t_u})/(\frac{1}{2}\rho U_R^2)$ = Perturbation in total to static pressure rise coefficient
$\delta\phi(x, \theta, \tau)$	=	$\delta C_x / U_R$ = Axial velocity perturbations
$\delta v(x, \theta, \tau)$	=	$\delta C_\theta / U_R$ = Circumferential velocity perturbations

2.1.3 Compression System Parameters

The mean compression system operating parameters are assumed to be uniform in time and space. The parameters that determine the linearized compression system dynamics, and hence, the stability of the flow field to non-axisymmetric disturbances, are given by:

$\frac{\partial \Psi}{\partial \Phi}$ = Slope of the steady state, inlet total to exit static compressor characteristic

λ = Inertia of fluid within Rotating blade rows [20]

$$\lambda = 2 \sum_{\text{Rotor}} \frac{c/R}{\cos \gamma_R} \tag{2.1}$$

μ = Inertia of fluid within all blade rows [20]

$$\mu = \lambda + 2 \sum_{\text{Stator}} \frac{c/R}{\cos \gamma_S} \tag{2.2}$$

The mass flow coefficient, defined as, :

$$\Phi = \frac{\dot{m}}{\rho A U_R} = C_x / U_R \tag{2.3}$$

enters the stability analysis implicitly. The mass flow coefficient and the slope of the steady state compressor characteristic are related through the steady state, constant speed, compressor performance characteristic, in which the inlet total to exit static pressure rise coefficient across the compressor is assumed to be a pure function of the mass flow coefficient.

$$\Psi = \Psi(\Phi) = \frac{P_{s_d} - P_{t_u}}{\frac{1}{2} \rho U_R^2} \tag{2.4}$$

2.2 Components of Stability Model

An unwrapped schematic of the two-dimensional model of the compressor flow field is shown in Figure 2.1. The coordinates are the circumferential and axial directions. The model consists of three components:

1) an incompressible, irrotational upstream flow field

2) the compressor, modeled as a semi-actuator disk

3) an incompressible, vortical flow field downstream of the compressor

The stability problem is posed as an eigenvalue problem. As such, the equations of motion governing the behavior of the small amplitude, non-axisymmetric perturbations are derived and natural modes of the system are determined by solving for non-trivial solutions to the homogeneous equations of motion. The details of the stability model are derived in Appendix A, but, an outline of the model is given below.

The axial and circumferential structure of the disturbances satisfy the governing equations in the upstream and downstream flow fields. The solutions are expressed in the form of traveling waves, decomposed into spatial harmonics. The perturbations in the upstream and downstream flow fields are matched across the compressor, modeled as a semi- actuator disk, by appropriate kinematic and dynamic boundary conditions. For the problem as posed, the stability of the individual spatial harmonics of the compression system are uncoupled and therefore, stability can be assessed on a harmonic by harmonic basis.

2.2.1 Upstream Flow Field

For simplicity, the mean upstream flow field is assumed to be uniform and axial, although the model can be modified to include an upstream flow field with mean swirl.

The analysis is performed using a non-dimensional, two-dimensional streamfunction (Ψ) defined by:

$$\delta\phi \equiv \frac{\partial \Psi}{\partial \theta} \quad \text{and} \quad \delta v \equiv -\frac{\partial \Psi}{\partial x} \qquad (2.5) \text{ and } (2.6)$$

where: $\delta\phi$ is normalized axial velocity perturbation and δv is normalized circumferential velocity perturbation

The disturbance streamfunction for the incompressible, irrotational upstream flow field must satisfy the Laplace equation and the disturbances must be bounded far upstream of the compressor. This leads to the following form for traveling wave solutions for the perturbation streamfunction in the upstream flow field:

$$\Psi_u = \sum_{n=1}^{+\infty} A_n e^{in(\theta - \sigma\tau) + nx} \qquad (2.7)$$

where: A_n is the Complex spatial Fourier component of the nth harmonic of upstream streamfunction, and σ is the complex, temporal eigenvalue

2.2.2 Downstream Flow Field

The mean flow in the downstream flow field is also assumed to be uniform and axial. This assumption does not affect the basic form of the model, and can be modified to include mean swirl, as has been done by many previous authors. However, assuming axial flow simplifies the results of the stability analysis and allows the physics of compression system instabilities to be more easily interpreted.

In the rotational, incompressible downstream flow field, the perturbation streamfunction must obey a Poisson equation as developed in Appendix A. The perturbations in the downstream flow field must be of the same temporal and circumferential structure of the

upstream flow field at the actuator disk. The downstream streamfunction is expressed as a superposition of a potential and a vortical flow field:

$$\Psi_d = \sum_{n=1}^{+\infty} B_n e^{in(\theta-\sigma\tau)-nx} + \sum_{n=1}^{+\infty} C_n e^{in(\theta-\sigma\tau)+in\frac{\sigma}{\Phi}x} \tag{2.8}$$

where: B_n is the Complex spatial Fourier component of the nth harmonic of downstream potential streamfunction, and C_n is the Complex spatial Fourier component of the nth harmonic of downstream vortical streamfunction.

2.2.3 Matching Conditions across the Compressor

The homogeneous equations of motion governing the small amplitude disturbances are defined by matching the upstream and downstream flow fields across the compressor. The three matching conditions imposed on the upstream and downstream flow fields are:

1) mass flow is continuous across the compressor
2) pressure rise across the compressor is a specified function of flow
3) angle of the flow exiting the compressor is fixed by blade exit angle

Mass conservation across the compressor

The flow through the compressor is assumed to be incompressible, and the axial flow perturbations are assumed to extend through the compressor. The axial velocity perturbations must therefore be continuous across the compressor at a given circumferential location.

$$\delta\phi_u = \delta\phi_d \tag{2.9}$$

Pressure rise across the compressor

The expression for the pressure rise across the compressor is derived by assuming that the compressor performance follows its linearized steady state performance characteristic except for the inertial effects due to the fluid within the blade rows of the compressor. The local pressure rise is assumed to be a pure function of the local mass flow coefficient, i.e. the compressor is taken to be insensitive to inlet swirl disturbances.

The compressor performance model requires that the reduced frequency of the disturbances is small. The reduced frequency is defined as:

$$f_{red} \equiv \frac{\omega c}{C_x} \tag{2.10}$$

For harmonic, traveling waves the reduced frequency for the rotor and stator are given by:

$$f_{red} = (1 - \omega_{rs}) \frac{c}{R} \frac{1}{\Phi} \text{ (for Rotor)} \tag{2.11}$$

$$f_{red} = (\omega_{rs}) \frac{c}{R} \frac{1}{\Phi} \text{ (for Stator)} \tag{2.12}$$

where ω_{rs} = Real(n σ) is the temporal frequency associated with the traveling wave disturbances as observed at a fixed circumferential position. For the first three spatial harmonics, the reduced frequencies for the rotor and stator are both well below unity.

The unsteady effects due to the inertia within the blade rows is included in the model because it adds an essential feature, as developed below. Accounting for the inertia of the fluid within the stationary and rotating blade rows [20] leads to the following expression for the pressure rise across the compressor:

$$\delta\Psi = \delta p_{s_d} - \delta p_{t_u} = \frac{\partial \Psi}{\partial \Phi}\delta\phi - \lambda\frac{\partial \phi}{\partial \theta} - \mu\frac{\partial \phi}{\partial \tau} \tag{2.13}$$

Exit Flow Angle

The flow angle of the fluid exiting the stator into the downstream duct is assumed to be fixed by the angle of trailing edge of the blade row. This assumption is reasonable for compressors with high solidity blading in the last blade row. For the case of interest here, the flow in the downstream duct is axial, so the circumferential component of velocity entering the downstream flow field is zero.

$$\delta v_d = 0 \tag{2.14}$$

The matching conditions across the compressor can be modified without changing the basic structure of the stability model. As examples, several authors have investigated the effects of introducing unsteady compressor performance [15, 31], swirl sensitivity [14], unsteady deviation [15] and other effects. The assumptions listed above, however, suffice to yield a useful representation of the rotating stall inception process in the class of axial flow compressors considered.

2.3 Stability Analysis for Basic Compression System

As developed in Appendix A, the homogeneous equation for the nth spatial harmonic of the upstream streamfunction is given by:

$$\left[i\sigma(4 + n\mu) + \frac{\partial \Psi}{\partial \Phi} - i n \lambda \right] A_n = 0 \tag{2.15}$$

For non-trivial solutions to exist for Eq. 2.15, the term in the square bracket must be zero. The eigenvalues are given by:

$$\sigma = \frac{i\frac{\partial \Psi}{\partial \Phi} + n\lambda}{4 + n\mu} \tag{2.16}$$

The imaginary part of the eigenvalue, σ, determines the growth rate of the disturbances and the real part of the eigenvalue determines the rotation rate of the disturbances. The growth rate of the disturbances is given by:

$$\text{growth rate} = e^{n\left(\frac{\frac{\partial \Psi}{\partial \Phi}}{4 + n\mu}\right)\tau}$$

Thus, the stability boundary of the compression system occurs at the peak of the total to static pressure rise characteristic, i.e. $\frac{\partial \Psi}{\partial \Phi} = 0$. At neutral stability, the perturbations rotate in a traveling wave form at a frequency given by the real part of σ:

$$\text{Rotation rate} = \frac{n\lambda}{4 + n\mu} \tag{2.17}$$

The non-dimensional frequencies associated with the traveling spatial harmonics observed at a fixed circumferential location are given by:

$$\omega_{rs} = \frac{n^2\lambda}{4 + n\mu} \tag{2.17a}$$

The stability analysis was used to predict the eigenvalues of a given compression system as a function of mass flow coefficient. The compressor pressure rise versus mass flow performance characteristic shown in Figure 2.2 is representative of a low speed

compressor and was used in the analysis. For the initial calculations the inertial parameter for the fluid in the rotating blade rows was taken to be ($\lambda = 1.0$) and the inertial parameter for the fluid within all the blade rows was taken to be ($\mu = 2.0$). This corresponds to a compressor with fluid inertia equally distributed between the rotating and stationary blade rows.

Figure 2.3 shows the behavior of the eigenvalues of the basic compression system parameterized by the mass flow coefficient for the three lowest spatial harmonics. The rotation rate for the first, second and third spatial harmonics is 17%, 25%, and 30% of rotor frequency, respectively, independent of mass flow coefficient, and hence slope of the compressor characteristic. However, as the mass flow coefficient is decreased, corresponding to increasing the slope of the compressor characteristic, the temporal decay rate, or damping rate, of the disturbances decreases until the axisymmetric flow field becomes unstable when the mass flow coefficient is reduced below the value at which the characteristic peaks. At the peak of the total to static characteristic ($\Phi = 0.528$), all spatial harmonics are predicted to become unstable simultaneously.

In summary, the individual compression system parameters play the following role in the predicted behavior of the non-axisymmetric disturbances.

1) The slope of the compressor characteristic, $\frac{\partial \Psi}{\partial \Phi}$, determines the stability of the compression system.

2) The inertial parameters affect the growth (or decay) rate and the rotation rate of the perturbations, but have no direct influence on system stability.

2.4 Unsteady Energy Considerations

The transition of the axisymmetric flow field into large amplitude rotating stall is a self-excited oscillation. In this section, the rotating stall dynamics will be discussed in terms of the energy balances needed to maintain this oscillation. The destabilizing mechanism associated with a positive compressor slope can be interpreted using energy balances for the unsteady perturbations. For an given oscillatory disturbance, if the system generates a net positive amount of unsteady energy (averaged over a cycle), the disturbance will grow. Whereas, if the system generates a negative amount of unsteady energy over a cycle (i.e. dissipates), the disturbance will decay [21].

2.4.1 Unsteady Energy Production

The rate at which the compressor performs work for a perturbation in volume flow around the annulus of the compressor can be defined as the product of the pressure rise perturbation and the axial velocity perturbation integrated over the annulus.

$$\delta E \equiv \int_{Annulus} \delta\Psi \, \delta\phi \quad dA \tag{2.18}$$

where, $\delta\Psi$ is the perturbation in total to static pressure rise coefficient across the compressor and $\delta\phi$ is the perturbation in flow coefficient through the compressor. The above definition of the unsteady energy is not a rigorous definition of unsteady energy, and is somewhat arbitrary. However, the quantity defined in Equation (2.18) does represent a useful quantity that scales with the square of the perturbation quantities and has the units of non-dimensional energy production.

The pressure rise across the compressor is related to the mass flow perturbation by the compressor pressure rise boundary condition described in section 2.2.3. The relation

between pressure rise across and mass flow oscillations through the compressor can be expressed in terms of a compressor transfer function.

$$M(s) \equiv \frac{\delta\Psi(s)}{\delta\phi(s)} = \text{Real}(M(s)) + i\,\text{Imag}(M(s)) \tag{2.19}$$

For a disturbance in axial velocity, the unsteady energy production, by the compressor, as defined in Eq. (2.18), is given by integrating the product of the pressure rise perturbation and the axial velocity perturbation over the annulus of the compressor. A harmonic perturbation in axial velocity can be represented by:

$$\delta\phi = \text{Real}\left(\tilde{\phi}\, e^{in\theta}\right) = \text{Real}\left(\tilde{\phi}\right)\cos(n\theta) - \text{Imag}\left(\tilde{\phi}\right)\sin(n\theta) \tag{2.20}$$

where $\tilde{\phi}$ is complex amplitude of the velocity disturbance of the nth spatial harmonic.

Using Eq. 2.19, the corresponding perturbation in pressure rise across the compressor is given by:

$$\delta\Psi = \text{Real}\left(M(s)\,\tilde{\phi}\, e^{in\theta}\right) = \text{Real}(M(s))\left[\text{Real}\left(\tilde{\phi}\right)\cos(n\theta) - \text{Imag}\left(\tilde{\phi}\right)\sin(n\theta)\right]$$

$$- \text{Imag}(M(s))\left[\text{Imag}\left(\tilde{\phi}\right)\cos(n\theta) + \text{Real}\left(\tilde{\phi}\right)\sin(n\theta)\right] \tag{2.21}$$

Integrating the product of the axial velocity perturbation and the pressure rise perturbation shows that only the component of pressure rise in phase with the axial velocity perturbation, i.e. the component determined by the real part of the compressor transfer function, affects the unsteady energy production, and hence, the stability of

system. The unsteady energy produced by the compressor for a harmonic disturbance is given by:

$$\delta E = \text{Real}\,(M(s))\,\pi\left(\left(\text{Real}(\tilde{\phi})\right)^2 + \left(\text{Imag}(\tilde{\phi})\right)^2\right) = \text{Real}\,(M(s))\,\pi\left|\tilde{\phi}\right|^2 \qquad (2.22)$$

Thus, the sign of the real part of the compressor pressure rise versus mass flow transfer function determines whether the compressor produces or dissipates unsteady energy.

Using Equation (2.13) to evaluate the compressor pressure rise versus mass flow coefficient transfer function for a harmonic perturbation in axial velocity in the form of a traveling wave leads to:

$$M(s) \equiv \left(\frac{\delta\Psi(s)}{\delta\phi(s)}\right)_{(s = in(\theta - \sigma\tau))} = \frac{\partial\Psi}{\partial\Phi} + in\,(\mu\sigma - \lambda) \qquad (2.23)$$

where σ is purely real

In this model, the slope of the steady state compressor characteristic determines the real part of the compressor transfer function, independent of temporal and spatial frequency. At neutral stability, the slope of the compressor characteristic determines the component of pressure rise in phase with the mass flow perturbations.

$$\text{Real}\,(M(s)) = \frac{\partial\Psi}{\partial\Phi} \quad \text{(at neutral stability)} \qquad (2.24)$$

For a harmonic disturbance in axial velocity through the compressor, the unsteady energy produced by the compressor is determined solely by the slope of the compressor characteristic:

$$\delta E = \frac{\partial \Psi}{\partial \Phi} \pi \left| \tilde{\phi} \right|^2 \tag{2.25}$$

Thus, for positive slopes, the compressor produces unsteady energy and the disturbances are predicted to grow. For negative slopes, the compressor dissipates unsteady energy and the disturbances decay, consistent with the results from the eigenvalue analysis.

Energy arguments also offer a physical interpretation of the result, from linear analysis, that the inertial terms do not directly affect the stability of the compression system. At neutral stability, the inertia of the fluid within the blade rows produces a component of pressure rise out of phase with the mass flow perturbations. It therefore does not directly effect the stability of the system.

$$\text{Imag}\ (\ M(s)) = n\ (\ \sigma \mu - \lambda\ ) \tag{2.26}$$

2.4.2 Definition of a Conserved Quantity

The unsteady energy analysis presented in section 2.4.1 gives a useful interpretation of the roles of the compression system parameters in determining the stability of the flow field. However, if one evaluates the mechanical work performed by the compressor on a harmonic mass flow perturbation, one finds that the mechanical work produced by the compressor is determined by the product of the axial velocity perturbations and the change in total pressure across the compressor. The compressor is thus energetically neutral when the slope of the inlet total to exit total pressure rise characteristic is zero. The total to total pressure rise characteristic is defined as:

$$\Psi_{tt} = \frac{P_{t_d} - P_{t_u}}{\frac{1}{2} \rho U_R^2} \tag{2.26a}$$

The stability analysis predicts, however, that the axisymmetric flow becomes neutrally stable when the slope of the total to static characteristic is zero. The slope of the total to total compressor characteristic is related to the slope of the total to static compressor characteristic by:

$$\frac{\partial \Psi_{tt}}{\partial \Phi} \equiv \frac{\partial \Psi_{ts}}{\partial \Phi} + 2\,\Phi \tag{2.27}$$

When the slope of the total to static characteristic is zero, the slope of the total to total characteristic is positive, $\frac{\partial \Psi_{tt}}{\partial \Phi} = 2\,\Phi$, indicating that the compressor is adding energy to disturbances at neutral stability.

To reconcile these two results, we can examine the linearized equations of motion to define a second order quantity that is conserved in an inviscid, incompressible flow. Equation (2.28) is a statement of such a quantity (in dimensional form) derived from the linearized momentum and continuity equations. The details of the analysis are given in Appendix D.

$$\rho \frac{\partial \left(\frac{\delta u^2 + \delta v^2}{2} \right)}{\partial t} + \nabla \cdot \left[\rho \frac{\delta u^2 + \delta v^2}{2} \vec{U} + \delta P_s \left(\delta u \vec{i} + \delta v \vec{j} \right) \right] = 0 \tag{2.28}$$

The above expression represents a conservation equation for the vector field, $\vec{F}$, in the square brackets.

$$\vec{F} \equiv \left[\rho \frac{\delta u^2 + \delta v^2}{2} \vec{U} + \delta P_s \left(\delta u \vec{i} + \delta v \vec{j} \right) \right] \tag{2.29}$$

The role that $\vec{F}$ (termed the *perturbation intensity*) plays in a two dimensional, linearized, incompressible, inviscid flow is similar to the role that acoustic intensity plays in an acoustic flow field in the absence of mean velocity [22].

Using the result that the perturbation intensity is conserved in the upstream and downstream flow fields, the role of the compressor at neutral stability can be examined. Applying the Divergence Theorem to evaluate the time averaged value of the perturbation intensity for harmonic disturbances within a volume of fluid in which the linearized momentum and continuity equations apply, shows that the time averaged flux of the perturbation intensity, $\vec{F}$, through a closed surface that surrounds the volume is equal to zero. The contribution to the annulus averaged, or equivalently the time averaged, flux of perturbation intensity across a control surface from regions of the flow field in which the flow is not governed by the linearized equations of motions used to derive the conservation principle can be expressed as a source term.

$$\int_{\text{Surface}} \left[\rho \frac{\delta u^2 + \delta v^2}{2} \vec{\vec{U}} + \delta P_s \left(\delta u \hat{i} + \delta v \hat{j} \right) \right] \cdot \vec{n} \, dS = \text{Source Term} \tag{2.30}$$

For the rotating stall analysis, the only region in which the source term can be non-zero is the compressor, or semi-actuator disk, so the net flux of $\vec{F}$ is zero for any closed surface not containing the compressor.

The results of perturbation intensity audit for the compression system at neutral stability, presented in Appendix D, yield three main points concerning the interpretation of unsteady energy production, or more rigorously, the perturbation intensity, of the compressor at neutral stability. These conclusions are useful in understanding the mechanism responsible for rotating stall in axial flow compressors.

1) The slope of the quasi-steady total to total (or equivalently the slope of the static to static) pressure rise characteristic determines unsteady mechanical energy production by the compressor for a perturbation in mass flow.

2) The vortical flow downstream of the compressor provides a mechanism for the compression system to convect unsteady energy downstream in the form of kinetic energy associated with the vortical perturbations. As shown in Appendix D, at neutral stability, the compressor is acting as a source for the perturbation intensity, which is convected downstream by the vortical mode of the downstream flow field. The magnitude of the vortical mode for a given mass flow perturbation through the compressor is governed by the exit flow angle condition.

3) The condition at which the compressor generates more perturbation intensity than the vortical mode can convect downstream corresponds to the condition for instability. For the compression system modeled (axial flow, constant leaving angle), this condition is satisfied when the slope of the total to static compressor characteristic becomes zero.

2.5 Aeromechanical Feedback

In this section, the conclusions from the above analyses are used to motivate the aeromechanical feedback control strategy. Following a qualitative discussion of the stabilizing effect of the control strategy, a model for the actuation and feedback associated with the aeromechanical control strategy is developed.

2.5.1 Role of Aeromechanical Feedback

From either an energy balance or a linear stability analysis, it is evident that the component compressor pressure rise perturbation which is in phase with the mass flow perturbation plays a dominant role in compression system stability. Said another way, it is the *real part of the compressor pressure rise versus mass flow transfer function that determines system stability.* Using feedback, the real part of the transfer function can be modified so that the steady state compressor characteristic slope will no longer solely determine its real part. The stability of the system can thus be modified, while the steady, axisymmetric performance remains unaltered.

From this point of view, the role of an effective feedback control strategy is to modify the (unsteady, non-axisymmetric) pressure rise versus mass flow transfer function. To illustrate this concept and motivate the present aeromechanical control strategy, consider the control strategy in Figure 2.4. In this strategy, termed dynamic mass / momentum injection, high momentum fluid is injected upstream of the compressor. The amount of high momentum fluid injected at a given circumferential position is governed by a circumferential array of reed valves which react locally to perturbations in the static pressure upstream of the compressor.

The stabilizing mechanism introduced by the proposed aeromechanical control strategy can be qualitatively understood as follows. For an initially steady, axisymmetric flow through the compressor, consider a disturbance which causes a small decrease in axial velocity in one region of the annulus. In this region, the static pressure in the potential flow field upstream of the compressor will increase (neglecting the unsteady effects). The increase in static pressure deflects the reed valves in that region which increases the amount of high momentum fluid injected, and hence, the local mass flow and pressure rise across the compressor. The net result is that the feedback increases the local pressure

rise across the compressor in the region of decreased axial velocity. In terms of the compressor pressure rise versus mass flow transfer function, the feedback serves to add a negative component to the real part of the compressor transfer function.

The effect of the aeromechanical feedback on compressor pressure rise versus mass flow performance is shown schematically in Figure 2.5. For unsteady perturbations, the effective slope of the compression system no longer follows the quasi-steady compressor characteristic, but rather is determined by the combined influence of compressor performance and of the feedback. To assess whether these qualitative ideas can be translated into a useful strategy, a more detailed, quantitative analysis is necessary.

2.5.2 Modeling of Aeromechanical Feedback

The structure of the present control scheme is based on locally reacting feedback control. The sensors and actuators are co-located, modifying the local unsteady pressure rise versus mass flow performance of the compression system. Although this approach differs from previous efforts to stabilize rotating stall based on independent control of the different spatial harmonics [17, 18], the use of aeromechanical feedback lends itself to such locally reacting control strategies. An outline of the stability analysis is presented below, and the details of the analysis are given in Appendix B.

2.5.2.1 Injection

Modeling the effect of injecting high momentum fluid into the upstream flow field on compressor performance is a complex problem. In the model presented below, the jets are assumed to mix out over the span of the annulus before entering the compressor. Another model of the injection process, which assumes that the jets influence the tip region, and therefore, effect the compressor by modifying the flow at the tip of the rotor,

is presented in Appendix C. It is to be noted, however, that both models produce the same qualitative effect, i.e. the local pressure rise increases with increasing injection.

The jets are injected from the outer casing, upstream of the compressor. Data implies that turbulent wall jets generally spread in the transverse direction at an angle of approximately 7.5 degrees [23], so the validity of the mixed out assumption will depend on the specific configuration. The analysis also assumes that negligible mixing occurs along the circumferential length scale before the fluid enters the compressor. A schematic of the model used to analyze the injection process is shown in Figure 2.6.

As modeled the effect of the jets is to create a change in the span-wise averaged static pressure, total pressure, and mass flow across the injection region as a function of the local reed valve area. Thus, the injection region can be modeled as a two-dimensional actuator disk. Pressure rise and mass flow boundary conditions across the injection region are derived by conserving mass and momentum across the injection region. The span-wise uniform, non-dimensional static pressure and axial velocity are related across the injection region by the following expressions which result from conserving axial momentum and mass flow:

$$p_{s_u} + \left(\Phi_u^2 + 2\,\Phi_i^2\,q\right) + \Phi_u^2 \frac{(1 - 2\,q)}{(1 - q)^2} = p_{s_b} + 2\,\Phi_b^2 \tag{2.31}$$

$$\Phi_u + \Phi_i\,q = \Phi_b \tag{2.32}$$

where: q is the local reed valve opening normalized by the annulus height, Φ_i is the injection velocity normalized by wheel speed, and b is the axial station downstream of injection region

Making additional assumptions that:

1) the nominal reed valve area opening is small compared to the annulus height, ($q << 1$) and,

2) the non-dimensional steady state mass flow injected by the reed valves is small compared to the mass flow through the compressor, $\frac{\Phi_i q}{\Phi_c} << 1$, and,

3) the total pressure supplying the jets is constant, (Φ_i = constant), the following linearized relations for the change in the span-wise uniform total pressure and axial velocity across the injection region can be derived:

$$\delta p_{t_b} - \delta p_{t_u} = 2 \Phi_i \left(\Phi_i - \Phi_u \right) \delta q \tag{2.33}$$

$$\delta \phi_b = \delta \phi_u - \Phi_i \delta q \tag{2.34}$$

By assuming the reed valves are only a short distance upstream of the compressor (compared to the length scale of the disturbances), the description of the effect of injection on the compression system dynamics can be further simplified by combining the two actuator disks, for the compressor and for the injection region, into one actuator disk. Thus, the model for the rotating stall dynamics with aeromechanical feedback retains the same structure as the model for the original system, with an irrotational upstream flow field and a vortical downstream flow field matched across a semi-actuator disk. Combining the boundary conditions across the two individual actuator disks leads to the matching conditions across the modified disk which relate perturbation variables in the upstream and downstream flow fields:

Continuity:

$$\delta \phi_u + \Phi_i \delta q = \delta \phi_d \tag{2.35}$$

Pressure Rise:

$$\delta\Psi = \delta p_{s_d} - \delta p_{t_u} = \frac{\partial \Psi}{\partial \phi}\delta\phi_d - \lambda\frac{\partial \phi_d}{\partial \theta} - \mu\frac{\partial \phi_d}{\partial \tau} + 2\,\Phi_i(\Phi_i - \Phi_u)\,\delta q \tag{2.36}$$

Exit Flow Angle:

$$\delta\nu_d = 0 \tag{2.14}$$

2.5.2.2 Structural Feedback

In this aeromechanical feedback control strategy, the response of the reed valves to the static pressure perturbations in the upstream flow field provides the feedback. The reed valves are modeled in their first cantilevered bending mode as single degree of freedom, mass-spring-damper systems, responding to perturbations in static pressure in the upstream flow field. A schematic of the reed valve dynamics is shown in Figure 2.7. The following non-dimensional, second order equation of motion governing the locally reacting reed valve dynamics is derived in Appendix B.

$$\frac{\partial^2 q}{\partial \tau^2} + 2\,Q\,\zeta\frac{\partial q}{\partial \tau} + Q^2\,\delta q = \frac{1}{6}\,W\,\delta p_{s_u} \tag{2.37}$$

where: Q is the reed natural frequency normalized by rotor frequency, ζ is the critical damping ratio of reed valves, and W is non-dimensional reed mass parameter

Equation (2.37) is based on the assumptions that the back pressure behind the reeds is independent of the perturbation flow field and reed displacement and that the reed motion does not directly effect the pressure field acting on the reeds.

The static pressure acting on the reed valves is assumed to be the static pressure in the flow field upstream of the injection region, i.e. the reed valves are modeled as short in axial length compared to the length scale of the disturbances. The pressure at the semi-actuator disk (x = 0) thus acts over the entire length of the reed valve.

The static pressure in the upstream potential flow field is related to the axial velocity perturbations via the linearized, unsteady, Bernoulli equation :

$$\delta p_{s_u} = (-2\ \Phi_u - \frac{1}{n}\frac{\partial}{\partial \tau})\ \delta \phi_u \tag{2.38}$$

The relationship between the static pressure and axial velocity perturbations is a function of the mean flow coefficient, temporal frequency and length scale (or harmonic number, n) of the disturbance.

2.6 Stability Analysis with Aeromechanical Feedback

Assuming solutions of the traveling wave form consistent with the governing equations of the flow fields, and matching the dynamic and kinematic boundary condition across the actuator disk, as developed in Appendix B, leads to the following third order, generalized, complex eigenvalue problem determining the stability of the flow field for each spatial harmonic.

$$[\mathbf{A} - \sigma \mathbf{B}] \begin{Bmatrix} A_n \\ \delta q_n \\ \delta z_n \end{Bmatrix} = 0 \tag{2.39}$$

In Equation (2.39), the **A** matrix is given by:

$$\mathbf{A} = \begin{bmatrix} \frac{\partial \Psi}{\partial \Phi} - i n \lambda & A_{12} & 0 \\ -\frac{1}{3} W n^2 \Phi_u & i n Q^2 & i n 2 Q \zeta \\ 0 & 0 & 1 \end{bmatrix}$$

where: $$A_{12} \equiv -\lambda \Phi_i - i \frac{\Phi_i}{n} \left(\frac{\partial \Psi}{\partial \Phi} + 2 (\Phi_i - \Phi_u) \right)$$

and the **B** matrix is given by:

$$\mathbf{B} = \begin{bmatrix} -i(4 + n\mu) & -(\frac{2}{n} + \mu)\Phi_i & 0 \\ -i\frac{1}{3} W n^2 & 0 & -n^2 \\ 0 & -in & 0 \end{bmatrix}$$

The stability matrices retain terms associated with the individual fluid dynamic and structural dynamics systems, however, the two systems are now coupled aeromechanically. With aeromechanical feedback, there are three natural modes of oscillation per spatial harmonic. The two additional modes per spatial harmonic compared to the basic compression system model (presented in section 2.3) are due to the second order reed dynamics introduced by the feedback. All modes for any harmonic are independent and stability can still be assessed on a harmonic by harmonic basis.

2.6.1 Aeromechanical Feedback Control Parameters

Stability is now a function of not only the original system parameters but also of an additional set of non-dimensional control parameters which determine the interaction between the reed valves and the fluid dynamic flow field. The control parameters defined below are derived in Appendix B.

$$Q \equiv \omega_n \frac{R}{U_R} \qquad \text{frequency parameter} \qquad (2.40)$$

$$\zeta \equiv \frac{b}{2 M \omega_n} \qquad \text{critical damping ratio} \qquad (2.41)$$

$$W \equiv \frac{\rho R^2 \tilde{L}}{M} \qquad \text{mass parameter} \qquad (2.42)$$

$$\Phi_i \equiv \frac{C_{x_i}}{U_R} \qquad \text{injection velocity parameter} \qquad (2.43)$$

$$\Phi_u \equiv \frac{C_{x_u}}{U_R} \qquad \text{mass flow coefficient} \qquad (2.3)$$

The amount of steady state mass flow injected does not directly influence stability, it is the velocity (or equivalently, the total pressure) of the injection fluid which is an explicit stability parameter. The steady state mass flow coefficient is now an explicit parameter in the stability model with aeromechanical feedback, although it did not appear explicitly in the basic compression system. The steady state mass flow coefficient enters because it influences the relation between axial velocity and static pressure perturbations (equation 2.38) in the upstream flow field and, thus, the feedback.

2.6.2 Parameter Optimization

One of the objectives of this research was to experimentally demonstrate aeromechanical feedback stabilization of rotating stall. To guide in the design of an experimental facility and to determine the effect of the control parameters on system stability, a parameter optimization study, based on the linearized stability analysis, was performed. Compressor parameters representative of the MIT low speed, single stage, research

compressor (described in Chapter 3) were selected, and the pressure rise versus mass flow characteristic shown in Figure 2.2 was used. The inertial parameters used in the basic compression system analysis were retained, i.e. (λ =1.0) and (μ =2.0), for the analysis of the compression system with aeromechanical feedback. With the compression system parameters defined, the control parameters were systematically varied to determine the influence on stability.

Initial results from the parameter study indicated that for properly tuned control systems, high injection parameters, Φ_i, and mass parameters, W, were desired. In order to design a physically realizable experimental apparatus, however, some practical constraints were imposed on the values of the control parameters. Based on the idea that, for practical compression systems, the high pressure injection source could be taken from behind the compressor, the injection pressure was restricted to be of the order of the dynamic head of the compressor based on wheel speed. The mass and frequency parameters of the reed valves used in the parameter study were restricted to physical realizable values for reed valves sized to fit the MIT low speed compressor and constructed from readily obtainable materials. These constraints restricted the injection parameter to $\Phi_i \approx 1$, and the mass parameter to $W \approx 3.5$.

Table 2.1 lists the control parameters optimized for each of the three lowest spatial harmonics. As shown, the optimized stability parameters vary for each spatial harmonic.

Design Configuration

It was desired to investigate the effect of one set of reed valves on compressor stability, i.e. one set of control parameters, and a parameter optimization study was performed to determine one set of control parameters that optimized the stability of only the two lowest

spatial harmonics. The justification for neglecting higher spatial harmonics was based on the following:

1) Experimental and analytical results indicate that the higher harmonics of compression system are stabilized, relative to lower spatial harmonics, due to unsteady aerodynamics within the compressor. This effect is not explicitly contained within the model used in this thesis.

2) The rate at which the disturbances decay exponentially (in the axial direction upstream of the compressor) scales with the length scale of the disturbances and hence the spatial harmonic number. The assumption that the reed valves are placed immediately upstream of the compressor thus becomes increasingly unrealistic for the higher harmonics for reed valves placed a finite distance upstream of the rotor.

The design configuration, resulting from the parameter study, is defined by the following control parameters:

$$\Phi_i = 1.0 \ ; W = 3.5 \ ; Q = 0.9 \ ; \ \zeta = 0.7$$

Figure 2.8 shows the predicted behavior of the eigenvalues for the first two harmonics as the compressor mass flow coefficient is reduced. For the optimized system, the first and second harmonics are predicted to become unstable at roughly the same mass flow coefficient. As shown, a mode associated with the second spatial harmonic of the compression system is predicted to be the mode that become unstable first as the flow coefficient through the compression system is reduced ($\Phi = 0.43$). The first mode associated with the first spatial harmonic is predicted to become unstable at a slightly lower flow coefficient ($\Phi = 0.40$).

Assuming that the neutral stability point of the least stable mode associated with the second spatial harmonic determines the stability of the compression system, the

optimized aeromechanical feedback is predicted to reduce the stalling mass flow coefficient of the compression system by 19%, compared to the stalling flow coefficient predicted for the basic compression system. The compressor slope at which instability occurs is predicted to be $\frac{\partial \Psi}{\partial \Phi} = 1.2$.

The least damped mode associated with the first spatial harmonic is predicted to rotate at 9% of the rotor speed and the least damped mode associated with the second spatial harmonic is predicted to rotate at 38% of the rotor speed. Comparing these rotation rates to those for the basic compression system, (17% and 25% of rotor speed for the first and second spatial harmonics) demonstrates that the aeromechanical feedback is predicted to change the rotation rates of the disturbances in addition to the stalling flow coefficient.

2.6.3 Robustness of Aeromechanical Feedback

The model is a simple model of a complex problem and, therefore contains uncertainties. To assess the sensitivity of the performance of the control strategy to variations in control parameters, the predicted stability boundary was determined by fixing all but one of the control parameters of the design configuration and systematically varying the free control parameter. Figure 2.9 shows the mass flow coefficient at which the least stable mode associated with the first and second spatial harmonics is predicted to become unstable as a function of the individual control parameters Φ_i, W, Q, and ζ for the design optimized configuration. A local maximum degree of stabilization exists for variations of each of the control parameters. The discontinuities in the curve of predicted flow coefficient at instability versus the individual control parameters is because each spatial harmonic contains three eigenmodes, any one of which can become unstable.

Figure 2.9 represents the behavior for a specific set of control parameters. In general, a significant increase in the injection parameter and / or the mass parameter would serve to

increase the stabilizing effect of the aeromechanical feedback. However, increasing Φ_i and W will result in increased stability enhancement only when the other control parameters, i.e. ζ and Q, are optimized for the system with the higher values of Φ_i and W.

2.7 Effect of Non-Linearities and Random Excitation

The linear model predicts significant stabilization can be achieved due to aeromechanical feedback. To assess the effect of non-linearities and random excitation, i.e. noise, on the compression system dynamics, a non-linear, numerical simulation was developed to predict the time resolved compression system behavior. The simulation technique used was a Galerkin-based [24] approximation to the first two spatial harmonics of the compression system to yield a non-linear, state space description of the compression system dynamics. The formulation of the non-linear simulation was based on the two-dimensional stability model developed in Appendix A, with the only non-linear term included being the non-linearity in the compressor pressure rise versus mass flow performance characteristic. The model thus retains the linearized description of the upstream and downstream flow fields. The time resolved system response was simulated numerically using a 4th order Runge-Kutta procedure. The details of the procedure are developed in Appendix E.

A noise model was also incorporated into the simulation procedure to assess the effect of random excitation on the compression system. The source of noise in compression systems is not well understood, and a random static pressure disturbance at the face of the compressor was used. The noise level was characterized by the rms level of the random perturbations. The details of the noise model are also developed in Appendix E.

The numerical simulation was developed for the compression system with aeromechanical feedback. The dynamics of the basic compression system were simulated by reducing the injection parameters to zero, thus decoupling the rotating stall dynamics from the reed valve dynamics.

2.7.1 Stall Inception of Basic Compression System

The non-linear simulation was carried out for the basic compression system operating near the stalling flow coefficient (within 0.5%) predicted by the linearized analysis. The characteristic shown in Figure 2.2, used for the linear analysis, was also used in the simulation.

Figure 2.10 shows the computed axial velocity perturbations through the compressor at eight equally spaced positions around the annulus during stall inception. The input parameters to the simulation are given in Table 2.2. Although the compression system is operating at a linearly stable flow coefficient, the non-linear calculation with finite amplitude, random excitation (2.5% of the dynamic head based on wheel speed), predicts that the initially axisymmetric flow field will transition to a large amplitude, non-axisymmetric flow field, indicating rotating stall.

The time resolved axial velocity perturbations at the various circumferential positions can be decomposed into spatial harmonics. The method used to decompose the velocity perturbations into the spatial Fourier harmonics, developed by other authors [13, 25] is given in Appendix F. The magnitude and phase of the first and second spatial harmonics, which are shown in Figure 2.11, grow in time as the flow field transitions to rotating stall. The magnitudes of the first two spatial harmonics are comparable during the stall inception process, indicating that both harmonics have roughly the same damping, consistent with the linear stability analysis.

The plot of unwrapped phase of the first and second spatial harmonics versus time indicates coherent traveling waves for both harmonics before the onset of large amplitude rotating stall. The rotation rates of the first two spatial harmonics (17% and 25% of rotor frequency, respectively) predicted by the simulation differ little from the values given by the linearized analysis.

The growth rate of the finite amplitude disturbances during stall inception, is strongly dependent on the shape of the compressor characteristic. As developed in Appendix F, the influence of the shape of the characteristic is primarily determined by whether the weighted average, over the annulus, of the compressor slope increases or decreases with the disturbance amplitude. For compressor characteristics in which the annulus averaged slope increases with disturbance size, finite amplitude disturbances can cause the system to transition to rotating stall while operating in a linearly stable region. For characteristics in which the annulus averaged slope decreases with disturbance size, the simulation predicts that small amplitude limit cycles can develop prior to the onset large amplitude rotating stall in linearly unstable regions. For a more detailed discussion of the effects of the non-linearity of the compressor characteristic on the stall inception process, the reader is referred to Paduano and Gysling [25].

2.7.2 Response of Compression System with Feedback

The simulation also was performed for the design configuration with aeromechanical feedback. The same noise level was used. The input parameters to the simulation are listed in Table 2.2. Figure 2.12 shows the simulated response of the axial velocity through the compressor at eight equally spaced circumferential position around the annulus for the compression system, with the design aeromechanical feedback parameters

and in operation near the neutral stability point ($\Phi = 0.43$) predicted by the linearized analysis.

The simulation predicts that the flow field does not transition into large amplitude, performance limiting rotating stall, consistent with the increase in stable flow range predicted by the linearized analysis. Figure 2.13 shows the spatial Fourier decomposition of the velocity disturbances into the first and second harmonics and demonstrates that system response is dominated by the second spatial harmonic. This is consistent with the linearized analysis which predicted that the a mode associated with the second spatial harmonic became unstable at a higher flow coefficient than the least stable mode associated with the first harmonic.

The plot of the unwrapped phase indicates that the second harmonic is traveling in a coherent manner for finite intervals prior to stall inception, while no such behavior exists for the first harmonic. If one associates coherent traveling waves with under damped modes, this result is also consistent with the results from the linear analysis. The rotation rate of the second harmonic agrees with the predicted rotation rate (38%) for the least damped mode associated with the second harmonic.

The corresponding reed valve deflections at 4 equally spaced circumferential position predicted by the simulation are shown in Figure 2.14. The rms of the oscillations in flow coefficient resulting from the random excitation in the simulation are roughly 2% of the mean mass flow coefficient through the compression system. The rms of the reed valve deflections corresponding the system oscillations are roughly 1% of the annulus height. If one assumes that a rms noise level 2.5% $\left(\text{of}\frac{1}{2}\rho\ U_R^2\right)$ is reasonable, the results from the non-linear simulation indicate that a nominal reed valve opening area of roughly 1- 3 % of the annulus height is required to prevent the reeds from becoming saturated, i.e.

becoming fully closed, or fully opened, prior to the compression system becoming linearly unstable.

2.8 Summary of Analysis

This section summarizes the results of the analytical investigation of the rotating stall onset in a compression system with aeromechanical feedback. First, using a simple stability model, the physical mechanism behind rotating stall was described and the role of feedback stabilization in the unsteady compression system dynamics was interpreted. The model was extended to include the effect of the aeromechanical feedback introduced by the dynamic mass / momentum injection on stability. The results showed that significant stabilization of the rotating stall dynamics can be achieved with properly tuned reed valve dynamics. In addition, a set of non-dimensional control parameters that determine the degree of stabilization due to dynamic mass / momentum injection were identified. A parameter optimization study was then performed to determine a set of physical realistic control parameters to stabilize rotating stall on a single stage compressor. A Galerkin-based non-linear simulation was carried out to examine the effects of a non-linear compressor characteristic and finite amplitude disturbances.

Table 2.1: Results from Parameter Optimization Study[1]

Configuration	Freq. Parameter (Q)	Damping Parameter (ζ)	Mass Parameter (W)	Inj. Parameter (Φ_i)	Flow Coef. at Nuetral Stability [2]
Optimized for First Spatial Harmonic	0.7	1.25	3.5	1.0	0.29
Optimized for SecondSpatial Harmonic	0.7	0.6	3.5	1.0	0.40
Optimized for ThirdSpatial Harmonic	1.25	0.4	3.5	1.0	0.43
Design Optimized for First and Second Spatial Harmonic	0.9	0.7	3.5	1.0	0.43

Note: 1) Compressor characteristic given by:

$$\Psi(\Phi) = 5.75\,\Phi^3 - 14.4\,\Phi^2 + 10.4\,\Phi - 1.94$$

and $\lambda = 1.0$ and $\mu = 2.0$

2) Flow coefficient at which a mode associated with the spatial harmonics considered becomes unstable

Table 2.2: Input Parameters for Non-Linear Simulations Presented in Chapter 2

Parameter	Simulation of Stall Inception of Basic Compression System	Simulation of Design Configuration in Stabilized Region
Φ	0.53	0.43
$\frac{\partial \Psi}{\partial \Phi_{Linear}}$	-0.02	1.07
λ	1.0	1.0
μ	2.0	2.0
Φ_i	0.000	1.0
W	3.5	3.5
Q	1.0	0.9
ζ	1.0	0.7
Noise Level $\left(\text{Based on } \frac{1}{2}\rho U_R^2\right)$	2.5%	2.5%
Time Step Frequency	26.67 Times Rotor Frequency	26.67 Times Rotor Frequency

Note: Characteristic Used in Simulations:

$$\Psi(\Phi) = 5.75\,\Phi^3 - 14.4\,\Phi^2 + 10.4\,\Phi - 1.94$$

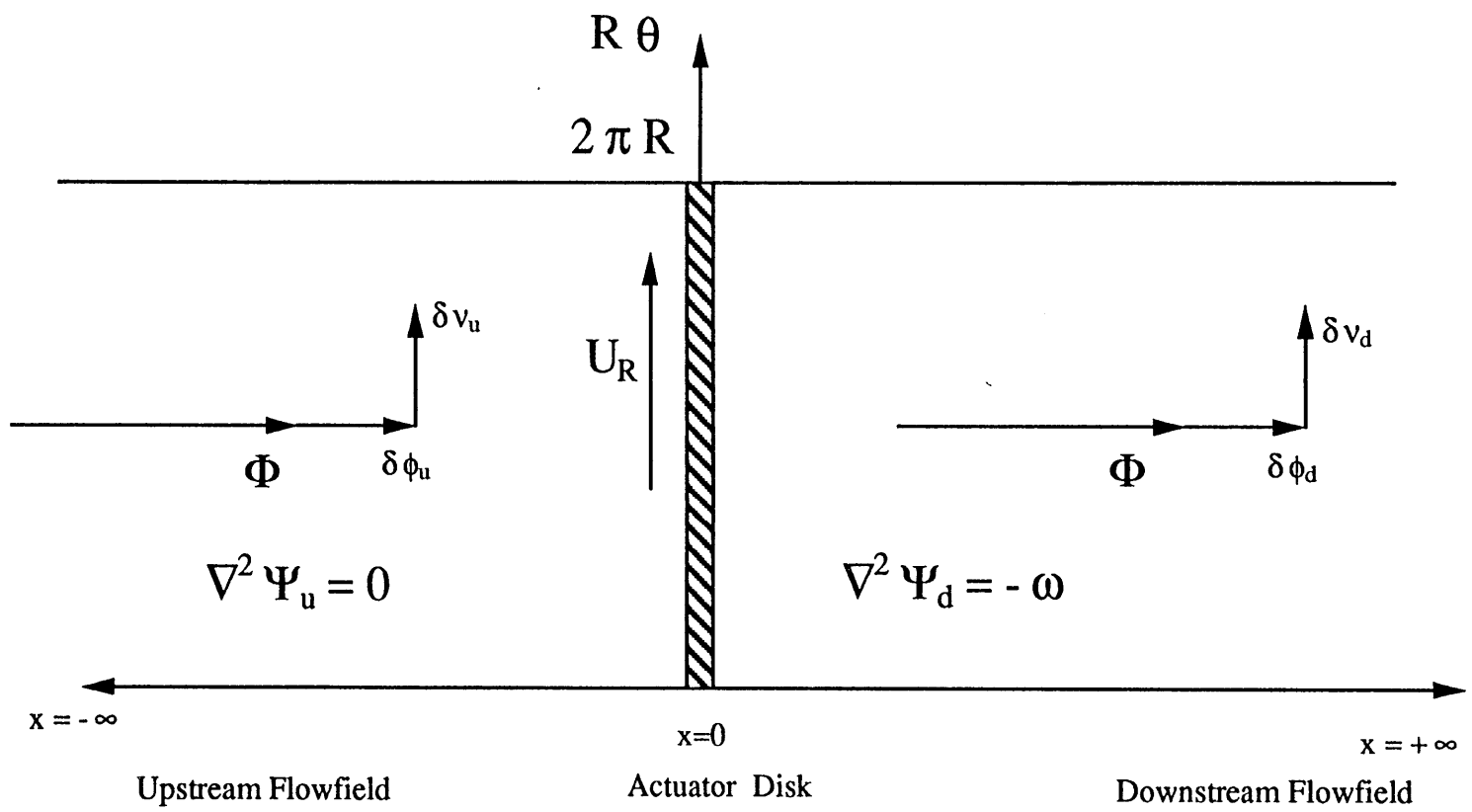

Figure 2.1: Schematic of 2-D Flowfield

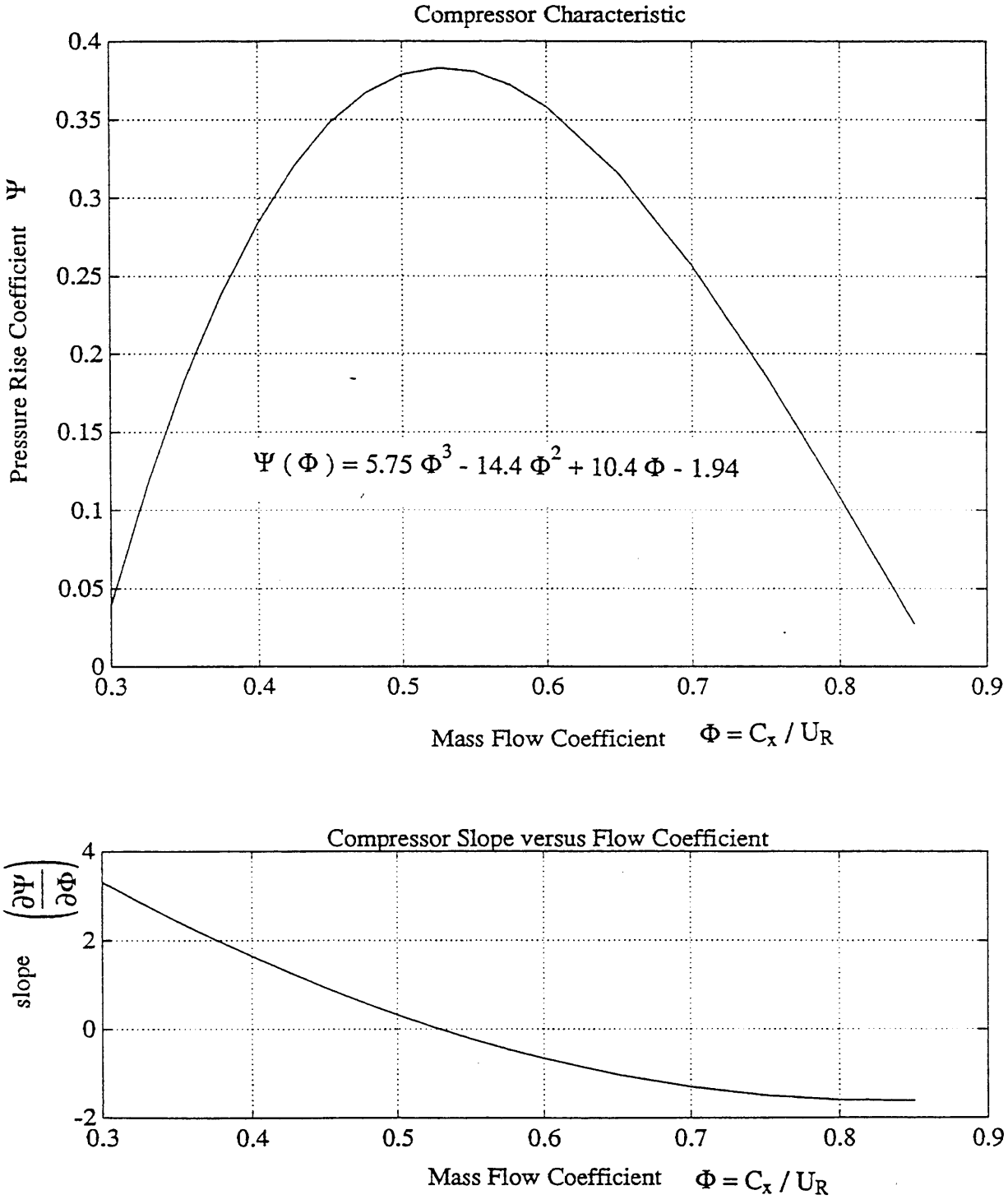

Figure 2.2 Compressor Characteristic and Slope of Characteristic versus Mass Flow Coefficient Used in Analysis

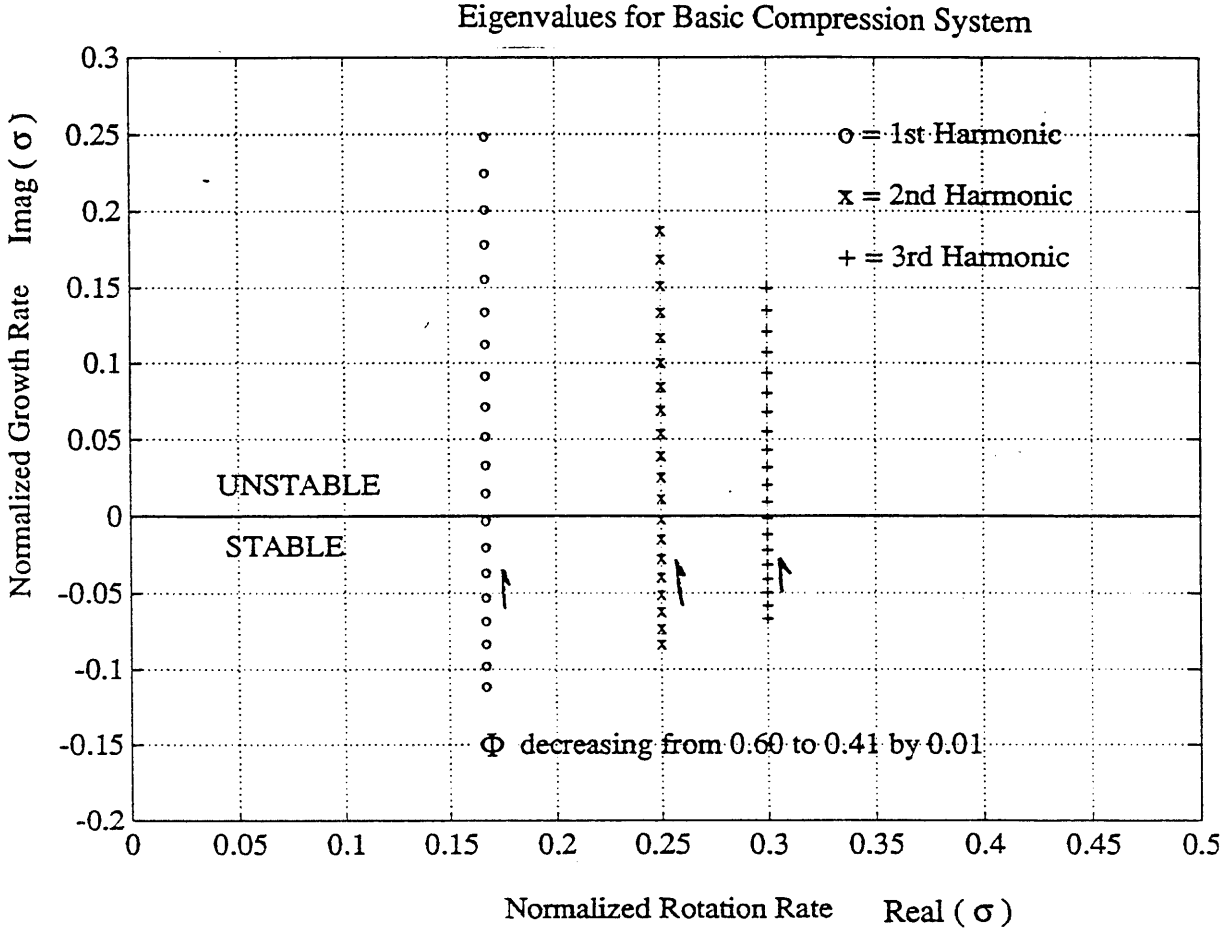

Figure 2.3 Eigenvalues of Basic Compression System Parameterized by Mass Flow Coefficient for First Three Spatial Harmonics (λ =1.0, μ = 2.0)

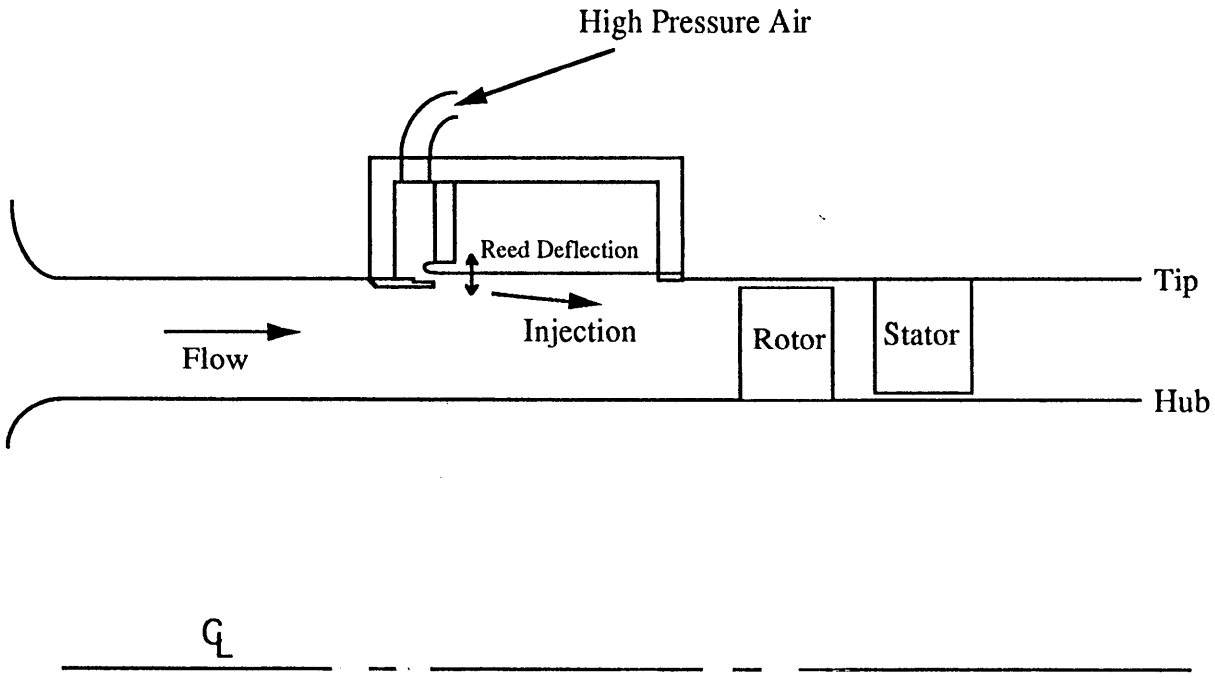

Figure 2.4: Schematic of Dynamic Mass / Momentum Injection Strategy

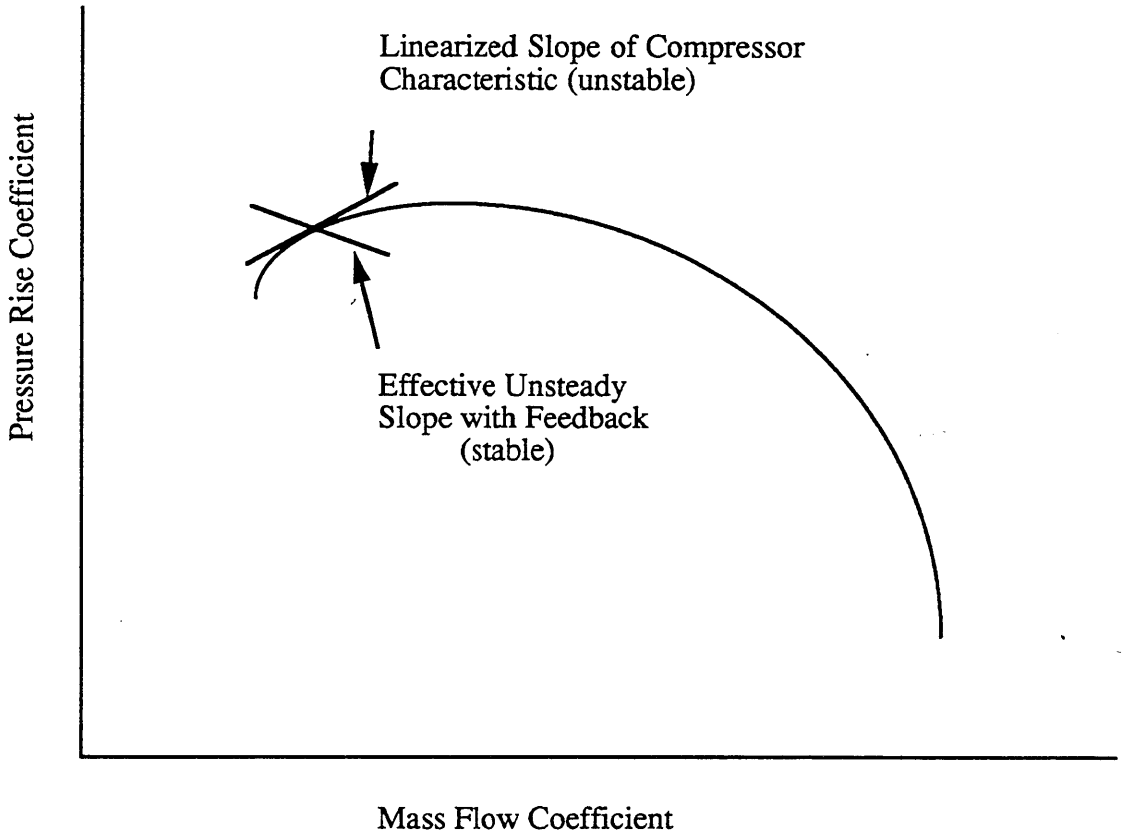

Figure 2.5: Effect of Dynamic Feedback on Unsteady Compressor Performance

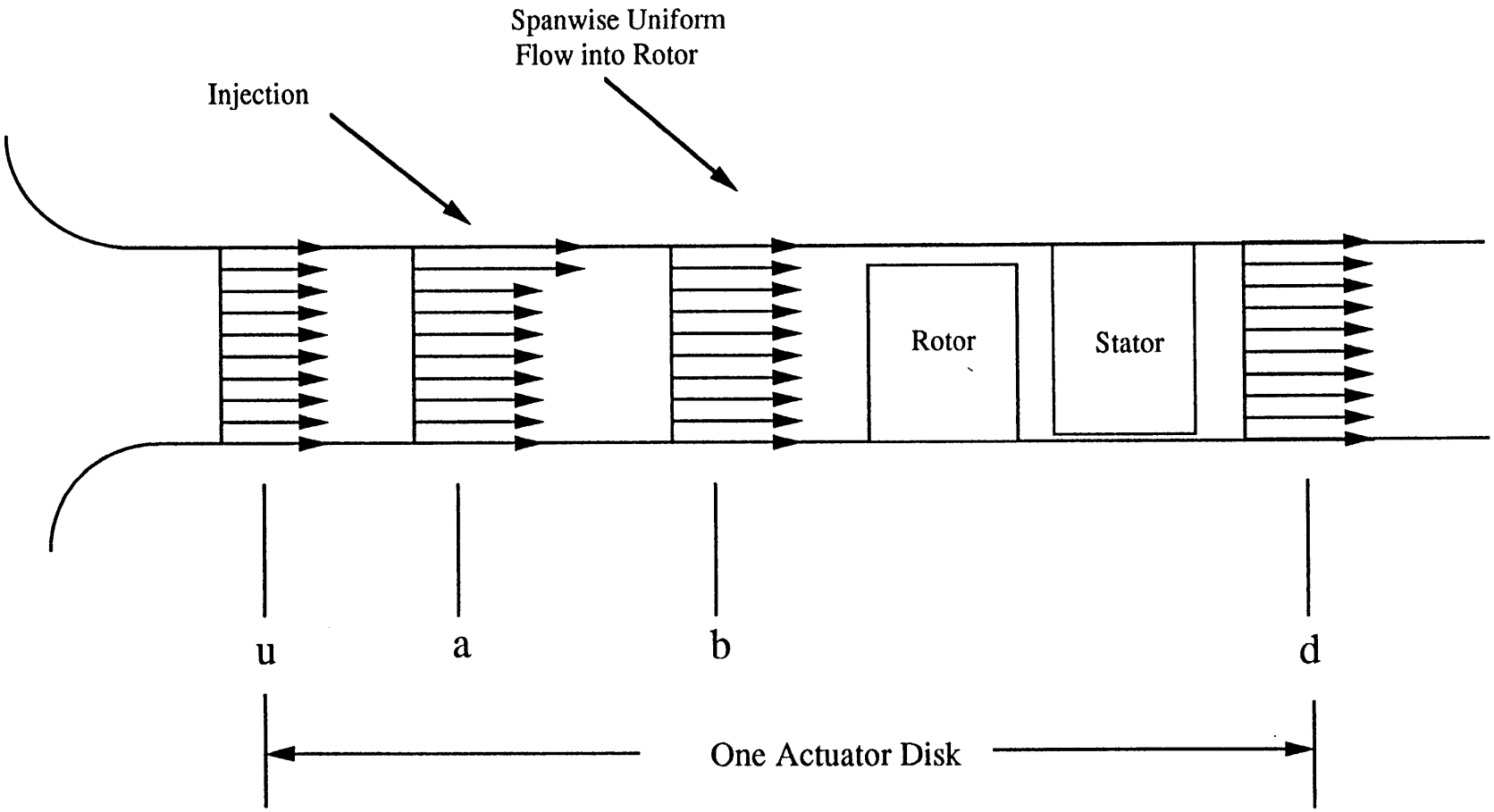

Figure 2.6: Schematic of Dynamic Mass / Momentum Injection Model

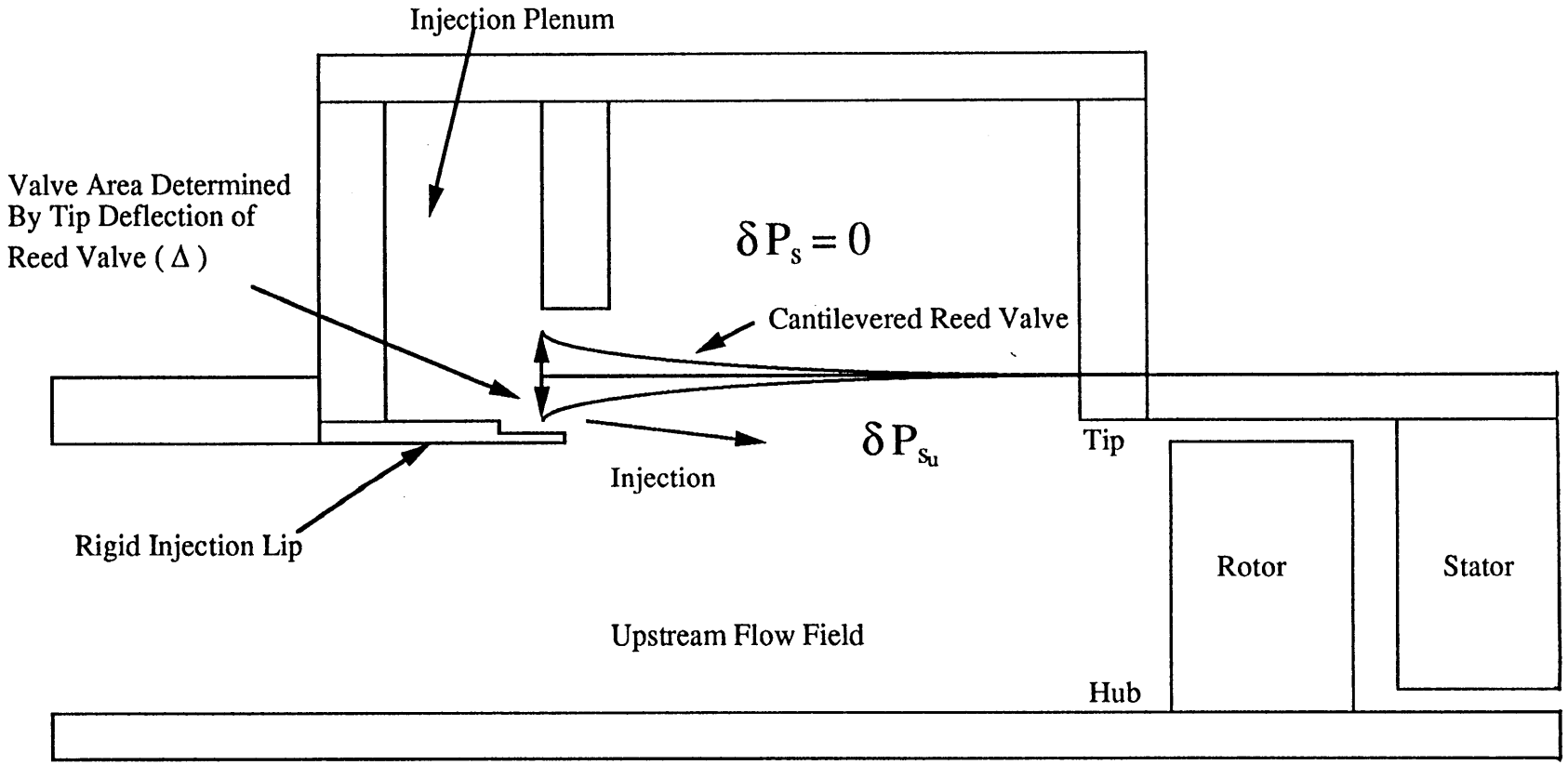

Figure 2.7: Schematic of Reed Valve Dynamics

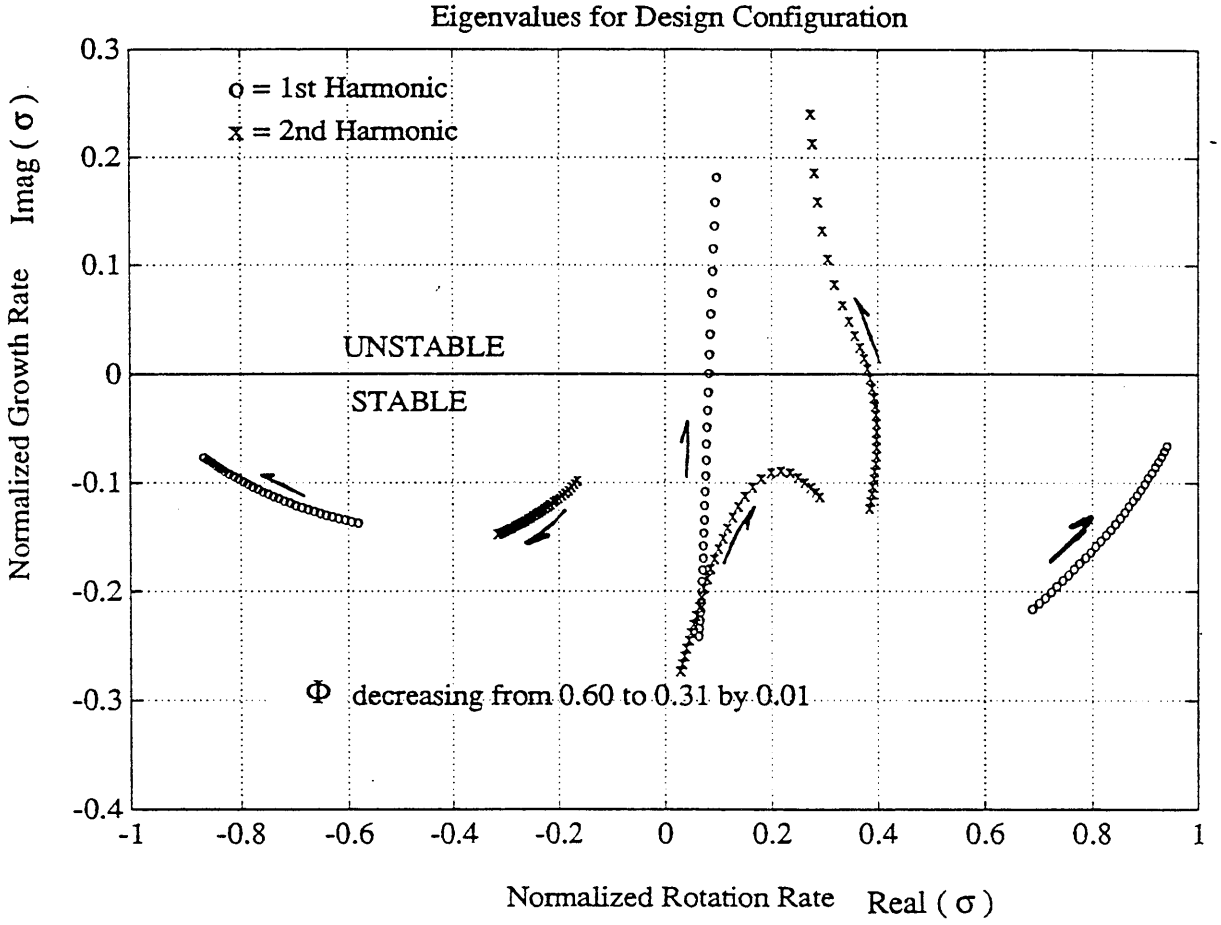

Figure 2.8 Eigenvalues for Compression System with Design Aeromechanical Feedback Parameterized by Flow Coefficient for First and Second Spatial Harmonics (λ =1.0, μ = 2.0, W = 3.5, Φ_i = 1.0, Q = 0.9, ζ = 0.7)

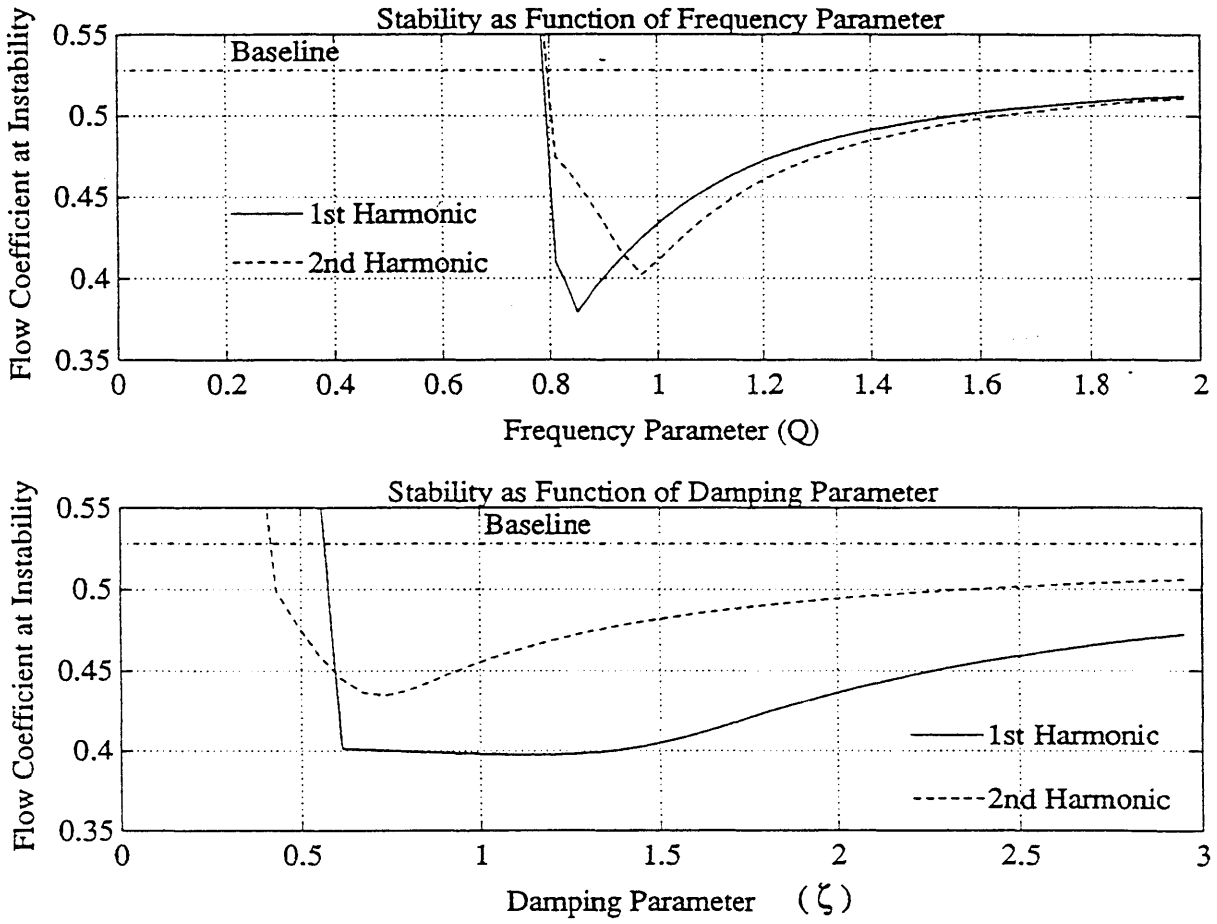

Figure 2.9a Flow Coefficient at Instability of First and Second Harmonics for Design Configuration as Function of Individual Control Parameters (Q and ζ)

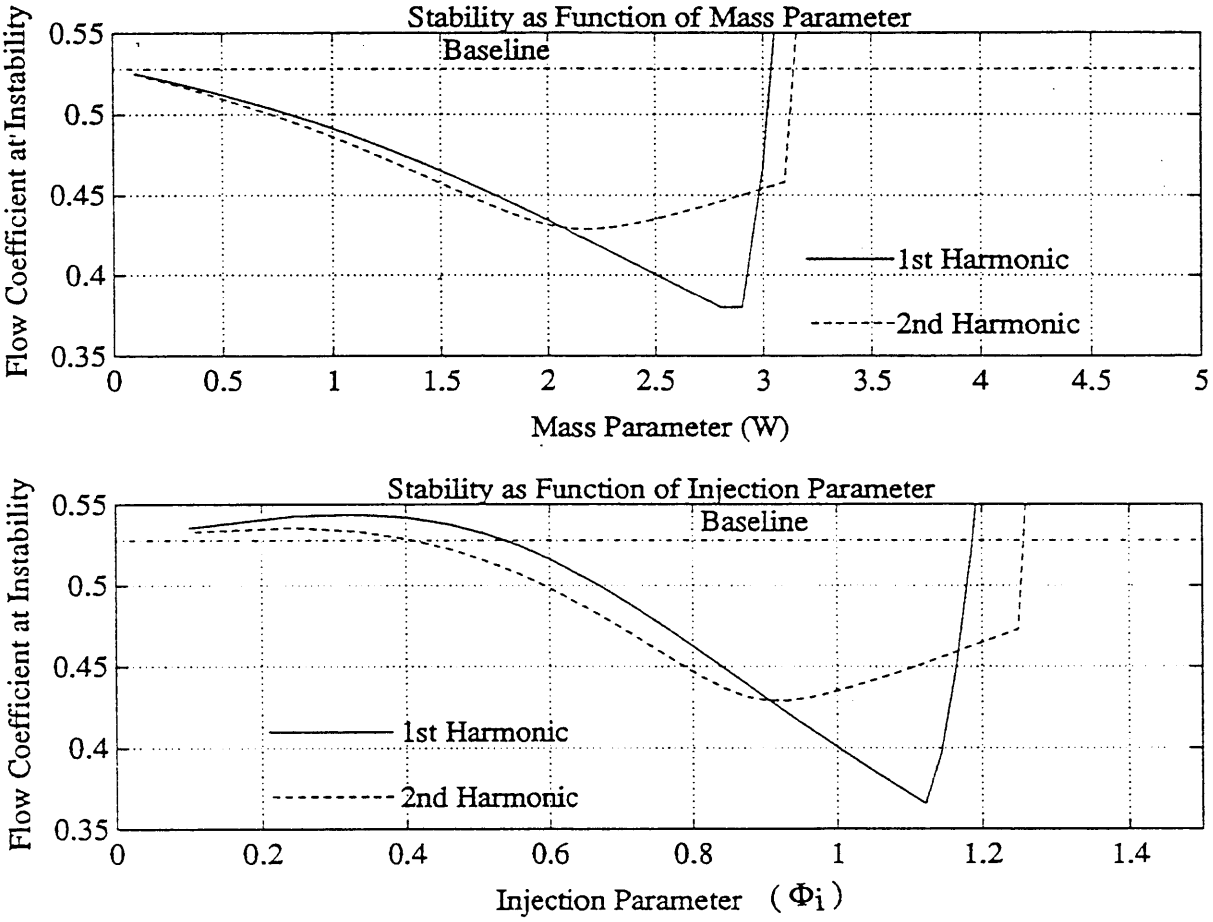

Figure 2.9b Flow Coefficient at Instability of First and Second Harmonics for Design Configuration as Function of Individual Control Parameters (W and Φ_i)

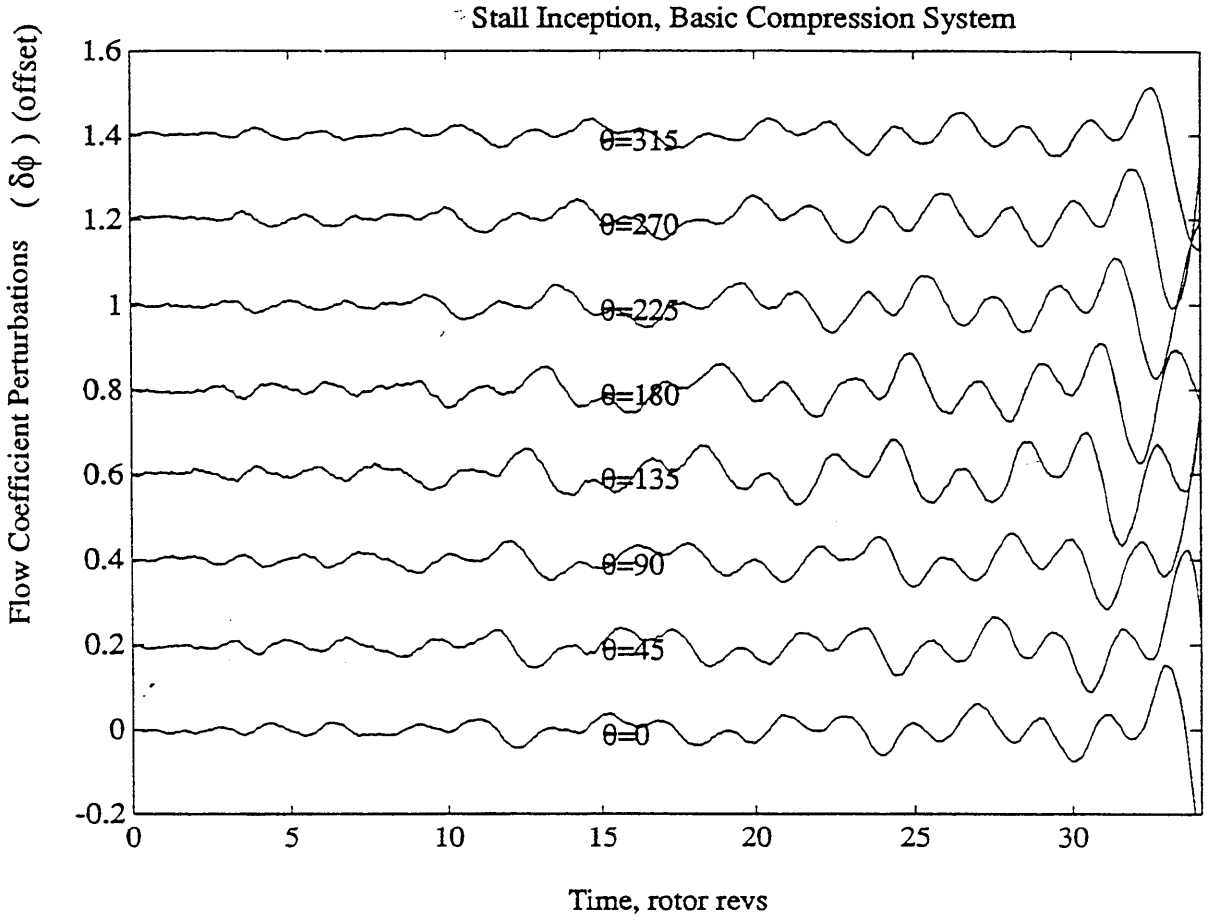

Figure 2.10 Normalized Axial Velocity Perturbations Through Compressor During Simulated Stall Inception, Basic Compression System ($\Phi = 0.53$)

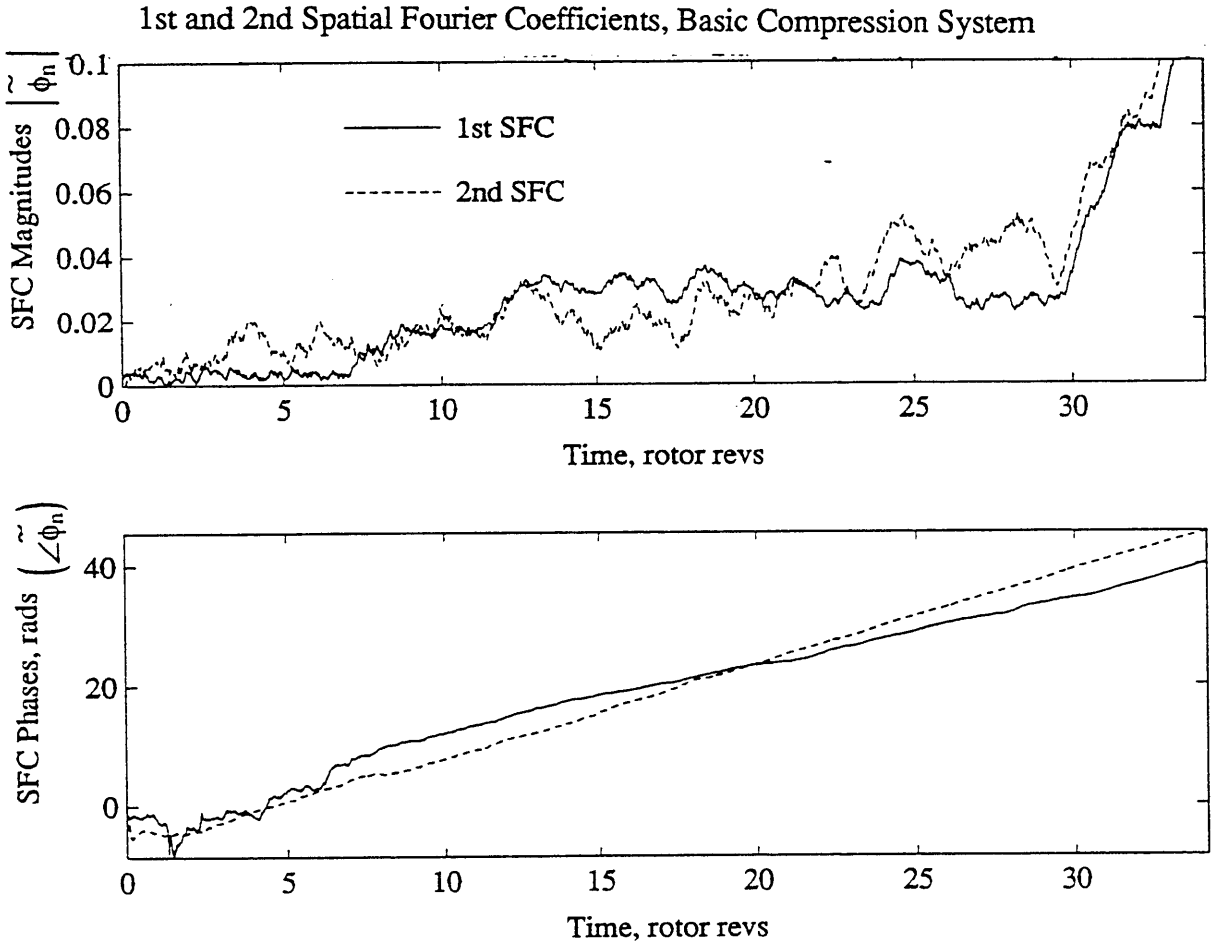

Figure 2.11 Spatial Fourier Decomposition of Normalized Axial Velocity Perturbations Through Compressor During Simulated Stall Inception of Basic Compression System (First and Second Spatial Harmonics)

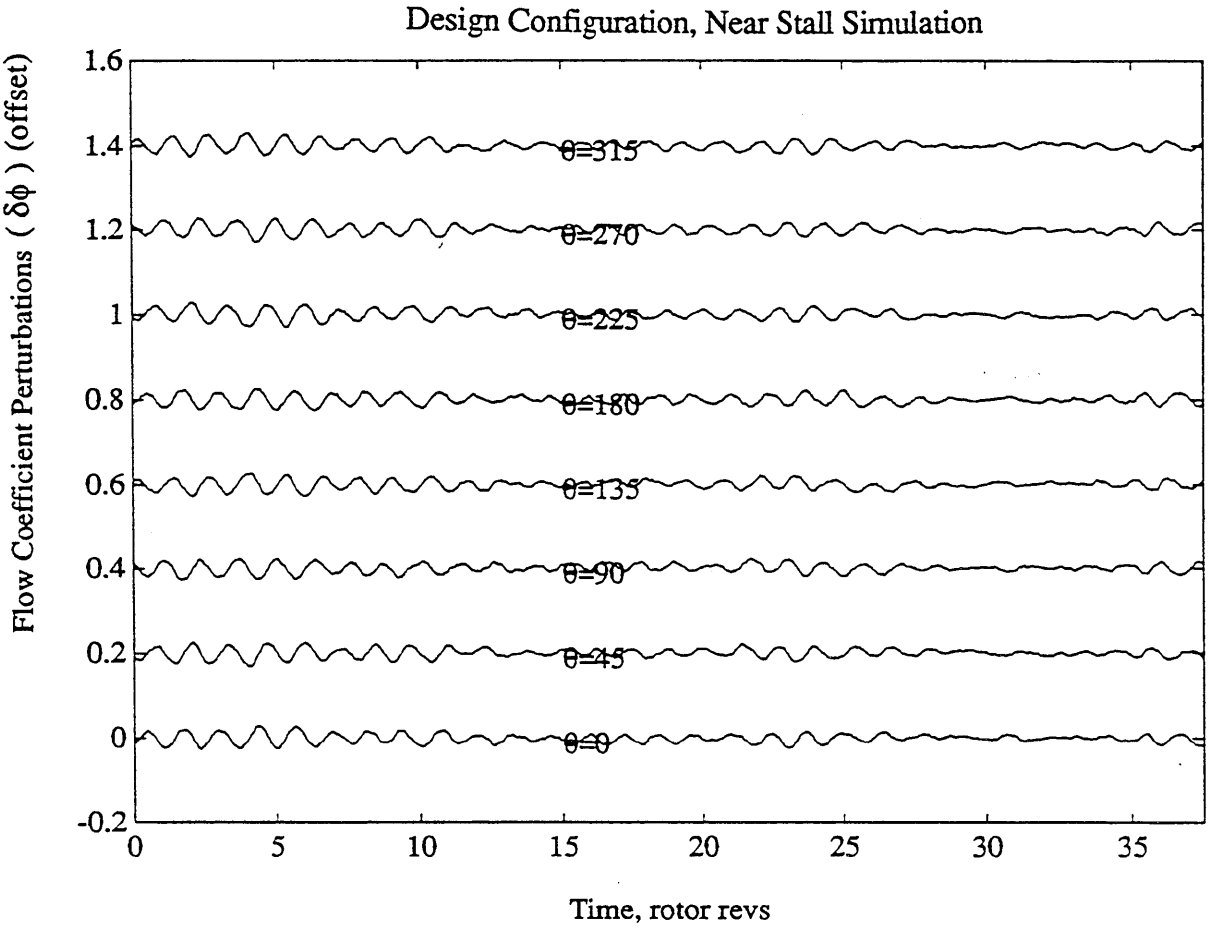

Figure 2.12 Normalized Axial Velocity Perturbations Through Compressor During Simulated Operation of Design Configuration Near Stall ($\Phi = 0.43$)

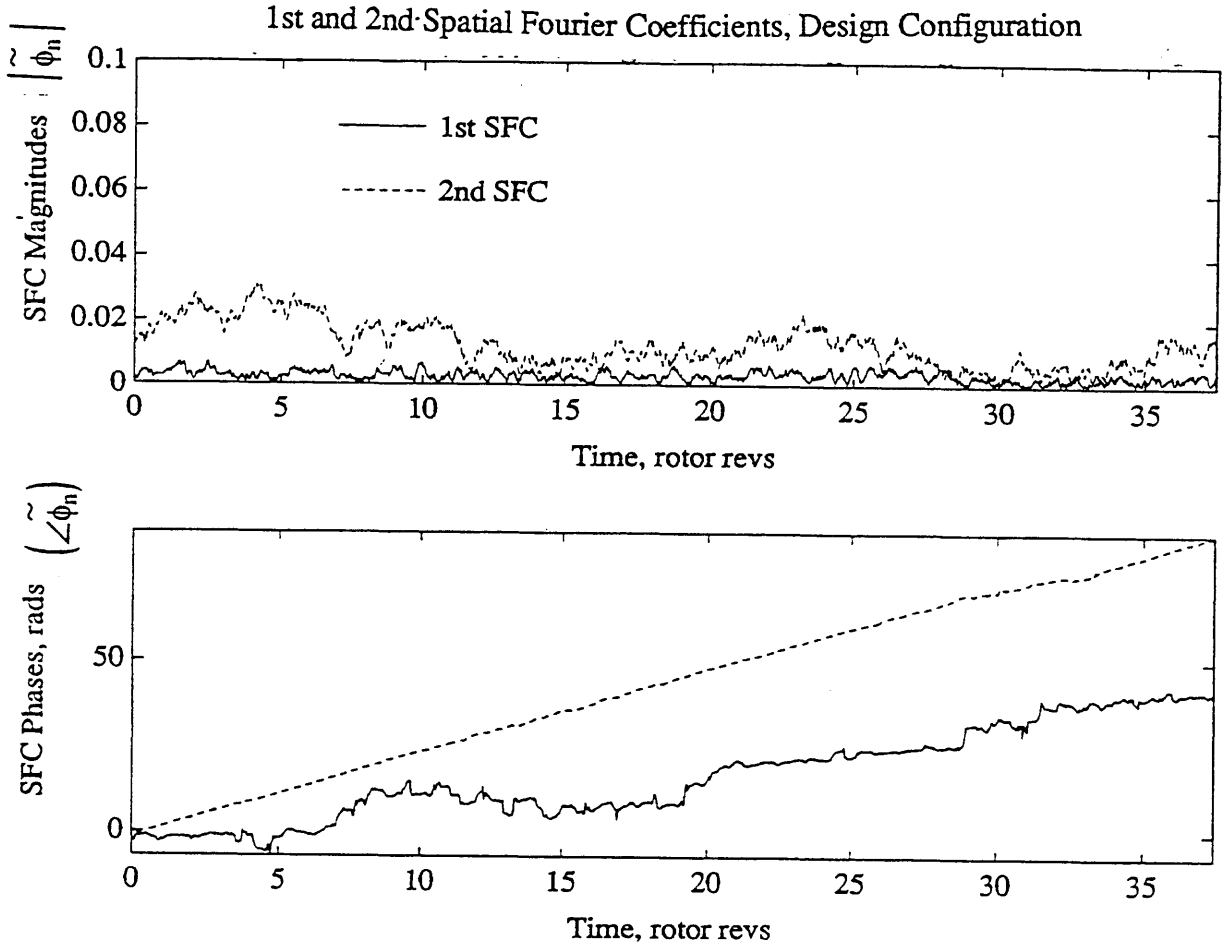

Figure 2.13 Spatial Fourier Decomposition of Normalized Axial Velocity Perturbations Through Compressor During Simulated Operation of Design Configuration Near Stall (First and Second Spatial Harmonics)

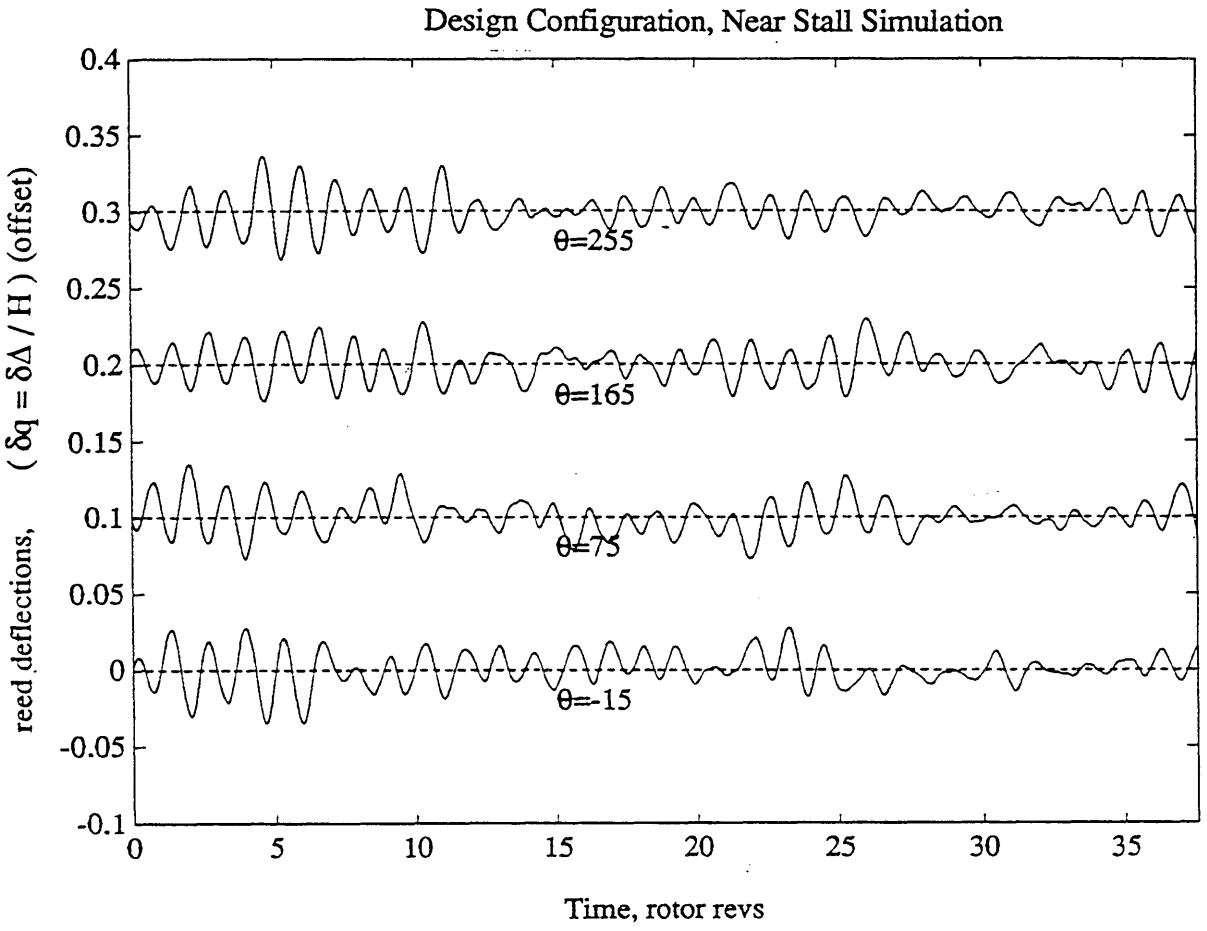

Figure 2.14 Normalized Reed Valve Deflections for Design Configuration During Simulated Operation Near Stall

Chapter 3: Experimental Facility

The experimental facility and instrumentation used in this research is described in this chapter, including the design and construction of the hardware necessary to implement the dynamic mass / momentum strategy developed in Chapter 2. Design of the dynamic mass / momentum injection facility was based on the results of the parameter optimization study presented there.

3.1 Compression System

The experimental phase of this research was conducted on a low speed, single stage compressor facility. A schematic of the MIT low speed, single stage compression system is shown in Figure 3.1. The compression system has a low B-parameter ($B < 0.1$), allowing the rotating stall dynamics to be studied in isolation from surge.

As shown, air is drawn into the compression system through a bell mouth inlet where it passes through a honeycomb flow straightener (not shown), and then travels through constant area, annular inlet duct into the single stage compressor. Downstream of the compressor, the air travels through another constant area, annular duct that leads to a conical throttle, which discharges into an exit plenum. The constant area ducts serve to isolate the rotating stall dynamics of the compressor from the other flow elements. Both the upstream and downstream ducts are roughly three compressor radii in length.

The exit plenum is connected to large diameter ducting which leads to an exhaust fan. With the exhaust fan running, the pressure in the exit plenum is drawn to below ambient pressure. The exhaust fan provides suction to overcome the flow resistance through the system to allow the compressor to operate over a larger range of conditions.

3.2 Single Stage Compressor

The compressor consisted of a rotor and stator, with no inlet guide vanes. The compressor has a hub to tip radius ratio of 0.75. The solidity of the blading in both the rotor and stator was 1. The degree of reaction based on the velocity triangles at mid-span was approximately 60%. In the experiments, the compressor was run at 2250 rpm, corresponding to a tip Mach number of 0.2, so that the flow can be considered incompressible.

The compressor geometry is defined in Figure 3.2, with details shown in Table 3.1. The mean compressor geometry was selected to be similar to a compressor build which was demonstrated to exhibit full span stall inception [25].

The aerodynamic design of this compressor build was not optimized for steady state aerodynamic performance. As an example, the predicted incidence angles for the rotor and stator are shown in Figure 3.3 as a function of span for a flow coefficient near the experimentally determined stalling flow coefficient of the compressor. The flow angles were calculated assuming uniform inlet flow and zero deviation. The results of this simplified velocity triangle analysis indicate that the incidence, and, hence, aerodynamic loading, of the rotor is highly non-uniform in the span-wise direction, with the hub more highly loaded than the tip.

The rotor blades used in this experimental investigation had extended chords at the hub and tip regions, as illustrated in Figure 3.4. These blades were used in an attempt to reduce the effect of the high incidence angle at the hub of the rotor. A detailed study of the aerodynamic characteristics of the rotor blades is given by Gopalakrishnan [27].

Paduano [25] and the author have independently investigated other geometries on the MIT single stage compressor which had more "conventional" span-wise loading and, therefore, better aerodynamic performance. However, these builds were found to exhibit part span stall inception and / or fully developed part span stall, and hence, were not suitable for the present study. Paduano [25] documented the steady state performance and time resolved stall inception behavior of the MIT single stage compressor for several compressor geometries.

Empirical evidence demonstrates that single stage compressors have a tendency to exhibit part-span rotating stall; whereas multistage compressors are more likely to exhibit full-span rotating stall [4]. A theoretical framework explaining these experimentally observed trends has yet to be developed.

Because the design was based on a model of the two-dimensional, compression system dynamics associated with full span stall inception, the sole criteria for selecting the compressor geometry used in this research was that the build exhibited full-span stall inception. The unconventional aerodynamic loading of the compressor used in this research should not be viewed as a requirement for compressors to exhibit full span, stall inception. Several researchers have independently verified full span stall inception in different compressors [12, 13, 18]. For example, a well documented investigation by Haynes [18] demonstrates full-span stall inception in a three-stage compressor designed by an aero-engine company.

3.3 Dynamic Mass / Momentum Injection System

The mechanical design of the dynamic mass / momentum injection system represents a first attempt to implement aeromechanical feedback stabilization of rotating stall in axial flow compressors. The design was intended to be as simple as possible to demonstrate

the concept. As discussed in Chapter 2, the design of the dynamic mass / momentum injection strategy was constrained to control parameters that were physically realistic for the present study and thus was not a globally optimized configuration.

3.3.1 Reed Valve Housing

The annular structure designed and constructed to house the reed valves is shown in Figure 3.5. The reed valve housing contained 24 discrete reed valves which regulated the amount of high pressure air injected axially in the face of the compressor as a function of the local reed valve area opening.

The length of the reed valve housing was primarily determined by the axial location of the injection. Turbulent wall jets spread at an angle of approximately 7.5 degrees [23], and to have the injected flow mix out over the span before entering the compressor requires that the axial distance between the face of the rotor and the location of the injection (termed injection / rotor gap) be large compared to the annulus height. The assumption that the reed valves are closed coupled to the flow through the compressor, however, requires that the injection / rotor gap be small compared to radius of the compression system. In the limit of high hub / tip radius ratios, these two constraints can be met, but, for the present compression system the axial location of injection was selected based on a compromise between two conflicting criteria.

In the present investigation, an injection / rotor gap of 5 inches was selected. The reed valves thus formed the outer casing wall of the upstream duct in a region between 1.5 inches and 5.0 inches upstream of the compressor. In this region, the 24 planar reed valves formed a 24 sided polygon, approximating the original circular outer casing wall. The axial position selected corresponds to the injection location being 1.5 annulus heights, or approximately 0.5 compressor mean radii, upstream of the rotor.

An important parameter for the aeromechanical feedback control strategy is the axial distance between the center of pressure (from disturbances in the upstream flow field) acting on the reed valves and the entrance to the rotor. For the present design, the center of pressure of the reed was 0.35 compressor radii upstream of the rotor closer to the face of the compressor than the injection location.

The reed valves consisted of reeds cantilevered from their downstream side (Figure 3.5). The radial distance between the free end of the cantilever and the rigidly mounted injection lip formed the variable injection area. The analytical model developed in Chapter 2 assumes a continuous, locally reacting array of reed valves, but 24 reeds was considered to be a good compromise between complexity and spatial resolution.

The reed valve housing also contains a continuous, annular injection plenum designed to maintain a constant total pressure air supply to the array of reed valves, uniform around the circumference. The volume of the injection plenum was approximately 150 cubic inches (0.0024 cubic meters). The design injection mass flow was roughly 0.1 kg/s, corresponding to a mean flow velocity on the order of 1 m/s within the injection plenum. This velocity is well below the injection velocity (roughly 60 m/s), so the static pressure around the circumference of the annular injection plenum was taken as uniform.

To minimize any steady state pressure differences across the reed valves, a circumferentially continuous annular cavity was used to provide a circumferentially uniform back pressure to the reed valves. The back pressure cavity is shown in Figure 3.5. The steady state pressure in the back pressure cavity was equalized, via leakage gaps between the discrete reed valves, with the free stream pressure in the duct upstream of the compressor. Note that for zero annulus averaged reed valve deflections, the volume of

the back pressure cavity remains constant to first order. The back pressure cavity thus provides no restoring force on the reed valve dynamics for the zero annulus averaged, non-axisymmetric disturbances of interest here.

3.3.2 Reeds

The reeds in the reed valves were fabricated from AW-193-PW graphite weave / 3501-6 epoxy composite material. The composite laminate contained two layers of 0-90 degree cross weave fabric. A schematic of a typical reed is shown in Figure 3.6, and the detailed properties are given in Table 3.2. The reeds were mounted individually to the housing by clamping the base of the reed between to steel plates. A thin layer (0.01 inches) of visco-elastic damping material was installed on both sides of each reed valve between the reed and the steel mounting plates. The forward facing edge of the mounting hardware was chamfered at a 45 degree angle to minimize the disruption to the flow field due to the mounting hardware.

As discussed in Chapter 2, the stability of the compression system was predicted to be a function of several parameters, including the geometry of the reed valves, the reed valve dynamics, and the injection pressure. The guideline used in selecting the reed valve design was to obtain reed valves with the least mass that could be constructed consistent with the constraints on the geometry and dynamic characteristics. Other materials for the reed valves were considered including steel, aluminum, and several conventional plastics. Of the materials considered, however, the graphite epoxy weave possessed dynamic characteristics that were predicted to have the largest stabilizing influence on the compression system.

In the consideration of design of the reed valves, the geometry of the reeds was restricted to flat plates, based on ease of construction considerations. By considering more

optimized reed geometries, it is reasonable to assume that a more optimized dynamic mass / momentum injection facility could be designed.

3.3.3 Pneumatic Dashpots

The optimized design parameters were based on representing the reed valve behavior as second order dynamic oscillators with a critical damping ratio roughly equal to unity. Although attempts were made to achieve these high levels of damping using several methods to introduce damping, including visco-elastic damping materials and auxiliary pneumatic damping cavities, auxiliary dashpots were deemed the most practical method. Thus, to provide additional damping in the reed valve dynamics, low friction, low mass, adjustable, pneumatic dashpots were installed on each reed valve.

A schematic of a typical pneumatic dashpot is shown in Figure 3.7. Each dashpot consisted of a low friction piston and cylinder configuration, with damping controlled by an adjustable orifice on the cylinder. The cylinders of the dashpots were mounted to the reed valve housing and the linkage attached to the piston was attached to the centerline of each reed valve near the tip of the cantilevered reed valve as shown in Figure 3.7. The properties of the commercially available dashpots are listed in Table 3.3.

3.3.4 Reed Valve Seals

Design of the reed valves required a sealing mechanism to isolate the high pressure air in the injection plenum from the back pressure cavity behind the reeds. The seals had to withstand steady state pressure loading, on the order of 1 psi, yet remain flexible in the transverse direction to minimize their effect on the reed valve dynamics. The seals were also designed to minimize aeroelastic interaction between reed valve deflection and the injection flow.

The final seal configuration, which was the result of experimentally testing several seal designs, used several materials including Dacron tape, Teflon tape, and Capton tape. Two copper stiffeners were also incorporated in each seal. A schematic of a typical seal is shown in Figure 3.8. The seals were assembled and installed in the reed valves using pressure sensitive adhesives on the tapes.

To minimize leakage of high pressure air from the injection plenum into the back pressure cavity, the inter-reed gap between two adjacent reed valves exposed to the high static pressure the injection region was covered using loose fitting strips of flexible rubber also shown in Figure 3.8. The rubber strips were attached to the inner wall of the injection plenum and to the reed valves approximately 0.75 inches downstream of the axial location of the injection. The loose fitting inter-reed seals allowed each reed to react independently of the adjacent reeds.

The flow deflectors shown in Figure 3.8 were installed within the injection plenum to minimize the effect of the jets associated with the discrete injection supply ports within the injection plenum impinging on the seals.

3.3.5 Injection Supply

Although, in principle, the high pressure air injected in front of the compressor could be bled from the compressor exit, an external source for the compressed air was used to allow greater flexibility in the injection parameters and reduced the complexity of the experiment. The oil-free shop air supply at the Gas Turbine Lab was used as the source for the injection air (up to 750 scfm (0.4 kg/s) at 100 psig). A schematic of the injection supply system is shown in Figure 3.9. Because the desired design injection pressure range was limited to 1 psig, the supply source was throttled with a choked butterfly valve. After this valve, the air passed through a Venturi flow metering device, through an

adjustable ball valve, into a distribution plenum. From the distribution plenum, the air was supplied to the annular injection plenum via ten, 1 - 1/2 inch diameter hoses. Immediately upstream of the injection plenum, each hose branched into two, so the air was delivered to the injection plenum at low velocity (roughly 10 m/s) via twenty ports distributed around the annulus. The amount of high pressure air injected into the compressor was regulated as a function of circumferential position by the displacement of the reed valves. Throughout the injection supply system, several safety blow-off valves were installed at various pressure ratings to prevent accidental over-pressurization of the injection system.

For non-axisymmetric, zero annulus-averaged, flow disturbances, the time resolved level of injection mass flow should be constant to first order. Therefore, the injection supply system dynamics were assumed to not interact with the injection dynamics.

3.4 Instrumentation

Time averaged compressor performance and injection parameters were measured in addition to time resolved pressure, velocity, and reed deflection perturbations. A schematic of the instrumentation layout is shown in Figure 3.10.

3.4.1 Steady State Measurements

Steady state compressor performance was measured using instrumentation of the existing facility. The instrumentation used to measure the steady state compressor performance is outlined in this thesis, and further details are presented by Paduano [25]. The compressor inlet mass flow calculated based on the annulus averaged total and static pressure. The total and static pressures were each measured at eight equally spaced angular positions around the annulus. The total pressure was measured using eight, axial Kiel probes mounted at mid-span, and the static pressure was measured using wall taps on the outer

casing. The pressures were measured at an axial station approximately one compressor radius upstream of the compressor as shown in Figure 3.10, upstream of the injection region. The annulus averaged total to static pressure rise was measured using annulus averaged upstream total pressure measurement described above and eight downstream static pressure measurements.

Time averaged pressure measurements were connected to a remote scanivalve via approximately 50 feet of flexible tubing. The pressures were measured using a 2.5 psi Spectra strain gauge type transducer.

Compressor wheel speed was monitored using a Hewlett Packard model 5300B frequency counter. Compressor wheel speed was maintained constant using manual control of a 250 HP DC drive motor.

Ambient temperature was measured using an Omega thermocouple, ambient pressure was taken as atmospheric pressure recorded at Logan airport.

Time averaged injection mass flow was measured using a B.I.F. Inc.(model UVT-PI-0182-022231) Venturi flow meter. The pressures were measured using a 0-5 psi Magnehelic differential pressure gauge and a Marshalltown 0-100 psig pressure gauge. The pressure within the injection plenum was measured relative to the free stream static pressure using a 0-2 psi Magnehelic differential pressure gauge. The details of the measurement of the mass flow and momentum injected through the reed valves are given in Appendix G. The steady state valve area was not monitored during the experiments.

Velocity profiles at the face of the compressor were recorded using a linear traverse, a Dantec hot-wire, and a Fluke 8062A true rms volt meter.

3.4.2 Time Resolved Measurements

The time resolved instrumentation consisted of ten hot-wires, two pressure transducers and four reed valves instrumented with strain gauges. The time resolved pressure and axial velocity measurements presented were recorded at various circumferential and span-wise locations at an axial station 1/3 chord (0.5 inches) upstream of the rotor (4.5 inches downstream of the injection location). The cutoff frequency of all the unsteady data was set at 100 Hz so that the effect of the filters on the phase relationship between time resolved signals would be minimized.

Dantec type 55-P11 hot-wire probes were used to measure time resolved axial velocity perturbations. The hot-wires were aligned perpendicular to the axis of the compression system. The hot-wires were driven by Dantec type 56C17 CTA bridge anemometers, Of the ten hot-wires, eight were placed at equal circumferential intervals, at mid span, approximately 1/3 chord upstream of the rotor. This spatial array of hot wires was capable of resolving the magnitude and phase of the three lowest spatial harmonics around the annulus. The remaining two hot-wires were placed at various locations to examine axial and radial variations in the flow field.

Calibration of the hot-wires was performed by recording the annulus averaged mass flow coefficient measured via the scani-valve to the rms of the hot-wire voltage. During calibration, the compressor was run at different speeds to allow a greater mass flow range for calibration. The hot-wires were calibrated using a specific form of the generalized King's Law for hot-wire anemometers:

$$(\text{Volts})^2 = A + B\,(C_x)^{\frac{1}{2}} \tag{3.1}$$

A typical hot-wire calibration is shown in Figure 3.11. The velocity perturbations were calculated for the hot-wire data based on the calibration linearized about the mean flow.

Time resolved pressure measurements were recorded with Druck model PDCR 820 (0-1 psig) pressure transducers. The high frequency response pressure transducers were mounted in a close-coupled manner to static pressure ports in the outer casing at various axial locations. The Druck pressure transducers were driven by Pacific Scientific 8650 signal conditioning amplifiers. The amplifiers contained built-in, low-pass filters which filtered the pressure signals at 100 Hz. The Druck pressure transducers were calibrated using a MKS Barotron. A typical calibration is shown in Figure 3.12.

Reed deflections were obtained using a strain gauge bridge designed to measure the bending strain at the root of the cantilevered reed valve. A schematic of the strain gauge bridge is shown in Figure 3.13. The strain gauge bridge consisted of two, type CEA-06-125UT-350, Micro-Measurement 90 degree "T" rosettes. As shown in Figure 3.13, two of the strain gauges were aligned with the axis of the cantilevered reed valves, and two were aligned perpendicular to the axis of the reed valves. The strain gauges were mounted on the side of the reed valves exposed to the back pressure cavity. Every other reed valve was instrumented with strain gauges, however, only 4 reeds, equally spaced around the annulus, were monitored during the experiments. The strain gauge bridges were driven by the same type of Pacific Scientific amplifiers used for the unsteady pressure measurements. The reed signals were low pass filtered at 100 Hz.

A static calibration of the reed valve strain gauges was performed using a dial indicator to measure the tip deflection of the reed valve. A typical calibration of tip deflection versus strain gauge amplifier output is shown in Figure 3.14. This calibration technique assumes that the mode shape of the dynamic reed deflection is similar to the static mode shape for a point load applied at the tip of the reed valve, along the centerline of the reed valve. For a uniform cantilevered beam, the second cantilevered bending mode occurs at a

frequency approximately six times that for the first bending mode, and the assumption that the reed motion is dominated by the first bending mode is reasonable. Because the shape of the first bending mode is similar to the static deflection shape of a uniform cantilevered beam, the calibration techniques was deemed adequate.

3.5 Data Acquisition

In addition to the manually recorded values, two computers were used to record data: a VAXStation II for steady state performance data and a HP 486 Vectra for time resolved data. The two computerized, data acquisition systems were operated independently.

3.5.1 Steady State Data

The VAX workstation operated and monitored the scanivalve to measure pressure signals used to calculate steady state performance of the compressor. The VAX used a Data Translations DT3382 A/D system to monitor the scanivalve. The A/D system averaged each pressure reading for 0.1 seconds operating at 1000 Hz. This system allowed for low frequency response, annulus averaged pressure rise and mass flow measurements to be recorded every ten seconds. During the experiment, the compressor total-to-static pressure rise coefficient versus mass flow coefficient performance characteristic was displayed graphically.

3.5.2 Time Resolved Data

Time resolved data was sampled using a HP 486 Vectra computer using a sixteen bit Analogic analog to digital converter. The computer recorded sixteen channels of data at 1000 Hz for five second intervals on command. The cutoff frequency of the filters used to filter time resolved measurements was set at 100 Hz, so the anti-aliasing Nyquist frequency requirement was satisfied. The A/D data sets were recorded on the hard drive

in the HP computer, and a 120 MB tape drive was used to store the data for off line processing.

Table 3.1: Compressor Geometry

Number of stages	1
Tip diameter	0.591 m
Hub diameter	0.445 m
Hub / tip radius ratio	0.75
Mean radius	0.259 m
Rotor / stator gap	48 mm

Blade Row	Number of Blades	Chord [1] (mm)	Camber [2] (deg)	Stagger (deg)	Twist [3] (deg)	Solidity [4]
Rotor	44	38 (midspan)	25 (midspan)	35 (midspan)	30	1.03
Stator	45	38	30	22.5 (midspan)	-5	1.08

Notes: 1) Rotor chord distribution is shown in Figure 3.4.
2) Rotor camber varies with span
3) Twist is linear function of span defined as (tip stagger - hub stagger)
4) Solidity is defined using the mid-span chord for the rotor

Table 3.2: Reed Properties

Material	[0 / 90] Graphite / Epoxy cross weave laminate
Elastic Modulus	9.0 Mpsi
Density	1500 kg/m^3
Length	4.0 in
Width	3.1 in
Thickness	0.015 in

Table 3.3: Pneumatic Dashpot Properties

Manufacturer	Airpot Corporation Norwalk, CT
Specification	S160A100F175
Piston Material	Graphite / Carbon
Cylinder Material	Pyrex
Damping Range[1]	0 -10 lbs/in/sec
Friction[1]	less than 1 gram
Mass of Piston Assembly[2]	4.7 grams
Cylinder Bore Diameter[1]	0.627 in
Cylinder Length[1]	1.00 in
Piston Length[1]	0.51 in

notes: 1) Supplied by manufacturer
2) Measured value

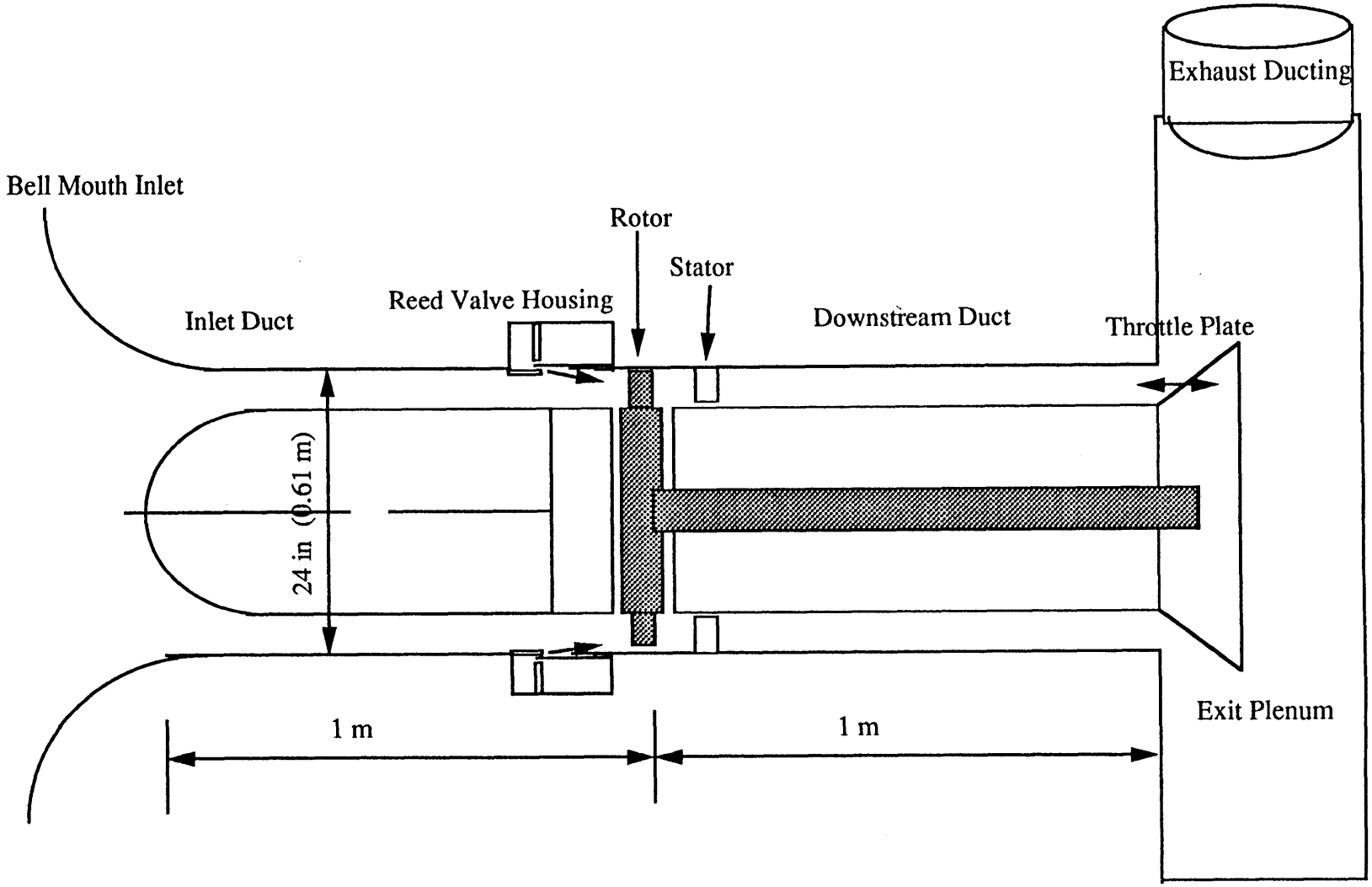

Figure 3.1: Schematic of MIT Single Stage Compressor with Dynamic Mass / Momentum Injection

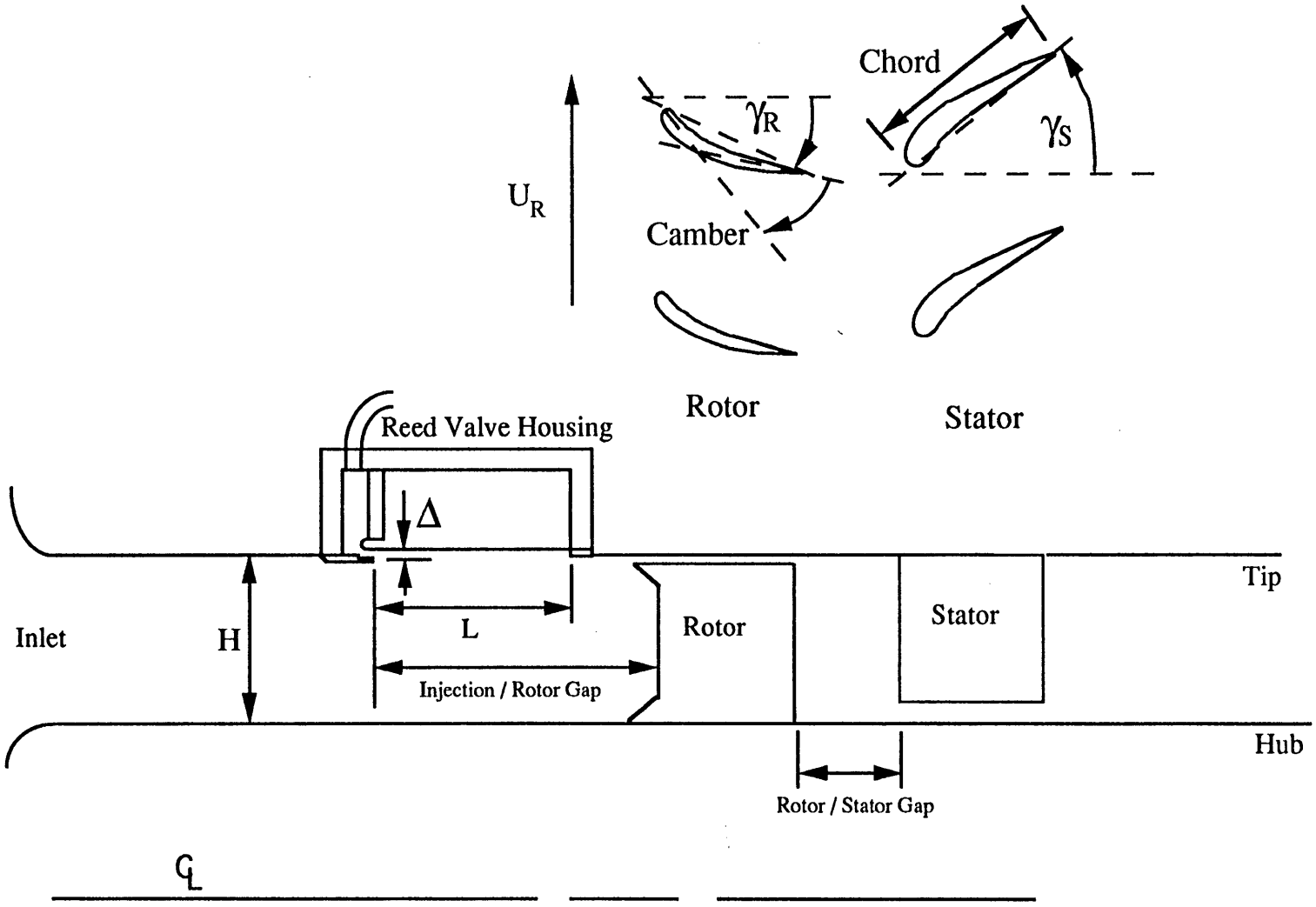

Figure 3.2: Schematic of Compressor Geometry

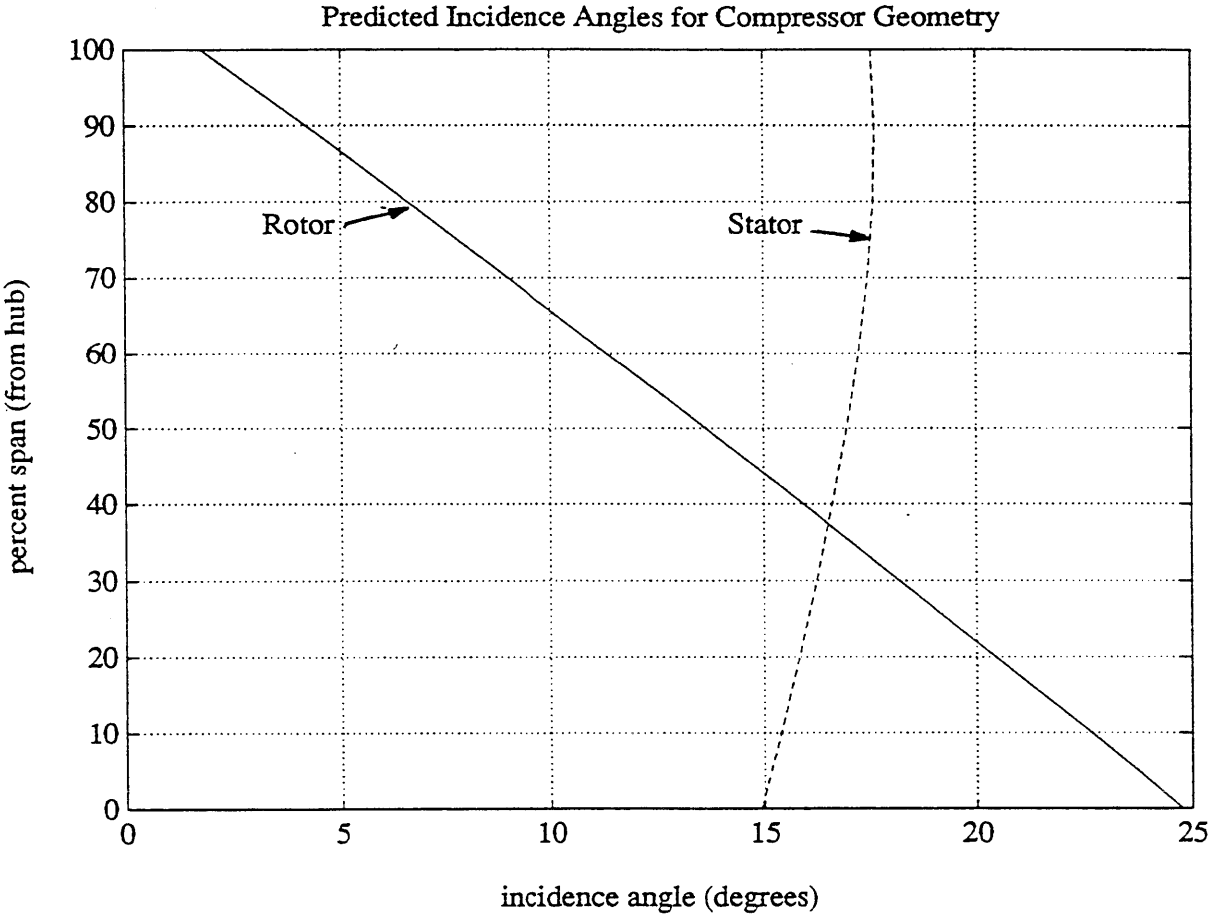

Figure 3.3 Calculated Aerodynamic Incidence Angle as a Function of Span for Compressor Build Near Stall (Φ=0.55 at mid-span)

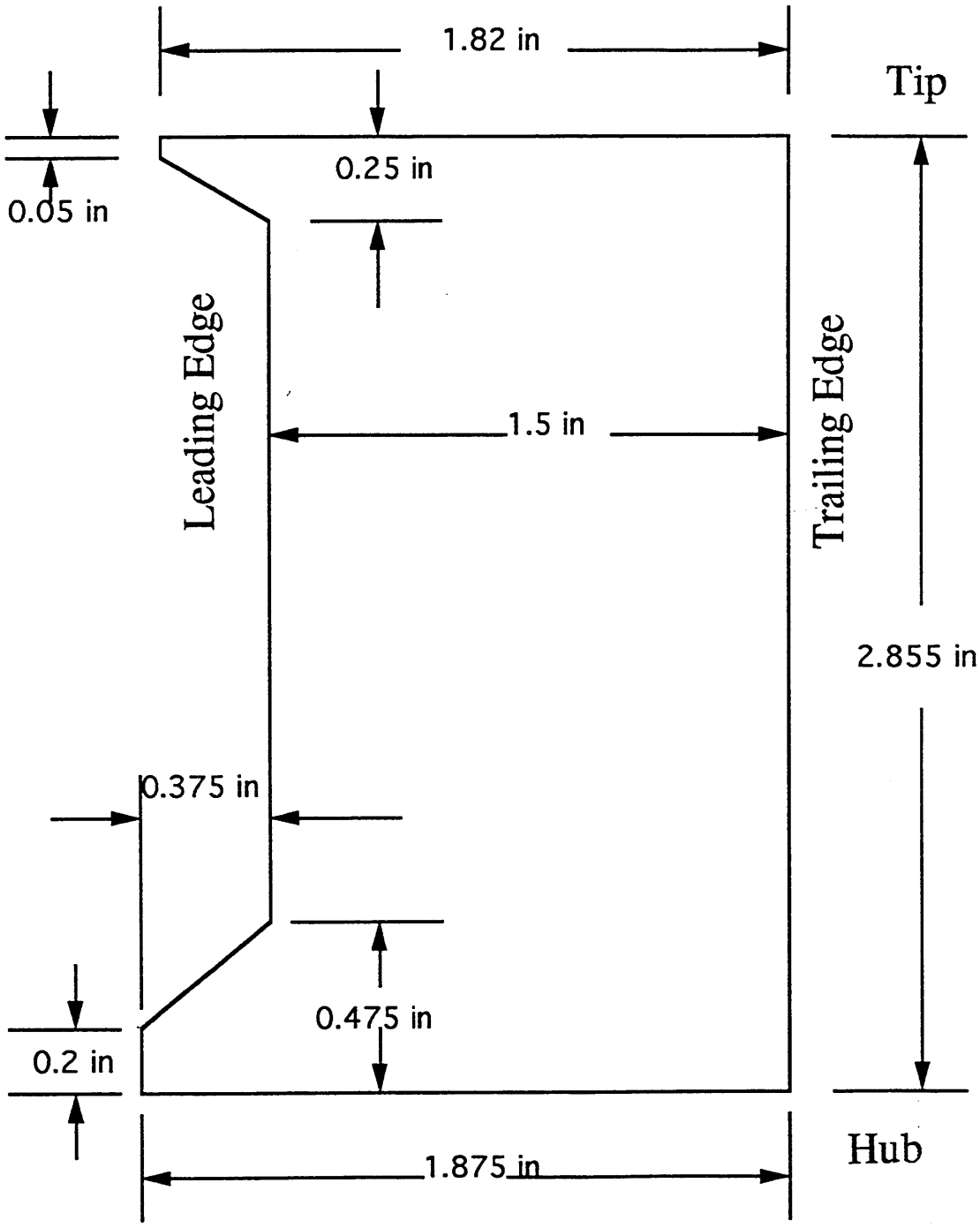

Figure 3.4: Schematic of Rotor Blade Geometry

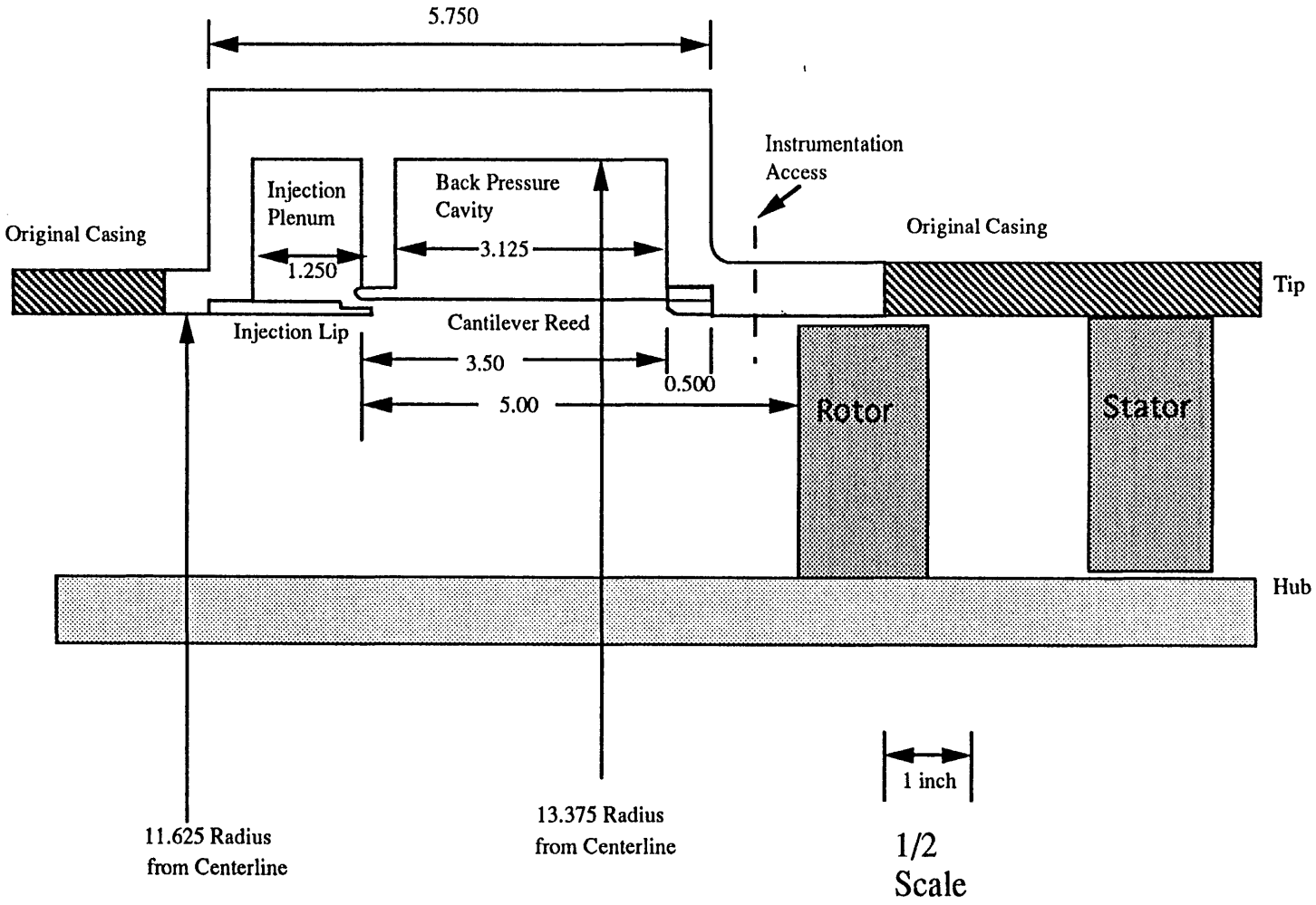

Figure 3.5: Scaled Drawing of Dynamic Mass / Momentum Injection Hardware

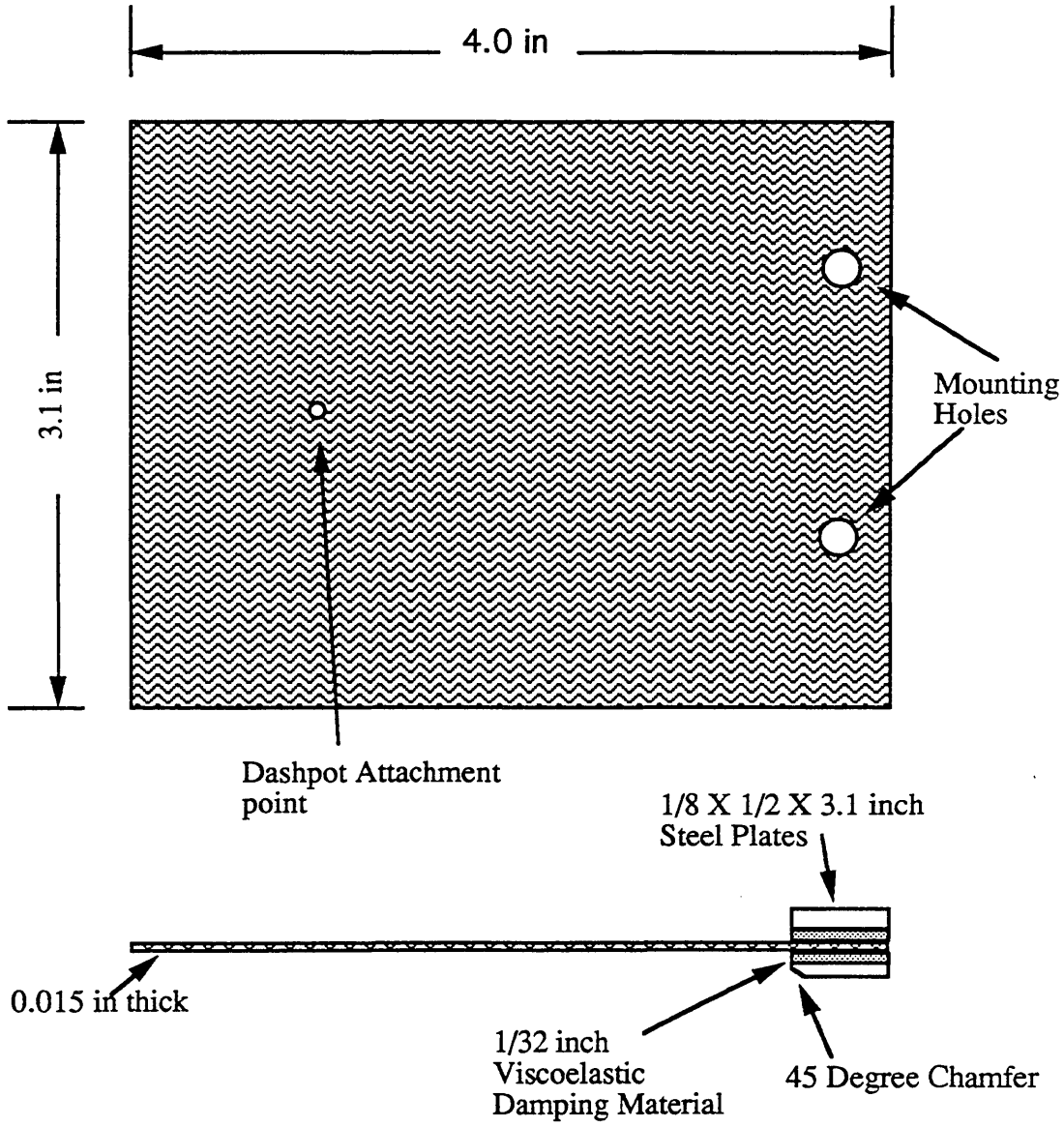

Figure 3.6: Schematic of Typical Reed Valve and Mounting Hardware

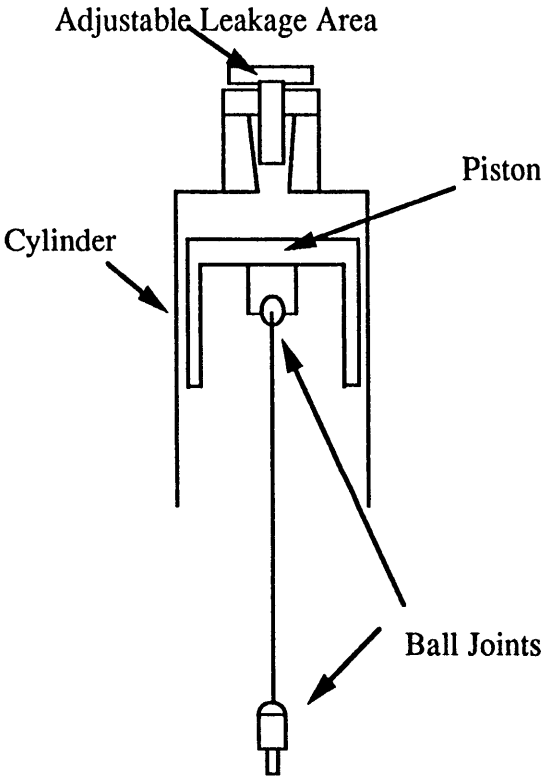

Detailed Schematic of Daspot

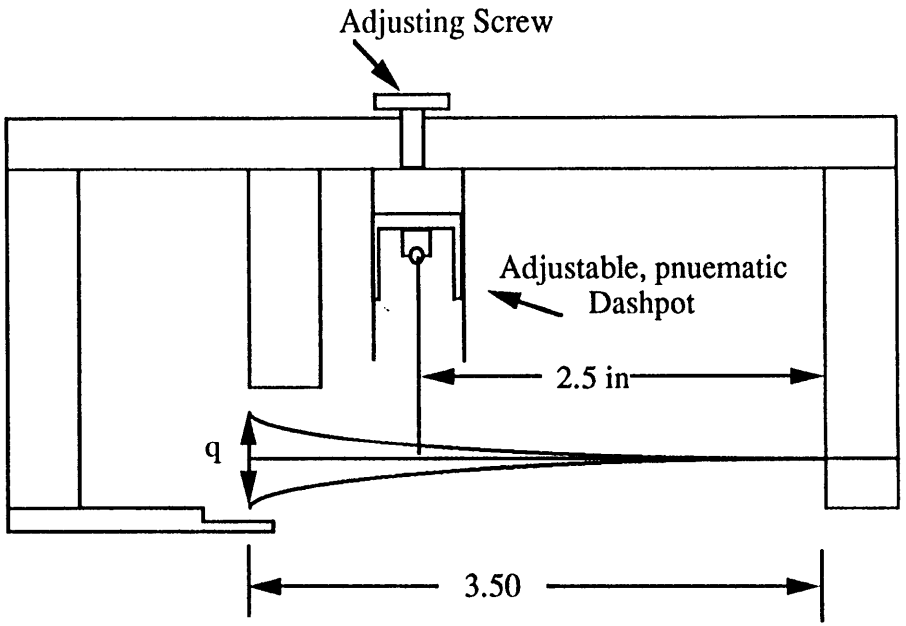

Dashpot Mounted in Reed Valve Housing

Figure 3.7: Schematic of Pneumatic Dashpots

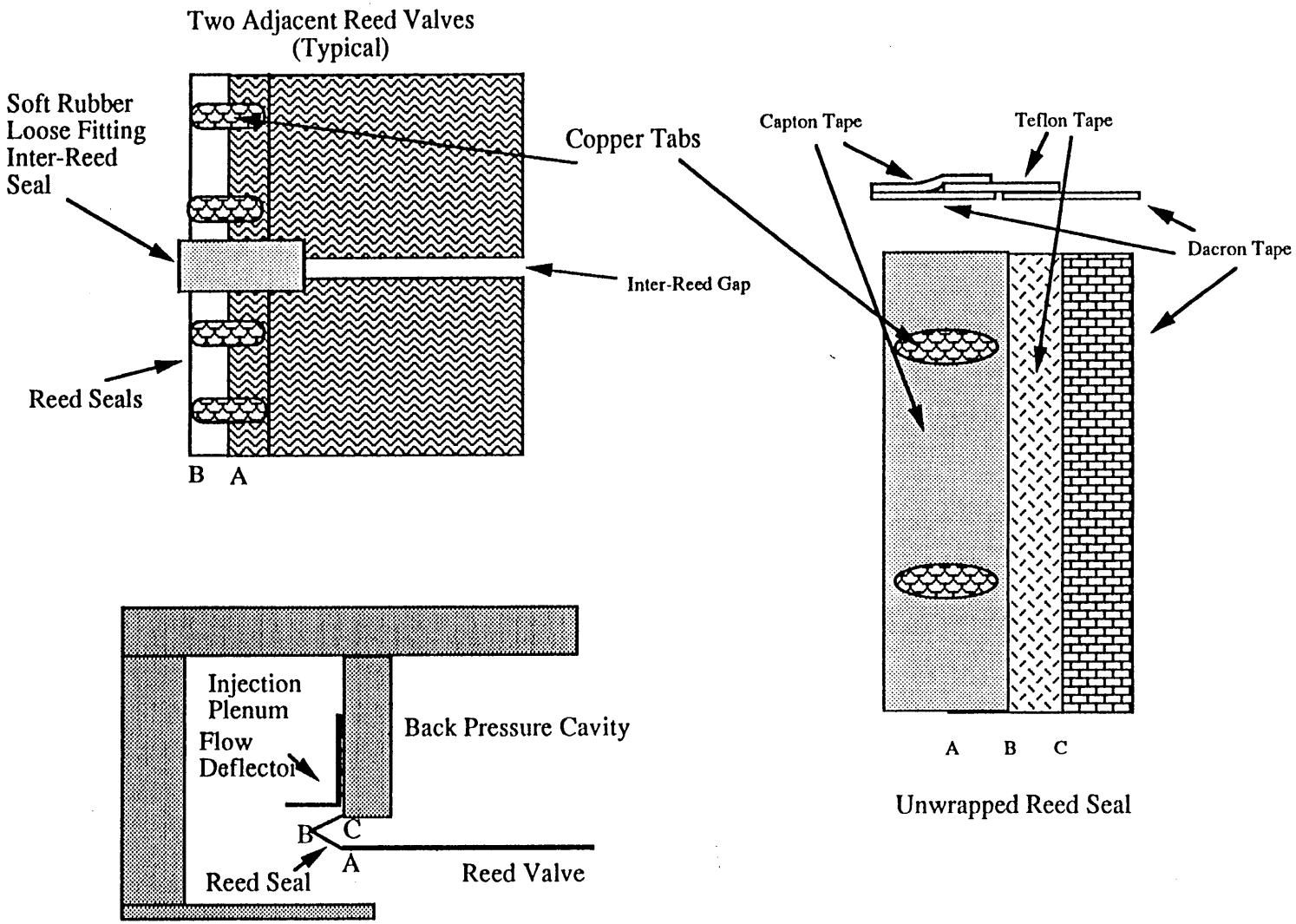

Figure 3.8: Schematic of Reed Valve and Inter-Reed Valve Seals

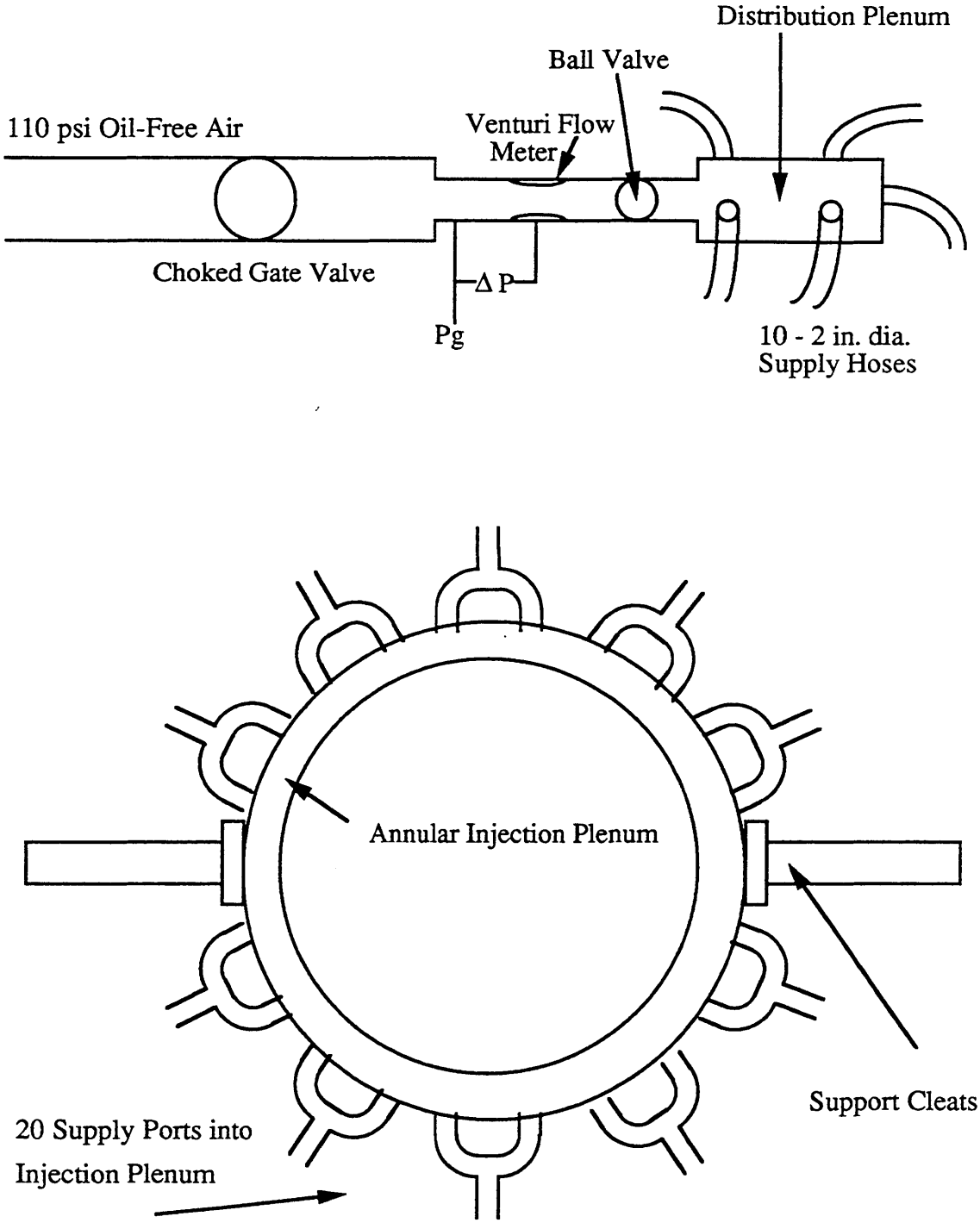

Figure 3.9: Schematic of Injection Supply System

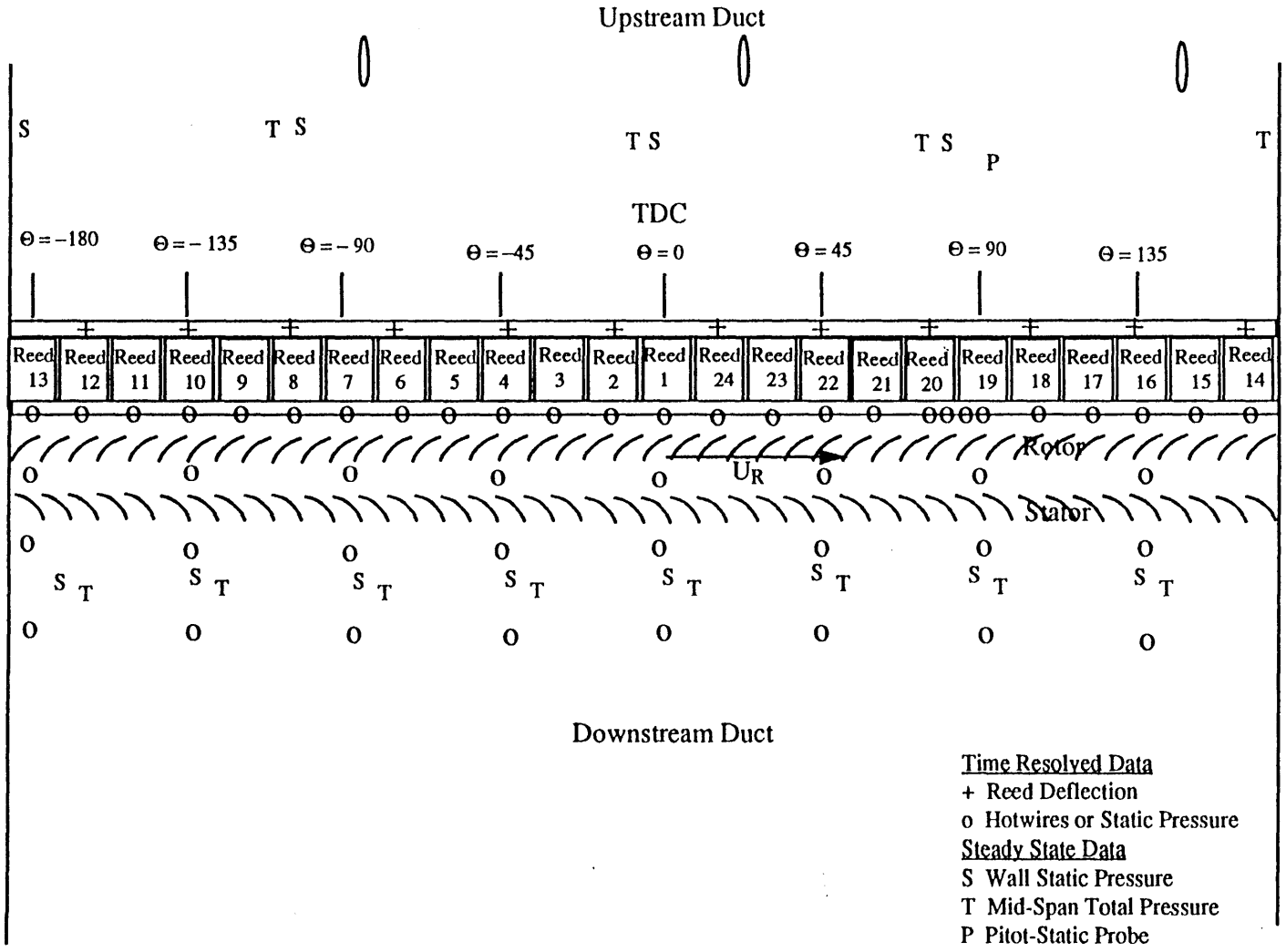

Figure 3.10: Instrumentation Layout

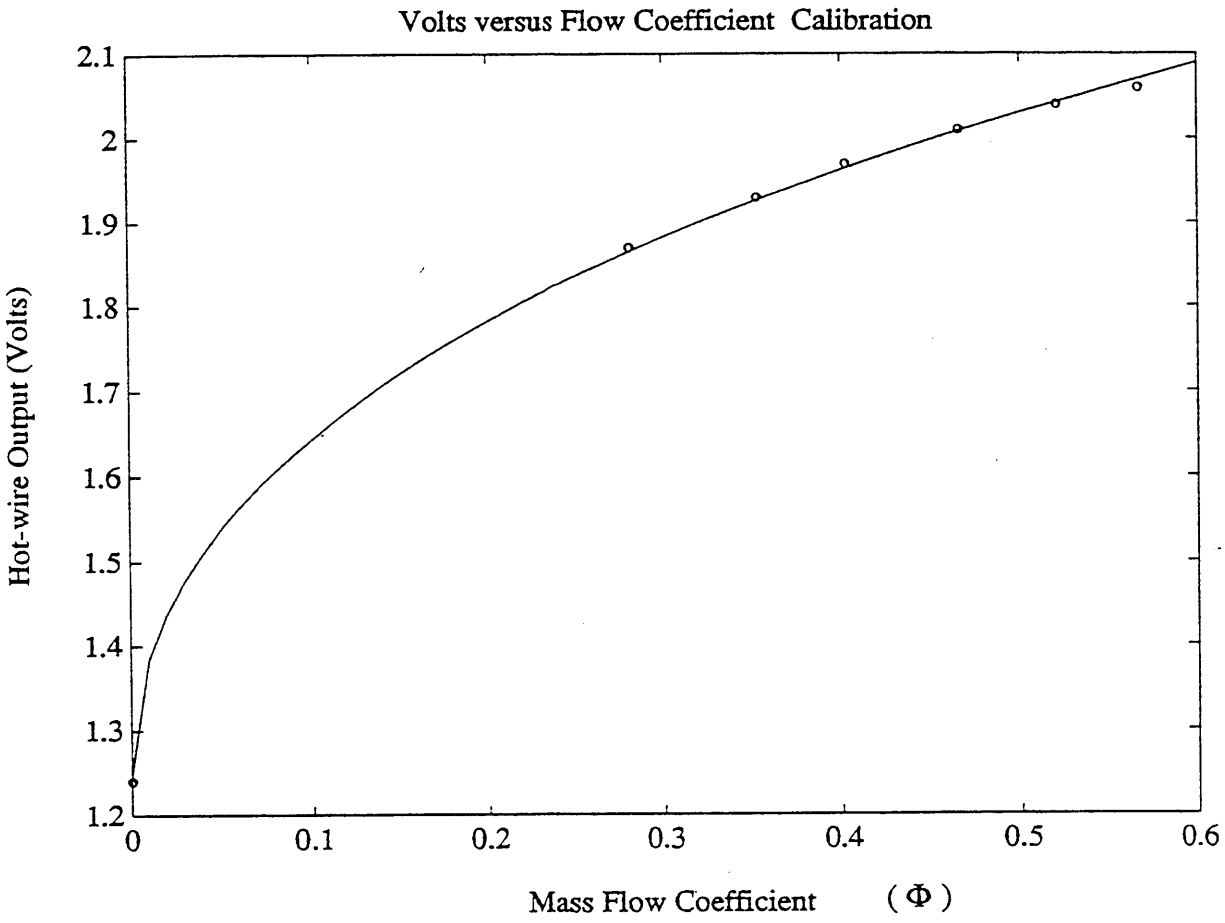

Figure 3.11 Typical Hot-Wire Voltage versus Flow Coefficient Calibration (2250 RPM)

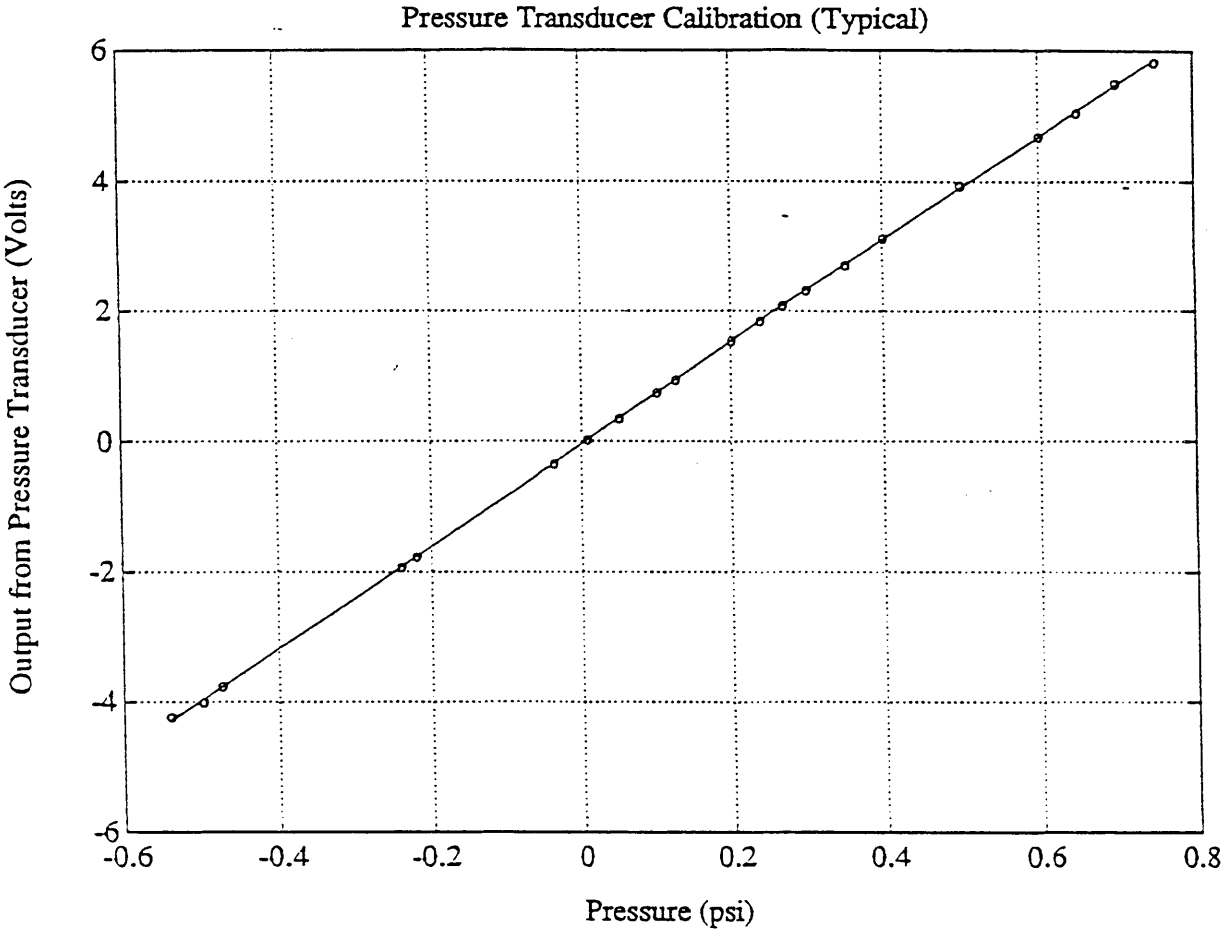

Figure 3.12 Typical Pressure Transducer Calibration

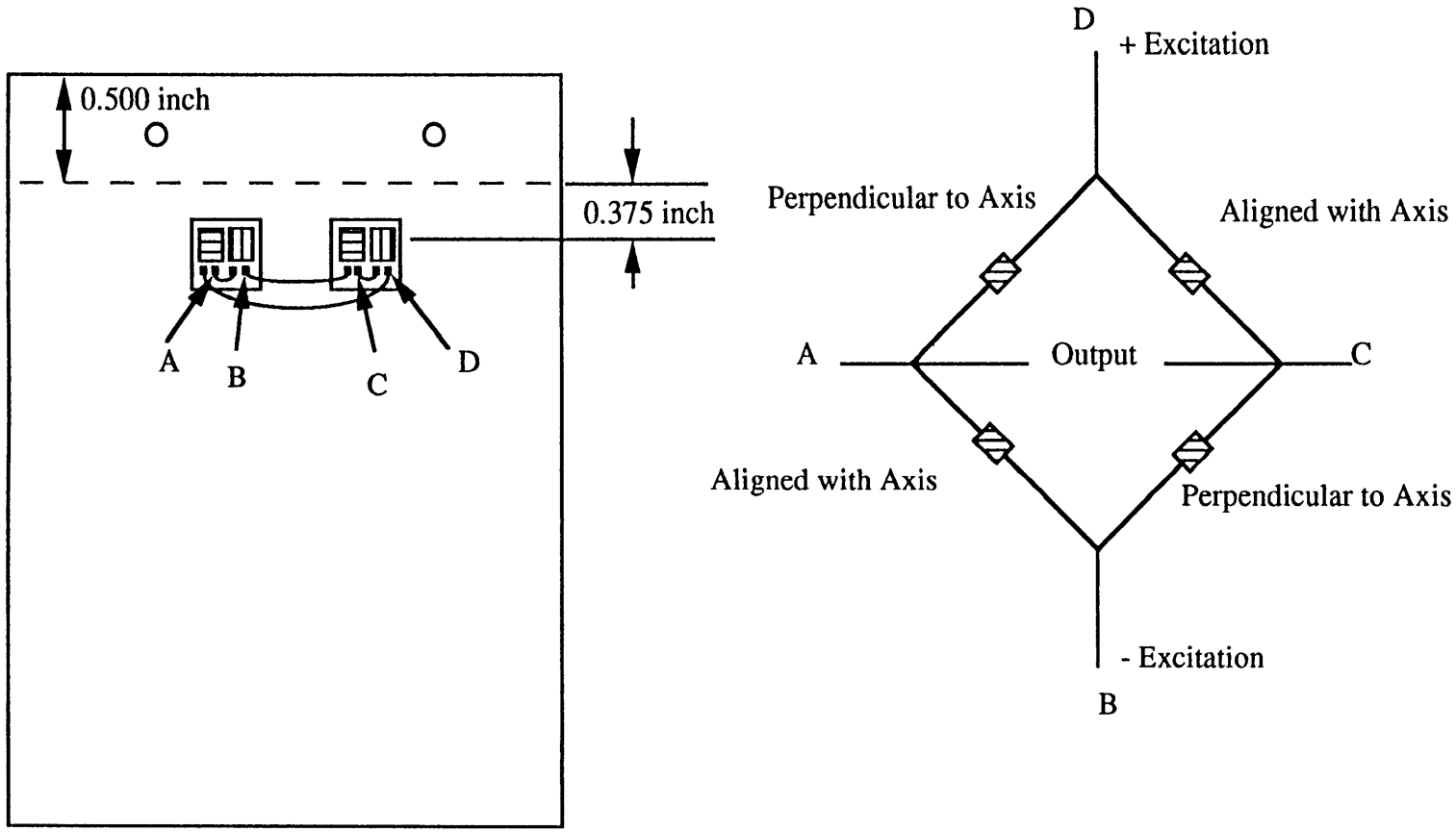

Figure 3.13: Strain Gauge / Wheatstone Bridge Used to Measure Tip Deflection via Root Bending Strain

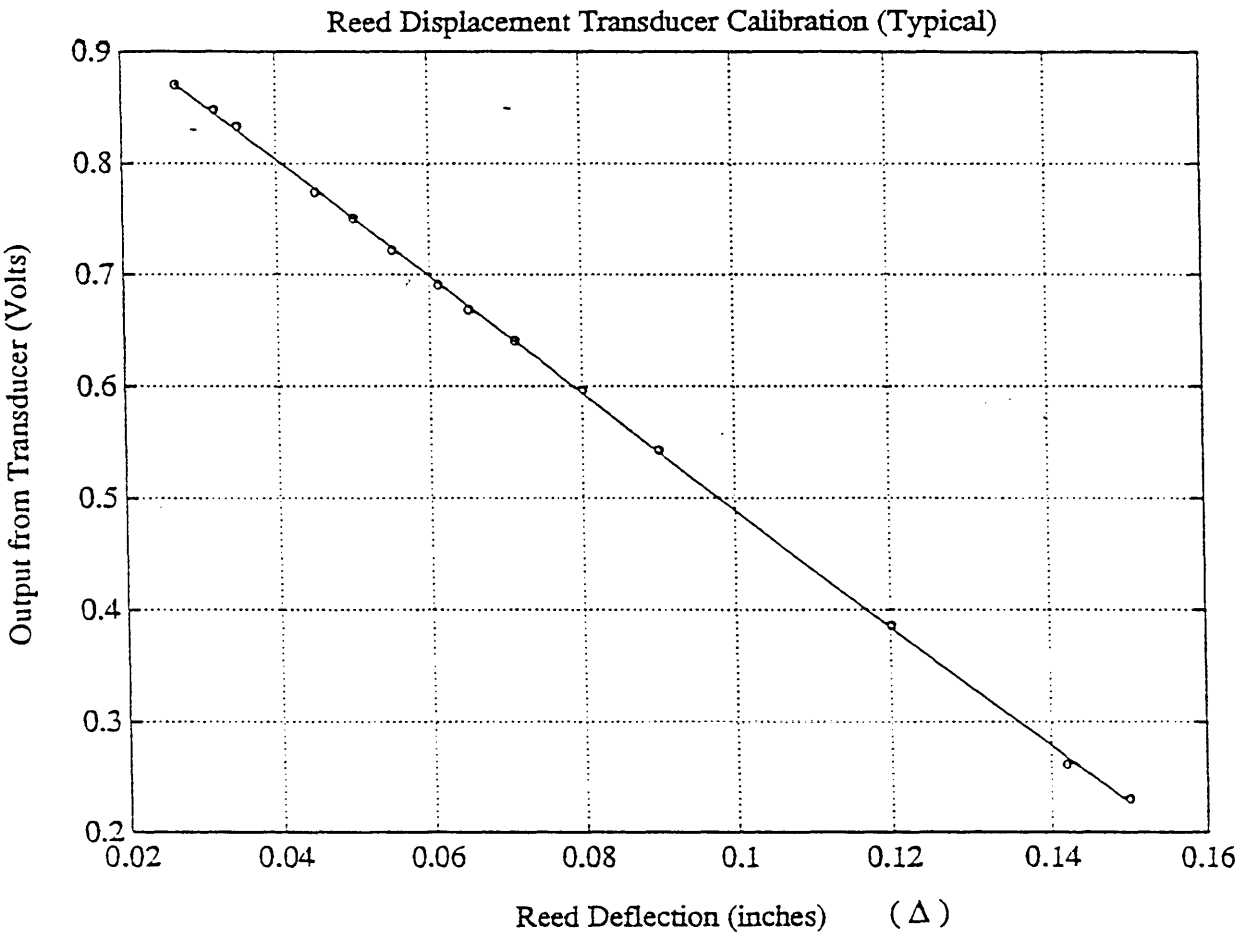

Figure 3.14 Typical Static Calibration for Reed Deflection

Chapter 4: Experimental Results and Comparison with Theory

4.1 Introduction

Experiments were carried out to assess the effect of aeromechanical feedback introduced by dynamic mass / momentum injection on the steady state and time resolved performance of a low speed, single stage, axial flow compressor. The objective of the experimental program was to:

1) demonstrate aeromechanical feedback stabilization of rotating stall

2) determine the effect of the control parameters on system stability

3) evaluate the conceptual framework of the dynamic model of the compression system

The behavior of the baseline compression system and of the reed valve dynamics were characterized independently. The effects of steady state injection and of aeromechanical feedback were then investigated and the experimental results compared to predictions of both a linearized stability model and a non-linear simulation.

4.2 Baseline Compression System Dynamics

The baseline compression system is defined here as the compressor operating with the reed valves installed upstream of the compressor, but with no time mean mass flow injected through the valves. All performance data presented in this thesis is for the compressor build described in Chapter 3, operating at 2250 rpm, with varying amounts of injection and reed valve dynamics.

4.2.1 Steady State Performance

Figure 4.1 shows the inlet total to exit static pressure rise coefficient, $\Psi \equiv [P_{s_d} - P_{t_u}] / \left[\frac{1}{2} \rho U_R^2\right]$, versus mass flow coefficient, $\Phi \equiv C_x / U_R$, for the baseline compressor operating at constant speed. The speedline was recorded by slowly closing the

throttle while manually maintaining constant compressor speed at 2250 +/- 2 RPM. The solid line Figure 4.1 is a third order fit of the performance curve data.

The stalling flow coefficient of the compression system was determined by slowly closing the throttle until the compressor exhibited large amplitude rotating stall. The baseline compression system encountered rotating stall at $\Phi = 0.435$. The slope of the compressor annulus averaged total to static pressure rise versus mass flow characteristic was slightly positive when the compressor stalled.

Once large amplitude stall was detected via an oscilloscope, the throttle was opened immediately to minimize fatigue of the reed valves. Instrumentation was not set up to accurately record the performance of the compression system operating in rotating stall.

4.2.2 Time Resolved Performance

Axial velocity and static pressure perturbations at a station 1/3 chord upstream of the rotor are shown in Figure 4.2 for three flow coefficients; $\Phi = 0.59$, 0.50, and 0.44, indicated on the compressor speedline in Figure 4.1 by points A, B, and C, respectively. The axial velocity traces were recorded at mid-span at $\theta = 90$ degrees and the static pressure was recorded from a wall static tap at $\theta = 75$ degrees, where θ is the circumferential position defined in Figure 3.10. In Figure 4.2, the pressure perturbation, normalized by the dynamic head based on compressor wheel speed, $\frac{1}{2} \rho U_R^2$, and the axial velocity perturbations, normalized by compressor wheel speed, U_R, are plotted versus time, normalized by rotor revolutions.

Well away from stall, at $\Phi = 0.59$ (Pt. A) , small amplitude perturbations exist about the essentially axisymmetric flow field. As the flow coefficient is reduced, the magnitude of

the perturbations increases and the perturbations appear to develop harmonic content at specific frequencies.

Figure 4.3 shows spatial Fourier decomposition (magnitude and unwrapped phase) of axial velocity perturbations plotted versus time for the basic compression system operating away from stall at $\Phi = 0.59$ (Pt. A). The velocity perturbations were recorded with a circumferential array of eight hot-wires, equally spaced around the annulus at mid span, 1/3 chord upstream of the rotor. The method used to decompose the axial velocity perturbations into the spatial Fourier components is developed in Appendix F. At this flow coefficient, the magnitudes of the first three spatial harmonics appear to exhibit random growth and decay with time. The plot of the unwrapped phase indicates that no coherent traveling wave are observed in the flow field.

Figure 4.4 shows similar data for operation at $\Phi = 0.44$ (Pt. C), near the stalling flow coefficient. The magnitudes of the spatial harmonics continue to fluctuate with time, however, the magnitudes of the first and second spatial harmonics are considerably larger than those seen in Figure 4.3, for the condition away from stall. The unwrapped phase, plotted as a function of time, for each of the spatial harmonics is also given in Figure 4.4; this shows that all three of the spatial harmonics exhibit intermittent periods in which coherent traveling waves are seen, but, the first and second spatial harmonics exhibit traveling waves for longer intervals than does the third harmonic. The phase speed of the three harmonics, indicated by the slope of the linear segments on the phase versus time plot, is 26%, 33% and 34% for the first, second, and third spatial harmonics, respectively.

Temporal power spectral density functions (PSD's) of the static pressure and axial velocity perturbations recorded for the three operating conditions of Figure 4.2 are shown in Figure 4.5. The PSD's were averaged using over five seconds of data, discretely sampled at 1000

Hz. Thus, the PSD's shown represent an average of the frequency content over approximately 200 rotor revolutions. The details of the PSD analysis are developed in Appendix F.

For the operating point well away from stall (Φ =0.59, Pt. A), disturbances associated with once and twice rotor revolution frequency have the largest frequency content. However, as the flow coefficient is reduced, disturbances with temporal frequencies of 26% and 66% increase in magnitude, while the once and twice-per rotor revolution disturbances remain at essentially the same level. Near stall, at $\Phi = 0.44$ (Pt. C), the disturbance flow field is dominated by disturbances at 26% and 66% of rotor frequency.

Data from single circumferential positions do not allow resolution of the spatial content of the disturbances. However, comparing the PSD's of the pressure and axial velocity perturbations for the operating point close to stall ($\Phi = 0.44$) with the spatial Fourier components obtained from the circumferential array of hot-wires confirms that the peaks in the power spectra are associated with traveling waves corresponding to the first and second spatial harmonics. Because the third harmonic only exhibited coherent traveling wave structure for intermittent periods, there is no significant peak in the power spectra at a temporal frequency (approximately 100% percent of the rotor frequency) which would correspond to a traveling third spatial harmonic. The PSD's of the pressure and velocity indicate that oscillations in the flow field near stall are dominated by traveling disturbances associated with the first and second spatial harmonics of the rotating stall dynamics for frequencies below 2.5 times the rotor frequency.

4.2.2.1 Stall Inception

A primary assumption in the modeling presented in Chapter 2 is that the compressor exhibits long wave length, full-span, stall inception. The compressor build was selected to

be similar to a compressor build that Paduano [25] demonstrated to exhibit this behavior. Figure 4.6 shows the axial velocity perturbations recorded during a stall inception event by eight equally spaced hot-wires around the annulus, 1/3 chord upstream of the rotor, at mid-span and aligned perpendicular to the axis of the compression system. The stall inception event was recorded by operating the compressor within 1% of the stalling flow coefficient and then closing the throttle at a rate of approximately 0.1% of the stalling flow coefficient per rotor revolution. The compressor transitions from essentially axisymmetric flow into fully developed rotating stall via the smooth growth of initially small amplitude, traveling waves, consistent with the predictions of the model.

Figure 4.7 shows the spatial Fourier decomposition of the velocity perturbations shown in Figure 4.6. The magnitude of the second spatial harmonic is the largest of the three prior to large amplitude rotating stall and appears to initiate the stall inception process. The unwrapped spatial phase of each of the first three spatial harmonics, plotted versus time during the stall inception process, shows that each of the three harmonics appear to travel in a coherent wave for intermittent periods prior to stall inception. However, the second harmonic exhibits a traveling wave pattern for the longest interval prior to large amplitude stall. During the intermittent periods prior to stall, the first three harmonics travel at 25%, 32%, and 35% of the rotor frequency, respectively. These rotation rates are similar to those observed at Φ =0.44 in the stable operating range near the stalling flow coefficient. Thus, the oscillations that develop into large amplitude rotating stall appear to be directly associated with the oscillations that exist in the compression system over a finite mass flow range prior to stall.

4.2.2.2 Radial Variations

Data were also recorded to determine the radial variation of the velocity perturbations during the stall inception process. Figure 4.8 shows the axial velocity perturbations

recorded by 3 hot-wires, closely spaced in the circumferential direction, at 85% (hub), 50% (mid-span), and 15 % (tip) immersion from the tip. The hot wires were located 1/3 of the rotor chord upstream of the rotor at $\theta = 85$ degrees (hub), 90 degrees (mid-span) and 80 degrees (tip). Although there is some span-wise non-uniformity, the stall inception process appears to occur on a full-span basis. The rotating stall dynamics are thus predominately full span events, indicating that a two dimensional model of the fluid dynamics should be adequate.

4.3 Reed Valve Dynamics

The reed valves were modeled as locally reacting, second order, dynamic systems with a critical damping ratio determined by the adjustable pneumatic dashpots. To assess the model and to determine the influence of any unmodeled aeroelastic interaction with the flow field, the reed valve dynamics were identified and the effect of the injection flow on their behavior was assessed.

4.3.1 Initial Condition Response

It was desirable to quantify the reed valve dynamics independent of the flow field through the compressor and the injection flow. The response of the reed valves to an initial condition was thus recorded for various pneumatic dashpot settings in the absence of flow through the compressor and in the absence of injection. The initial condition response was recorded with the reeds in place in the housing, complete with seals, by displacing and impulsively releasing a single reed valve. Data on reed valve dynamic response are displayed in Figure 4.9. The solid lines show the time resolved displacement of a reed valve, as recorded by the root bending strain gauges, for four dashpot settings that span the range of dashpots settings from fully closed to fully opened. In the experiment, the dashpot setting was characterized by the number of turns that the adjusting screw was opened from the fully closed position; ten turns corresponds to the adjusting screw

removed. Figure 4.9 shows that oscillatory frequency of the reed valves changes significantly as a function of the dashpot setting. For the dashpot setting near, or at totally, closed (high damping constants), the reed exhibited a lightly damped oscillation at 125 Hz, whereas, for more opened settings (lower damping constants), the frequency of the oscillations was approximately 55 Hz. The change in frequency with dashpot setting indicates that a second order system with a variable damping ratio is not adequate to capture the essential features of the reed dynamics over the range of dashpot settings tested.

4.3.2 Visco-Elastic Dashpot Model

The transient response of the reed valves can be understood by considering the visco-elastic nature of the pneumatic dashpots. In the low frequency limit, the behavior of a pneumatic dashpot approaches that of a viscous dashpot, but, in the high frequency limit, the behavior approaches that of a spring. This effect can be incorporated into the description of the reed dynamics by modeling the pneumatic dashpot as a visco-elastic dashpot. Details of the model and analysis are given in Appendix H.

Modeling the pneumatic dashpot as a visco elastic dashpot adds an additional degree of freedom to the reed dynamics, compared to the second order model with a viscous dashpot, and an additional parameter is required to characterize the reed valve dynamics. The additional parameter is defined as the ratio between the spring constant of the visco-elastic dashpot and the spring constant of the reed valve.

$$\alpha \equiv \frac{K_{Dashpot}}{K} \tag{4.1}$$

Using this model, the dashed lines in Figure 4.9 show the simulated initial condition response of the reed valves matched to the experimental data as a function of the damping constant in the visco-elastic model. The values for spring stiffness ratio parameter (α =

5.0) and the natural frequency parameter (Q = 1.5) for which the simulation best matched the data over the range of dashpots setting tested were held constant for the simulations shown in Figure 4.8. The initial condition of the additional state variable in the reed valve dynamics introduced by the visco-elastic model was not monitored in the experiments and was estimated for the analytically predicted initial condition responses. Using this procedure, the visco-elastic model was found to well simulate the oscillatory frequency and decay rate of the reed valve response over the full range of dashpot settings, from fully closed to fully open.

The influence of the visco-elastic behavior of the dashpot on the reed valve dynamics is characterized by the following non-dimensional quantity, derived in Appendix H.

$$\chi \equiv \frac{2\zeta}{\alpha Q}$$

For low values of the product of this parameter (χ) and the normalized (by rotor frequency) frequency, (ω), compared to unity, i.e.($\omega\chi << 1$), the behavior of the visco-elastic system approaches that of the original, second order model of the reed valve dynamics. For low damping constants (ζ =0.3), obtained by removing the adjusting screw in the pneumatic dashpots, the natural frequency of the reeds was determined to be 55 Hz. For the compressor operating at 2250 RPM (37.5 Hz.), this corresponds to a frequency parameter of Q=1.5, approximately 67% higher that the design value (Q = 0.9). The higher frequency parameter obtained in the experiment can be attributed to the additional stiffness introduced by the seals, i.e., the seals added more stiffness in the transverse direction than anticipated in the original design.

Figure 4.10 represents the damping constant of the pneumatic dashpots, defined in equation 2.41, versus dashpot setting. This was determined by matching the experimental and simulated initial condition response.

4.3.3 Effect of Injection on Reed Valve Dynamics

The nature of the control strategy requires that the reeds (aeroelastically) interact with the flow field. A model of the interaction was developed in Chapter 2. In this description, the reeds were assumed to respond to static pressure perturbations in the two-dimensional upstream flow field, and not to be directly influenced by the injection process. However, since the reduced frequency (based on the natural frequency of the reed valves, the length of the reed valves, and the nominal injection velocity) was on the order of unity, the reed valves were considered susceptible to unmodeled aeroelastic interaction with the injection. To determine the extent of any such interaction, the effect of the high pressure injection flow over the reeds on the reed valve dynamics was assessed by recording the initial condition response of the reeds for the range of injection pressures used, with the compressor not operating.

4.3.3.1 Dynamic Interaction

The initial condition response for the reeds with the maximum injection rate used, injection pressure = 0.5 psi, is shown in Figure 4.11 for two dashpots settings: fully closed and fully open. Comparing these responses to those for the same dashpots setting without injection, also shown in Figure 4.11, shows that the injection does have a slight effect on the reed dynamics. Injection decreases the frequency slightly and decreases the decay rate (damping), but, the behavior of the reeds as a function of dashpot setting is not significantly affected. The reed dynamics were, therefore, assumed to be independent of injection rate.

4.3.3.2 Static Interaction

Although injection had negligible effect on the dynamic response of the reed valves, it did change the nominal valve opening area. Figure 4.12 shows the static reed valve opening area as a function of injection pressure with the compressor was not operating. The nominal valve opening area increased with increasing injection pressures, and the steady state reed valve opening increased approximately 1.6% of the annulus height over the range of injection pressures tested (0 to 0.5 psi). This static interaction was presumably due to the aerodynamic loading around the seal. Since the effect of steady state injection was removed in the experimental procedure, this steady state interaction was considered acceptable.

4.4 Axial Velocity Profiles

Figure 4.13 shows axial velocity profiles recorded by a hot-wire located 1/3 chord upstream of the rotor (approximately 4.5 inches downstream of the injection region) for the range of injection levels tested in this research. The throttle position was held constant for the various injection rates. The velocity profiles were recorded at a fixed circumferential location (θ = 15 degrees) along the centerline of a reed valve with the compressor operating at Φ=.45 (2250 RPM), near the stalling flow coefficient for the baseline compression system .

The parameters of the injection associated with the velocity profiles shown in Figure 4.12 are given in Table 4.1. The injection parameter $\left(\Phi_i \equiv \frac{C_{x_i}}{U_R}\right)$ was calculated using the static pressure measured in the injection plenum, referenced to the static pressure of the upstream flow field at the entrance to the compressor. Injected mass flow was measured using the Venturi flow meter and the momentum of the injected fluid was calculated using the injection plenum pressure and the injection mass flow. The details are developed in Appendix G.

With the lower injection levels ($\Phi_i < 1$), the injection of fluid fills in the axial casing boundary layer. For higher injection rates, an axial jet persists into the face of the compressor. The fluid mechanic effects of the axially boundary layer and/or jet entering the compressor on compressor performance is not addressed in this thesis. However, for the lower injection rates, the assumption that the jet mixes outs, i.e., there is no high total pressure region associated with the injection entering the compressor, appears to be reasonable, although the details of the interaction between the injected fluid and the free stream are somewhat different than the process modeled in Chapter 2.

The axial momentum deficit of the casing boundary layer for the compressor operating without injection can be quantified by comparing the momentum in the measured axial velocity profile to the momentum of a span-wise uniform flow. Defining the axial velocity of the span-wise uniform flow as $\overline{C}_x$, the normalized difference in axial momentum of the measured velocity profile and a span-wise uniform flow is given by:

$$\text{normalized momentum difference} = \frac{\int_0^H \rho \left[\overline{C}_x^2 - C_x^2 (h) \right] d\, h}{\rho\, H\, \overline{C}_x^2} \qquad (4.2)$$

Using a simple linear approximation to the velocity profile for the baseline compressor, shown as the dashed line in Figure 4.13, the momentum deficit associated with the casing boundary layer is roughly 6% of the axial momentum associated with uniform flow. As shown, a wall jet is apparent in the velocity profiles for the highest injection rate investigated, $\Phi_i \equiv \frac{C_{x_i}}{U_R} = 1.12$, corresponding to $\alpha_i \equiv \frac{\dot{m}_i\, C_{x_i}}{\rho\, A\, \Phi^2\, U_R^2} = 11.6\%$, where Φ_i and α_i where calculated based on annulus averaged quantities. However, the velocity profile for $\Phi_i = 0.96$, corresponding to $\alpha_i = 6.6\%$, is essentially flat. Thus, the effect of the

injection on the local casing boundary layer is consistent with that anticipated from the annulus-averaged injection parameters.

The velocity profiles shown in Figure 4.12 indicated that the extent of the mixed region at 4.5 inches downstream of the injection region is 20% of the span. The jets are shown to spread at an angle of approximately 7 degrees.

4.5 Steady State Performance with Injection

The effects of injection and of aeromechanical feedback on the steady state compression system performance are described in this section. In the experiments, two non-dimensional control parameters were systematically varied: reed dashpot setting (or damping ratio, ζ) and injection pressure, (or injection parameter, Φ_i). The reed mass parameter, W, and frequency parameter, Q, were maintained at fixed values as were compressor geometry and rotational speed.

4.5.1 Procedure

As implemented here, the dynamic mass / momentum injection results in a non-zero temporal and annulus averaged component of mass and momentum into the compressor. The steady state performance, and hence, the stability boundary of the compression system, is a function of this steady state injection. It is emphasized that the scope of the research here is not to analyze quantitatively the effect of steady-state injection on compressor performance, but rather, the impact of aeromechanical feedback on compression system stability. The effect of the injection on the steady state performance was therefore experimentally determined and used as a benchmark in evaluating the stability gain due to aeromechanical feedback.

To isolate the effect of the unsteady aeromechanical feedback from that of steady state injection, the change in stalling flow coefficient was determined as a function of damping ratio (dashpot setting) for fixed levels of steady state injection. This directly assesses the change in stalling flow coefficient due to changes in reed dynamics, in other words, due to aeromechanical feedback.

In all the experiments, the amount of steady state mass flow injected was approximately 4% of the steady state mass flow, $\frac{\Phi_i\, q}{\Phi_c} << 1$. Therefore, based on the linearized analysis, the amount of mass flow injected was predicted to have a negligible effect on the aeromechanical feedback. Only the non-dimensional total pressure of the injection fluid, which determines the injection parameter ,Φ_i, is predicted to influence the aeromechanical feedback.

The relationship between injected mass flow and total (or equivalently, static) pressure in the injection plenum is a function of the nominal reed valve area opening. To minimize steady state injected mass flow for a given injection pressure, the nominal reed valve area was designed to be as small as possible, constrained principally by the mechanical tolerances of the reed valves. However, because the steady state injection pressure affected the nominal reed valve opening area (as shown in Figure 4.11), more mass flow was injected at a given injection pressure than was intended in the design. To compensate, small vents in the back pressure cavity behind the reed valves were opened to ambient pressure. The vents were three 0.25 square inch holes equally spaced around the annular back pressure cavity. These served to slightly increase the mean pressure in the back cavity, with respect to the static pressure in the upstream duct, which reduced the nominal valve area opening.

Because the mean static pressure in the upstream flow field, relative to atmospheric pressure, changed with flow coefficient, opening the vents caused the nominal reed valve area to vary weakly with flow coefficient. Figure 4.14 shows the injection parameter, Φ_i, for constant levels of injected mass flow as a function of flow coefficient for the injection levels investigated. As shown, the injection parameter, Φ_i, decreases with the mass flow coefficient for fixed level of mass flow injected at approximately $\left(\frac{\partial \Phi_i}{\partial \Phi}\right)_{\substack{\text{constant} \\ \text{injected} \\ \text{mass flow}}} = -1$.

To be conservative in accounting for this effect in the experiments, the injection mass flow was held constant for the assessment of the aeromechanical feedback on the stalling flow coefficient. The injection pressure was thus reduced with decreasing mass flow coefficient. Since the stalling flow coefficient was experimentally determined to monotonically increase with decreasing injection pressures (over the range of injection pressures tested), this approach yielded an underestimation of the decrease in stalling flow coefficient due to aeromechanical feedback.

4.5.2 Injection without Feedback

Figure 4.15 shows compressor speedlines for the various levels of constant steady state injection mass flow tested. The scale is expanded to show details. The speedline for the baseline compressor with no injection is also shown for reference. The mass flow coefficient is based on the mass flow through the compressor, which is the sum of the mass flow measured far upstream of the injection region and the injected mass flow. The inlet total to exit static pressure rise coefficient in Figure 4.15 is based on the difference in pressures measured upstream of the injection region and downstream of the compressor. For the data set in Figure 4.15, the reed valve dashpots were closed, so that the reed dynamic behavior approached that of rigid reeds. Although the reed valves are not

completely rigid with the dashpots closed, this configuration was used as a benchmark for assessing the effect of the aeromechanical feedback.

Figure 4.15 shows that increasing levels of steady state injection decreased the stalling mass flow coefficient and increased the overall pressure rise. The only exception was at the lowest injection level, $\Phi_i = 0.80$, where the pressure rise remained essentially the same as the baseline compressor. The stalling flow coefficients for the rigid reed valve configuration with the various injection levels are denoted by large X's in Figure 4.15. The steady state performance is a function of the injection parameter, but the shape of the speedlines are similar to that with no injection.

Figure 4.16 shows the percentage of the mass flow injected, $\frac{\rho \Delta C_{x_i}}{\rho H C_x} = \frac{q \Phi_i}{\Phi_c}$, as a function of the nominal injection parameter (Φ_i) based on total mass flow through the compressor at the stalling flow coefficient for the rigid reed configuration The percentage of the axial momentum injected into the compressor, normalized by the axial momentum of a uniform flow entering the compressor operating at the stalling flow coefficient, $\frac{q \Phi_i^2}{\Phi_c^2}$, is also shown in Figure 4.16. It should be noted that the mass flow and axial momentum injected were measured based on the pressure in the injection plenum and the injection mass flow meter; the steady reed valve opening was not monitored in the experiments.

4.5.3 Injection with Aeromechanical Feedback

Once the stalling flow coefficient of the compression system for the rigid reed valve configuration was determined, the effect of aeromechanical feedback on the stalling flow coefficient was assessed as a function of reed dashpot setting for various injection levels.

The stalling flow coefficients for the various compression system configurations are tabulated in Table 4.3. Figure 4.17 shows the percentage decrease in stalling flow coefficient obtained for various injection levels and dashpot settings. The stalling flow coefficient is defined as the flow coefficient at which the compressor transitioned to large amplitude rotating stall. The decrease in stalling mass flow is given as a percentage of the stalling mass flow coefficient for the rigid reed valve configuration at the same injection level.

$$\Delta\,\Phi\,\% \equiv \left(\frac{\Phi_{\text{rigid}} - \Phi_{\text{w/ feedback}}}{\Phi_{\text{rigid}}} \right)_{\text{const. inj.}} \tag{4.3}$$

Figure 4.17 shows that the amount of stabilization is a function of injection parameter and dashpot setting. At each injection level tested, the rigid reed valve configuration stalled at the highest mass flow coefficient over the range of dashpot settings, i.e. opening the dashpots from the closed position was never destabilizing. A 10% decrease in stalling flow coefficient due to aeromechanical feedback was demonstrated at Φ_i=1.0 with the screw removed from the dashpots (ζ=0.3). At these conditions, the amount of flow injected was 4% of the compressor mass flow and the amount of momentum injected was 6% of the axial momentum entering the compressor.

Figure 4.18 shows compressor characteristics for the compressor operating with optimized aeromechanical feedback, for the compressor with rigid reeds at the same injection level,

and for the baseline compression system are also shown. The stalling flow coefficient for the optimized configuration was $\Phi = 0.369$ and the stalling flow coefficient for the rigid reed valve configuration with the same injection mass flow was $\Phi = 0.409$. In the regions of the compressor characteristic that are stable without feedback, the aeromechanical feedback has no apparent effect on steady state compressor performance. At flow coefficients below the rigid reed valve compression system stalling flow coefficient, the aeromechanical feedback smoothly extends the stable operating region of the compressor.

Comparing the stalling flow coefficient of the optimized aeromechanical feedback configuration to the baseline compressor, the overall effect of the injection reduced the stalling flow coefficient by 15%. Steady state injection, i.e. injection with the rigid reed valves, reduced the stalling flow coefficient by 6%, and aeromechanical feedback reduced the stalling flow coefficient an additional 9% of the stalling flow coefficient of the baseline compression system.

Figure 4.19 shows the effect of aeromechanical feedback on compressor performance for the range of injection levels tested. As with Figure 4.15, the scales are expanded to show the region near the stalling flow coefficient. The data shown represent configurations with dashpot settings which achieved the largest amount of range extension for a given injection level (shown in Figure 4.17). The stalling flow coefficients for the optimized configuration are denoted with large "O's", and the stalling flow coefficients for the rigid reed valve configurations are denoted with large "X's". As shown, the amount of stabilization is dependent on the injection rate, but in all cases, aeromechanical feedback extended the stable flow range.

4.6 Time Resolved Performance with Injection

Data presented in this section show time resolved behavior with various aeromechanical control parameters at different flow coefficients. Stall inception transients and transients showing radial variations of axial velocity perturbations prior to stall are also presented.

4.6.1 Behavior in Stable Flow Range

Time resolved measurements of flow perturbations within the compression system were used to qualitatively assess the effect of aeromechanical feedback. Time resolved traces presented in this section are limited to two configurations: that which demonstrated optimized stabilization and the rigid reed valve configuration at the same injection level.

4.6.1.1 Rigid Reed Configuration

Figure 4.20 shows the time resolved normalized pressure (δp) and axial velocity ($\delta\phi$) perturbations recorded 1/3 chord upstream of the rotor, at θ = 75 and 90 degrees respectively, for the rigid wall configuration with the optimal injection parameter (Φ_i =1.0). Data are shown for two mass flow coefficients. The first flow coefficient , Φ = 0.52, is well away from stall and the second, Φ =0.41, is near stall. The operating points corresponding to the two time resolved data sets are shown on Figure 4.18 as points D and E. Pressure and velocity perturbations exist well away from stall, but the magnitude of the perturbations increases as the flow coefficient is reduced.

Figure 4.21 shows the time resolved reed valve deflections (δq) corresponding to the data shown in Figure 4.20. Comparing the time resolved static pressure signal with the reed deflection indicates that the reeds are not completely rigid and respond to the static pressure perturbations in the flow field. From the data, it is evident that even though the pneumatic dashpots are closed, the reed valves are introducing some degree of aeromechanical feedback.

The spatial Fourier decomposition of the axial velocity perturbations, measured 1/3 chord upstream of the rotor at mid-span, for the two operating points, Points D and E, for which the time resolved data were shown in Figure 4.20, is given in Figures 4.22 and 4.23, respectively. In Figure 4.22, the magnitude of the first three spatial harmonics, for the compression system operating well away from stall ($\Phi = 0.52$), appear to grow and decay in time in a random manner. No coherent traveling waves are seen in the plot of the unwrapped phase versus time.

For the compression system operating at $\Phi = 0.41$, near the stalling flow coefficient, the disturbance flow field is much different. Spatial Fourier decomposition of the velocity perturbations shown in Figure 4.23 indicate that the magnitude of the first and second spatial harmonics have increased an order of magnitude from those at $\Phi = 0.52$. The unwrapped phase indicates that the first and second spatial harmonics exhibit substantial periods (10's of rotor revolutions) of coherent traveling wave structure. Although the third harmonic also exhibits periods of coherent traveling wave structure, these are more intermittent than the first two spatial harmonics. The phase speeds of the first, second and

third traveling spatial harmonics are 26%, 30%, and 37% of the rotor frequency, respectively. In summary, the spatial Fourier decomposition of the disturbance flow field for the rigid reed configuration, both away from and near stall, shows features very similar to those of the baseline compression system.

The PSD's of pressure and velocity perturbations recorded for the operating conditions of Figure 4.20 are shown in Figure 4.24. Away from stall, the temporal frequency content of the disturbances exhibits no peaks larger than those associated with the once and twice per rotor revolution disturbances, similar to the behavior of the baseline compression system operating away from stall shown in Figure 4.5. Near stall, the PSD's indicate that disturbances with temporal frequency of 25% and 60% of the rotor frequency, associated with the traveling first and second spatial harmonics, have the largest power spectra densities. Thus, the temporal frequency content of the disturbances behave similarly to the baseline compression system, but, disturbances with a temporal frequency associated with a traveling second spatial harmonic appear to play a larger role in the rigid reed valve configuration disturbance flow field with injection than in the baseline compression system.

4.6.1.2 Optimized Aeromechanical Feedback

Figure 4.25 shows time resolved, normalized, pressure (δp) and axial velocity ($\delta \phi$) perturbations recorded for the compression system with the experimentally optimized control parameters at three mass flow coefficients, ($\Phi = 0.52$, 0.41, and 0.37). The steady state operating points corresponding to the time resolved data are indicated by points F, G, and H, respectively, on the compressor characteristic in Figure 4.18. The data were

recorded at the same axial and circumferential locations as those of Figure 4.20 for the rigid reed valve configuration.

Comparing Figure 4.25 with Figure 4.20 shows that the pressure and axial velocity perturbations for the two systems away from stall (Point F and Point D) are similar. Comparing data from Point G to that from Point E shows that the amplitude of the oscillations are reduced in the optimized configuration compared to the rigid valve configuration at a given mass flow coefficient near stall. Comparing data from Points G and H indicates that the time resolved behavior of the aeromechanically stabilized configuration exhibits no distinct change in behavior in the stabilized region below the rigid wall stalling flow coefficient.

Figure 4.26 shows the time resolved reed valve deflections corresponding to the data presented in Figure 4.25. In the stabilized region, Point H, the reed valves are modulating +/- 1% of the height of the annulus.

The spatial Fourier decomposition of the axial velocity perturbations at the face of the compressor for the optimized configuration operating at conditions away from and close to stall are shown in Figures 4.27 and 4.28, respectively. In Figure 4.27, at $\Phi = 0.52$ (away from stall), the magnitude of the spatial harmonics appear to grow and decay randomly with time. The plot of the unwrapped phase indicates that no coherent traveling waves are present. In Figure 4.28, close to stall, the magnitude of the spatial harmonics are significantly larger, similar to the behavior with rigid reeds. The plot of the unwrapped

phase indicates that the first, second and third spatial harmonics all exhibit periods of coherent traveling waves. The rotation rate of the traveling waves associated with the three lowest spatial harmonics is 25%, 29%, and 33% of the rotor frequency, respectively.

The PSD's of the axial velocity and pressure perturbations for the optimized configuration at operating points corresponding to the time traces shown in Figure 4.25 are shown in Figure 4.29. Away from stall, the disturbance flow field is characterized by perturbations with magnitudes similar to the once and twice per rotor revolution disturbances seen in Figure 4.24. As the flow coefficient is reduced, peaks in the PSD's corresponding to the first and second harmonic traveling waves associated with rotating stall develop and dominate the disturbance flow field. This trend is similar to that observed for the rigid reed configuration with the same steady state injection, as well as that for the baseline compression system.

For comparison, the rms amplitude of the normalized axial velocity perturbations recorded at a station 1/3 chord upstream of the rotor is shown in Figure 4.30 as a function of flow coefficient for three configurations: (1) baseline compressor, (2) rigid reed valve configuration and, (3) optimized configuration. The level of unsteadiness is seen to increase as the configurations approach their respective stalling flow coefficients. The functional dependence of the level of unsteadiness on flow coefficient in the three systems roughly scales with the difference between the flow coefficient and the stalling flow coefficient. Away from stall (at, say, $\Phi > 0.50$), the level of unsteadiness in the three

configurations is similar (rms of the normalized axial velocity perturbations is roughly 0.01), indicating that the level of unsteadiness in the compression system operating away from stall is not significantly influenced by aeromechanical feedback or steady state injection.

4.6.2 Stall Inception

Figures 4.31 shows axial velocity perturbations recorded during stall inception for the rigid wall. An array of eight equally spaced hot-wires, placed 1/3 chord upstream of the rotor at mid-span, was used. The spatial Fourier decomposition of the velocity perturbations during the stall inception event is shown in Figure 4.32. Similar data are presented in Figures 4.33 and 4.34, respectively, for the configuration with optimized aeromechanical feedback With both configurations, a smooth transition from axisymmetric flow into fully developed rotating stall is exhibited, indicating long wave length stall inception consistent with the two-dimensional model. The spatial Fourier decomposition of the axial velocity shows that the second spatial harmonic dominates the rigid reed valve stall inception, similar to the baseline stall inception process shown in Figures 4.6 and 4.7. For the optimized configuration, however, the first spatial harmonic appears to play a larger role in the stall inception process.

The reed valve deflections at four locations, equally spaced around the annulus, are shown in Figures 4.35 and 4.36 for the rigid reed and for the optimized configuration. The data corresponds to the same stall inception events shown in Figures 4.31 and 4.33, respectively. The reeds can be seen to participate in the stall inception event for both configurations.

4.6.3 Radial Variations

Figure 4.37 shows span-wise variations of the velocity perturbations at the face of the rotor during the stall inception transients for the rigid reed valve configuration as recorded by 3 closely circumferentially spaced hot-wires at 15%, 50% and 85% immersion. Similar data are presented for the optimized configuration in Figure 4.38. Both configurations demonstrated essentially full-span stall inception, similar to the basic compression system and consistent with the two-dimensional model.

4.6.4 Effect of Feedback on Dynamics

Steady state data showed that the stalling flow coefficient was a function of dashpot setting for a given injection pressure. In this section we address the effect of dashpot setting (damping ratio) on system oscillations at operating points slightly above stall for configurations with the optimized injection level (Φ_i=1.0).

Figures 4.39a and 4.39b show the PSD of a single normalized axial velocity measurement ($\delta\phi$) and that of a single normalized pressure measurement (δp) for the compression system operating at a fixed injection level near stall for six dashpot settings which span the range of dashpot settings investigated. For each data set, the compressor was operating within 1% of the stalling mass flow coefficient. The PSD's were averaged over 5 seconds (approximately 200 rotor revolutions) of time resolved data, sampled at 1000 Hz. If we assume that the temporal frequencies correspond to traveling spatial harmonics, we can infer that the relative amplitude of the spatial harmonics is affected by the dynamic behavior of the reed valves.

Although the time traces are not completely stationary signals over the sampling interval, a trend in the frequency content of the disturbance flow field is evident. With the dashpot setting at 1.5 turns (high damping), the magnitude of the PSD's at the temporal frequency

corresponding to a traveling second spatial harmonic (60% of rotor frequency) is larger than that associated with the first spatial harmonic (25% of rotor frequency). However, as the damping constant is reduced, the magnitude of the PSD at the frequency associated with the first harmonic becomes larger relative to that associated with the second. The aeromechanical feedback thus modifies the pre-stall system dynamics in addition to the stalling flow coefficient.

4.7 Component Performance

Time resolved data recorded from the compression system can be used to estimate the frequency domain transfer functions between two flow variables. These transfer functions not only give information on system dynamic properties, but they also can be compared to transfer functions predicted by the analytical model. The following relationships were examined:

1) reed displacement and pressure perturbations in the upstream flow field, $(\delta q / \delta p)$

2) static pressure and axial velocity perturbations in the upstream flow field, $(\delta p / \delta \phi)$

3) reed displacement and axial velocity perturbations in the upstream flow field, $(\delta q / \delta \phi)$

The transfer functions were estimated based on time resolved measurements at two, closely spaced circumferential positions. Input was generated by the naturally occurring unsteadiness within the compression system; no external excitation was used. The transfer function between two time resolved signals (an input and output signal) can be estimated using the ratio of the cross power spectrum between the input and output signals and the power spectrum of the input signal [28]. For high coherence levels (close to unity), this ratio represents a transfer function between the two signals. The transfer function estimates were calculated by averaging the power spectra over approximately five 1024 point (approximately 1 second or 37.5 rotor revolutions) segments of data. The method used to

estimate the transfer functions is developed in Appendix F. The cutoff frequency of the time resolved measurements was set at 100 Hz, or 2.67 times the rotor frequency.

4.7.1 Reed Deflection / Pressure Transfer Functions

Figure 4.40 shows the magnitude and phase of the measure transfer function between time resolved reed deflections and static pressure perturbations for the optimized configuration operating near stall. The transfer function is presented as a function of frequency, normalized by the rotor frequency, in non-dimensional form, with the reed deflection normalized by annulus height and the static pressure perturbations normalized by the dynamic head based on compressor wheel speed. The pressure was recorded 1/3 chord upstream of the rotor and both the pressure and reed deflection signals were recorded at the same circumferential position, $\theta = 75$ degrees. The coherence function is also shown in Figure 4.40. The coherence between the two signals approaches unity at the frequencies associated with the first (25%), second (60%) and third harmonics (105%), indicating a good estimate of the transfer function at these frequencies.

The transfer function between the reed deflection and the static pressure predicted using the model developed in Chapter 2 is given by:

$$\frac{\delta q(\omega)}{\delta p(\omega)} = \frac{\frac{1}{6}W}{(Q^2 - \omega^2) + 2Q\zeta(i\omega)} \qquad (4.4)$$

where ω is the temporal frequency normalized by rotor frequency.

In section 4.3.1, the natural frequency and damping ratio of the reeds for the optimized dashpot setting (in the absence of mean flow) were determined to be (Q=1.5 and ζ =0.3). Using these values, a transfer function can be computed for an arbitrary mass parameter (W).

There is one addition to the prediction that should be made; Equation 4.4 predicts the transfer function between reed deflection and static pressure perturbations that occur at the same spatial position. However, the center of pressure of the reed valves is approximately 0.35 compressor radii upstream of the axial location of the static pressure measurement. Since the static pressure field is predicted to decay exponentially (as e^{-nx}, where: n is the spatial harmonic number and x is the axial distance upstream of the compressor), the axial spacing between the measurements will effect the magnitude of the measured transfer function. From spatial Fourier decomposition of the disturbance flow field, the first, second, and third harmonics are associated with temporal frequencies, as recorded by a single transducer, of approximately 25%, 60%, and 105% of rotor frequency. If one assumes that disturbances at these frequencies are primarily traveling waves, the analytically predicted transfer function (eq. 4.4) can be "corrected" for the effect of axial spacing by multiplying the magnitude of the predicted transfer function by: $e^{-(n*.35)}$ for n = 1, 2, 3 at the temporal frequencies associated with the spatial harmonics. The temporal phase between the two signals should not be affected by the axial spacing.

Matching the amplitude of the transfer function for the frequencies with high coherence and accounting for the exponential decay of the pressure field, the mass parameter (W) can be estimated. The dashed lines shown in Figure 4.40 shows the analytically predicted transfer function using Equation 4.4 corresponding to a value of W= 3.5. The symbols (⊗) on the plot of the magnitude of the transfer function indicate the calculated transfer function, corrected for the exponential decay, for the first three harmonics. The good agreement between the calculated and the experimentally determined phase of the transfer functions indicates that natural frequency and damping ratio determined from the initial condition response are consistent with the dynamic performance of the reed valves. Thus, modeling

the reeds valves as a second order systems which respond to pressure perturbations in the upstream flow field appears to be reasonable for the optimized configuration.

Figure 4.41 shows the reed / pressure transfer function for the rigid reed configuration with the optimized injection level operating near stall. As with Figure 4.40, the transfer function is presented in non-dimensional form. The model for the visco-elastic reed valve dynamics, developed in Appendix H, predicts that the reed valve / pressure transfer function is given by:

$$\frac{\delta q(\omega)}{\delta p_u(\omega)} = \frac{\frac{1}{6}W}{(Q^2 - \omega^2) + \frac{2Q\zeta\omega(i + \chi\omega)}{1 + (\chi\omega)^2}} \qquad (4.5)$$

where: $\chi \equiv \frac{2\zeta}{\alpha Q}$

The transfer function predicted for the rigid reed configuration using the visco-elastic model for the reed dynamics using the control parameters determined from the initial condition response, ($Q = 1.5$, $\zeta = 3.0$ and $\alpha = 5.0$) and the mass parameter determined above ($W = 3.5$), is shown on Figure 4.41 as a dashed line. The symbols (⊗) on the plot of the magnitude of the transfer function represent the analytical model corrected for the axial decay, as developed above. The model yields a reasonable representation of the reed dynamics with the pneumatic dashpots closed.

As indicated by Figure 4.41, and by time resolved data in Figures 4.21 and 4.35, the reeds are not completely rigid with the pneumatic dashpots closed, and the reeds respond to the pressure fluctuations. Comparing Figures 4.40 and 4.41 shows that the magnitude of the reed deflection / pressure transfer function for the "rigid" reeds is roughly half that of the optimized configuration at the frequencies associated with the first three harmonics.

4.7.2 Pressure / Velocity Transfer Function

The flow field upstream of the compressor was assumed to be two-dimensional incompressible and irrotational. Based on this idea, in the region downstream of the reeds, but before the injected flow mixes out, the static pressure acting on the reeds is that corresponding to the incompressible and irrotational upstream flow. The transfer function between static pressure and axial velocity perturbations is given by:

$$\frac{\delta p(\omega)}{\delta \phi(\omega)} = -2\Phi - \frac{1}{n}(i\omega) \qquad (4.6)$$

where: n is the spatial harmonic number

Figure 4.42 shows the experimentally determined, non-dimensional pressure / velocity transfer function in the stabilized flow regime for the compression system with optimized aeromechanical feedback. Both pressure and velocity were recorded at 1/3 chord upstream of the rotor. The velocity signal was recorded at mid span at (θ = 90 degrees) and the pressure was recorded at (θ = 75 degrees). The coherence between the two signals is also shown.

The transfer function predicted by the linearized unsteady Bernoulli's equation is a function of the disturbance harmonic number (n). Using Φ = 0.39, the predicted transfer function for the first three spatial harmonics (n = 1, 2 and 3) is shown on Figure 4.43.

Equation 4.6 assumes colocated measurements, however, the measurements were recorded with a finite circumferential spacing ($\Delta\theta$ = 15 degrees). For constant amplitude, traveling wave disturbances, the circumferential spacing introduces a temporal phase shift between the measurements that depends on the length scale of the disturbances which is given by

(n $\Delta\theta$ where: n is the spatial harmonic number). Using information derived from the array of eight equally spaced hot wires, the symbols (⊗) on the phase versus frequency plot in Figure 4.43 represent the phase of the predicted transfer function for the nth harmonic corrected (at the temporal frequency associated with that harmonic) for the temporal phase shift introduced by the circumferential spacing between the measurements. Since the measurement were recorded at the same axial station, the magnitude of the transfer function is not affected. The relationship between static pressure and axial velocity perturbations in the upstream flow field appears to be modeled reasonably well by a two-dimensional potential flow field description.

4.7.3 Reed Deflection / Velocity Transfer Functions

Figure 4.43 shows the magnitude and phase of the reed deflection / axial velocity transfer function for the optimized configuration near stall. The transfer function is presented in non-dimensional form. The coherence between the two signals is also shown. The axial velocity measurements were recorded 1/3 chord upstream of the rotor at $\theta = 90$ degrees. The centerline of the reed valve was located at $\theta = 75$ degrees.

The predicted reed deflection / axial velocity transfer function, for colocated measurements, is given by:

$$\frac{\delta q(\omega)}{\delta \phi(\omega)} = \frac{-\frac{1}{6} W (2\Phi + \frac{1}{n}(i\omega))}{(Q^2 - \omega^2) + 2Q\zeta(i\omega)} \qquad (4.7)$$

The analytical transfer functions for the first three spatial harmonics, using the experimentally determined reed parameters in the viscous, second order, dashpot model for the reed dynamics, are also shown in Figure 4.43. The input parameters were: W=3.5, Q=1.5, $\zeta = 0.3$ and $\Phi = 0.39$ for n = 1, 2 and 3. The symbols (⊗) on the plot of the magnitude of the transfer function represent the analytical model corrected for the

exponential decay of the axial velocity perturbations due to the axial spacing between the measurements (0.35 compressor radii) and the symbols (⊗) on the phase plot represent the analytical model corrected for the temporal phase shift introduced by the circumferential spacing ($\Delta\theta$ = 15 degrees) between the two measurements, as developed above. The model agrees well with the experimental estimate of the transfer function.

Figure 4.44 shows the non-dimensional reed deflection / axial velocity transfer function recorded for the rigid reed configuration operating near the stalling flow coefficient. The coherence between the two signals is also shown.

Using the visco-elastic model of the reed valve dynamics, the predicted transfer function is given by:

$$\frac{\delta q(\omega)}{\delta \phi_u(\omega)} = \frac{-\frac{1}{6} W \left(2\Phi + \frac{1}{n}(i\omega) \right)}{\left(Q^2 - \omega^2\right) + \frac{2 Q \zeta \omega (i + \chi \omega)}{1 + (\chi \omega)^2}} \qquad (4.8)$$

where: $\chi \equiv \frac{2\zeta}{\alpha Q}$

The transfer function predicted by equation 4.8 is shown in Figure 4.44 using W=3.5, Q=1.5, ζ =3.0, α = 5.0, Φ = 0.41 for n = 1, 2 ,and 3. The symbols (⊗) on Figure 4.44 indicate the analytical model corrected for the axial and circumferential spacing as described above. As shown the combination of the two-dimensional model of the upstream flow field and the visco-elastic model of the reed valve dynamics yields a fairly good representation for the reed deflection / axial velocity transfer function measured for the rigid reed configuration.

4.8 Comparison to Theory

We have examined so far the components that make up the overall model description of the dynamic system. In this section the general predictions of the compression system behavior are compared to the experimental results. The primary object of the comparison is to determine if the simple model yields a useful description of the compression system dynamics. Specifically, this section assesses calculated versus experimentally determined:

1) phase speed of the spatial harmonics

2) stalling flow coefficient as a function of control parameters

3) relative stability of the spatial harmonics as a function of control parameters

4.8.1 Phase Speed of the Spatial Harmonics

The linearized stability analysis developed in Chapter 2 for the basic compression system predicts that the spatial harmonics travel around the annulus at a phase speed dependent on the spatial harmonic number. For the simple model of compressor performance used, the inertial parameters determine the rotational frequency of the disturbances, given by:

$$\text{real}(\sigma) = \frac{n\lambda}{4 + n\mu} \tag{2.17}$$

The inertial parameters, defined in equations (2.1) and (2.2), for the compressor based on geometry are ($\lambda = 0.4$ and $\mu = 0.7$). Using these values in the model predicts rotation rates of 9%, 15%, and 20% of the rotor frequency for the first three harmonics respectively. For the basic compression system the first three harmonics were measured to travel at 25%, 32%, and 35% of the rotor frequency, respectively. Thus, the predictions of the rotation rates of the disturbances using this simple model are poor. The poor prediction of the rotation speeds can primarily be attributed to the simplicity of the model, which does not account unsteady aerodynamics, inter blade row gaps, and sensitivity of the rotor to swirl in the upstream flow field. As developed by other authors, and presented in

Appendix A, accounting for swirl sensitivity of the rotor would serve to increase the rotation rate of the disturbances.

Although the model does not accurately predict the rotation rate of the disturbances, it does predict the qualitative features of the flow field. The model can be modified to yield a more accurate description of the flow field, while maintaining the same structure, by modifying the inertial parameters of the fluid within the compressor. It is emphasized that using a more accurate model, specifically, modeling the swirl sensitivity of the rotor, could be expected to yield more accurate predictions of the rotation frequencies of the disturbances. The inertial parameters of ($\lambda = 1.0$ and $\mu = 2.0$) were selected to yield a qualitative representation of the rotating stall dynamics and were not based on the geometry of the compressor. Moore [19] found that using inertial parameters that are roughly twice the values corresponding to those based on geometry resulted in good agreement between the rotation rates calculated using the theory and those observed experimentally. Using these values for the inertial parameters results in predictions of 17%, 25%, and 30% of the rotor frequency for the first three spatial harmonics, respectively. Thus, the quantitative rotational frequencies were reasonably represented.

To compare the rotation rates of the disturbances for the compression system with aeromechanical feedback, the linear analysis was modified to include a visco-elastic model of the pneumatic dashpot, which the initial condition response indicated was required to adequately characterize the reed dynamics over the range of dashpot setting investigated. Details of the analysis are given in Appendix H.

A fourth order fit of the performance data recorded for the baseline compressor (pressure rise coefficient versus mass flow coefficient)was used in the analysis. The experimental data and the fourth order curve fit are shown in Figure 4.45, as is the slope (of the curve

fit representing the speedline),as a function of flow coefficient. The inertial parameters of $\lambda = 1.0$ and $\mu=2.0$ were used in the analysis.

Figure 4.46 shows the behavior of the eigenvalues of the model of the compression system as the flow coefficient is reduced for the optimized configuration, W =3.5, Q = 1.5, ζ = 0.3, $\alpha = 5.0$, and $\Phi_i = 1.0$. The rotation rate of least stable modes associated with the first and second spatial harmonics for the compression system with optimized aeromechanical feedback are seen to be 13% and 20% of the rotor frequency. The time resolved data indicated that the first and second spatial harmonics rotate at 25% and 29% of the rotor frequency. Again, only the qualitative trend is consistent.

4.8.2 Prediction of Change in Stalling Flow Coefficient

Two control parameters, the injection parameter (Φ_i) and the damping parameter (ζ), were varied systematically in the experimental phase of this research. The experimentally determined effect of each control parameter on the stalling flow coefficient can be compared to the effect predicted by the analysis.

Figure 4.47a shows the predicted stability boundary for the first two harmonics as a function of the damping in the visco-elastic dashpot. The other control parameters were held constant at W = 3.5, Q = 1.5, $\alpha = 5.0$ and $\Phi_i = 1.0$. Figure 4.47b shows the stability boundary for the first two harmonics as a function of the injection parameter,Φ_i, with the other control parameters held constant at W = 3.5, Q = 1.5, α =5.0, and $\zeta = 0.3$. Figures 4.48a and 4.48b show similar predictions using a viscous dashpot model. There is little difference in the stability boundaries predicted by the two models, and one can infer that the visco-elastic behavior of the dashpot has little effect on predicted system stability over the range of parameters tested.

It can be remarked that this result is not at all obvious from the initial condition response, where the visco-elastic dashpot added features to the reed dynamics not predicted by the viscous dashpot model. The lack of influence of the visco-elastic dashpot behavior on the system stability can be interpreted by considering that, for damping ratios in which the visco-elastic behavior becomes important, the reeds are de-tuned from the system dynamics, and thus, have little effect on system stability. However, it is emphasized that this conclusion is specific to the experimentally determined control parameters and is not universal.

Data, such as that shown in Figure 4.41, demonstrated that reed dynamics with the pneumatic dashpots closed were not completely rigid, and that the reeds were responding to static pressure perturbations in the upstream flow field. To estimate the effect of the feedback introduced by the "rigid reed " configuration (dashpots closed), stability was assessed as a function of injection parameter for the "rigid reed" configuration, i.e. W=3.5, Q=1.5, α=5.0, and ζ = 3.0. Figure 4.49 shows the flow coefficient at which the linear model with the visco-elastic dashpot predicts the first and second harmonic to become unstable is plotted as a function of the injection parameter for the "rigid reed" parameters. For the injection parameters tested, the stalling flow coefficient predicted for the configuration with the dashpots closed occurs at a lower flow coefficient than the stalling flow coefficient predicted for the configuration with infinitely rigid reed valves. Thus, using the experimentally determined stalling flow coefficient for the rigid reed valve configuration, i.e. the closed dashpots, as a benchmark to assess the aeromechanical feedback, is predicted to underestimate of the amount of stabilization due to the aeromechanical feedback.

4.8.2.1 Damping Ratio

In Figure 4.17, the decrease in stalling flow coefficient for the experimentally optimized injection rate (Φ_i =1.0) was shown to increase with decreasing damping ratio. Figure 4.50 shows the measured change in stalling flow coefficient and the analytically predicted change in flow coefficient at instability for the first two harmonics as a function of damping constant in the visco-elastic reed valve model. The changes in stalling flow coefficient were referenced to the corresponding values (experimentally determined and analytically predicted) for the rigid reed configuration. According to the linear model, the behavior of the first harmonic should limit the increase in stable flow range, but, the data is more consistent with the change in stalling flow coefficient predicted for the second harmonic.

4.8.2.2 Injection Parameter

The injection pressure was also varied parametrically to determine its influence on compression system dynamics. Figure 4.51 shows the predicted change in flow coefficient at instability between the closed dashpot configuration (ζ =3.0) and the optimized dashpot setting configuration (ζ =0.3) as a function of injection parameter. This is shown for the first and second spatial harmonics. The visco-elastic dashpot model was included in the analysis. The experimentally determined reduction in stalling mass flow coefficient is also given in Figure 4.51. The results are similar to the results shown in Figure 4.50 for the effect of damping parameter; the prediction is that the change in stability associated with the first harmonic should determine the measured change in stalling mass flow coefficient, but, the data appears to be somewhat more consistent with the change in stability of the second harmonic.

4.8.3 Relative Stability of the First and Second Spatial Harmonics

The linear analysis predicts that the effect of aeromechanical feedback depends on the spatial harmonic number of the disturbances, and that relative stability of the spatial

harmonic is a function of damping ratio. Figure 4.47a showed the mass flow coefficient at instability for the first two harmonics predicted by the visco-elastic stability analysis as a function of the damping ratio for the optimized injection level. At high damping ratios (above $\zeta = 1.25$), the second harmonic is predicted to be less damped than the first at a given stable operating point, but at low damping ratios (below $\zeta = 1.25$), the converse is true.

For under-damped, linear systems operating with white noise, random excitation, the shape of the peak of the PSD is indicative of the damping, and hence the stability, of a given mode of oscillation. Using this idea, we can compare the relative stability of the spatial harmonics. PSD's of a single pressure and axial velocity measurement recorded for configurations operating near stall with the optimized injection level and several dashpot settings were presented in Figures 4.39a and 4.39b. The relative magnitude of the PSD's of the oscillations for frequencies associated with the first and second harmonics are found to be influenced by the damping ratio. As shown in Figures 4.39a and 4.39b, the magnitude of the PSD at the frequency associated with the first harmonic increases relative to that of the second harmonic as the damping ratio is decreased. This trend agrees with that predicted by the model, as described above.

4.9 Non-Linear Numerical Simulations

The linear model assumes that the slope of the compressor characteristic is set by conditions at the mean mass flow coefficient. For finite amplitude oscillations, however, the compressor performance at any given point around the annulus may differ significantly from compressor performance at the mean flow. The amplitude of the coherent oscillations found prior to large amplitude rotating stall were on the order of 10-20% of the mean flow coefficient. Although these oscillations are small enough that many features can be represented with a linearized description of the upstream and downstream flow fields, the

influence of the non-linearity in the compressor characteristic could be significant for disturbances of this magnitude.

To assess the predictions of the model with finite amplitude disturbances, the two spatial harmonic Galerkin, non-linear simulation with the random noise modeled, described in Chapter 2 was used to numerically simulate the compression system dynamics with aeromechanical feedback. The annulus averaged mass flow coefficient was held constant. The fourth order curve fit of the experimentally determined annulus average compressor characteristic shown in Figure 4.45 was used to represent the compressor behavior. Since finite amplitude oscillations existed and the flow through the compressor was transiently accessing the nominally unstable region of the compressor characteristic, the axisymmetric characteristic was smoothly extended into the nominally unstable region, as shown. The shape of the characteristic in the nominally unstable region has a large effect on the predicted compression system dynamics for compression systems operating near the linear stability limit, and time resolved data can be used to estimate the shape of the compressor characteristic in this region [26] In this thesis, however, no attempt was made to fit the detailed shape of the characteristic in the unstable region to match the experimental data, and the characteristic was extended such that the characteristic was approximately symmetric about the peak of the characteristic.

Noise was introduced in the simulation as a random static pressure disturbance at the face of the compressor. The details of the noise model are developed in Appendix E.

Figure 4.52 shows the predicted rms of the compressor inlet axial velocity perturbations (normalized by mid-span compressor wheel speed) as a function of mass flow coefficient for the baseline compression system and the optimized compression system. The rms of noise level is 2.5% of the dynamic head based on the mid-span compressor wheel speed

and the input parameters to the calculation are listed in Table 4.4. The amplitude of the velocity perturbations increase for the fixed noise level as the compression systems approach their respective stalling flow coefficients. The simulated behavior of the compression systems is similar to the experimental data shown in Figure 4.30.

It should be emphasized that the behavior of the compression system operating in regions where the non-linearity of the compressor characteristic becomes important is strongly dependent on the shape of the characteristic assumed in the nominally unstable region. Thus, the level of unsteadiness occurring in the compression system is not directly related to noise levels in regions where the non-linearity of the compressor characteristic is important. Comparing the numerical results shown in Figure 4.51 with experimental data shown in Figure 4.30 for flow coefficients well away from stall indicates that the simulation with a noise level on the order of 2.5% of the mean dynamic head based on wheel speed yields a useful description of the effect of noise on the compression system.

Figure 4.53 shows the simulated normalized axial velocity perturbations ($\delta\phi$) at eight equally spaced locations around the annulus. The spatial Fourier decomposition of the axial velocity perturbations are shown in Figure 4.54. The reed valve deflections at four equally spaced positions around the annulus corresponding to the velocity perturbations shown in Figure 4.53 are shown in Figure 4.55. The axial velocity perturbations were calculated assuming that the injection mixes out in the span-wise direction before entering the compressor. Spatial Fourier decomposition of the numerical results predict that the oscillations associated with the first and second spatial harmonics grow and decay in a random manner for the compression system operating near the linear stability boundary. In the periods in which there is significant harmonic content, the simulation predicts that the harmonics form coherent waves traveling around the compressor. The phase speed of the coherent traveling waves predicted by the simulation is 13% and 20% of the rotor

frequency for the first two spatial harmonics. This is consistent with the results of the linear stability analysis for the least stable modes associated with the first and second spatial harmonics.

The spatial Fourier decomposition of the simulated velocity perturbations can be compared to the experimental data presented in Figure 4.28. Although the third spatial harmonic is not modeled in the simulation, the qualitative behavior of the first and second spatial harmonics is captured. Based on these comparisons, the two spatial mode Galerkin procedure appears to offer a description of the flow field with aeromechanical feedback which captures the basic structure of the system dynamics.

4.10 Summary of Experimental Results

The results of the experimental phase of the research and the evaluation of the analytical model are summarized below:

1) 10% decrease in stable flow coefficient was achieved due to aeromechanical feedback.

2) Control effectiveness was shown to be a function of control parameters tested.

3) Control smoothly extended the compressor speedline into previously unstable region.

4) The rotating stall dynamics remained essentially full-span.

5) The reed valves responded to the static pressure perturbations in the upstream flow field essentially as modeled

6) The experiment did not achieve the design control parameters.

7) The model predicted trends stalling flow coefficient versus control parameters and the relative stability of spatial harmonics. The model did not, however, accurately predict the rotation rate of the disturbances. This was attributed to the simplicity of the model.

8) The noise level in the compression system was estimated.

9) The non-linear, two spatial harmonic Galerkin simulation captured the qualitative behavior of the compression system both with and without aeromechanical feedback.

Table 4.1: Injection Quantities for Velocity Profiles shown in Figure 4.13

Injection Pressure (psi)	Injection Paramter (Φ_i)	Change in Flow Coefficient due to Injection	% of Flow Injected ($\Phi_c = 0.45$)	% of Axial Momentum Injected ($\Phi_c = 0.45$)
0	0	0	0	0
0.2	0.79	0.008	1.8%	3.1%
0.3	0.96	0.014	3.1%	6.6%
0.4	1.12	0.021	4.7%	11.6%

Table 4.2: Injection Quantities Tested

Injection Pressure (psi)	Injection Paramter (Φ_i)	Mass Flow Injected (kg/s)	% of Flow Injected ($\Phi_c = 0.40$)	% of Axial Momentum Injected ($\Phi_c = 0.40$)
0	0	0	0	0
0.21	0.81	0.07	2.0%	4.1%
0.28	0.93	0.11	3.0%	7.0%
0.34	1.03	0.14	4.0%	10.3%
0.38	1.08	0.18	5.0%	13.5%
0.42	1.14	0.21	6.0%	17.1%
0.48	1.22	0.24	7.0%	21.4%

Table 4.3: Stalling Flow Coefficients For Various Control Parameters[1]

Nominal Injection Parameter (Φ_i)	Mass Flow Coefficient Injected ($\dot{m}_i / \rho A_c U_R$)	Dashpot Setting (# of Turns From Closed[2])	Stalling Flow Coefficient	% Change in Stalling Flow Coefficient
0.81	0.008	0	0.426	---
0.81	0.008	1.5	0.421	1.2
0.81	0.008	3.0	0.418	1.9
0.81	0.008	4.5	0.417	2.1
0.81	0.008	6.0	0.417	2.1
0.81	0.008	10.0	0.419	1.6
0.93	0.012	0	0.420	---
0.93	0.012	1.5	0.410	2.4
0.93	0.012	3.0	0.402	4.3
0.93	0.012	4.5	0.397	5.5
0.93	0.012	6.0	0.400	4.8
0.93	0.012	10.0	0.394	6.2
1.03	0.016	0	0.409	---
1.03	0.016	1.5	0.394	3.7
1.03	0.016	3.0	0.378	7.6
1.03	0.016	4.5	0.378	7.6
1.03	0.016	6.0	0.376	8.1
1.03	0.016	7.5	0.374	8.6
1.03	0.016	10.0	0.369	9.8
1.08	0.020	0	0.395	---
1.08	0.020	1.5	0.378	4.3
1.08	0.020	3.0	0.375	5.1
1.08	0.020	4.5	0.368	6.8
1.08	0.020	6.0	0.365	7.6
1.08	0.020	7.5	0.366	7.3
1.08	0.020	10.0	0.366	7.3
1.22	0.028	0	0.373	---
1.22	0.028	3.0	0.349	6.4
1.22	0.028	6.0	0.357	4.3
1.22	0.028	10.0	0.355	4.8

1) All data recorded at 2250 RPM and Q =1.5, W =3.5
2) 0 turns = adjusting screw closed
10 turns = adjusting screw removed

Table 4.4: Input Parameters for Non-Linear Simulation Presented in Chapter 4

Parameter	Simulation of Basic Compression System	Simulation of Optimized Configuration
λ	1.0	1.0
μ	2.0	2.0
Φ_i	0.00	1.0
W	3.5	3.5
Q	1.0	1.5
ζ	1.0	0.3
Noise Level	2.5%	2.5%
Time Step Frequency	26.67 Times Rotor Frequency	26.67 Times Rotor Frequency

Note: Characteristic Used in Simulations:

$$\Psi(\Phi) = -18.7\,\Phi^4 + 35.5\,\Phi^3 - 27.1\,\Phi^2 + 9.84\,\Phi - 1.05$$

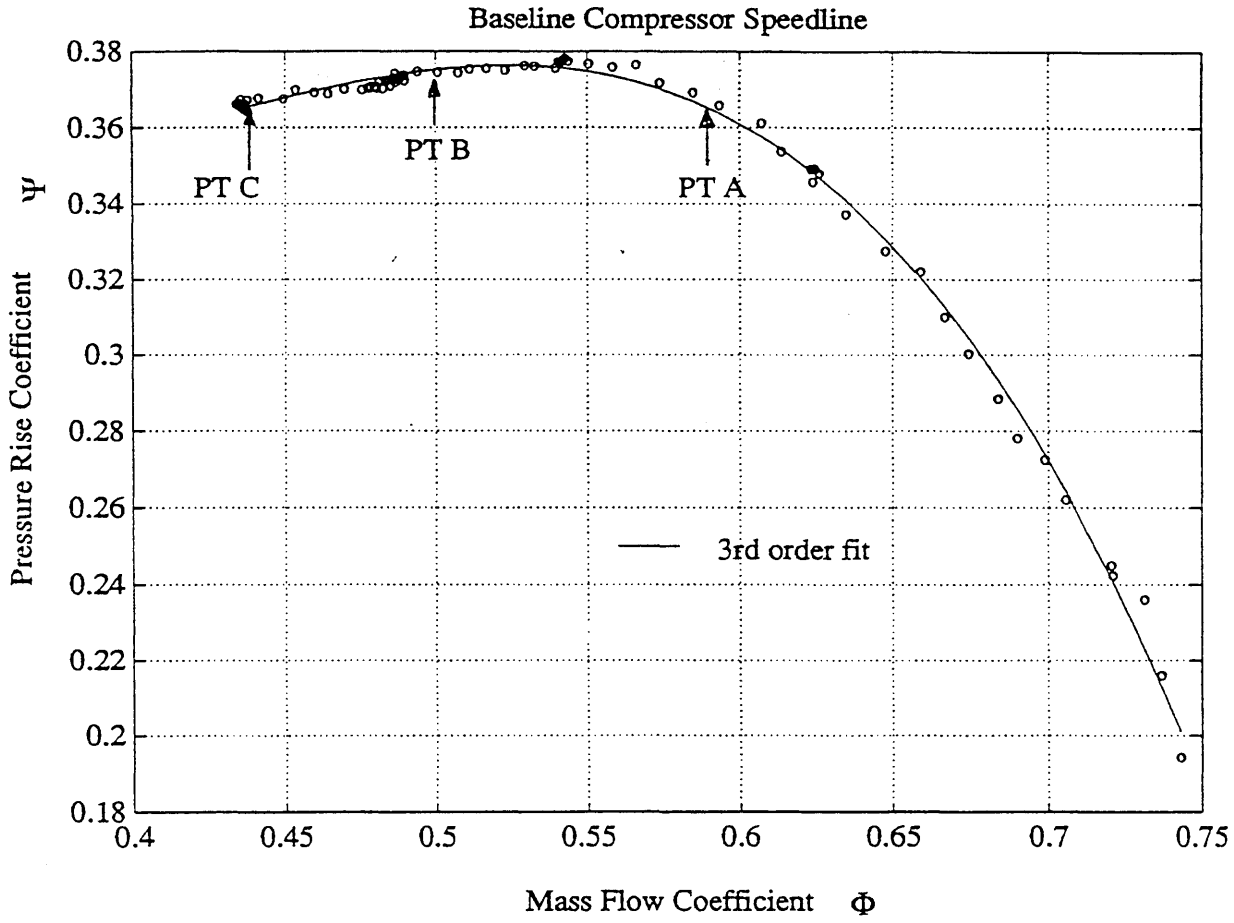

Figure 4.1 Inlet Total to Exit Static Pressure Rise Coefficient $\left(P_{s_d} - P_{t_u} / \frac{1}{2} \rho U_R^2\right)$ versus Flow Coefficient $(\dot{m} / \rho A U_R)$ Constant Speed Performance Characteristic for Baseline Compressor (2250 RPM) with Third Order Curve Fit also shown

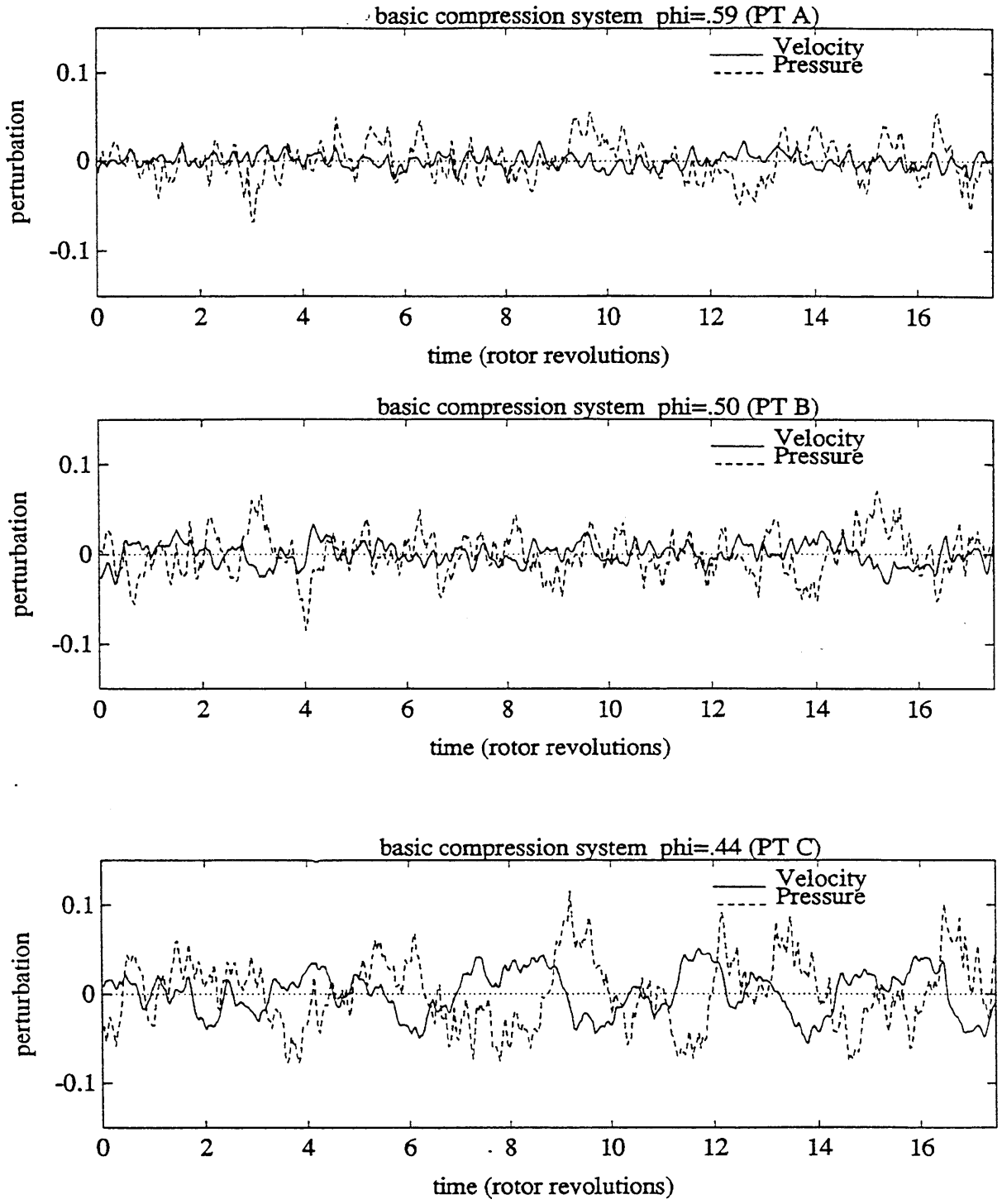

Figure 4.2 Time Resolved, Normalized Static Pressure $\left(\delta p / \frac{1}{2} \rho U_R^2\right)$ and Axial Velocity Perturbations $\left(\delta C_x / U_R\right)$ for Basic Compression System at Entrance to Compressor for Three Flow Coefficients (Φ = 0.59, 0.50, and 0.44)

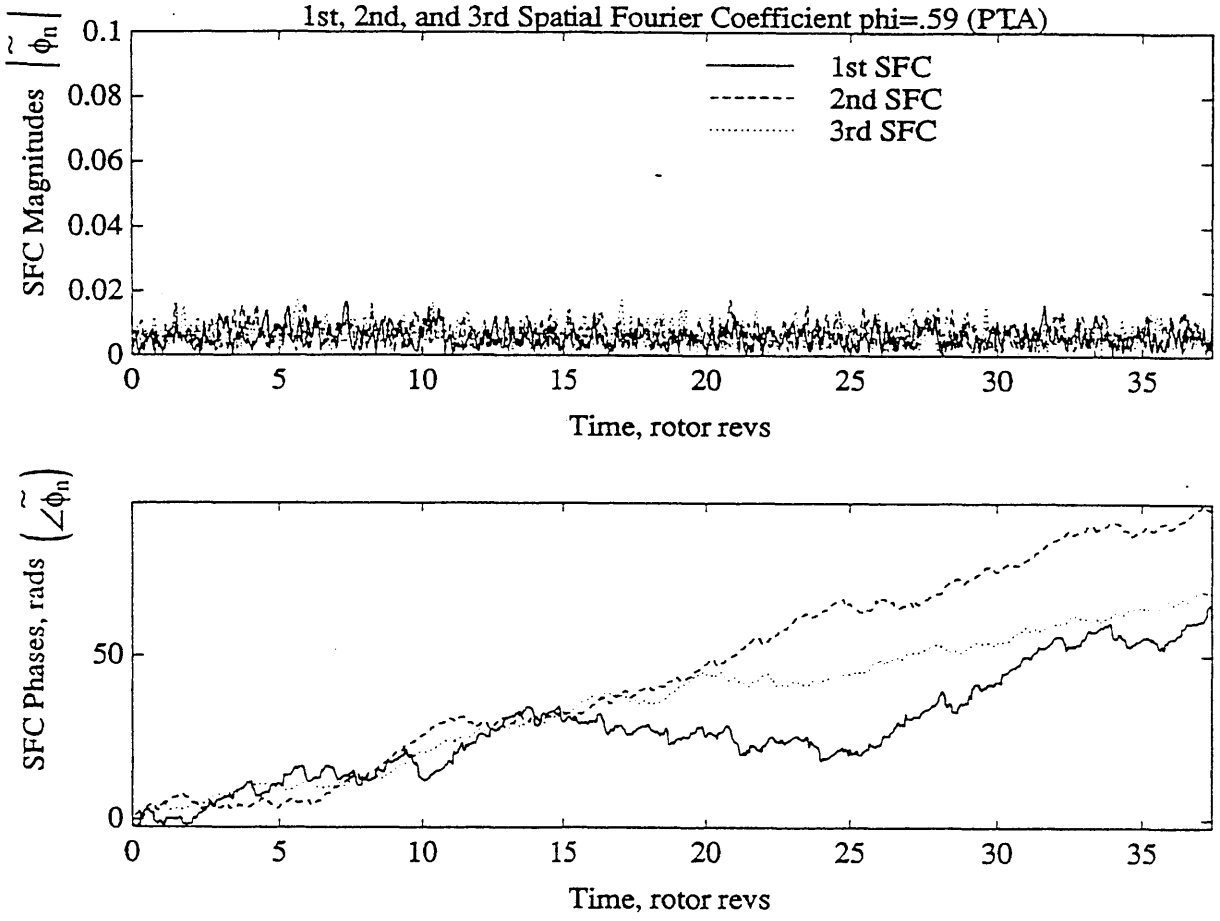

Figure 4.3 Spatial Fourier Decompostion of Normalized Axial Velocity Perturbations for Basic Compression System Operating Away From Stall ($\Phi = 0.59$) (PT A)

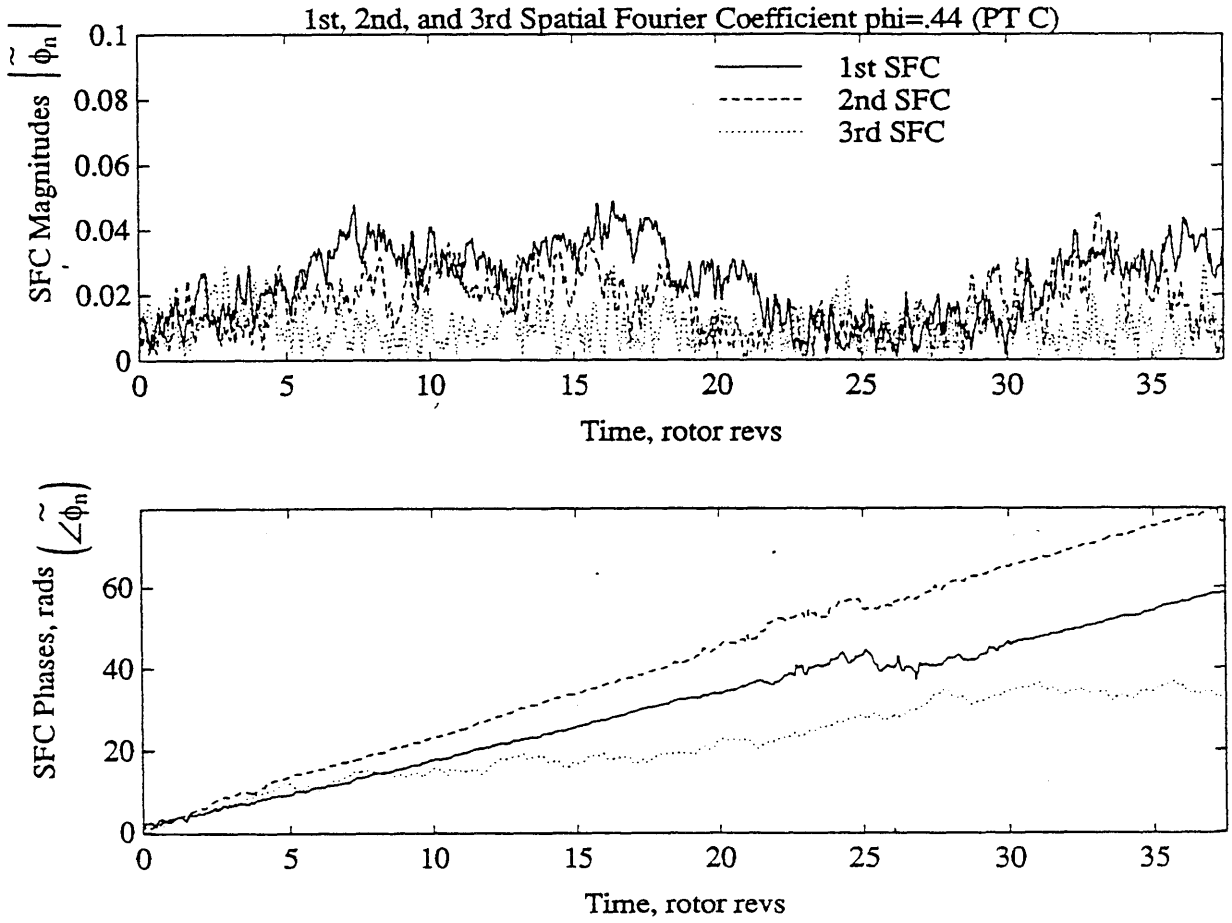

Figure 4.4 Spatial Fourier Decompostion of Normalized Axial Velocity Perturbations for Basic Compression System Operating Near Stall ($\Phi = 0.44$) (PT C)

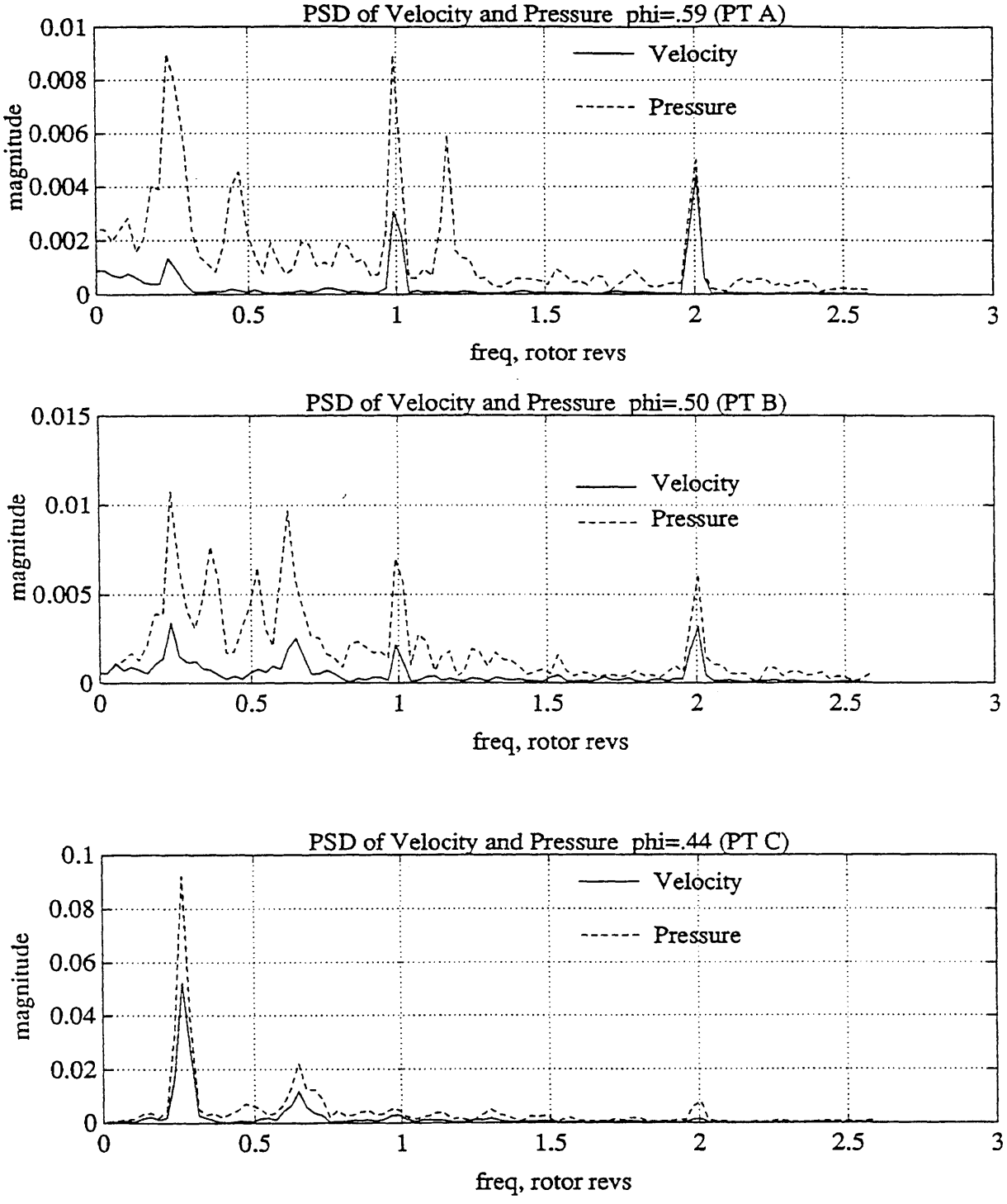

Figure 4.5 PSD's of Normalized Static Pressure and Axial Velocity Perturbations for Basic Compression System Operating at Three Mass Flow Coefficients (Φ = 0.59, 0.50, and 0.44)

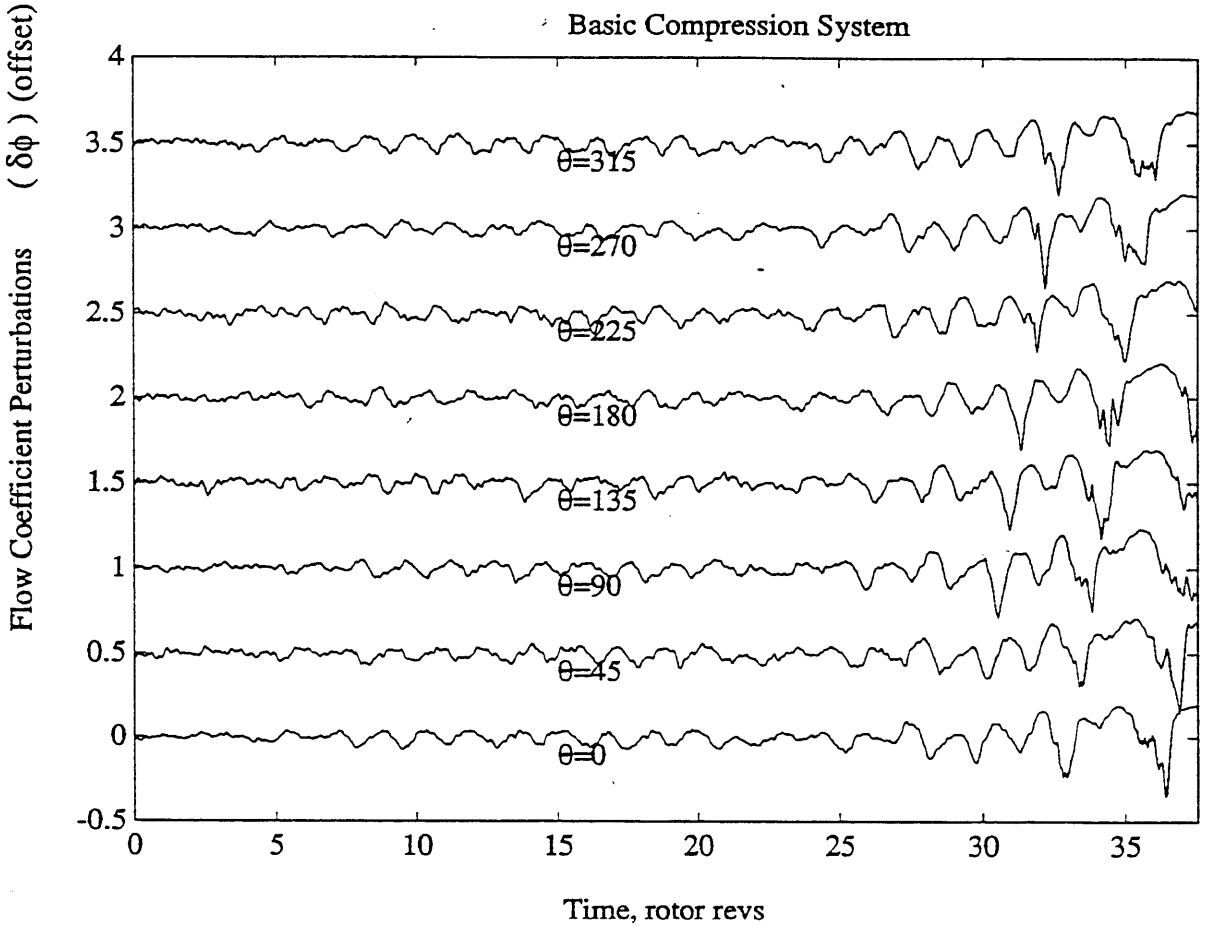

Figure 4.6 Normalized Axial Velocity Perturbations $(\delta C_x / U_R)$ During the Stall Inception Process of Basic Compression System

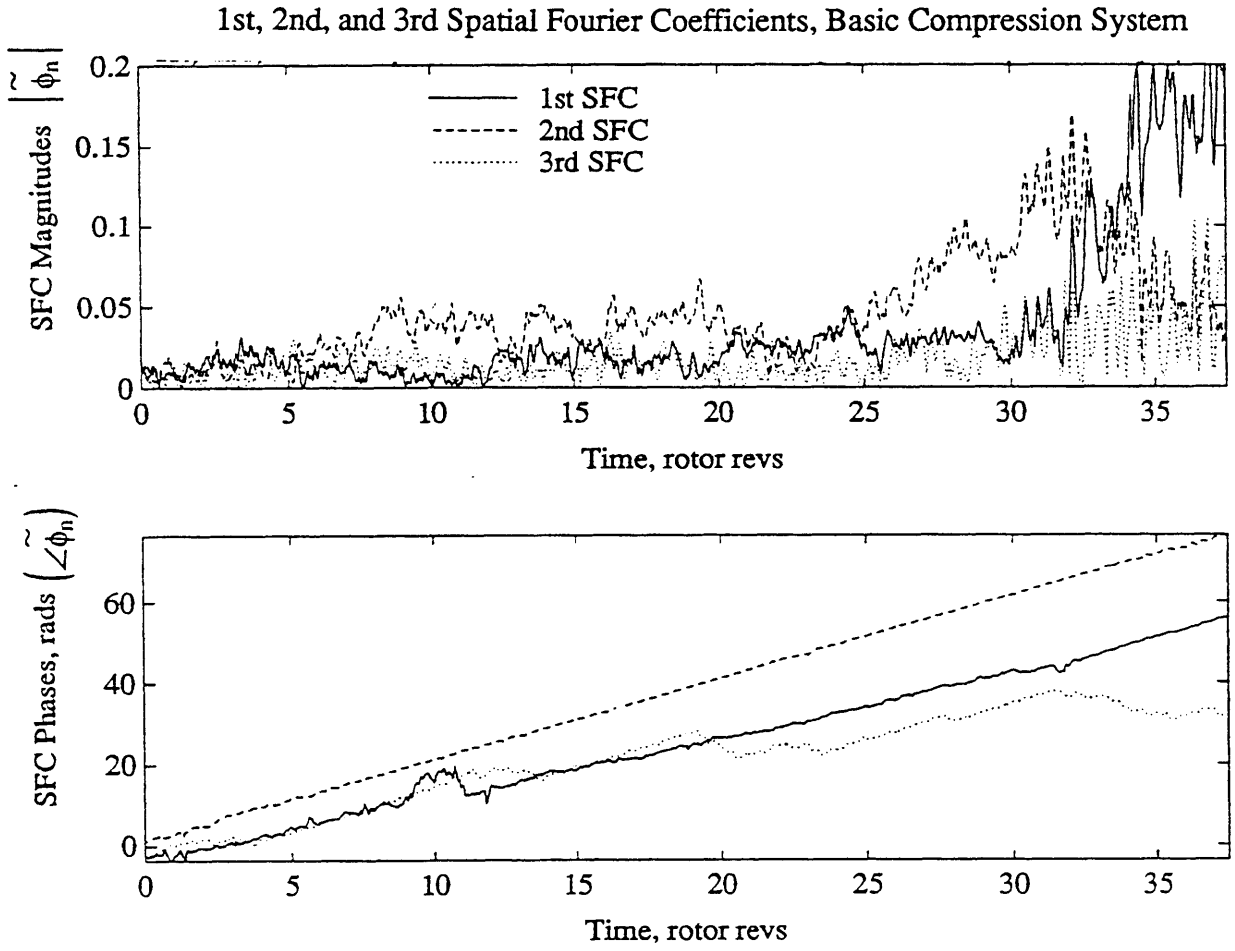

Figure 4.7 Spatial Fourier Decompostion of Normalized Axial Velocity Perturbations During Stall Inception of Basic Compression System

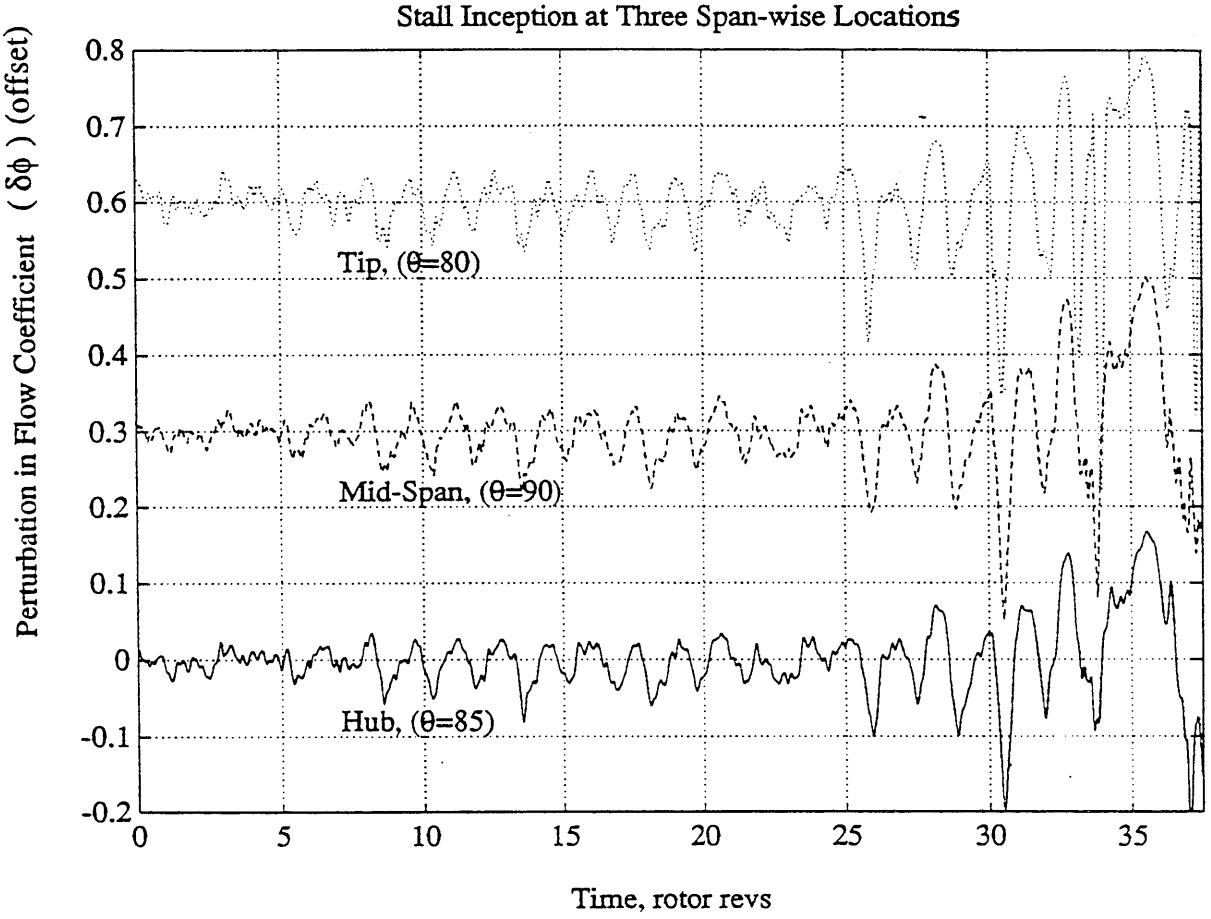

Figure 4.8 Normalized Axial Velocity Perturbations $(\delta C_x / U_R)$ from Three Closely Spaced Hot-Wires at 15%, 50%, and 85% Spanwise Imersion During Stall Inception of Basic Compression System

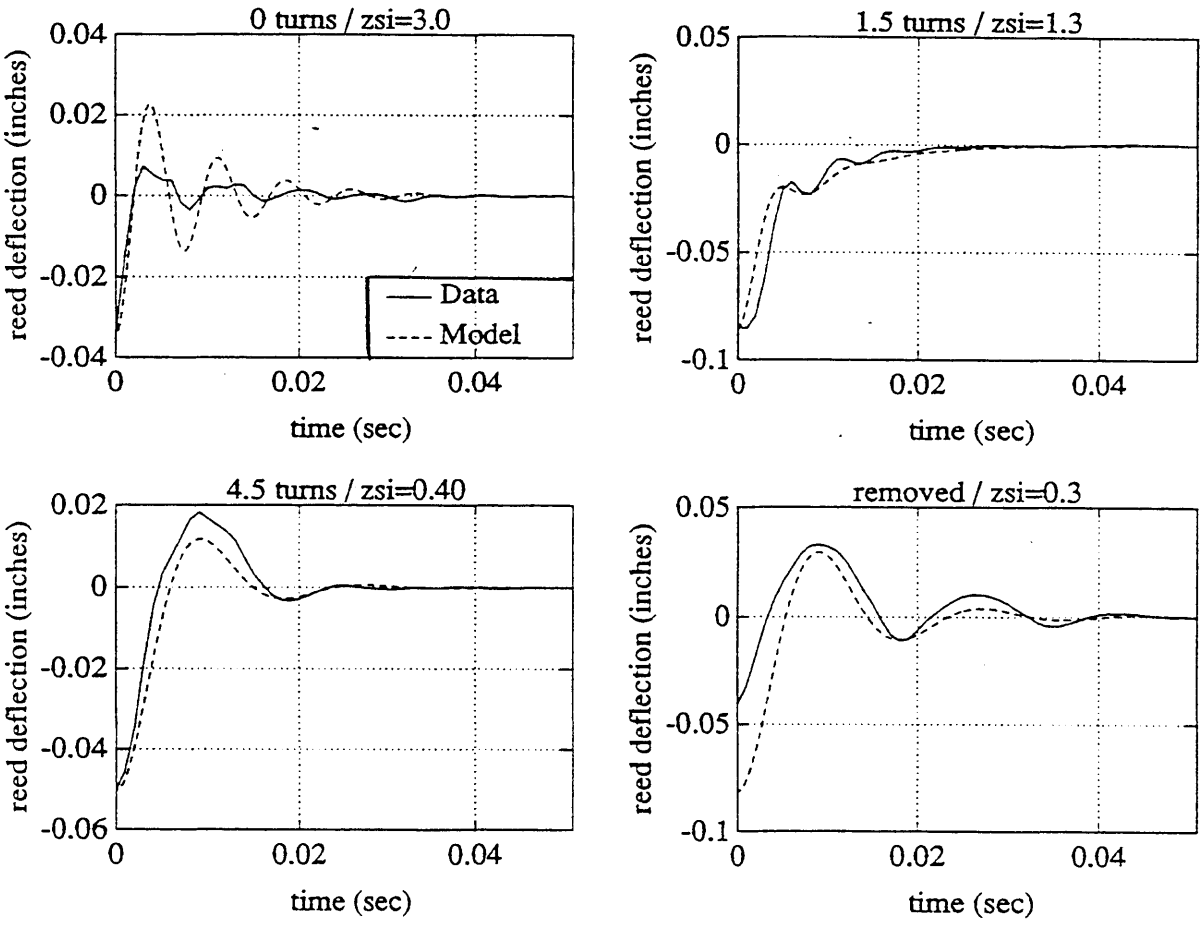

Figure 4.9 Initial Condition Response of Typical Reed Valve for Four Pneumatic Dashpot Settings without Injection,

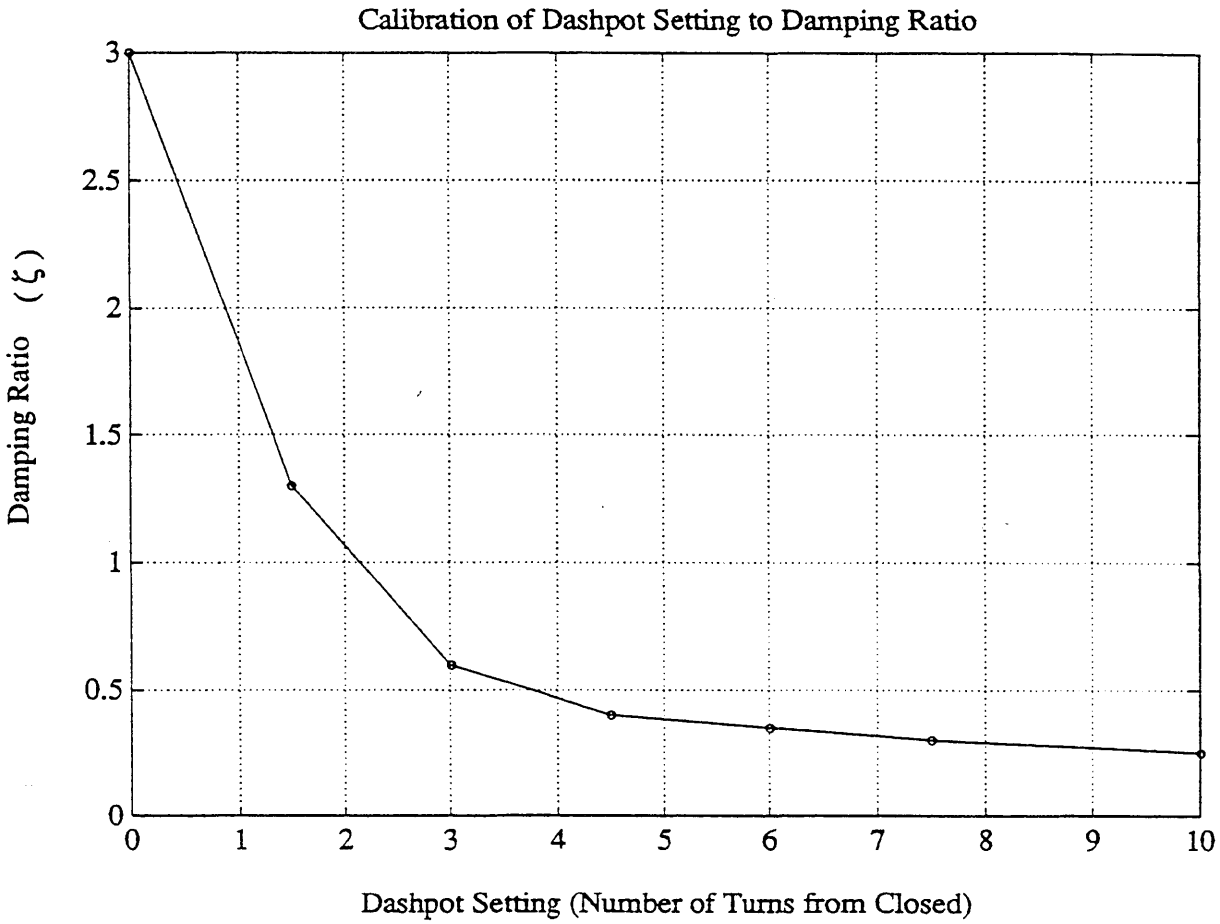

Figure 4.10 Calibration of Pneumatic Dashpot Damping Ratio (ζ) versus Dashpot Setting (Number of Turns from Closed) Based on Initial Condition Response

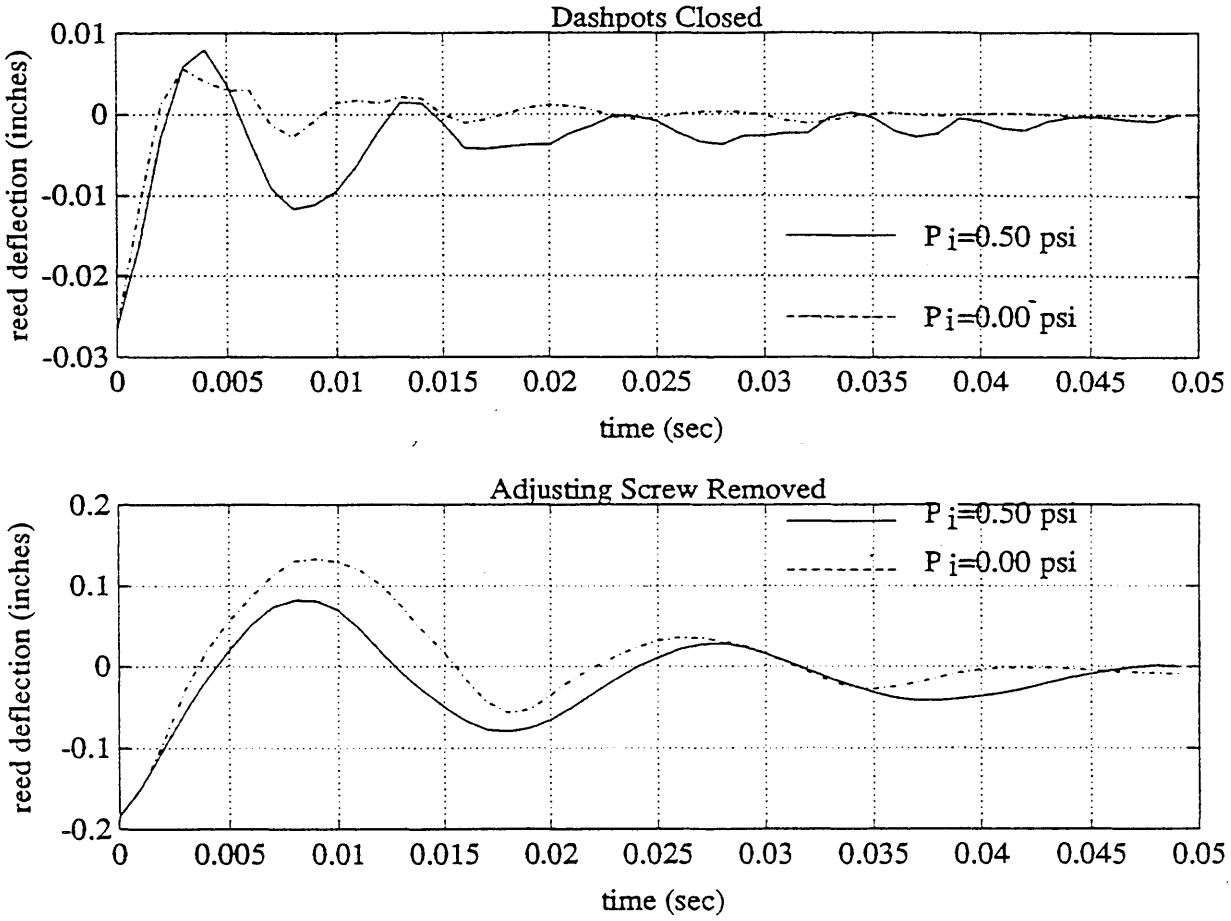

Figure 4.11 Initial Condition Response of Reed Valves at Two Dashpot Settings with and without Injection

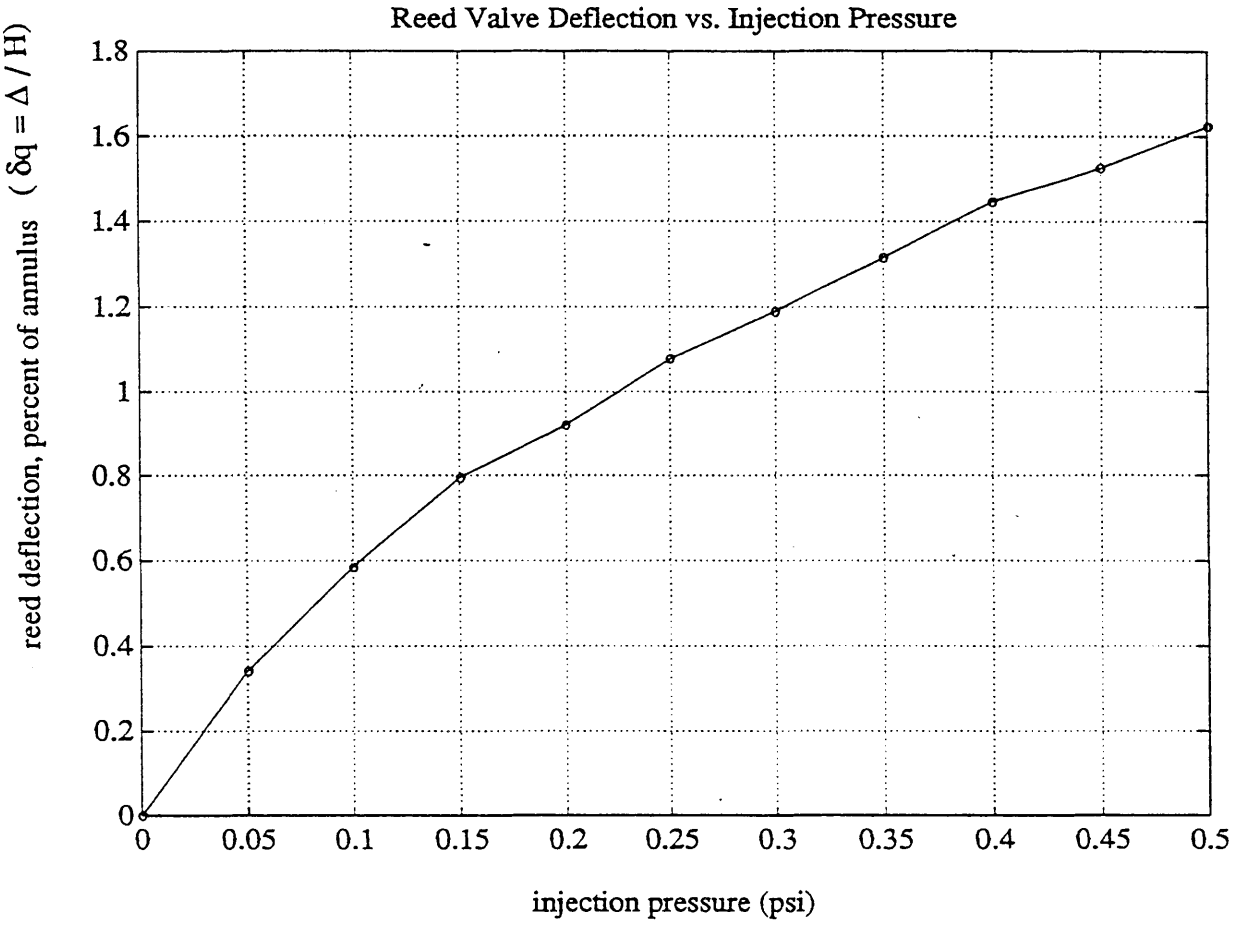

Figure 4.12 Static Reed Valve Deflection (δΔ / H) versus Injection Pressure (Compressor not Operating)

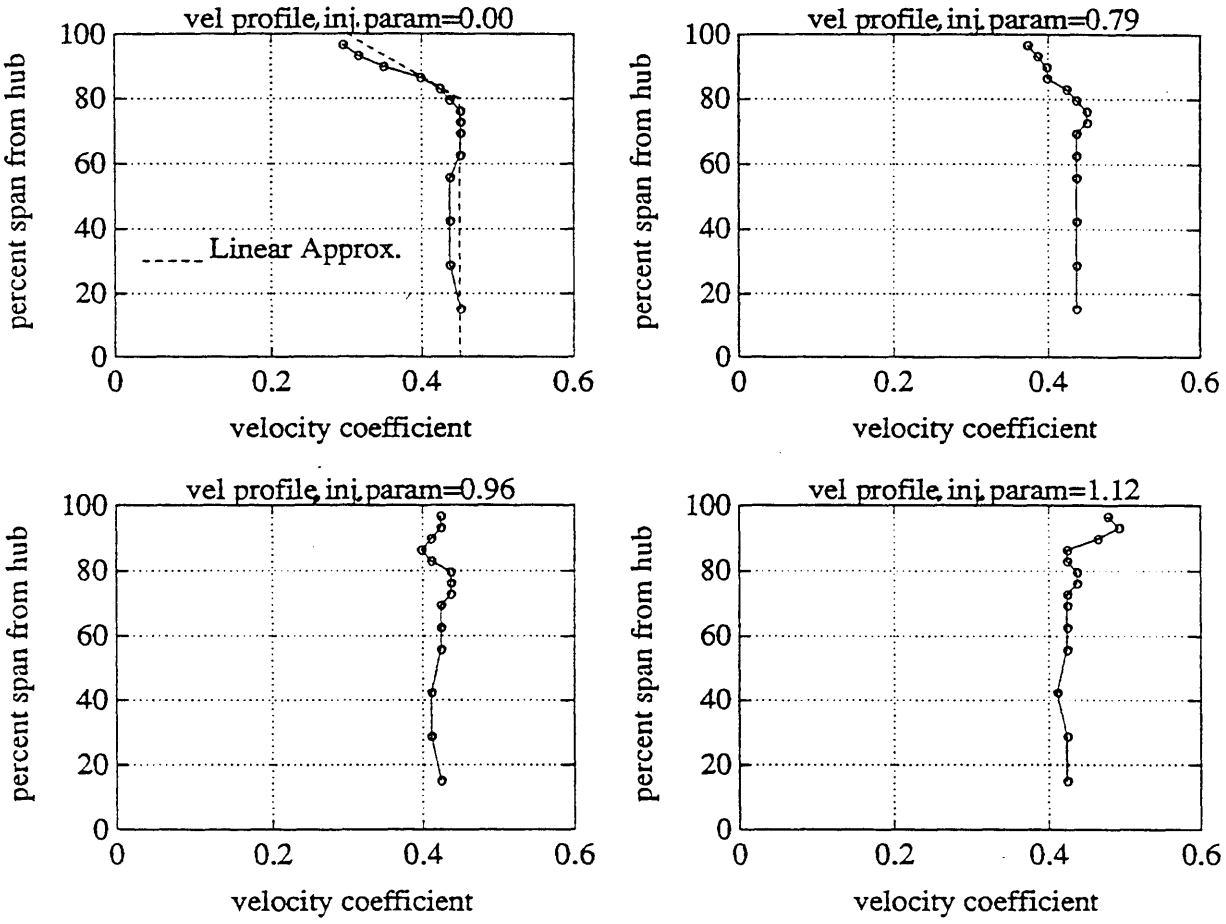

Figure 4.13 Velocity Profiles at Entrance to Compressor for Four Injection Levels with the Compression Operating at $\Phi = 0.45$.(2250 RPM)

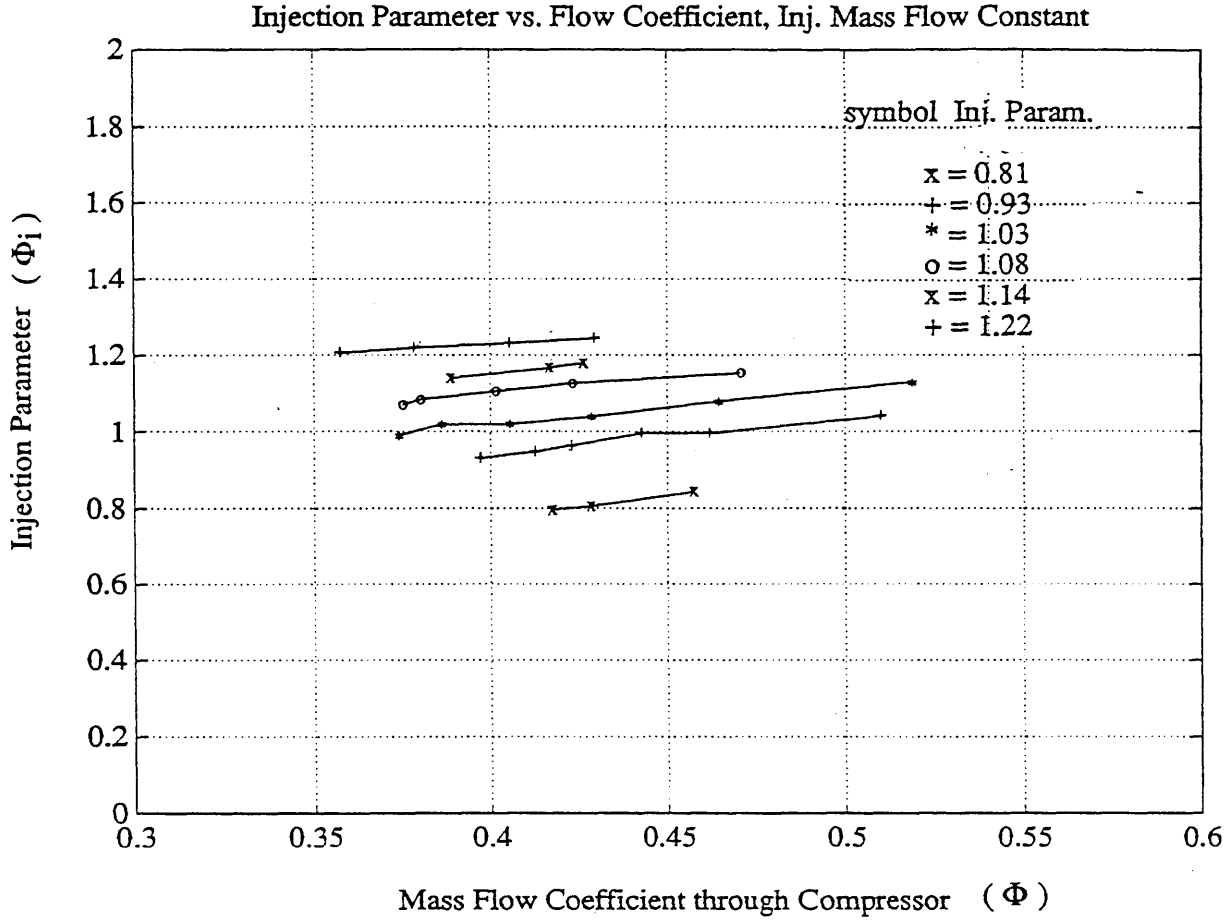

Figure 4.14 Injection Parameter (Φ_i) as a function of Flow Coefficient (Φ)for Six Fixed Amounts of Injection Mass Flow

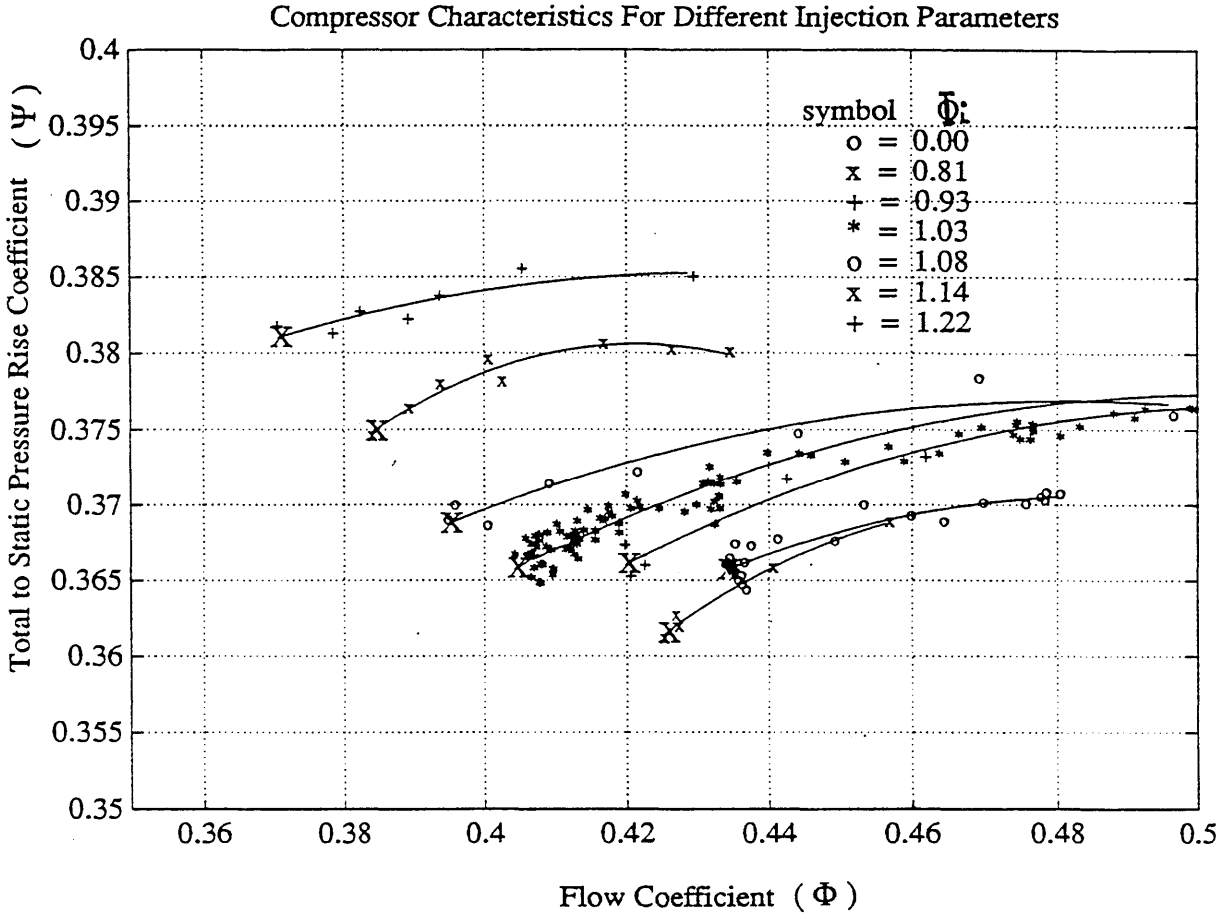

Figure 4.15 Compressor Speedlines for Seven Injection Levels with Reed Dashpots Closed at 2250 RPM

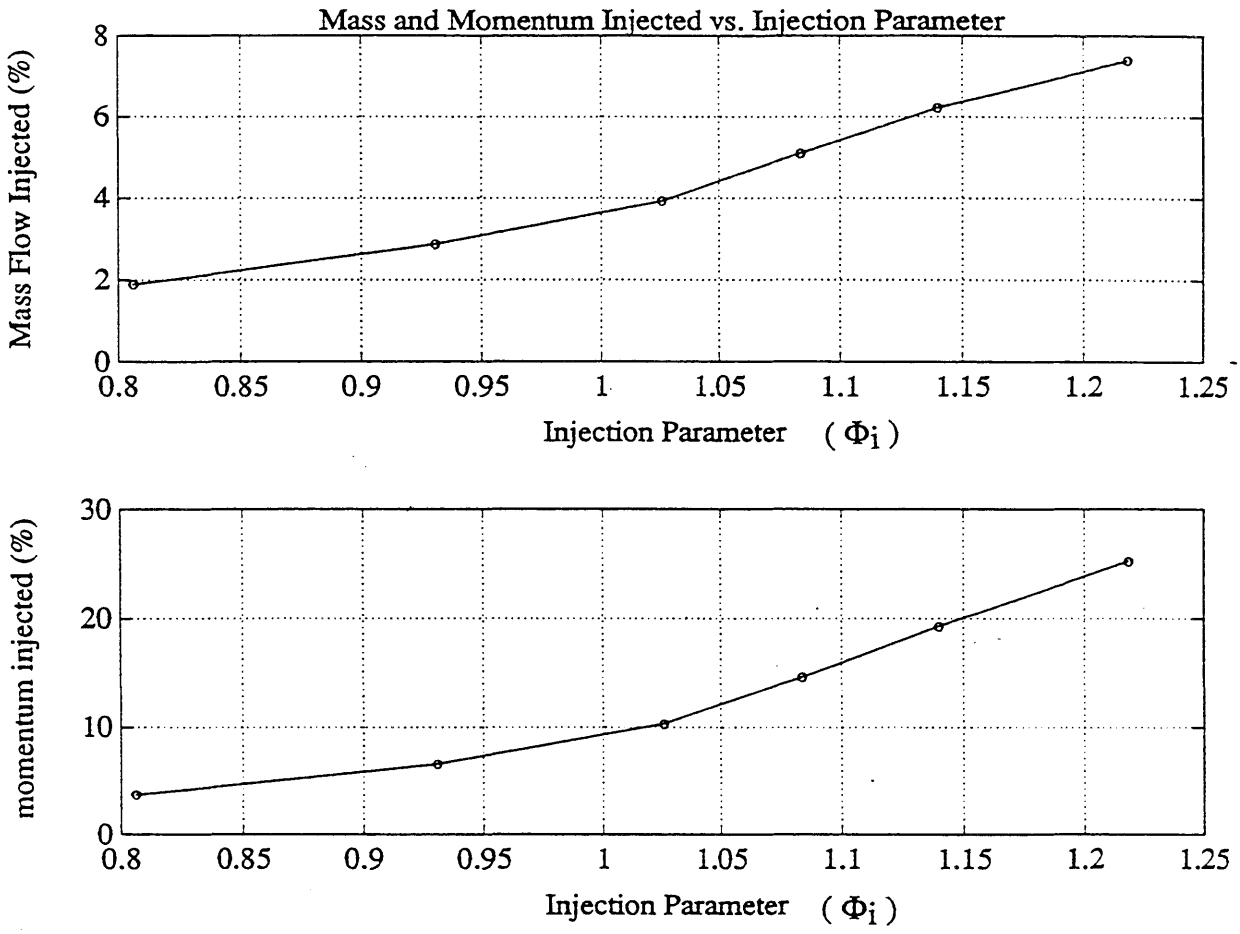

Figure 4.16 Percentage of Mass Flow and Momentum Injected Based on Stalling Flow Coefficient for the Rigid Reed Valve Configuration as a Fuction of Injection Parameter

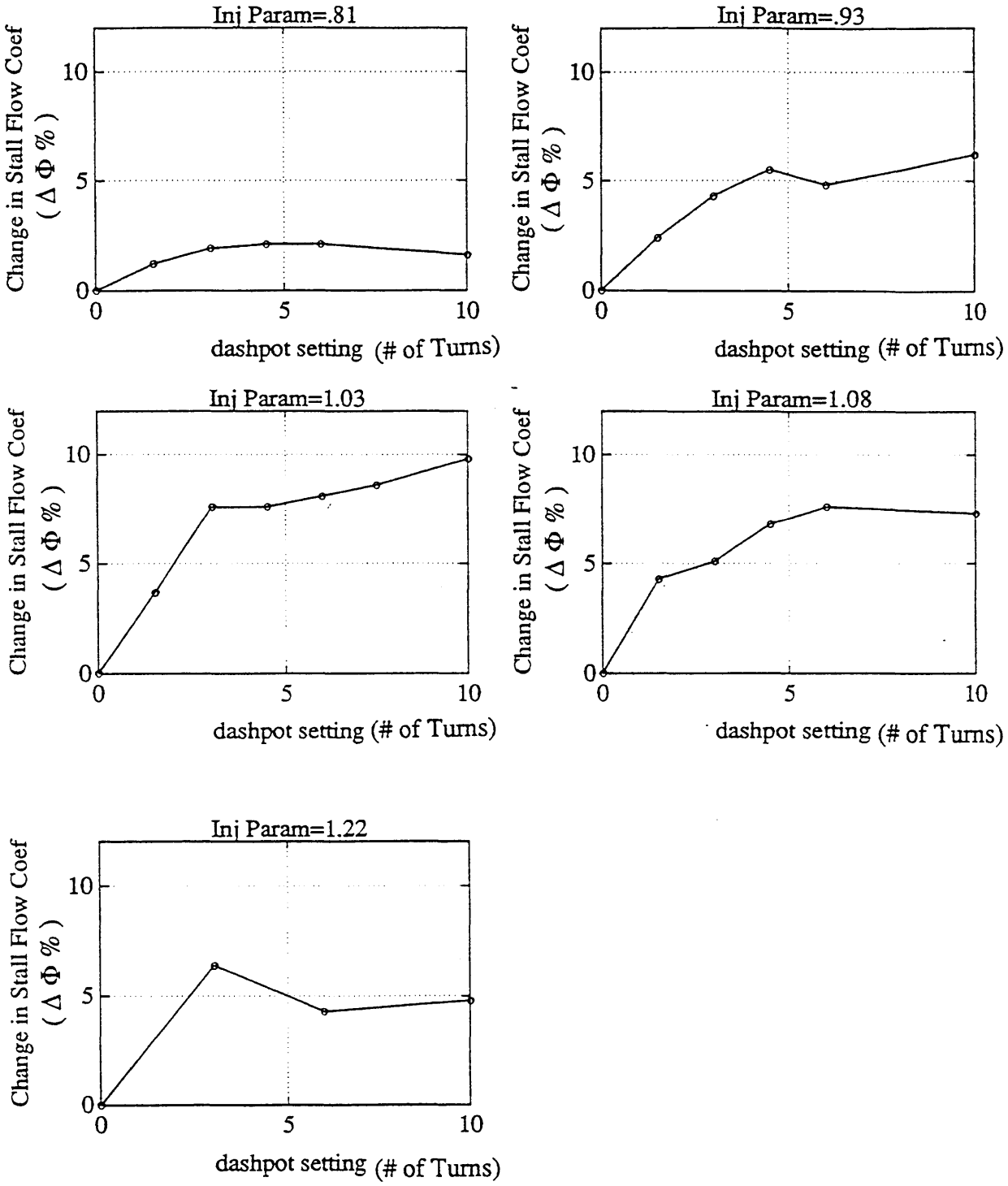

Figure 4.17 Change in Stalling Flow Coefficient as a Function of Dashpot Setting for Five Injection Levels

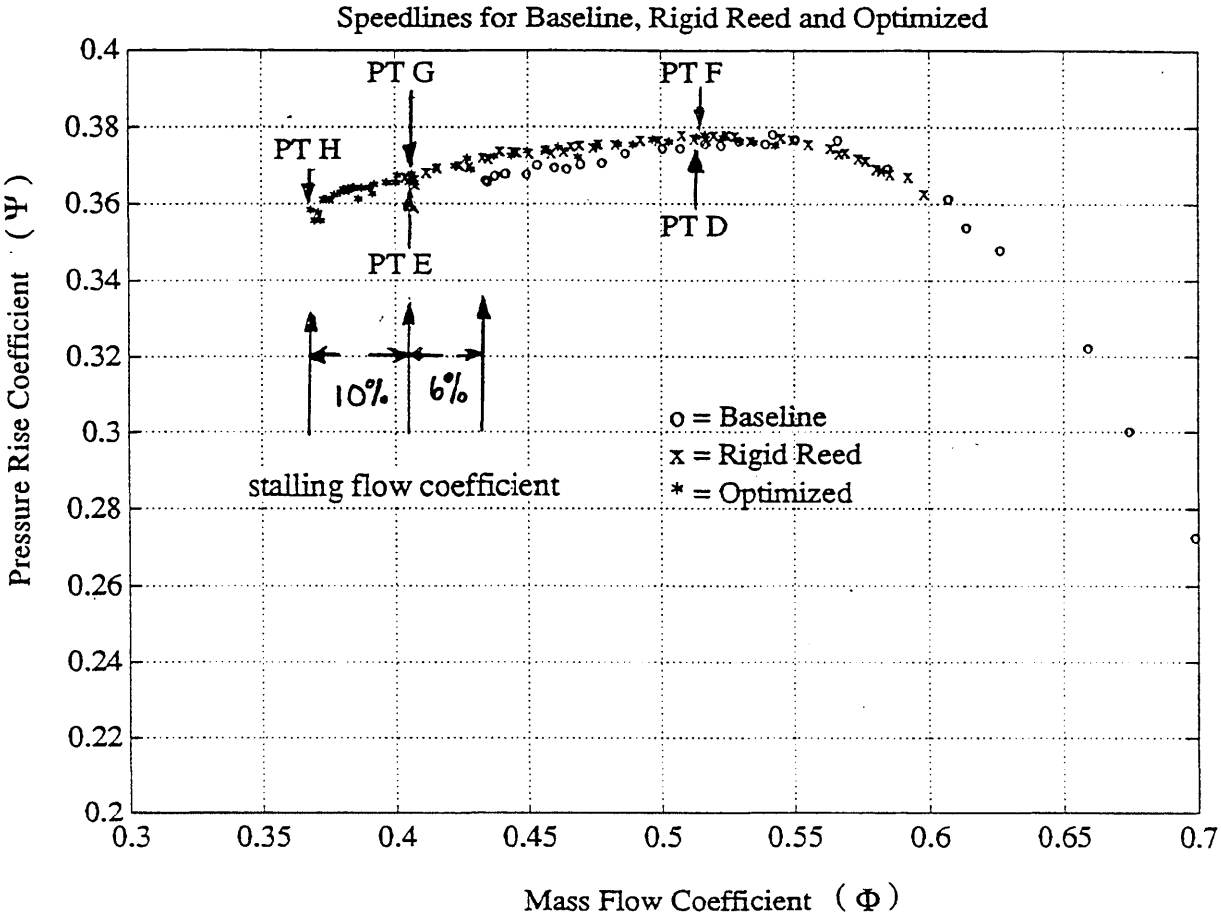

Figure 4.18 Compressor Speedlines for Basic Compression System, Rigid Reed Valve Configuration with Injection, and the Experimental Optimized Configuration with Injection (2250 RPM)

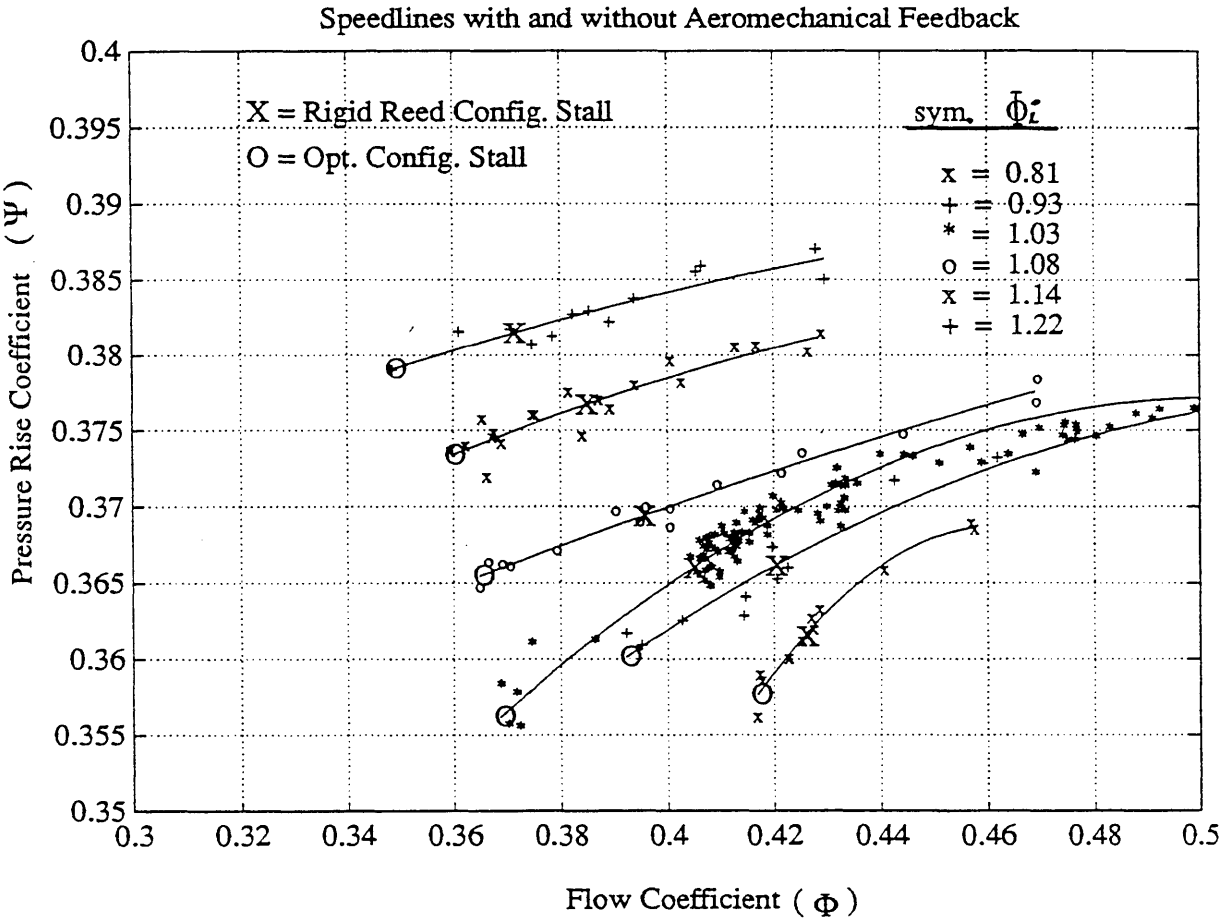

Figure 4.19 Compressor Speedlines for Several Injection Levels with Dashpot Settings Optimized for Each Injection Level (2250 RPM)

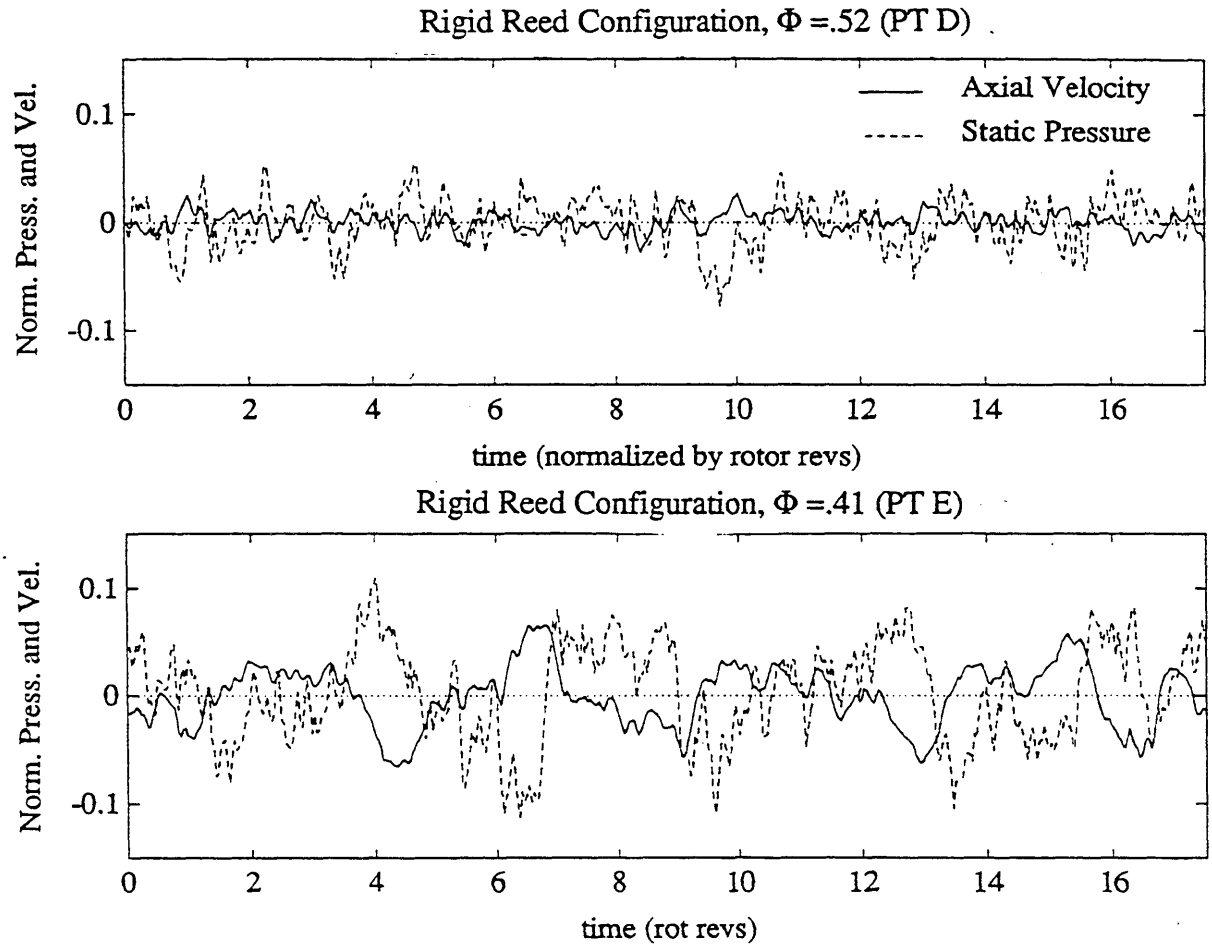

Figure 4.20 Time Resolved, Normalized Static Pressure $\left(\delta p / \frac{1}{2} \rho U_R^2\right)$ and Axial Velocity Perturbations $\left(\delta C_x / U_R\right)$ for Rigid Reed Valve Configuration with the Experimentally Optimized Injection Level ($\Phi_i = 1.0$) Operating at $\Phi = 0.52$ (PT D) and $\Phi = 0.41$ (PT E).

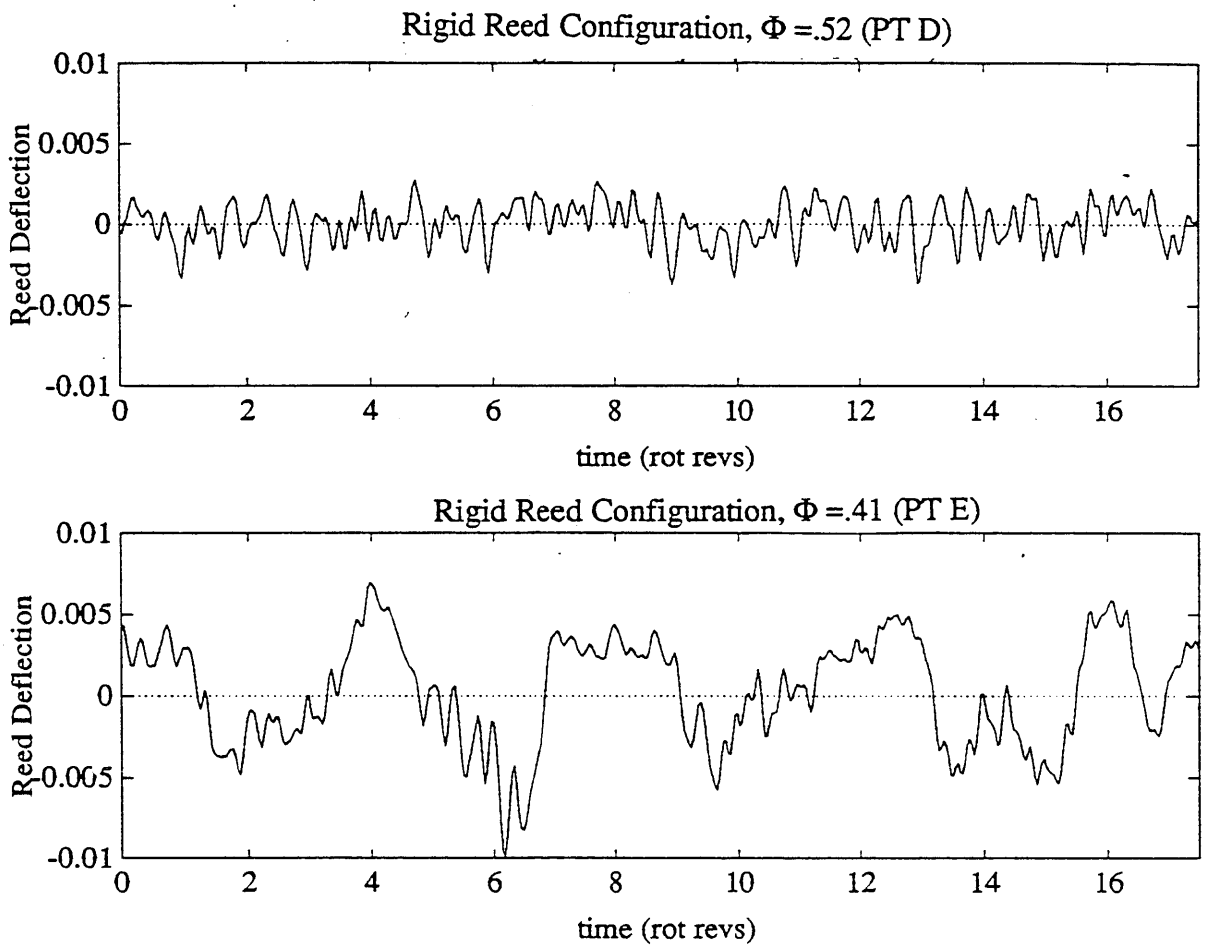

Figure 4.21 Time Resolved, Normalized Reed Valve Deflections ($\delta\Delta$ / H) for Rigid Reed Configuration Operating at Φ = 0.52 (PT D) and Φ = 0.41 (PT E)

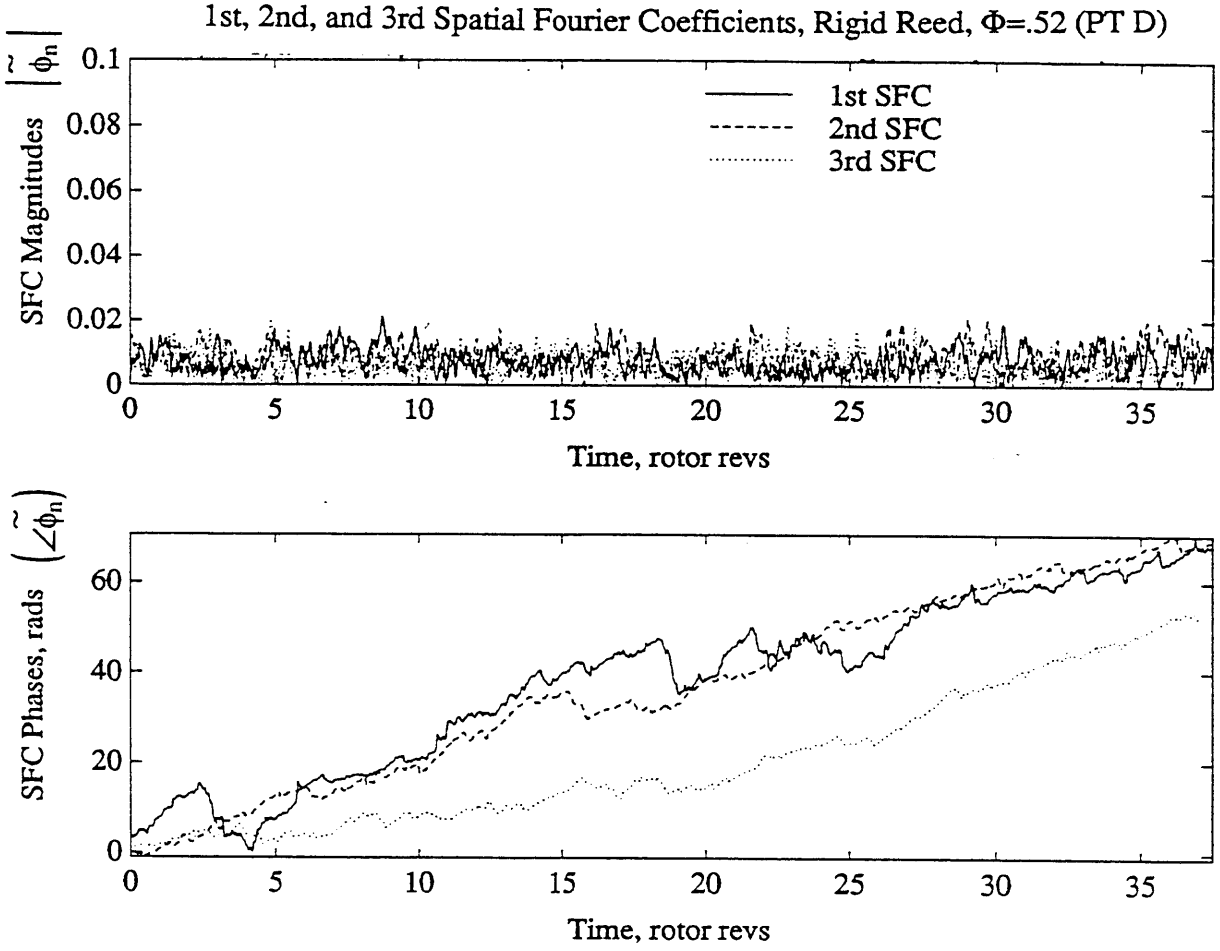

Figure 4.22 Spatial Fourier Decomposition of Normalized Axial Velocity Perturbations for the Rigid Reed Valve Configuration Operating Away from Stall at $\Phi = 0.52$ (PT D)

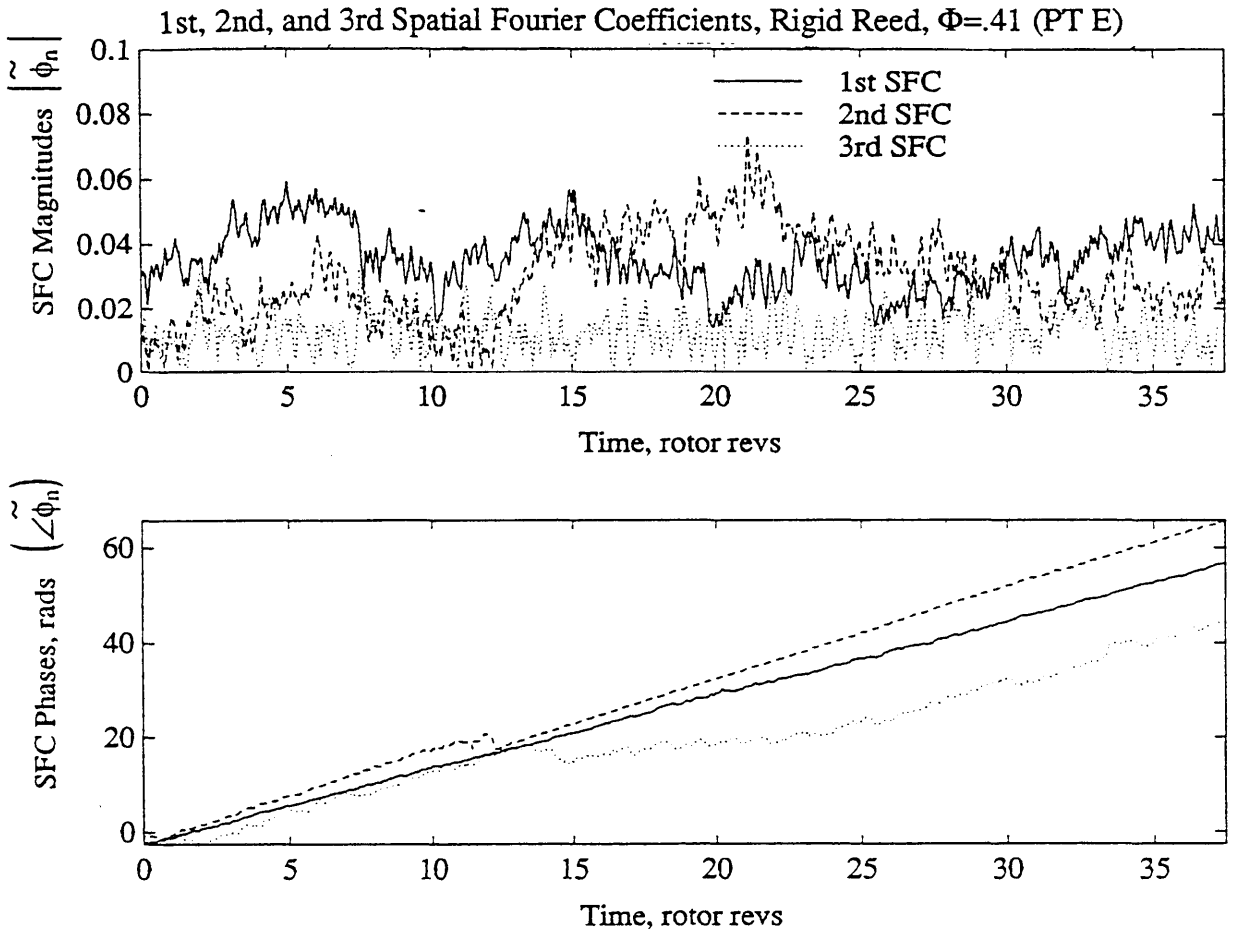

Figure 4.23 Spatial Fourier Decomposition of Normalized Axial Velocity Perturbations for the Rigid Reed Valve Configuration Operating Near Stall at $\Phi = 0.41$ (PT E)

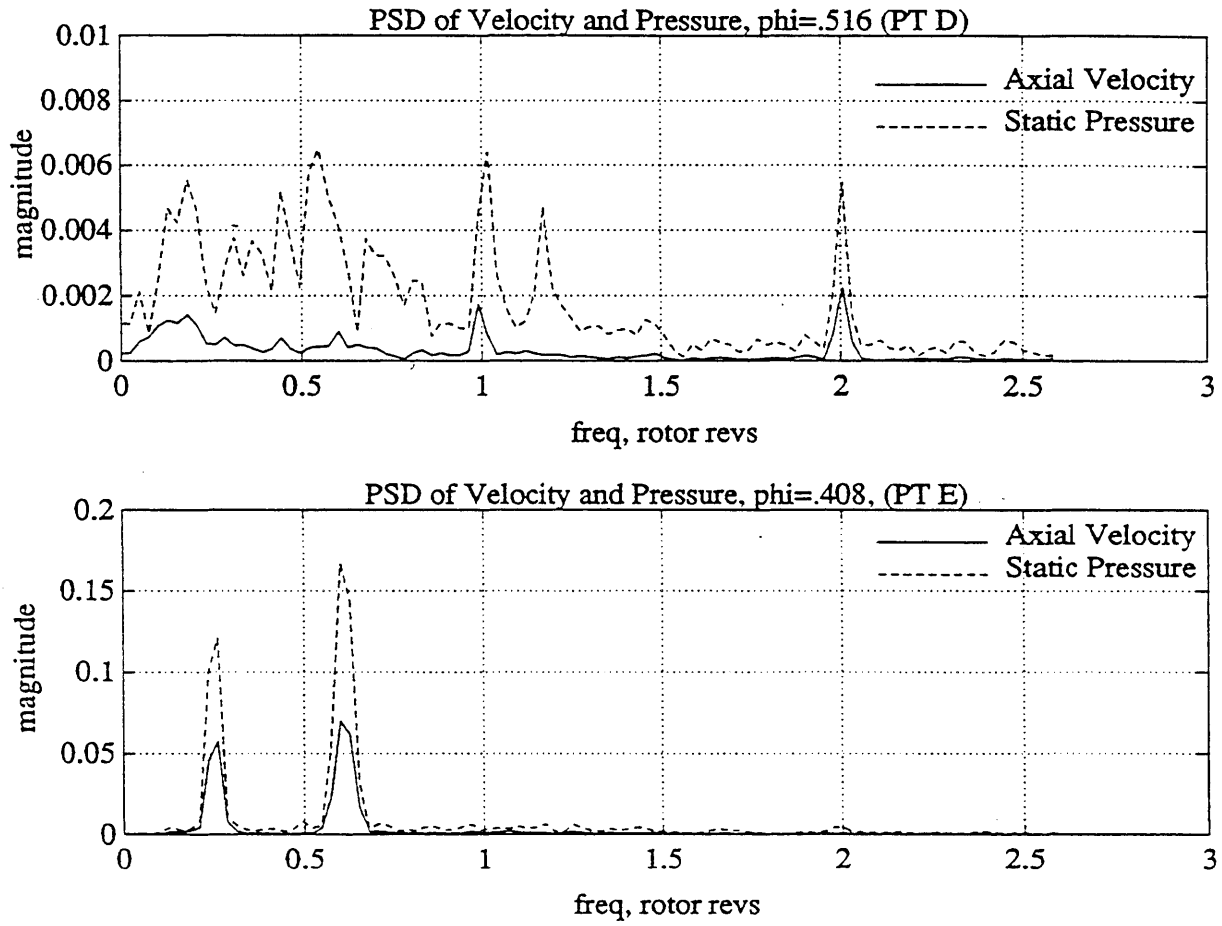

Figure 4.24 PSD's of Normalized Static Pressure and Axial Velocity Perturbations for the Rigid Reed Valve Configuration Operating at $\Phi = 0.52$ (PT D) and $\Phi = 0.41$ (PT E)

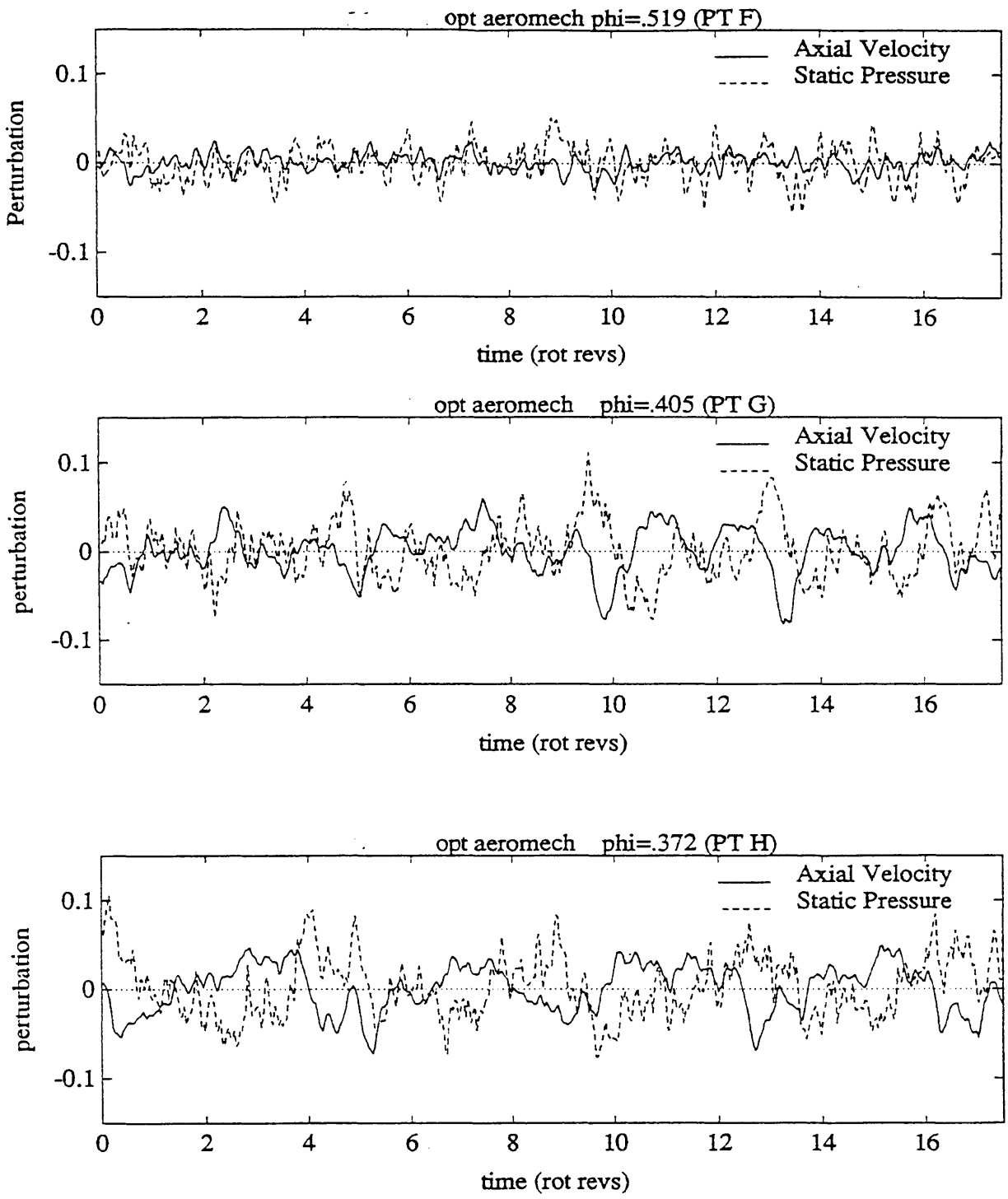

Figure 4.25 Time Resolved, Normalized Static Pressure $\left(\delta p / \frac{1}{2} \rho U_R^2\right)$ and Axial Velocity Perturbations $\left(\delta C_x / U_R\right)$ for Optimized Configuration Operating at Three Flow Coefficients (Φ = 0.52, 0.41, and 0.37)

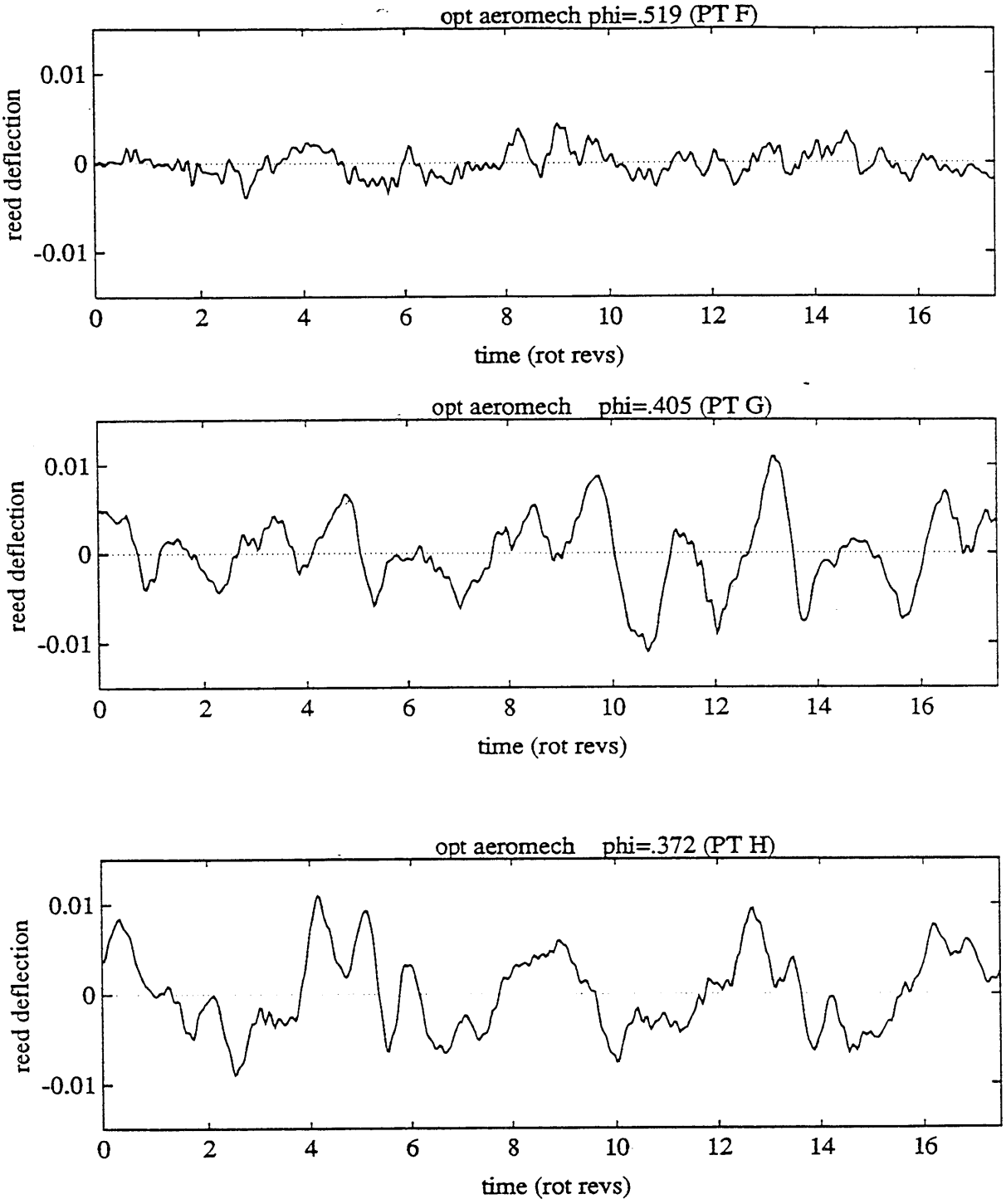

Figure 4.26 Time Resolved, Normalized Reed Deflections ($\delta\Delta$ / H) for Optimized Configuration Operating at Three Flow Coefficients (Φ = 0.52, 0.41, and 0.37)

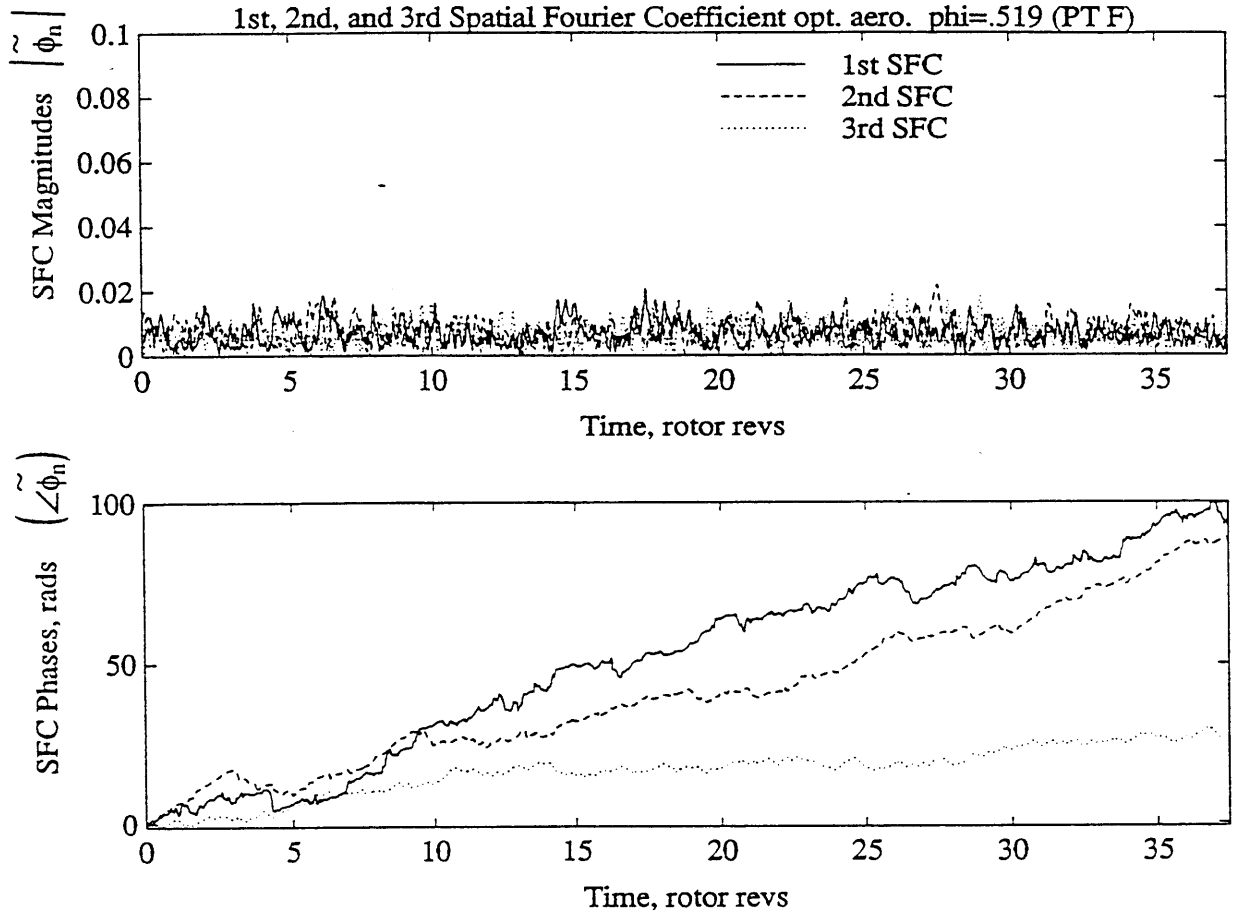

Figure 4.27 Spatial Fourier Decomposition of Normalized Axial Velocity Perturbations for Optimized Configuration Operating Away from Stall at $\Phi = 0.52$(PT F)

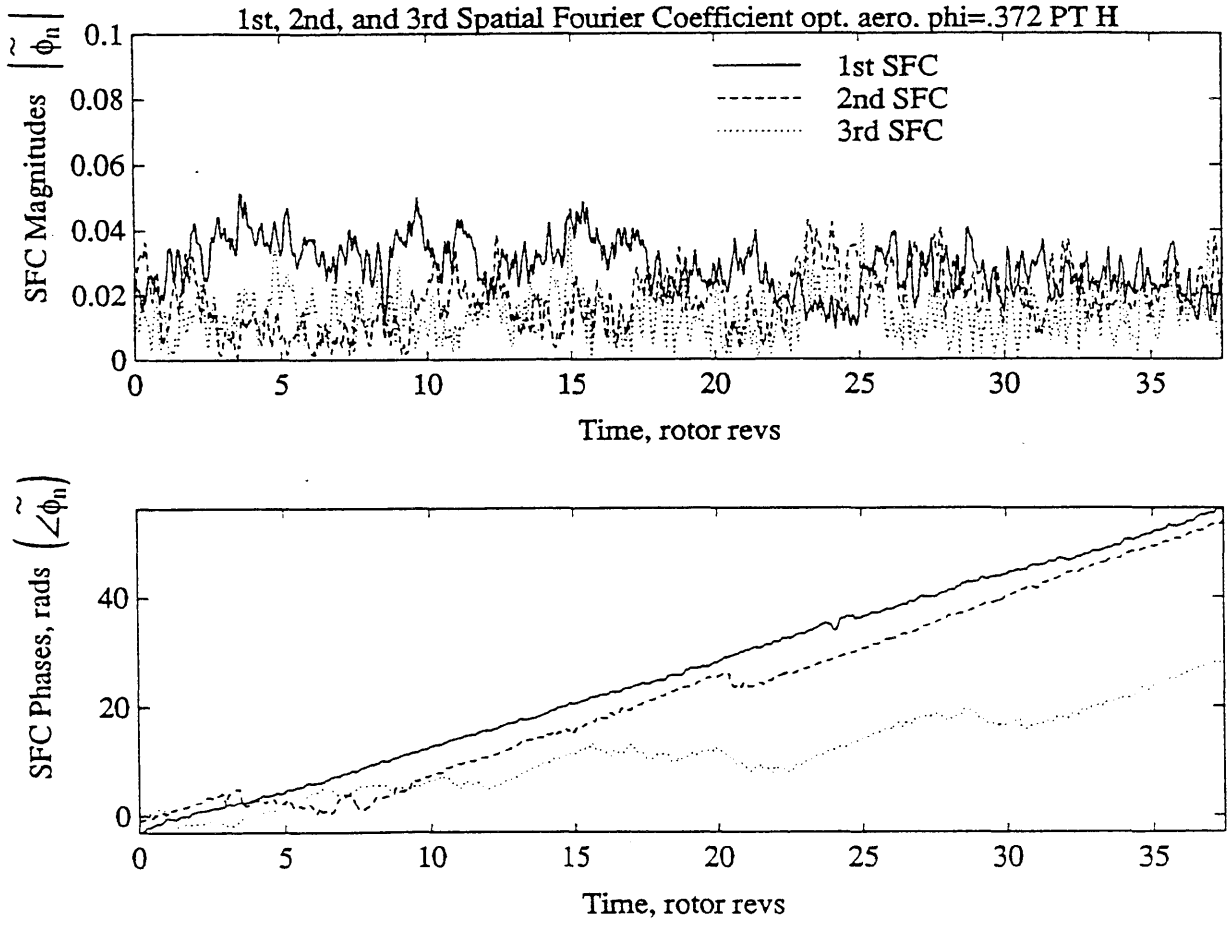

Figure 4.28 Spatial Fourier Decomposition of Normalized Axial Velocity Perturbations for Optimized Configuration Operating Near Stall at $\Phi = 0.37$ (PT H)

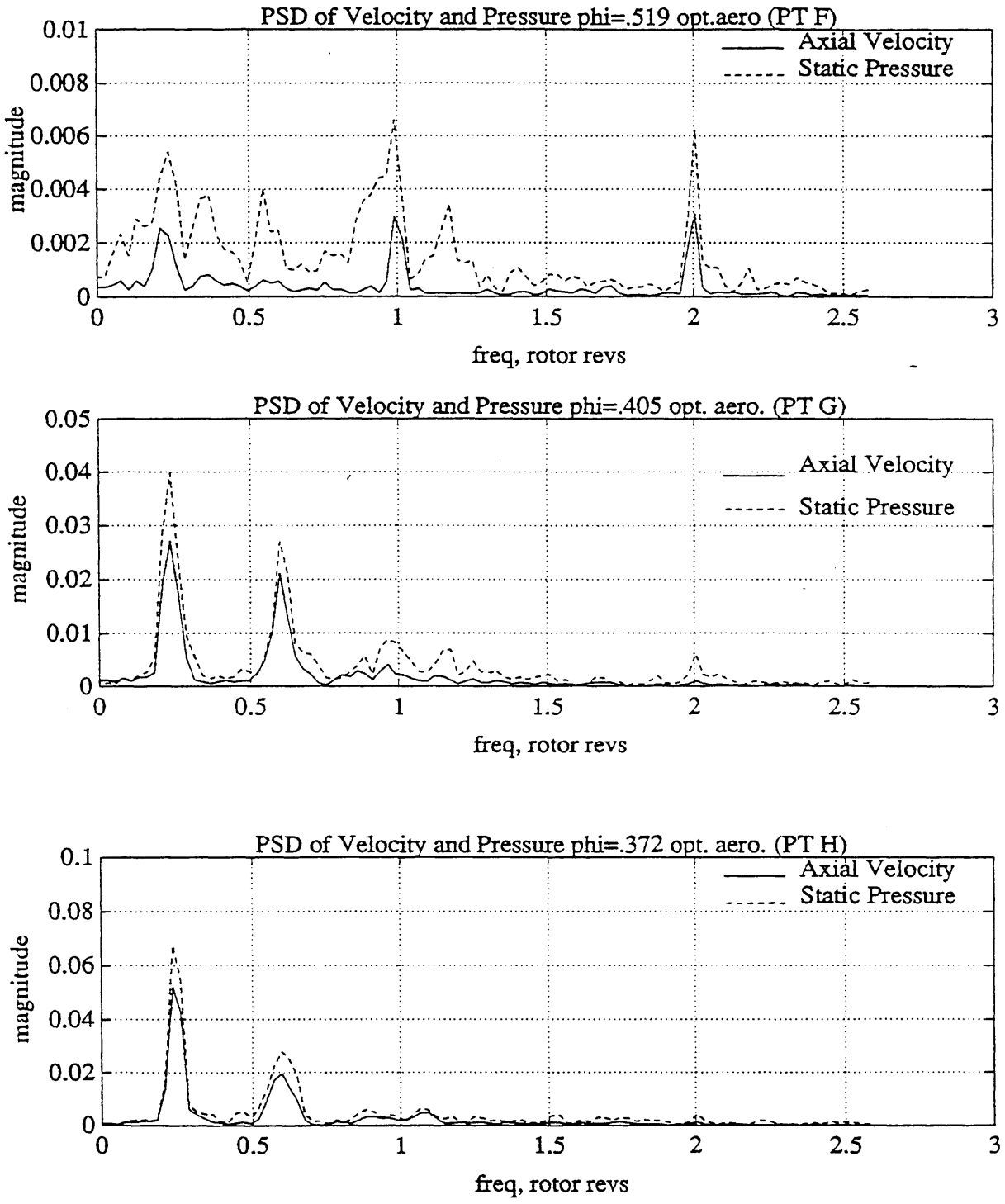

Figure 4.29 PSD's of Normalized Static Pressure and Axial Velocity Perturbations for Optimized Configuration Operating at Three Flow Coefficients, (Φ = 0.52, 0.41, and 0.37)

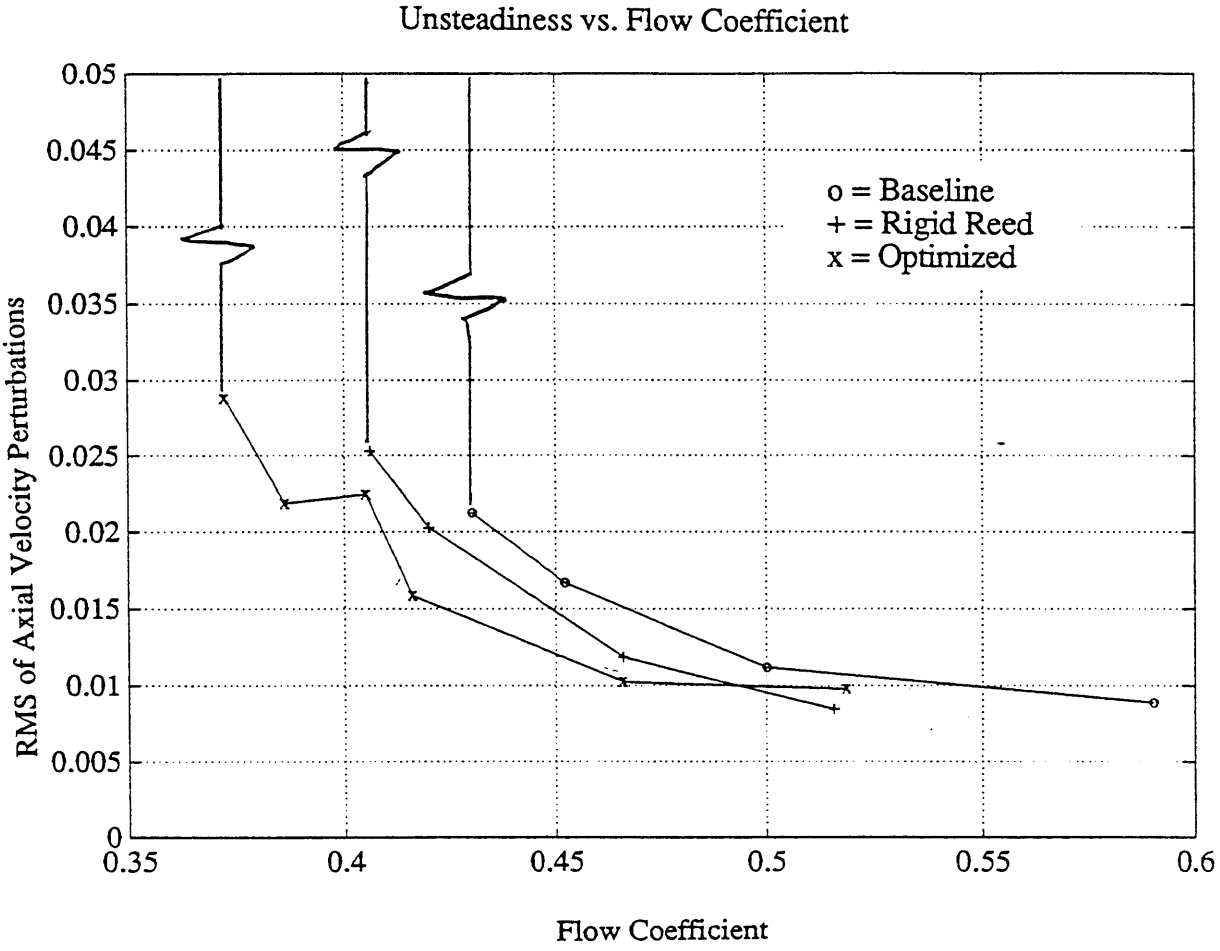

Figure 4.30 RMS of Normalized Axial Velocity Perturbations $(\delta C_x / U_R)$ as a Function of Mean Flow Coefficient (Φ)for the Baseline, Rigid Reed Valve, and Optimized Configurations

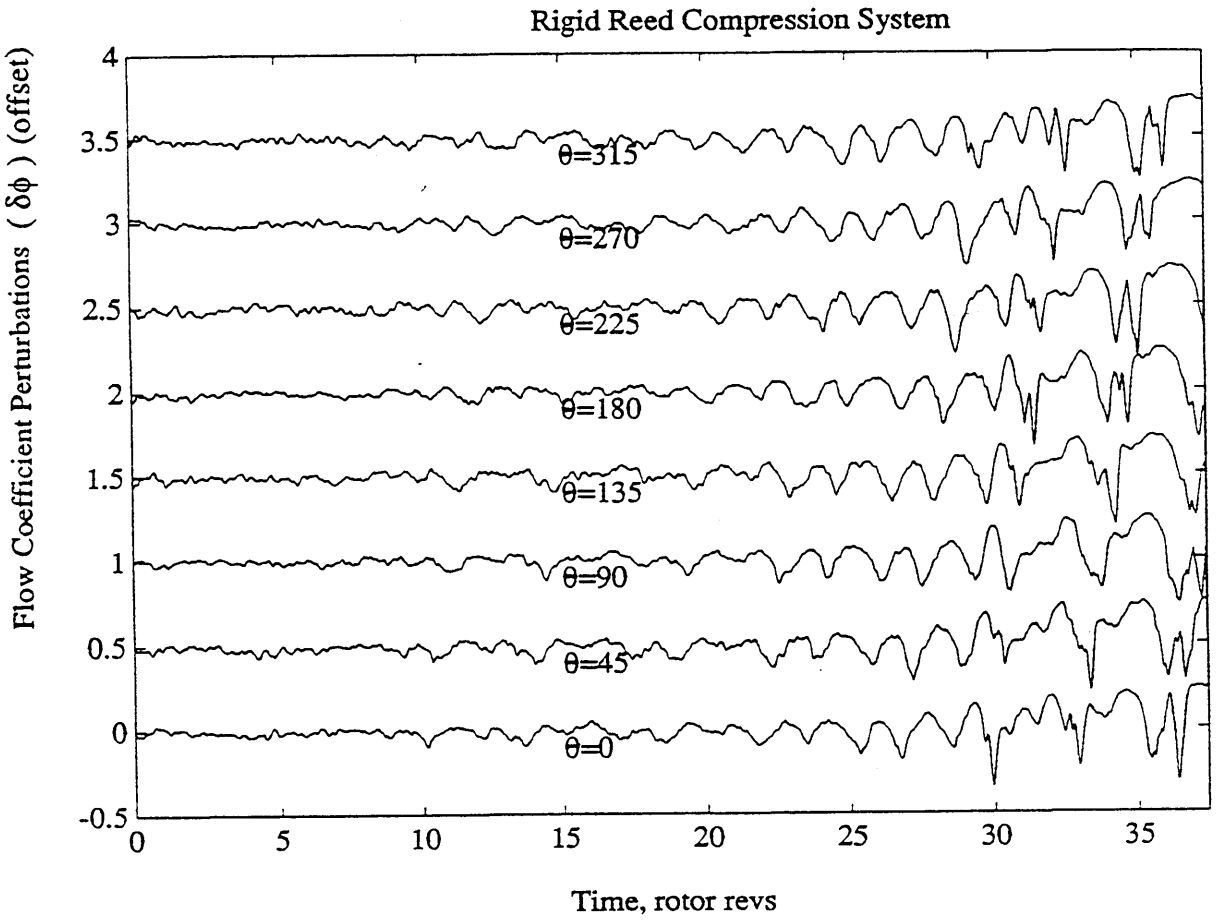

Figure 4.31 Normalized Axial Velocity Perturbations $(\delta C_x / U_R)$ During Stall Inception Process of Rigid Reed Valve Configuration with Optimized Injection Level

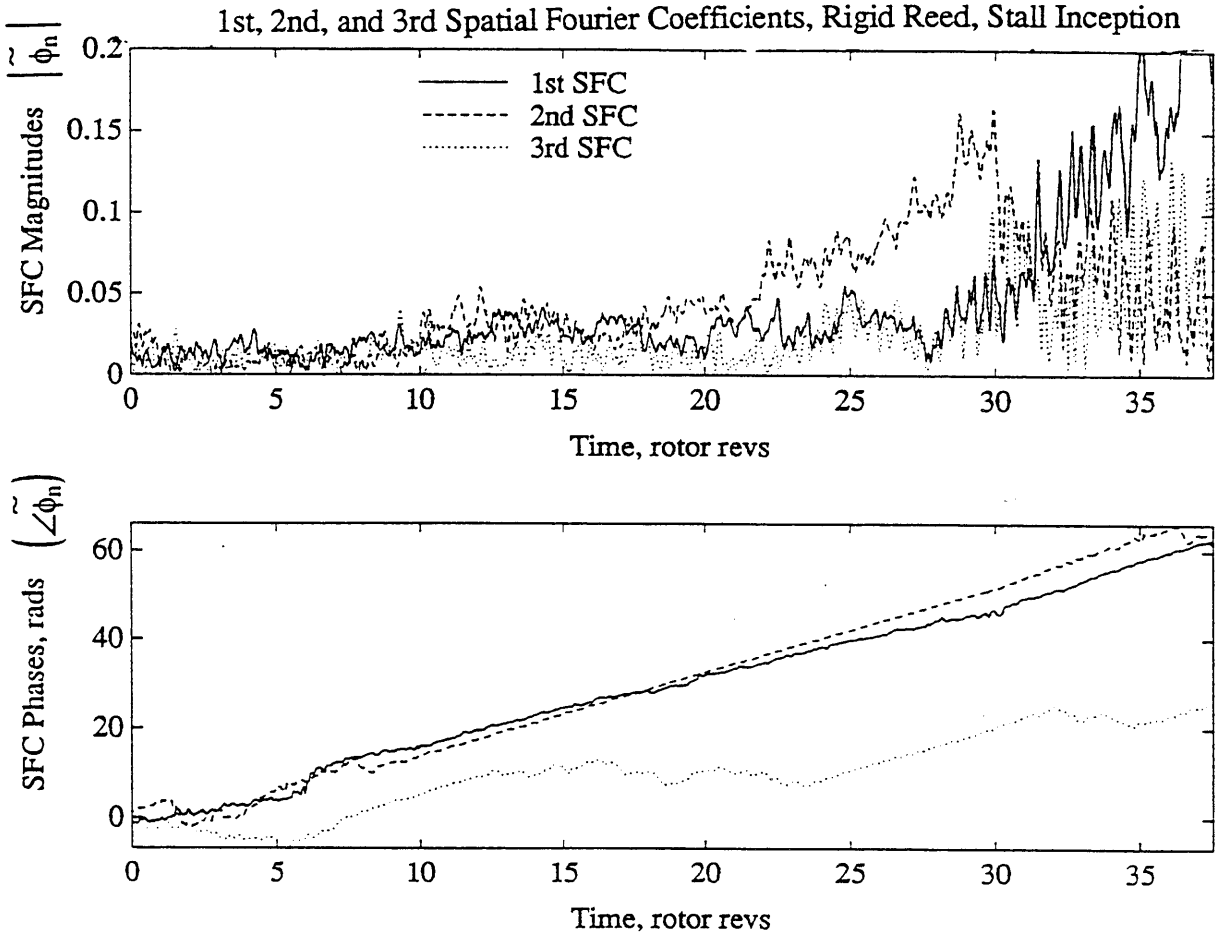

Figure 4.32 Spatial Fourier Decompositon of Normalized Axial Velocity Perturbations During Stall Inception Process of Rigid Reed Valve Configuration with Optimized Injection Level

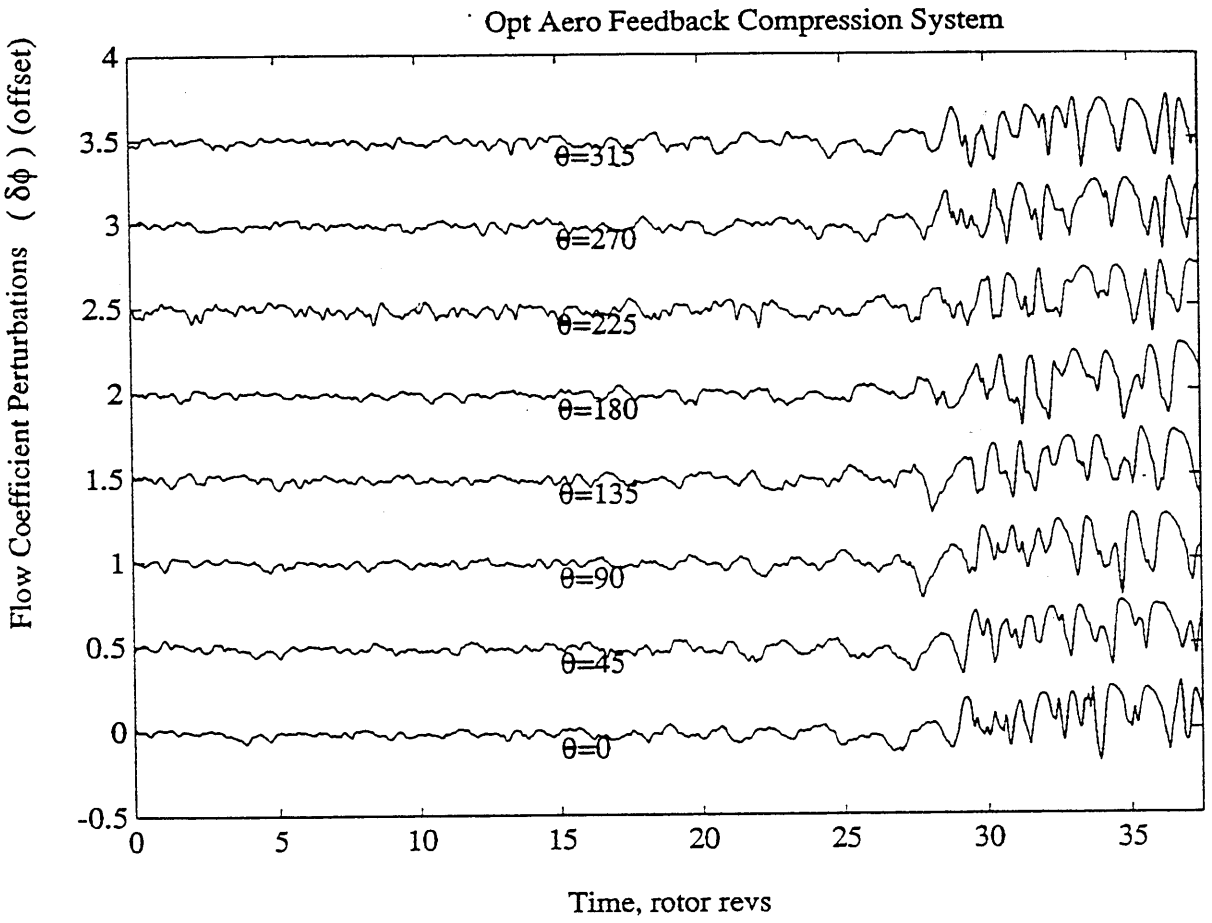

Figure 4.33 Normalized Axial Velocity Perturbations $(\delta C_x / U_R)$ During the Stall Inception Process of Optimized Configuration

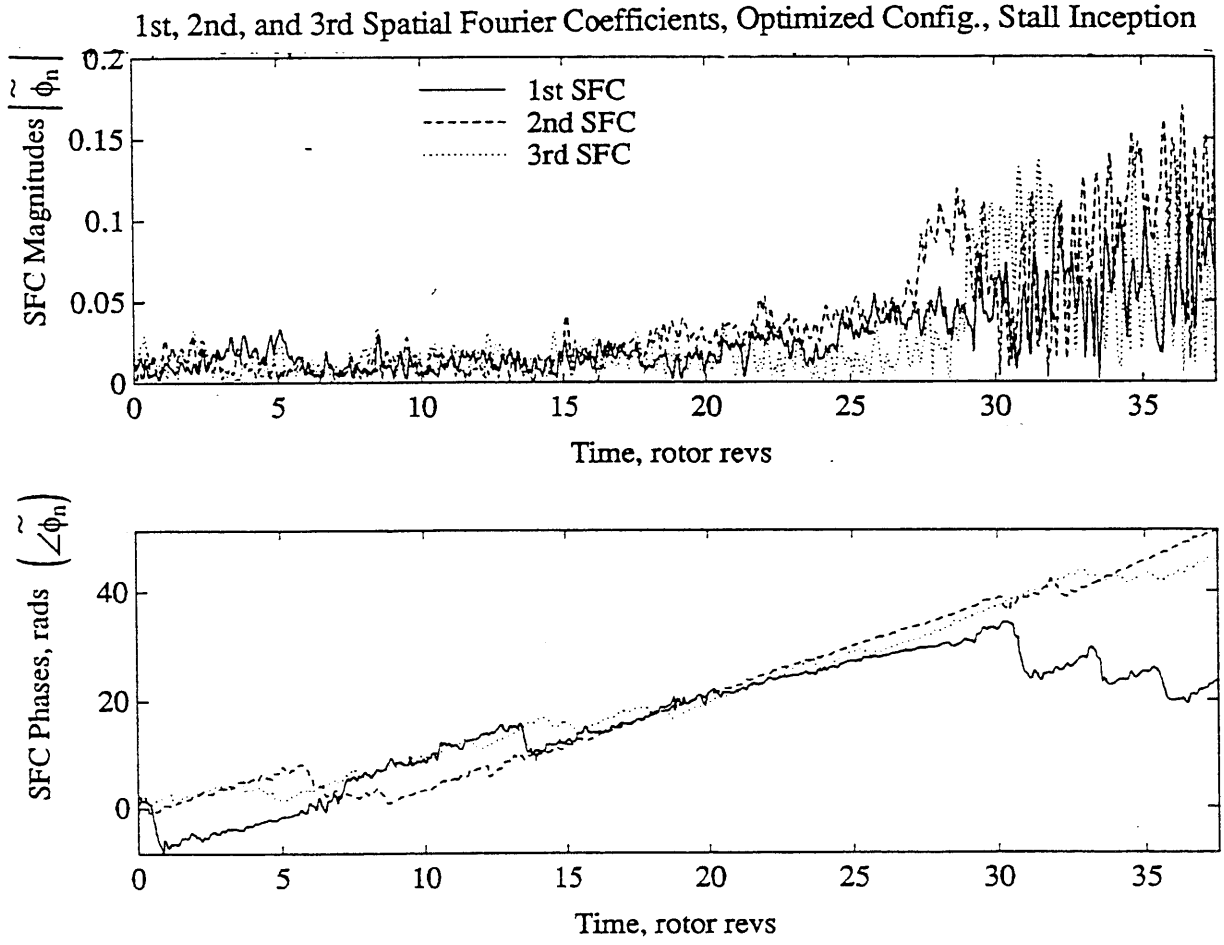

Figure 4.34 Spatial Fourier Decompositon of Normalized Axial Velocity Perturbations During the Stall Inception Process of Optimized Configuration

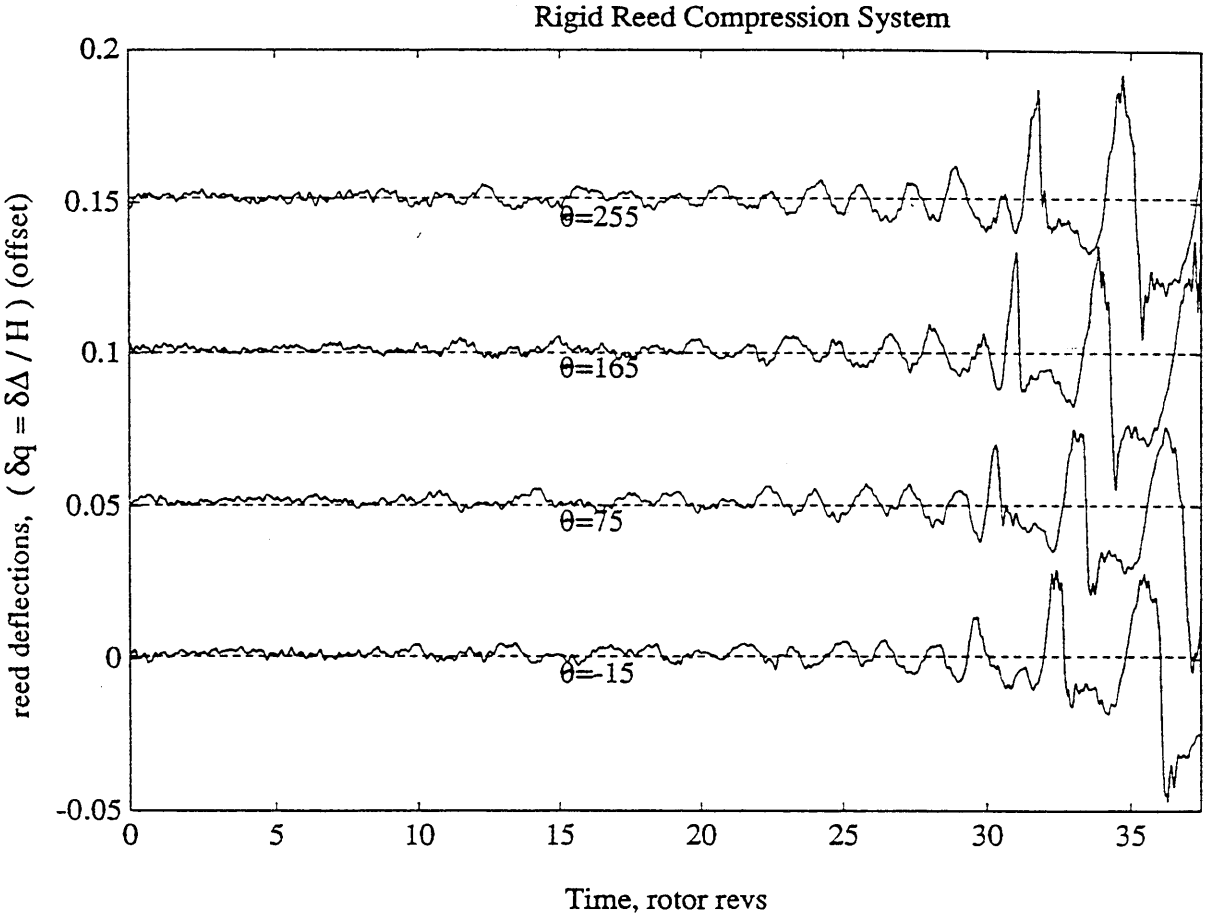

Figure 4.35 Time Resolved, Normalized Reed Valve Deflections ($\delta\Delta$ / H) for the Rigid Reed Valve Configuration with Optimized Injection Level During Stall Inception

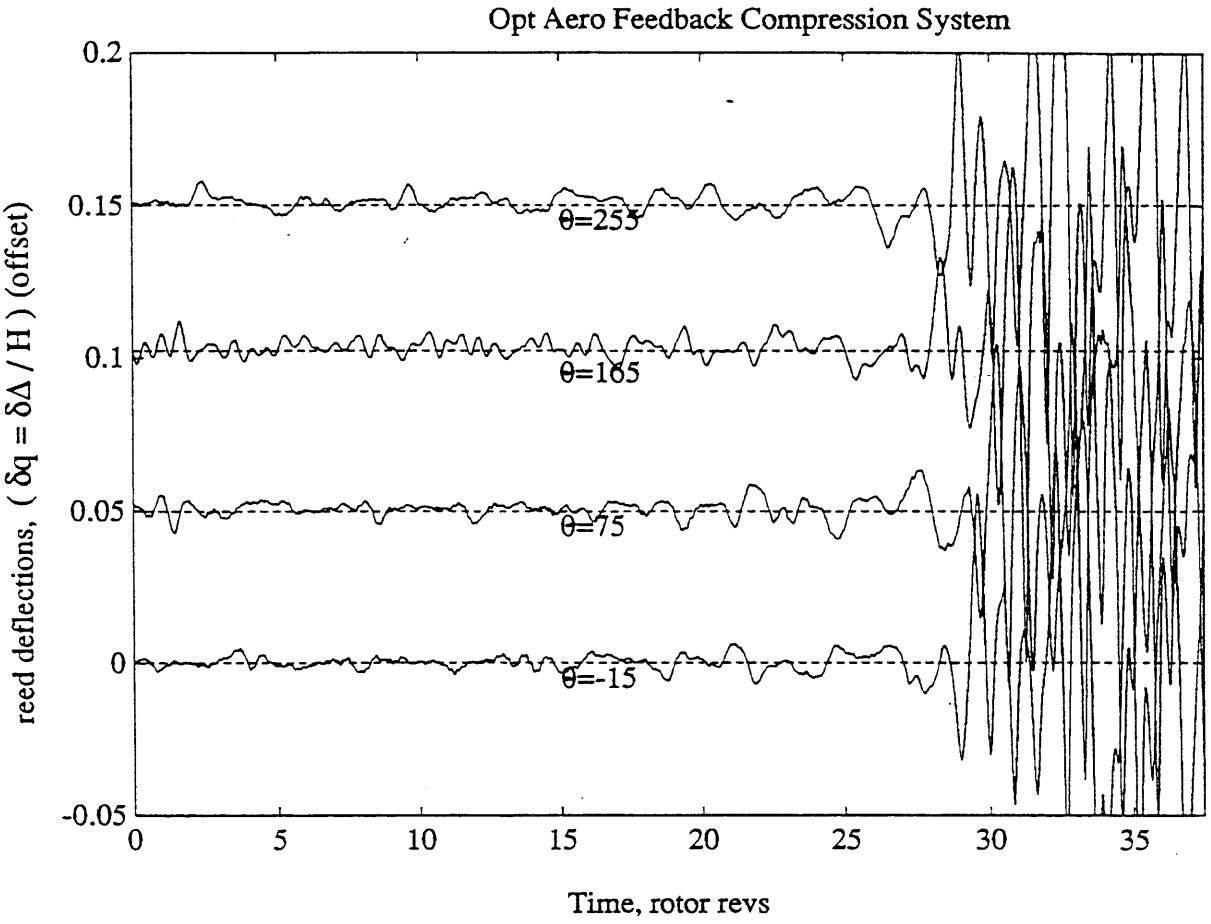

Figure 4.36 Time Resolved, Normalized Reed Valve Deflections ($\delta\Delta$ / H) for the Optimized Configuration During Stall Inception

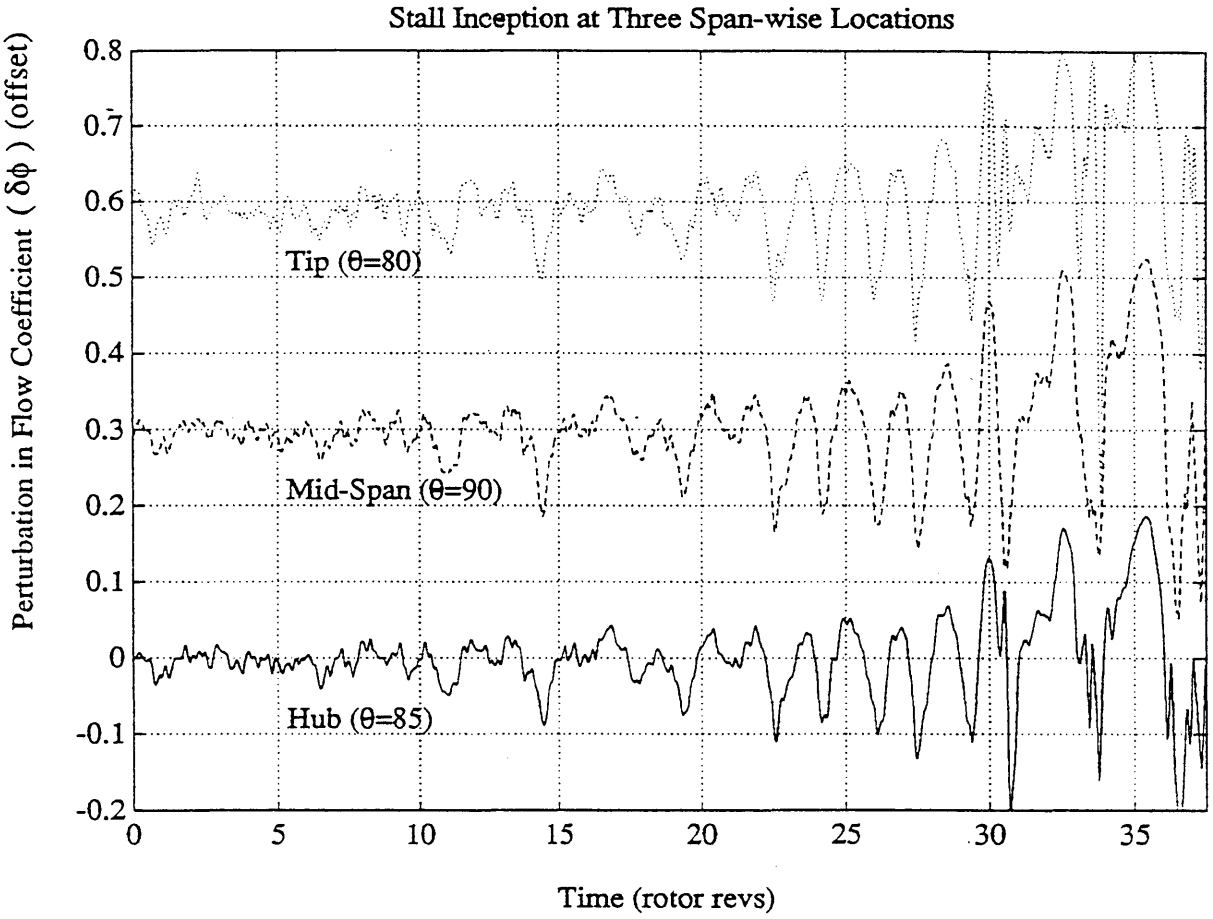

Figure 4.37 Normalized Axial Velocity Perturbations $(\delta C_x / U_R)$ From Three Closely Spaced Hot-Wires at 15%, 50%, and 85% Span-wise Immersion During Stall Inception of the Rigid Reed Valve Configuration with Optimized Injection Level

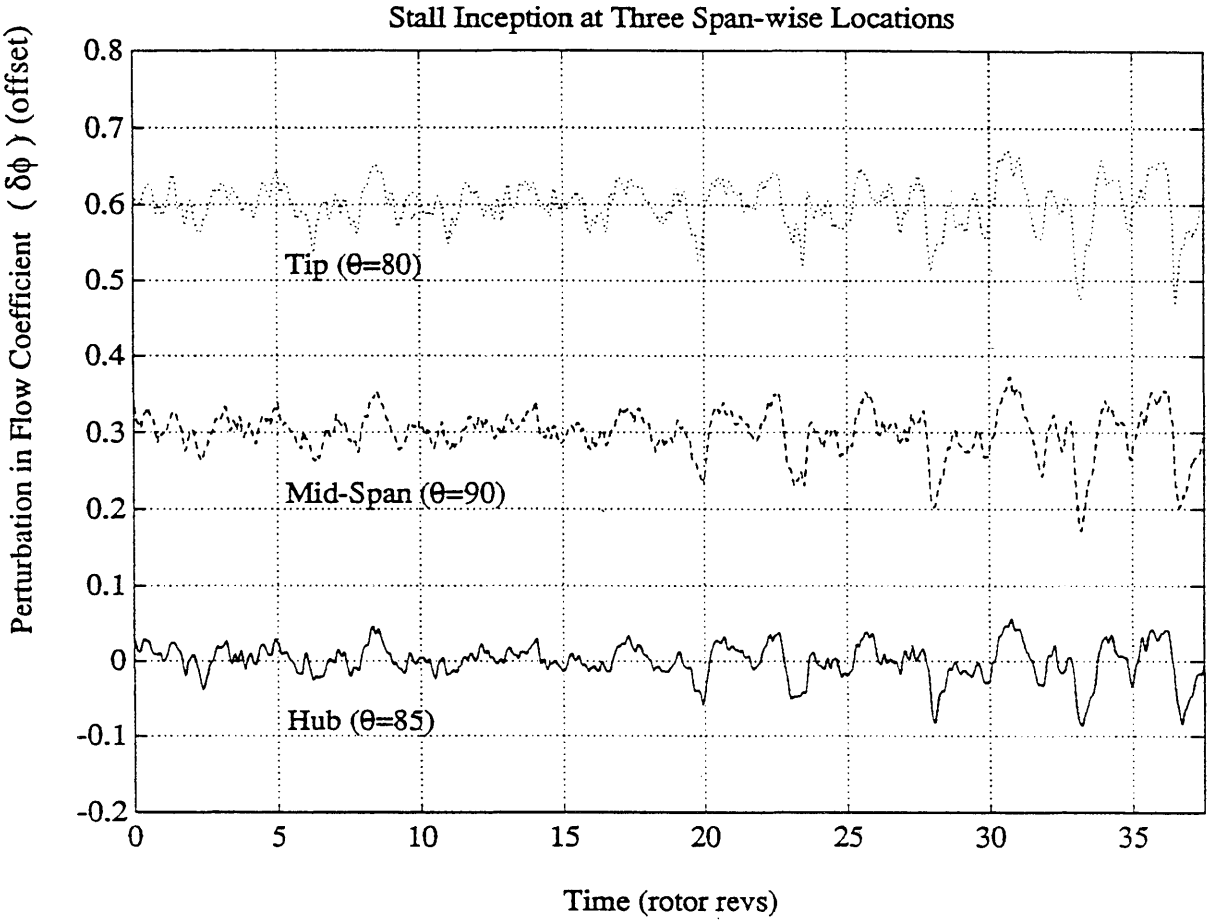

Figure 4.38 Normalized Axial Velocity Perturbations $(\delta C_x / U_R)$ From Three Closely Spaced Hot-Wires at 15%, 50%, and 85% Span-wise Immersion During Stall Inception of Near Optimized Configuration (Φ_i=1.0, ζ= 0.35)

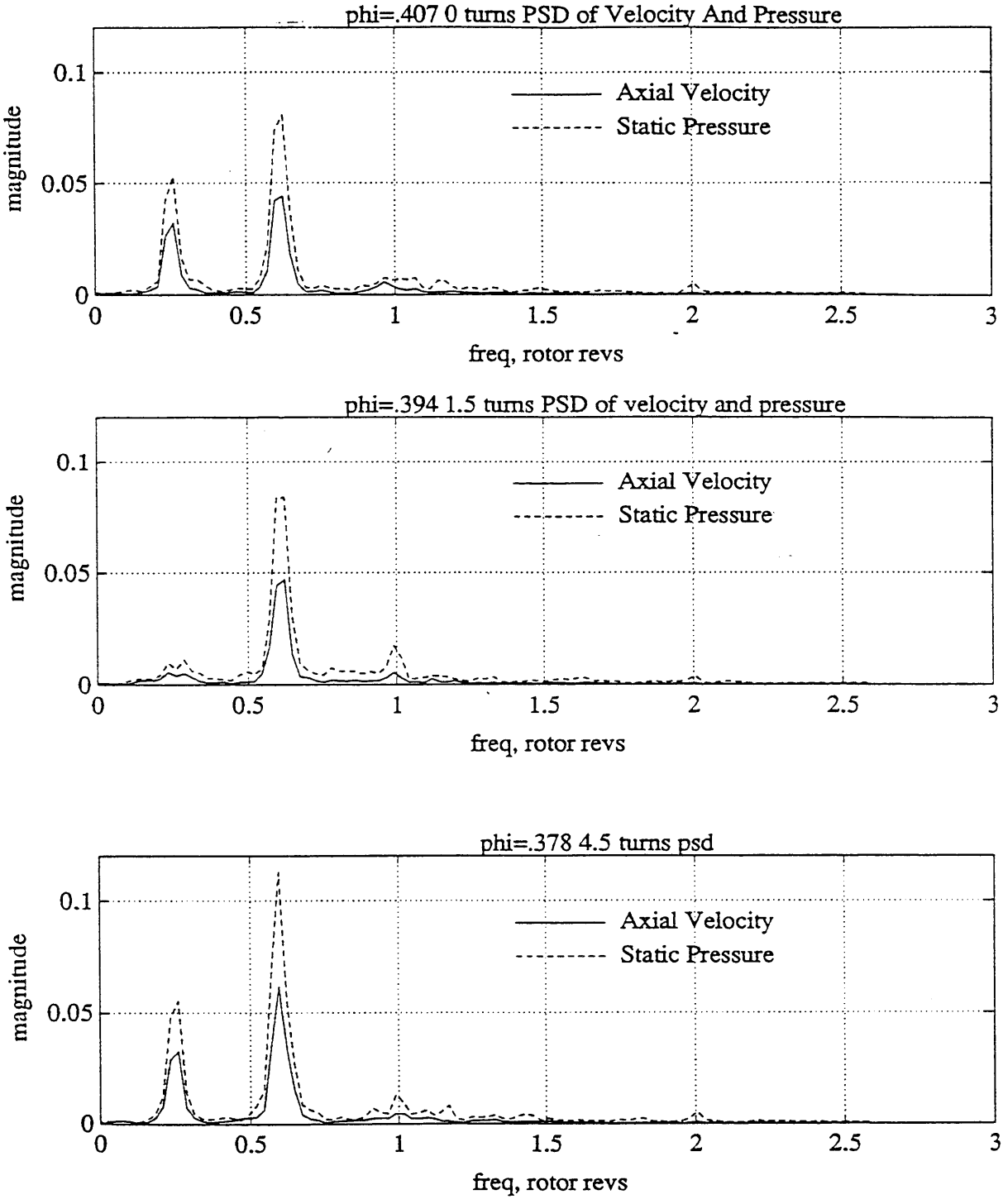

Figure 4.39a PSD's of Normalized Static Pressure and Axial Velocity Perturbations for the Compression System with the Optimized Injection Levels for Three Dashpot Settings Operating Near the Stalling Flow Coefficient

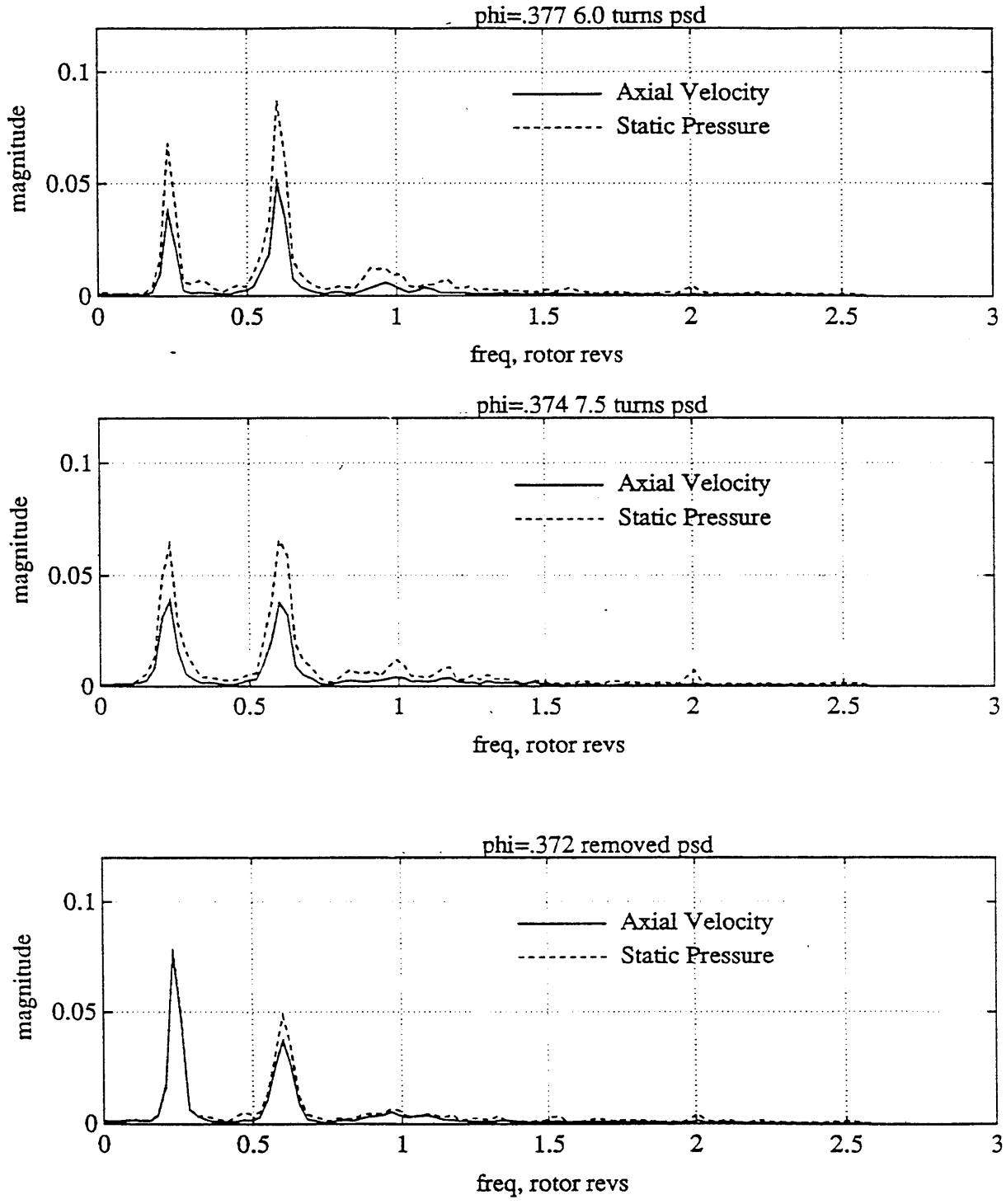

Figure 4.39b PSD's of Normalized Static Pressure and Axial Velocity Perturbations for the Compression System with the Optimized Injection Levels for Three Dashpot Settings Operating Near the Stalling Flow Coefficient

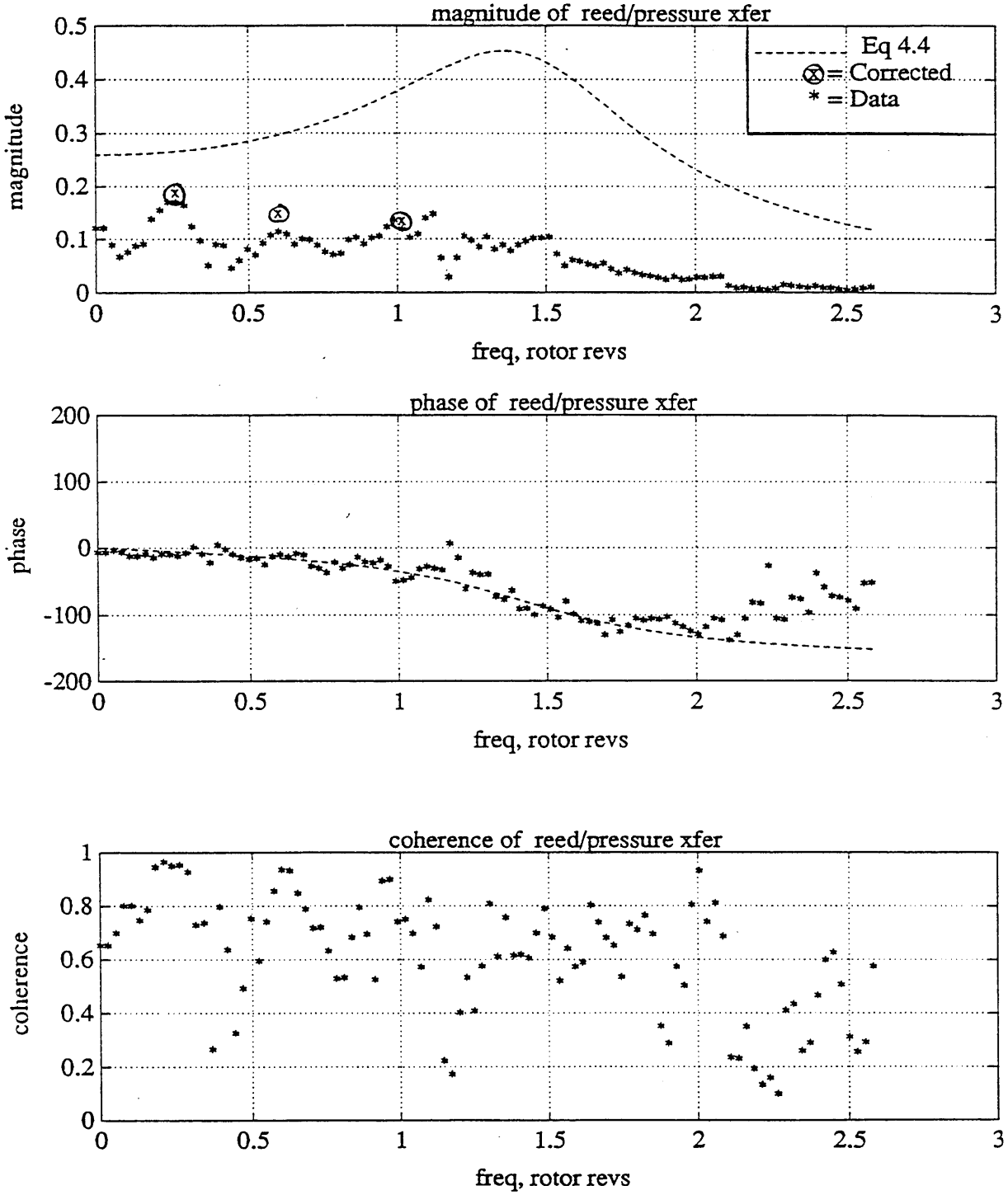

Figure 4.40 Magnitude and Phase of Normalized Reed Valve Deflection / Static Pressure Transfer Function $(\delta q / \delta p)$ with Coherence Function for the Optimized Configuration Operating Near Stall

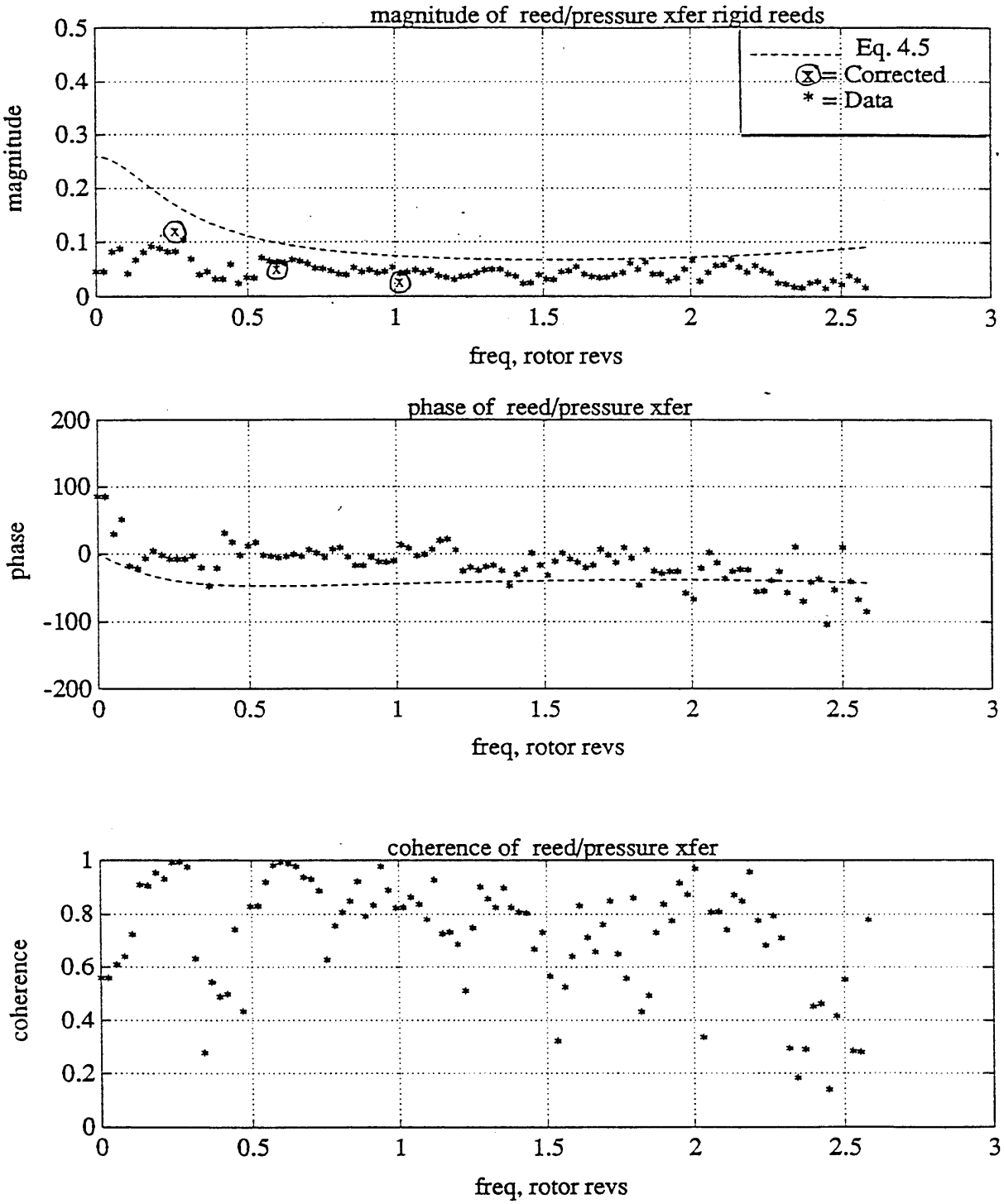

Figure 4.41 Magnitude and Phase of Normalized Reed Valve Deflection / Static Pressure Transfer Function $(\delta q / \delta p)$ with Coherence Function for the Rigid Reed Configuration with Optimized Injection Level Operating Near Stall

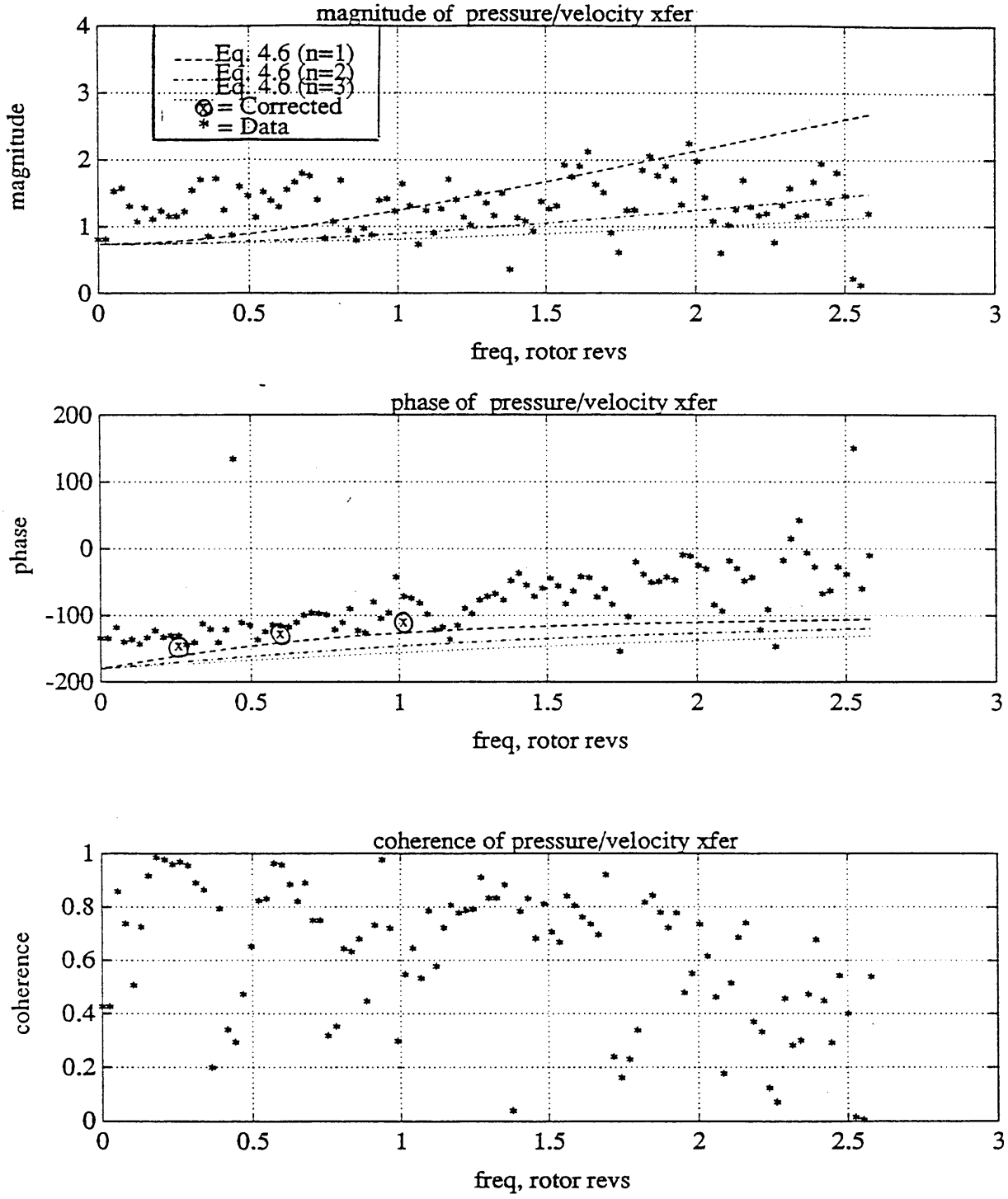

Figure 4.42 Magnitude and Phase of Normalized Static Pressure / Axial Velocity Transfer Function $(\delta p / \delta \phi)$ with Coherence Function for the Optimized Configuration Operating Near Stall

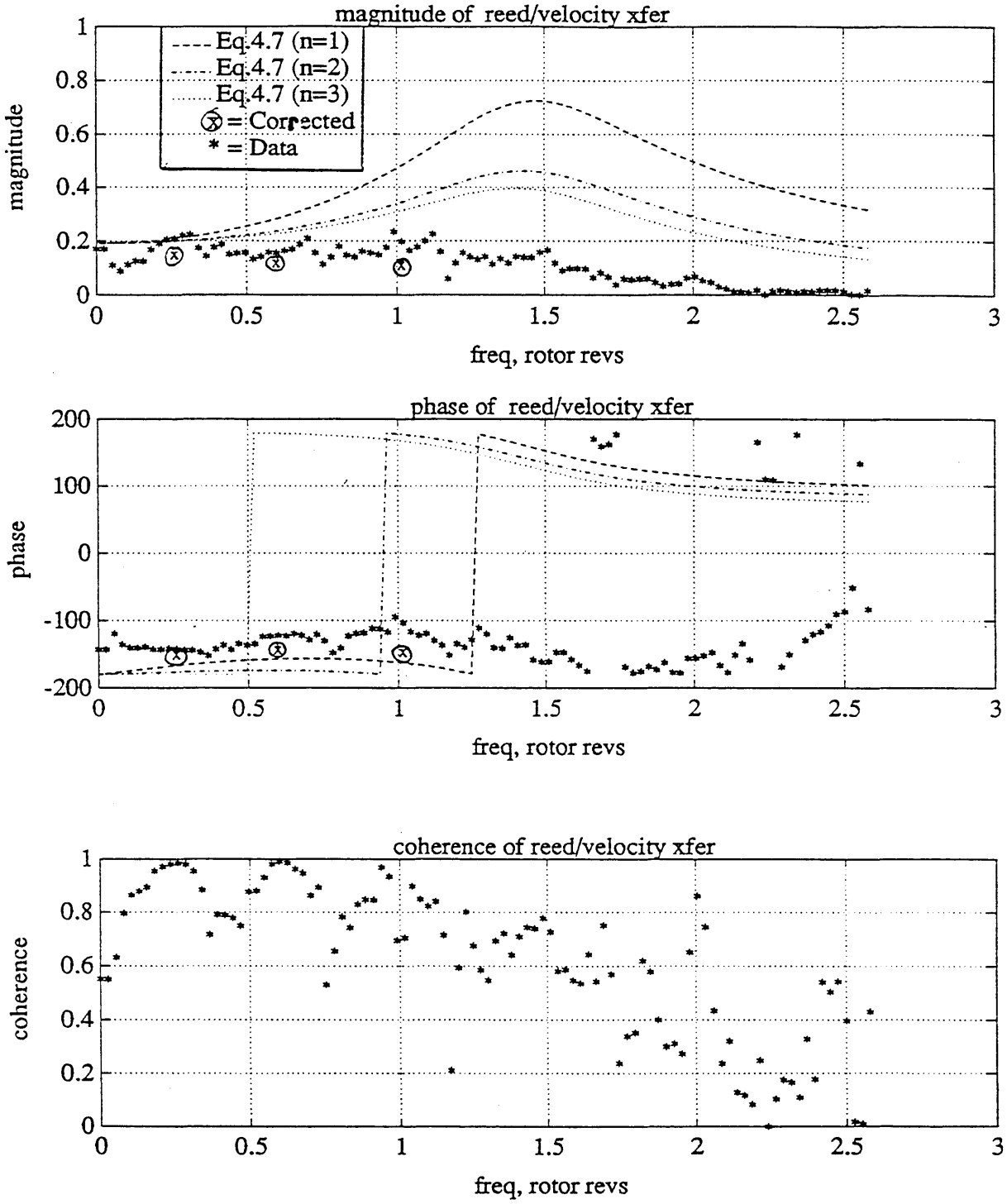

Figure 4.43 Magnitude and Phase of Normalized Reed Valve Deflection / Axial Velocity Transfer Function $(\delta q / \delta \phi)$ with Coherence Function for the Optimized Configuration Operating Near Stall

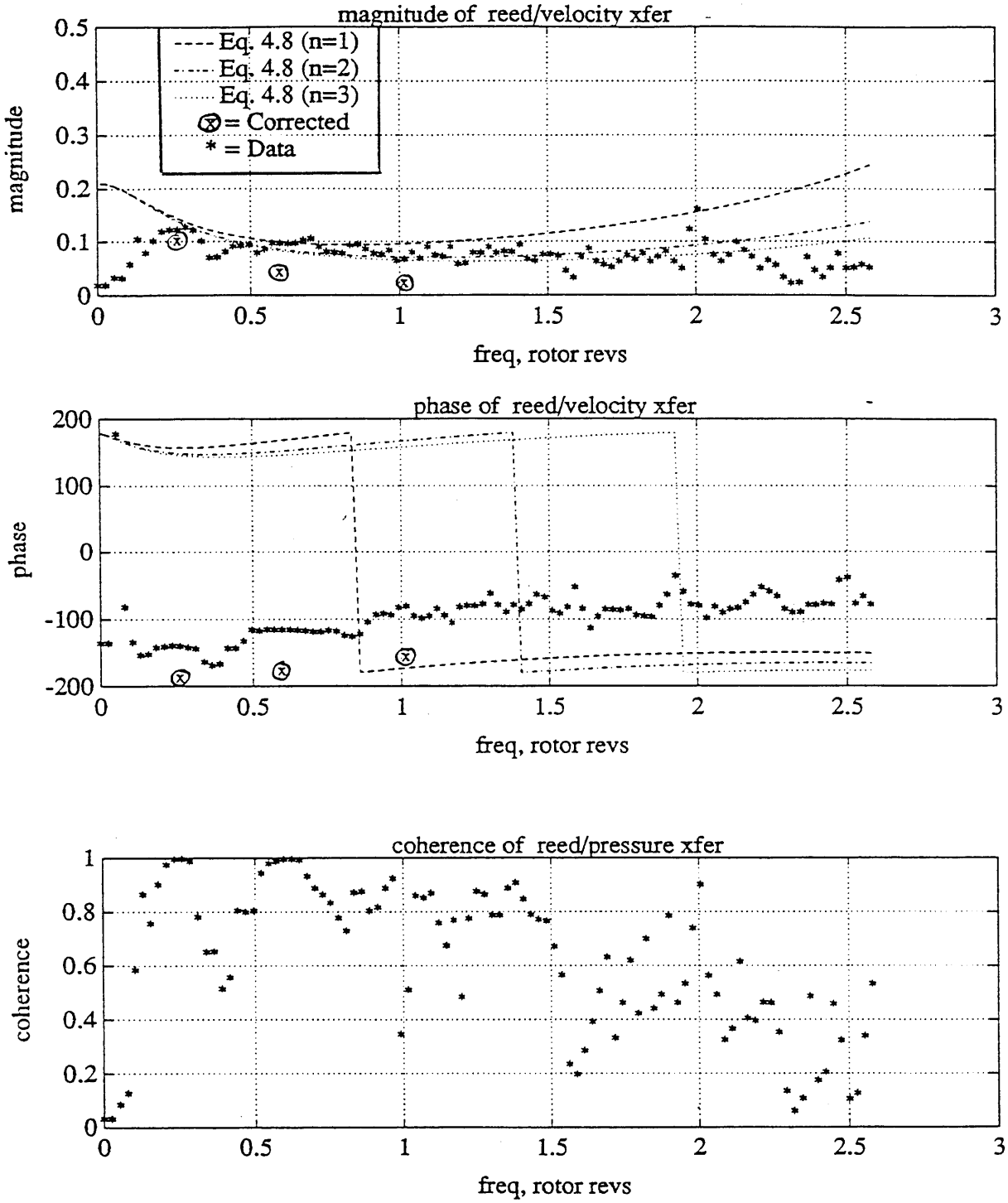

Figure 4.44 Magnitude and Phase of Normalized Reed Valve Deflection / Axial Velocity Transfer Function $(\delta q / \delta \phi)$ with Coherence Function for the Rigid Reed Configuration Near Stall

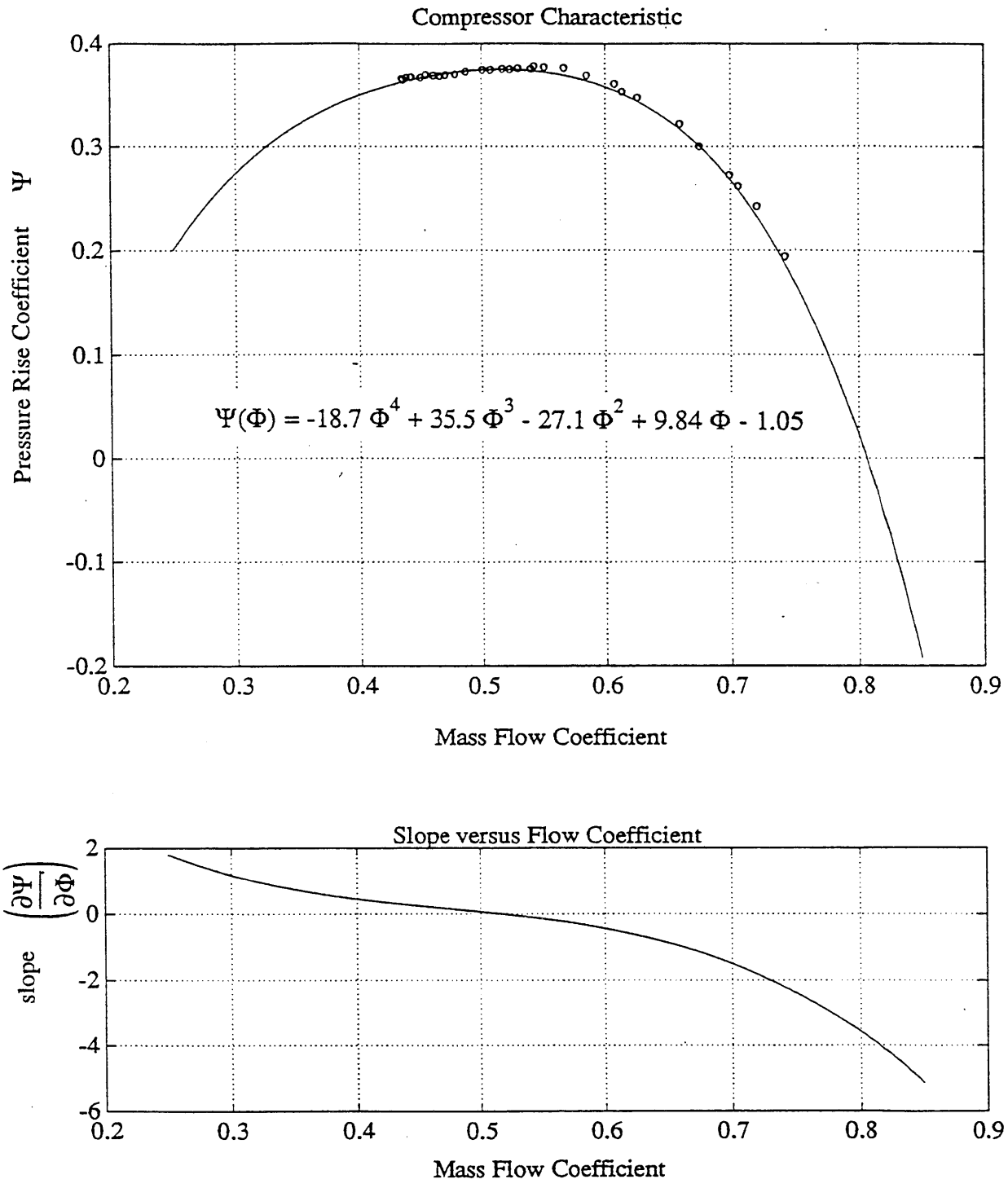

Figure 4.45 Fourth Order Polynominal Curve Fit of the Experimentally Determined Pressure Rise Coefficient $\left(P_{s_d} - P_{t_u} / \frac{1}{2} \rho U_R^2\right)$ versus Flow Coefficient $\Phi = C_x / U_R$ Constant Speed Compressor Characteristic for the Basic Compressor System (with Slope vs. Flow Coefficient also shown)

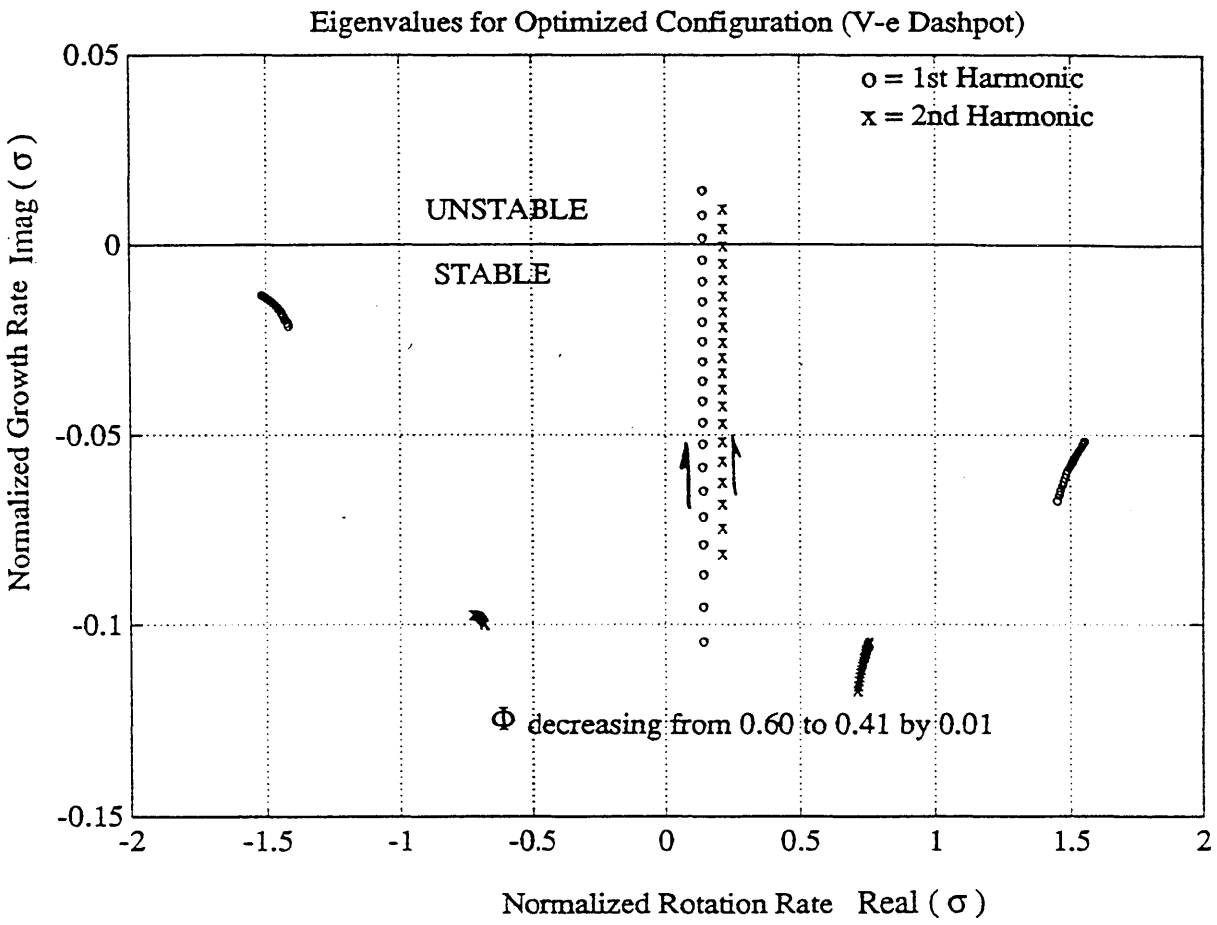

Figure 4.46 Eigenvalues of First and Second Spatial Harmonics Parameterized by Flow Coefficient for the Compression System with the Experimentally Determined, Optimized Control Parameters
($W = 3.5$, $Q = 1.5$, $\zeta = 0.3$, $\Phi_i = 1.0$) with ($\lambda = 1.0$ and $\mu = 2.0$)

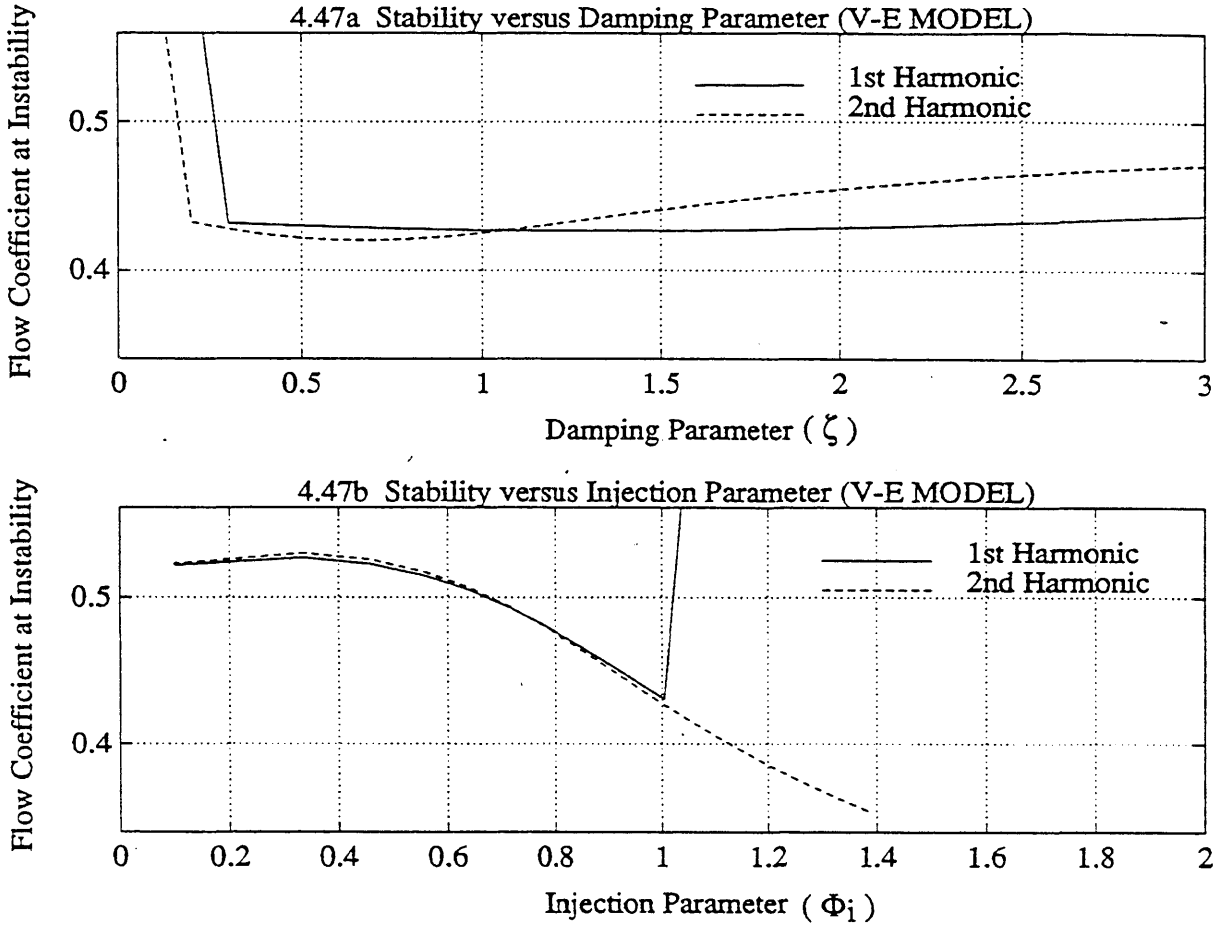

Figure 4.47 Predicted Flow Coefficient at Neutral Stability for the First and Second Spatial Harmonics of the Experimentally Optimized Configuration as a Function of (a) Damping Ratio Parameter and (b) Injection Parameter Using Visco-Elastic Dashpot Model

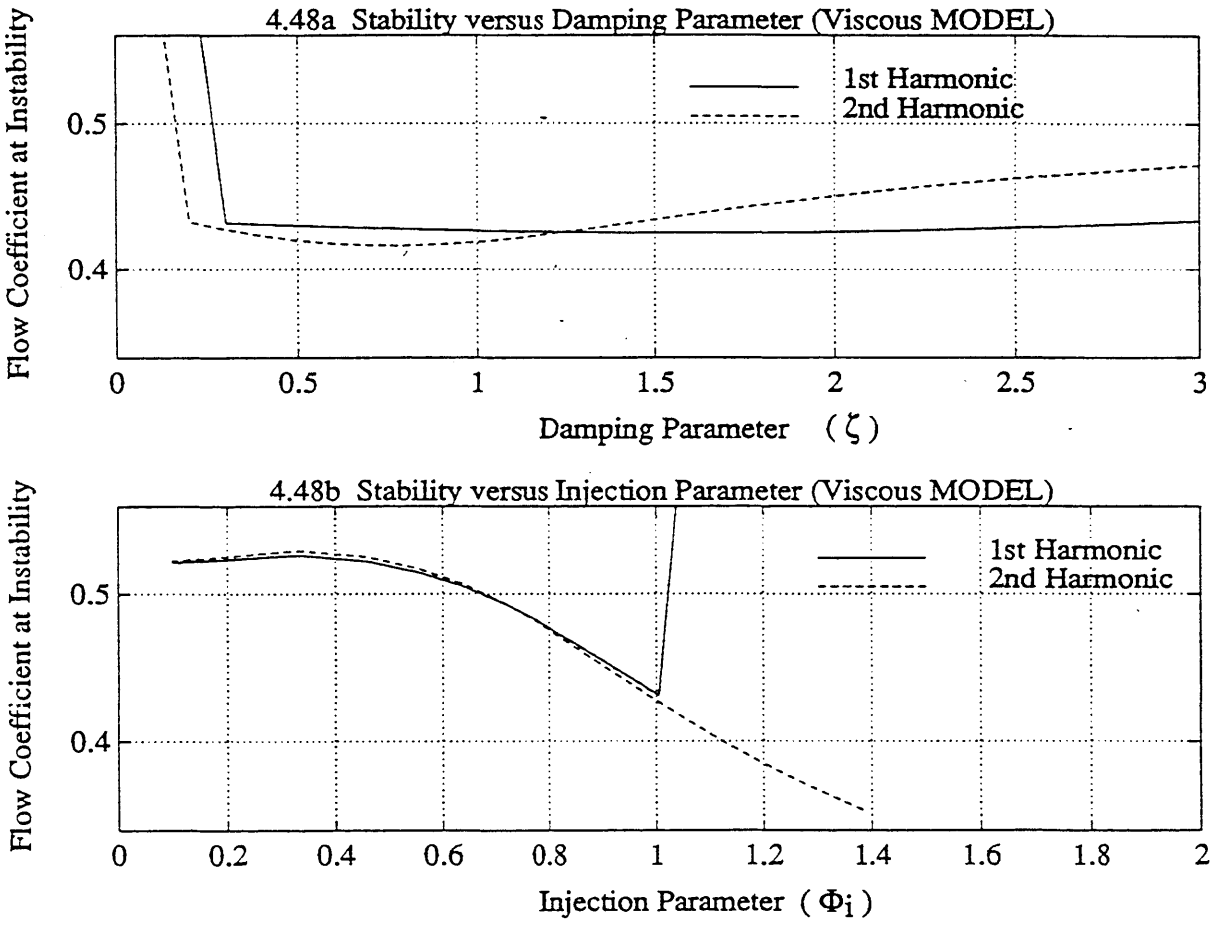

Figure 4.48 Predicted Flow Coefficient at Neutral Stability for the First and Second Spatial Harmonics of the Experimentally Optimized Configuration as a Function of (a) Damping Ratio Parameter and (b) Injection Parameter Using Viscous Dashpot Model

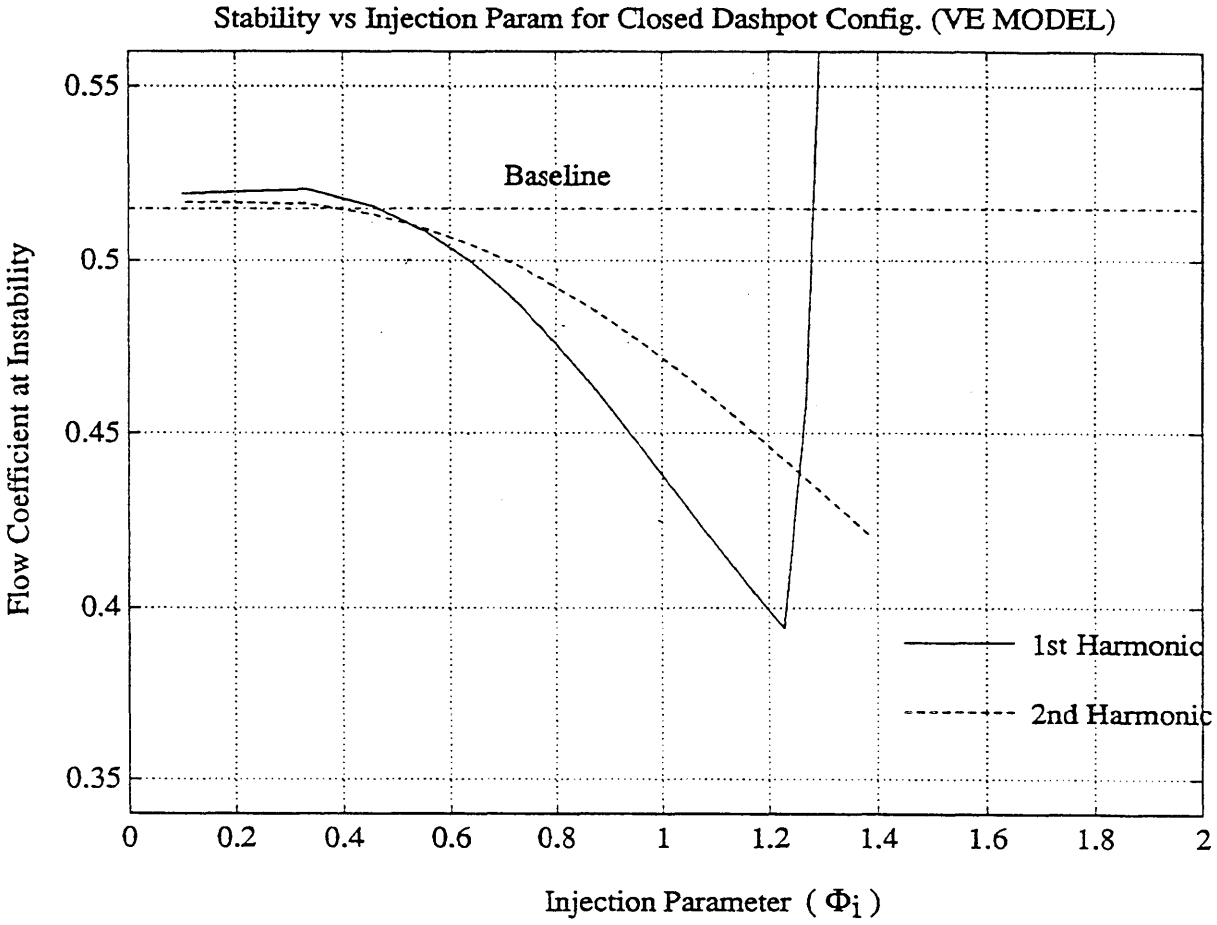

Figure 4.49 Predicted Flow Coefficient at Neutral Stability for the First and Second Spatial Harmonics of the Rigid Reed Valve Configuration with Injection as a Function of the Injection Parameter in the Visco-Elastic Dashpot Model

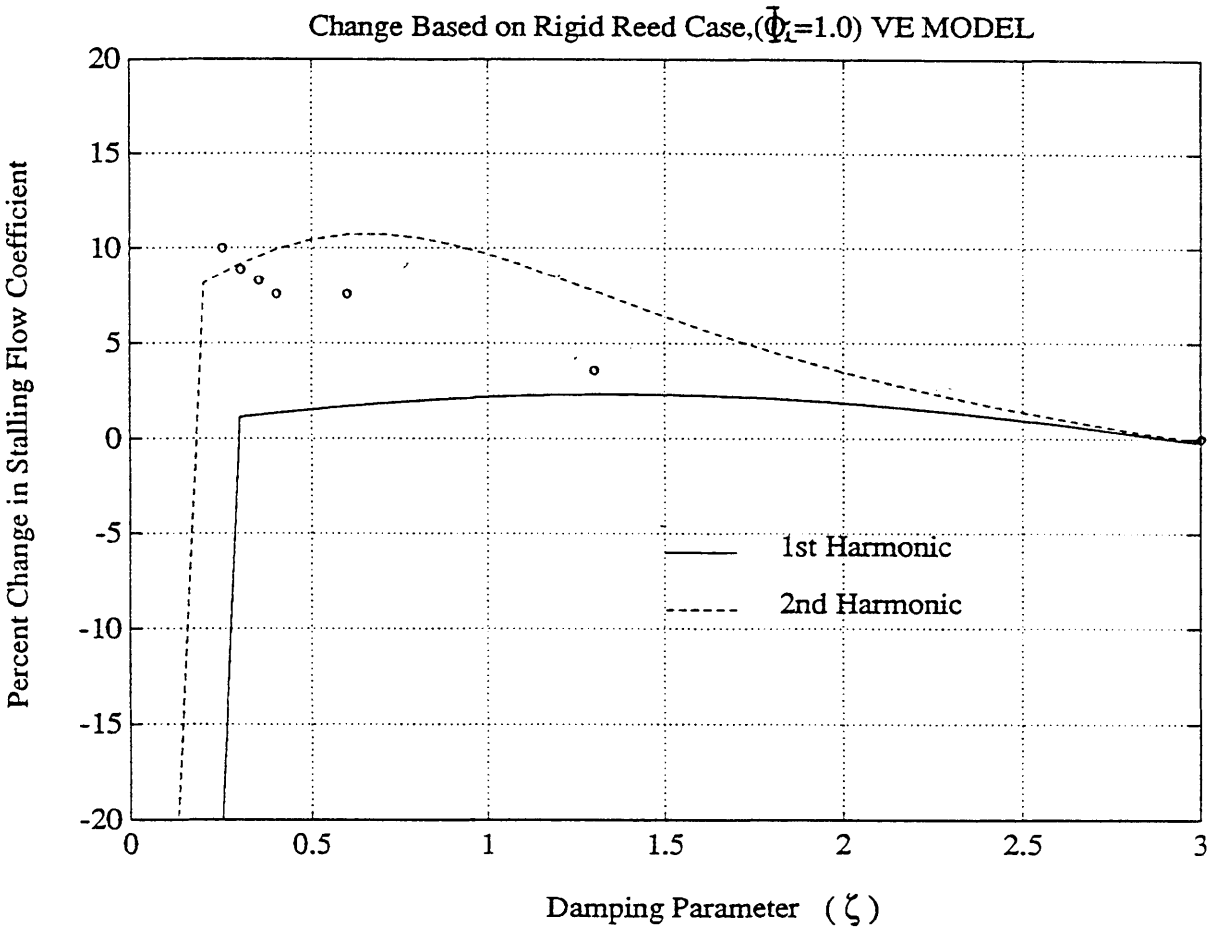

Figure 4.50 Experimentally Determined Change in Stalling Flow Coefficient, as a Function of Damping Parameter, based on Rigid Reed Configuration, for Φ_i = 1.0 with the Predicted Change in Mass Flow Coefficient at Instability for the First and Second Spatial Harmonics also Shown

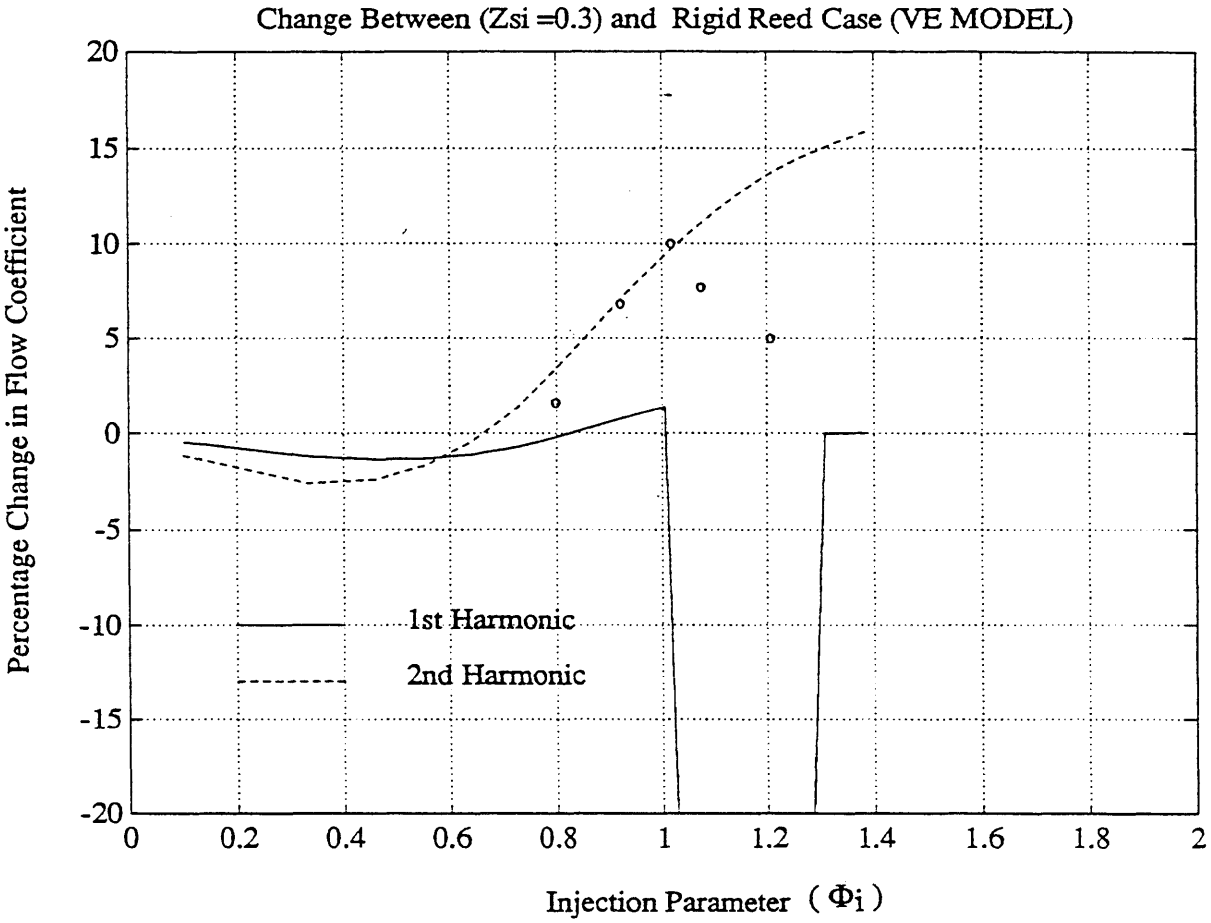

Figure 4.51 Experimentally Determined Change in Stalling Flow Coefficient as a Function of the Injection Parameter between the Optimized Damping Parameter (ζ=0.3) and the Rigid Reed Configuration (ζ=3.0) with the Predicted Change in Mass Flow Coefficient at Instability for the First and Second Spatial Harmonics also Shown

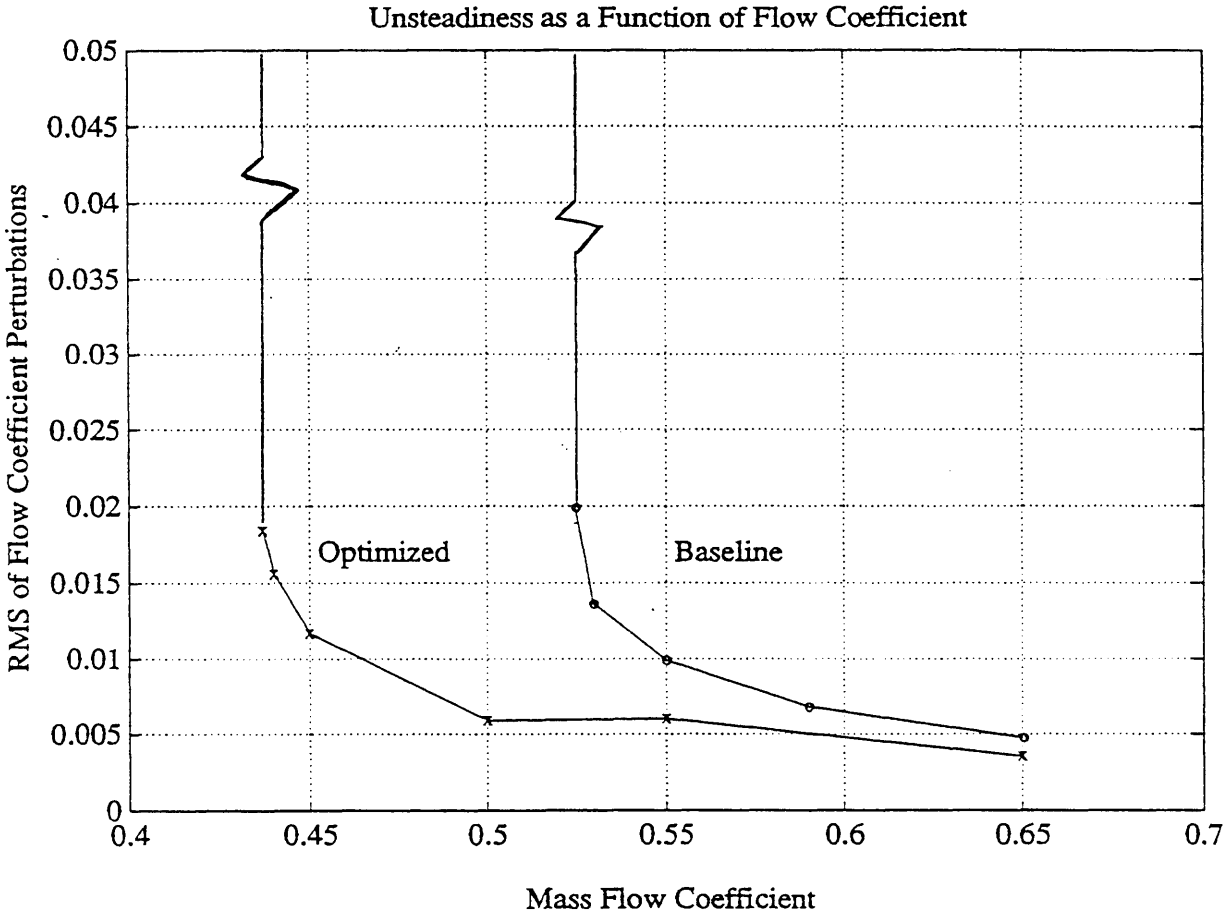

Figure 4.52 RMS of Normalized Axial Velocity Perturbations $(\delta C_x / U_R)$ Predicted by Non-Linear Simulation as a Function of Mean Mass Flow Coefficient for the Basic Compression System and the Optimized Configuration

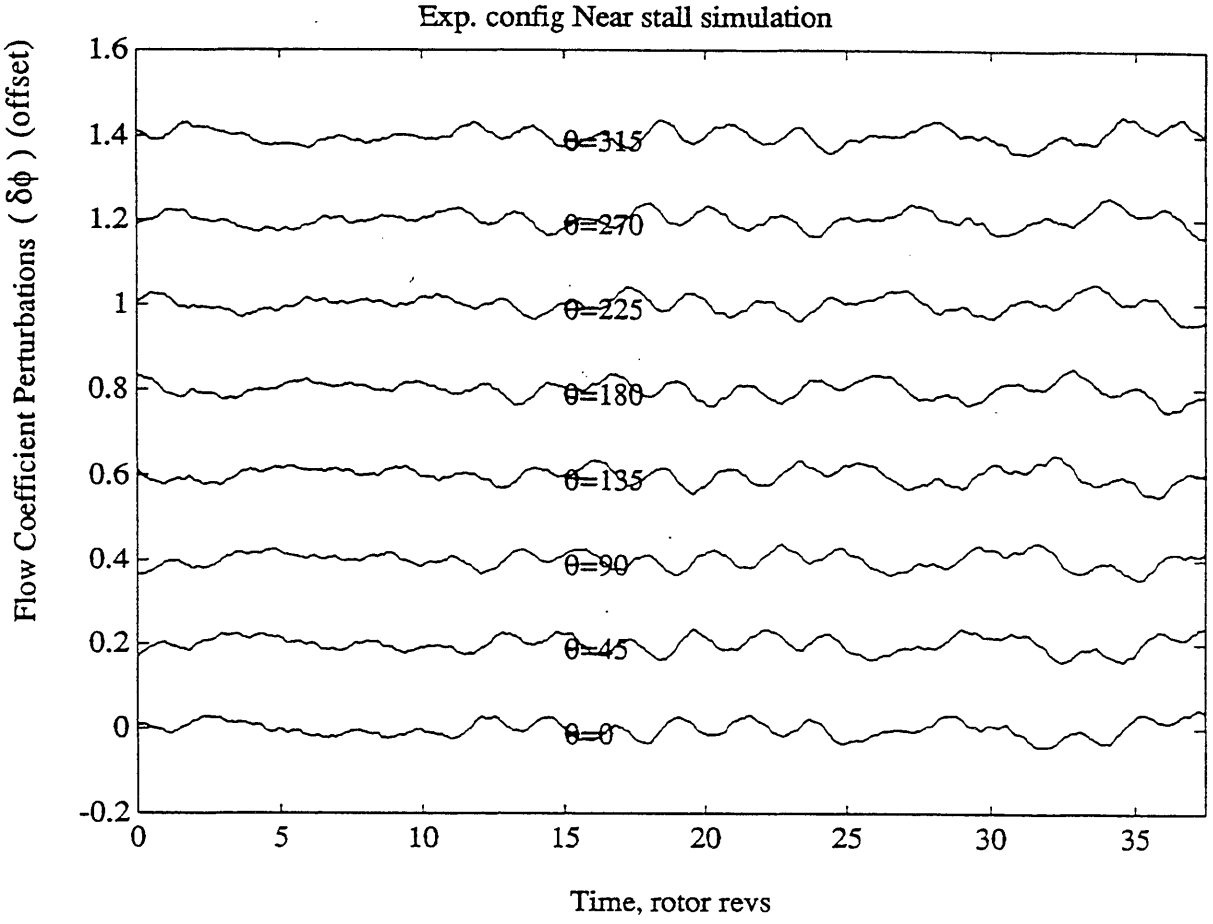

Figure 4.53 Simulated, Normalized Axial Velocity Perturbations $(\delta C_x / U_R)$ for the Optimized Configuration Operating Near Stall at $\Phi = 0.44$, with Noise Model

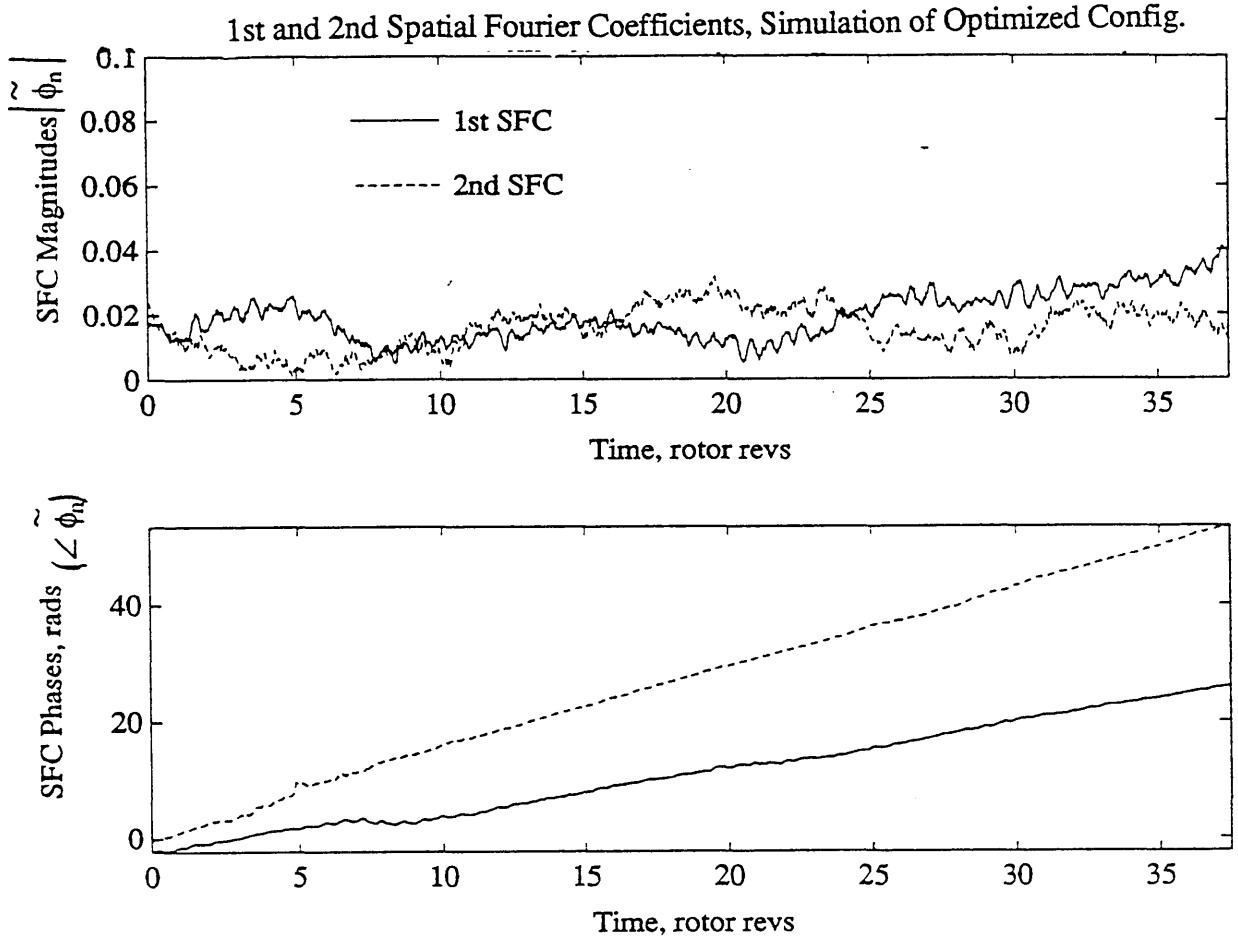

Figure 4.54 Spatial Fourier Decomposition of Simulated, Normalized Axial Velocity Perturbations $(\delta C_x / U_R)$ for Optimized Configuration Operating Near Stall at $\Phi = 0.44$ with Noise Model

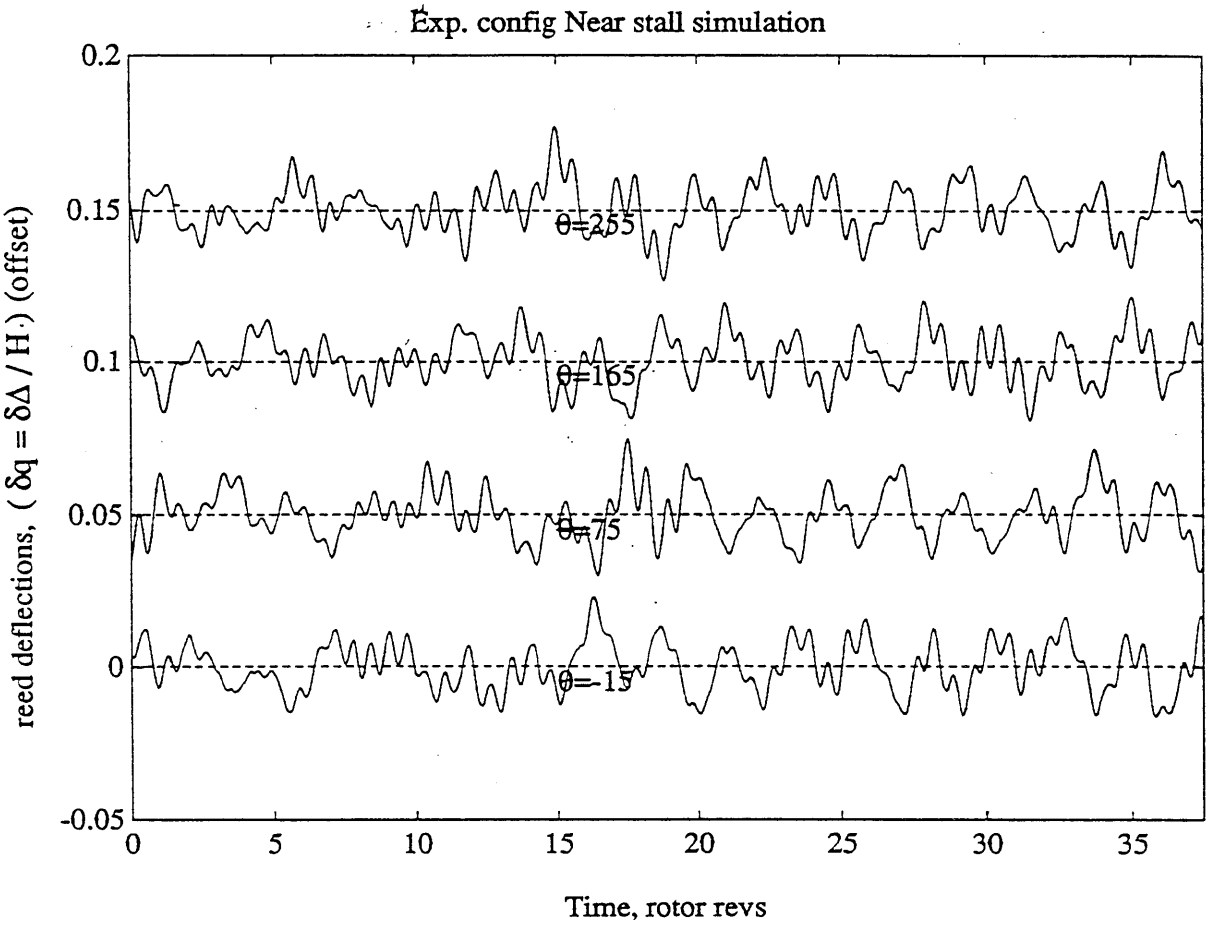

Figure 4.55 Simulated, Normalized Reed Valve Deflections ($\delta\Delta$ / H)for Optimized Configuration Operating Near Stall at $\Phi = 0.44$ with Noise Model

Chapter 5: One-Dimensional Acoustic Oscillations in Compression Systems

5.1 Introduction

The primary focus of this research was on control of the multi-dimensional instability associated with rotating stall. To avoid one-dimensional (annulus averaged) oscillations, a compression system with a low B-parameter ($B < 0.1$) was used in the experimental investigation. One-dimensional, surge type oscillations were designed to be stable over all operating conditions of interest. In spite of this, disturbances inconsistent with a multi-dimensional, incompressible model of the flow field were observed when the compression system , as originally configured, was stabilized using aeromechanical feedback. No such oscillations were observed in the compression system when operated away from the stalling flow coefficient.

These disturbances are described in this chapter. They are shown to be associated with one-dimensional acoustic oscillations within the compression system. An acoustic model of the compression system is presented to identify the parameters that influence the acoustic behavior. Based on conclusions drawn from the analytical model, the acoustic parameters of the compression system were modified to effectively eliminate the acoustic oscillations for the operating range of the compression system investigated.

5.2 Experimental Measurements

Figure 5.1 shows PSD's of the static pressure and axial velocity perturbations (recorded simultaneously) for the original configuration of the compression system operating near the stalling flow coefficient at $\Phi = 0.354$. The aeromechanical control parameters were $W = 3.5$, $Q = 1.5$, $\zeta = 0.35$, and $\Phi_i = 1.2$. The hot-wire and wall static pressure transducer were approximately 1/3 chord upstream of the rotor and were closely spaced in the

circumferential direction. There is a peak in the PSD of the pressure signal at 75% of the rotor frequency (28 Hz), but no correspondingly large peak at this frequency in the PSD of the axial velocity disturbances.

The magnitude of the transfer function between the pressure and velocity measurements is also shown in Figure 5.1. The predicted transfer function, based on the two-dimensional incompressible flow field model (see Eq.4.6) for the first three spatial harmonics (n = 1,2, and 3), is shown in Figure 5.1. The magnitude of the predicted transfer function is qualitatively consistent with the data except for frequencies near 75% of the rotor frequency, where the magnitude of the transfer function is an order of magnitude larger than that predicted by the two-dimensional, incompressible theory.

Further investigation revealed that the spatial mode shape, as well as the temporal frequency, of the oscillations were both consistent with a one-dimensional acoustic oscillation roughly corresponding to a quarter wave length organ pipe mode of the compression system. The PSD of the pressure oscillations thus appeared to represent an under-damped acoustic oscillation being excited by random noise.

5.3 Overview of Acoustic Model

To investigate these oscillations and to assess the role of compression system parameters on their generation, a one-dimensional acoustic analysis of the compression system was developed. In this section, an outline of the analytical model is presented with the details given in Appendix I. More detailed discussion of analyses of this type is given in references [29] and [30].

The acoustic behavior of the compression system was analyzed using acoustic transmission matrices. Acoustic transmission matrices relate the acoustic state variables across a flow

element, and the matrices can be readily assembled to give a description of a complex system. The format of the transmission matrices used in this thesis is given below.

$$\begin{Bmatrix} p_1 \\ \rho c u_1 \end{Bmatrix} = \begin{bmatrix} T_{11} & T_{12} \\ T_{21} & T_{22} \end{bmatrix} \begin{Bmatrix} p_2 \\ \rho c u_2 \end{Bmatrix} \tag{5.1}$$

where: $p \equiv$ acoustic pressure perturbation, $u \equiv$ acoustic velocity perturbation, and

$T_{ij} \equiv$ Element in Transmission Matrix

Figure 5.2 shows a schematic of the one-dimensional acoustic model of the compression system. The analysis includes models of four acoustic elements that comprise the compression system:

1) the flow field in the upstream duct
2) the compressor, modeled an as actuator disk
3) the flow field in the downstream duct
4) the throttle, also modeled as an actuator disk.

The acoustic behavior of the overall compression system can be modeled by combining the transmission matrices of the individual components to form a single, overall transmission matrix which represents the entire compression system. The overall transmission matrix relates the acoustic state variables upstream of the inlet to the acoustic state variables downstream of the throttle, as a function of frequency and of compression system parameters.

5.3.1 Transmission Matrices of Components

The transmission matrices of the individual components are developed below.

5.3.1.1 Upstream and Downstream Ducts

Solving the one-dimensional convective wave equation in a subsonic, constant area duct with axial flow, as developed in Appendix I, leads to the following transmission matrix for a duct of length L:

$$\begin{Bmatrix} p \\ \rho c u \end{Bmatrix}_{x=-L} = \begin{bmatrix} \frac{1}{2}\left(e^{i k_1 L} + e^{-i k_2 L}\right) & \frac{1}{2}\left(e^{i k_1 L} - e^{-i k_2 L}\right) \\ \frac{1}{2}\left(e^{i k_1 L} - e^{-i k_2 L}\right) & \frac{1}{2}\left(e^{i k_1 L} + e^{-i k_2 L}\right) \end{bmatrix} \begin{Bmatrix} p \\ \rho c u \end{Bmatrix}_{x=0} \tag{5.2}$$

where: $$k_1 \equiv \frac{\omega}{c}\frac{1}{1+M_x} \quad ; \quad k_2 \equiv \frac{\omega}{c}\frac{1}{1-M_x}$$

5.3.1.2 The Compressor

The acoustic oscillations observed in the experiment were on the order of 30 Hz. This corresponded to a reduced frequency based on the frequency of the oscillation, the chord of the blading, and the rotor speed, of roughly 0.1. Therefore, the compressor was assumed to respond to the acoustic oscillations in a quasi-steady manner. Since the single stage compression system was operated at low speed, $M_R \approx 0.2$, and since the compressor was short in axial length compared to the upstream and downstream ducts, the flow through the compressor was assumed to be incompressible.

The inertia of the fluid within the blade rows was neglected in the acoustic model. This seems reasonable because the inertia of the fluid within the ducts participating in the acoustic oscillations is far greater than the inertia of the fluid within the blade rows.

The aeromechanical feedback could also influence the response of the compressor to acoustic oscillations. However, both for simplicity and because data indicated that the reed valves were insensitive to annulus averaged disturbances (compared to non-axisymmetric disturbances), the aeromechanical feedback was taken to have negligible effect on the response of the compressor to the acoustic oscillations.

Applying conservation of mass and assuming that the compressor responds as a quasi-steady actuator disk, leads to the following transmission matrix across the compressor:

$$\begin{Bmatrix} p \\ \rho c u \end{Bmatrix}_u = \begin{bmatrix} 1 & -\beta \\ 0 & 1 \end{bmatrix} \begin{Bmatrix} p \\ \rho c u \end{Bmatrix}_d \tag{5.3}$$

$$\text{where } \beta \equiv \left(\frac{1}{2} M_R \frac{\partial \Psi}{\partial \Phi} + M_x \right) = \text{Acoustic Compressor Slope}$$

The acoustic compressor slope, (β) is expressed in terms of the slope of the inlet total to exit static pressure rise versus mass flow characteristic to be consistent with convention used in bulk of this thesis. The acoustic compressor slope can also be expressed in terms of the slope of the total to total compressor characteristic.

$$\beta \equiv \left(\frac{1}{2} M_R \frac{\partial \Psi_{tt}}{\partial \Phi} \right) \tag{5.4}$$

5.3.1.3 The Throttle

The flow through the throttle is assumed incompressible and quasi-steady. Applying conservation of mass and momentum across the throttle leads to the following transmission matrix across the throttle:

$$\begin{Bmatrix} p \\ \rho c u \end{Bmatrix}_u = \begin{bmatrix} 1 & \kappa \\ 0 & 1 \end{bmatrix} \begin{Bmatrix} p \\ \rho c u \end{Bmatrix}_d \tag{5.5}$$

where:

$$\kappa \equiv \frac{1 - \sigma}{\sigma} M_{x_{th}} = \text{Acoustic Throttle Slope}$$

$$\sigma \equiv \frac{A_{orifice}}{A_{duct}} \equiv \text{Area Ratio of Orifice}$$

$$M_{x_{th}} = \text{Axial Mach Number of Flow through Orifice}$$

5.3.2 Transmission Matrix for Overall Compression System

Combining the transmission matrices for the four acoustic elements of the compression system leads to the overall system transmission matrix. This relates the acoustic flow variables upstream of the inlet duct (x= - L) to those downstream of the throttle (x= αL).

$$\begin{Bmatrix} p \\ \rho c u \end{Bmatrix}_{x=-L} = \begin{bmatrix} \frac{1}{2}\left(e^{i k_1 L} + e^{-i k_2 L}\right) & \frac{1}{2}\left(e^{i k_1 L} - e^{-i k_2 L}\right) \\ \frac{1}{2}\left(e^{i k_1 L} - e^{-i k_2 L}\right) & \frac{1}{2}\left(e^{i k_1 L} + e^{-i k_2 L}\right) \end{bmatrix} X \begin{bmatrix} 1 & -\beta \\ 0 & 1 \end{bmatrix}$$

$$X \begin{bmatrix} \frac{1}{2}\left(e^{i k_1 \alpha L} + e^{-i k_2 \alpha L}\right) & \frac{1}{2}\left(e^{i k_1 \alpha L} - e^{-i k_2 \alpha L}\right) \\ \frac{1}{2}\left(e^{i k_1 \alpha L} - e^{-i k_2 \alpha L}\right) & \frac{1}{2}\left(e^{i k_1 \alpha L} + e^{-i k_2 \alpha L}\right) \end{bmatrix}$$

$$X \begin{bmatrix} 1 & \kappa \\ 0 & 1 \end{bmatrix} \begin{Bmatrix} p \\ \rho c u \end{Bmatrix}_{x=+\alpha L} \tag{5.6}$$

Defining Z_i as the elements of the individual transmission matrices for the components defined in equation (5.6), the overall system acoustic transmission matrix can be expressed as:

$$\begin{Bmatrix} p_1 \\ \rho c u_1 \end{Bmatrix}_{x=-L} = \begin{bmatrix} Z_1 & Z_2 \\ Z_2 & Z_1 \end{bmatrix} \begin{bmatrix} 1 & Z_3 \\ 0 & 1 \end{bmatrix} \begin{bmatrix} Z_4 & Z_5 \\ Z_5 & Z_4 \end{bmatrix} \begin{bmatrix} 1 & Z_6 \\ 0 & 1 \end{bmatrix} \begin{Bmatrix} p_2 \\ \rho c u_2 \end{Bmatrix}_{x=\alpha L} \tag{5.7}$$

Defining $\xi_{i\,j}$ as the elements in the overall system transmission matrix (Equation 5.7) can be written as:

$$\begin{Bmatrix} p \\ \rho\, c\, u \end{Bmatrix}_{x=-L} = \begin{bmatrix} \xi_{1\,1} & \xi_{1\,2} \\ \xi_{2\,1} & \xi_{2\,2} \end{bmatrix} \begin{Bmatrix} p \\ \rho\, c\, u \end{Bmatrix}_{x=+\alpha L} \tag{5.8}$$

5.4 Eigenvalue Stability Analysis

An eigenvalue problem can be defined by setting conditions on the acoustic field upstream and downstream of the compressor. For the system of interest here, the acoustic pressure perturbations in the free field regions upstream and downstream of the compression system are taken to be zero. The relationship between the static pressure perturbations upstream of the compression system and the acoustic state variables downstream of the compression system can be determined by expanding equation (5.8):

$$p(x=-L) = \xi_{1\,1}\, p(x=+\alpha L) + \xi_{1\,2}\, \rho\, c\, u(x=+\alpha L) \tag{5.9}$$

Applying the pressure boundary conditions leads to:

$$0 = \xi_{1\,2}\, \rho\, c\, u(x=+\alpha L) \tag{5.10}$$

For non-trivial solutions for equation (5.10) to exist, $\xi_{1\,2}$ must be zero and this determines the system eigenvalues. Using the elements of the transmission matrices for the individual components (Equation 5.7), the eigenvalues of the acoustic oscillations are solutions to the complex equation below:

$$\xi_{1\,2} \equiv Z_6\,(Z_1\,Z_4 + Z_5(Z_1\,Z_3 + Z_2)) + Z_1\,Z_5 + Z_4\,(Z_1\,Z_3 + Z_2) = 0 \tag{5.11}$$

Solving Equation 5.11 for the complex time dependence, ω, determines the frequency and decay (or growth) rate of the natural acoustic modes of the compression system. The eigenvalues were found using an iterative technique.

There are several non-dimensional parameters which determine the acoustic behavior of the compression system:

L = length of upstream duct

α = ratio of upstream and downstream ducts

β = acoustic compressor slope

κ = acoustic throttle slope

M_X = axial Mach number in ducts

The analysis was used to determine the effect of the acoustic compressor slope (β) and the acoustic throttle slope (κ) on the acoustic oscillations in the compression system used in the experimental phase of this research. The acoustic parameters of the MIT single stage compression system were estimated to be the following:

L = length of upstream duct =1 meter

α = ratio of upstream and downstream ducts = 1.2

M_R = Mach Number of Blades on Rotor = 0.2

The axial Mach number for the upstream and downstream duct is $M_X = 0.07$. Assuming the mean flow is incompressible, the mean flow coefficient (Φ) and the rotor Mach number determine the relation between the throttle Mach number and the throttle area ratio:

$$\Phi M_R = M_X = \sigma M_{X_{th}} \tag{5.12}$$

To help interpret the behavior of the acoustic oscillations, the decay (or growth) rates predicted by the eigenvalue analysis were related to the critical damping ratio of an

equivalent second order system. The details are given in Appendix I. With this terminology, positive damping ratios indicate a stable system and negative damping ratios indicate an unstable system.

Figure 5.3 shows the predicted frequency and damping ratio of the lowest frequency acoustic mode for the compression system as a function of the acoustic throttle slope. The three curves are for different compressor slopes, $\frac{\partial \Psi}{\partial \Phi} = -10,\ 0,$ and $10.$ The model predicts that both frequency and damping ratio of the acoustic mode are influenced by both the acoustic compressor slope and the acoustic throttle slope. For low acoustic throttle slopes, the frequency and damping ratio of the acoustic oscillations is insensitive to the slope of the compressor; the frequency remains near the half wave length frequency and the damping ratio remains positive (stable) over the range of compressor slopes investigated. However, for steep acoustic throttle slopes, the frequency approaches the quarter wave length frequency. Instability is possible, and the stability of the acoustic mode is primarily determined by the slope of the compressor.

5.5 Discussion of Results from Model

The acoustic stability analysis illustrates the roles of the compression system parameters in determining the system behavior. The analysis predicts that compressors operating with positive acoustic compressor slopes are capable of driving the one-dimensional acoustic mode of the compression system unstable. For the range of compressor and throttle slopes investigated, the acoustic mode is predicted to become unstable when the acoustic compressor slope is positive and acoustic throttle slope is steep.

As shown in equation (5.4), the sign of the acoustic compressor slope is determined by the sign of the slope of the total to total compressor characteristic. The mechanism responsible for the acoustic instability, i.e. the compressor feeding energy into the disturbances, is thus

similar to the mechanism responsible for rotating stall and surge. All three types of instability can be viewed in the same general context.

Although the compressor is the only element capable of providing the mechanism for an acoustic instability, the acoustic slope of the throttle has a large effect on the behavior of the acoustic oscillations. This can be seen by comparing the results of the analysis for the system with the compressor operating at the peak of the total to static characteristic, (small acoustic compressor slope), to the results of a simple organ pipe analysis. For shallow acoustic throttle slopes, the throttle approaches a pressure release, or open ended pipe. For an organ pipe with two open ends, the natural frequency, corresponding to the half wave length frequency, is

$$f = \frac{c}{\lambda} = \frac{c}{2L(1+\alpha)} \tag{5.13}$$

This frequency agrees with the analysis in the limit of shallow acoustic throttle slopes.

For steep acoustic throttle slopes, the throttle appears as a closed end for the acoustic perturbations. The natural frequency of an organ pipe with one closed and one opened end corresponds to the quarter wavelength frequency, or:

$$f = \frac{c}{\lambda} = \frac{c}{4L(1+\alpha)} \tag{5.14}$$

This frequency is also consistent with the analysis in the limit of steep throttle slopes. A schematic of the organ pipe analogy is shown in Figure 5.4.

The analysis predicts that the damping ratio of the acoustic mode in the compression operating near the peak of the total-to-static compressor characteristic is maximized for acoustic throttle slopes between these two limits. The occurrence of a maximum in

damping ratio, or equivalently a maximum in the dissipation across the throttle, as a function of acoustic throttle slope can be interpreted as follows. At either of the two limits, the throttle reflects all incident acoustic energy, and the unsteady energy dissipation across the throttle approaches zero. At intermediate values of the acoustic throttle slope, the throttle dissipates a portion of the incident acoustic energy, adding damping to the acoustic oscillations.

5.6 Experimental Results

Since the primary objective of the research addressed rotating stall, it was desired to reduce, or eliminate, the apparent resonance of the acoustic oscillations. The observations indicated that an acoustic mode resembling the quarter wave length organ pipe mode was becoming under-damped. It was deduced, therefore, that the throttle was acting primarily as velocity node (i.e. the acoustic throttle slope was steep). For the compression system operating with a steep acoustic throttle slope, the analysis showed that decreasing the acoustic throttle slope would serve to increase the damping ratio of the acoustic mode, and hence reduce the amplitude of the acoustic oscillations.

The acoustic throttle slope in the experimental facility was reduced by opening a vent, approximately 1 square foot in area, in the exit plenum behind the throttle to ambient pressure. Since the pressure in the exit plenum was below atmospheric pressure due to the exhaust fan, opening the vent increased the exit back pressure from approximately -0.75 psig to -0.25 psig. This lead to a decrease in the Mach number through the throttle and, for a given mass flow coefficient, an increase in the throttle area. Both of these effects reduced the acoustic throttle slope.

Although this change was predicted to have a negligible effect on the small amplitude surge dynamics, and no effect on the small amplitude rotating stall dynamics, changing the acoustic throttle slope effectively eliminated the acoustic oscillations observed near stall. As evidence of this, the PSD's of a pressure signal and mass flow signal is shown in Figure 5.5 for the same operating conditions as the PSD's shown in Figure 5.1, except for the change in the throttle slope. No significant acoustic oscillations are detectable in the compression system operating with the shallow acoustic throttle slope. Figure 5.5 also shows the magnitude of the pressure / velocity transfer function. The transfer functions predicted for the two-dimensional, incompressible flow field are also indicated and are seen to be consistent with the data.

All of the experimental investigations of the rotating stall dynamics presented in this thesis were recorded for the compression system operating with the shallow throttle slope, i.e. the vent was open in the exit plenum downstream of the throttle. Over the range of operating conditions, therefore, no acoustic oscillations of the order of the unsteadiness associated with rotating stall were observed for the compression system operating with the shallow acoustic throttle slope.

5.6 Conclusion from Acoustic Analysis

Several conclusions can be drawn from the experimental and analytical results presented in this chapter.

1) Compressors operating with positive slopes can cause one-dimensional acoustic oscillations to become unstable.

2) The one-dimensional acoustic oscillations are related to, but different than, the classical surge dynamics of the compression system.

3) Since the acoustic compressor slope is proportion to the product of the slope of the compressor characteristic and the compressor Mach number, increasing the Mach number of a compressor operating in a positively sloped region is predicted to be destabilizing to the acoustic oscillations.

4) The acoustic throttle slope can play an important role in determining the behavior of acoustic oscillations in compression systems.

5) The acoustic behavior of a compression system is dependent on the specific compression geometry and operating parameters.

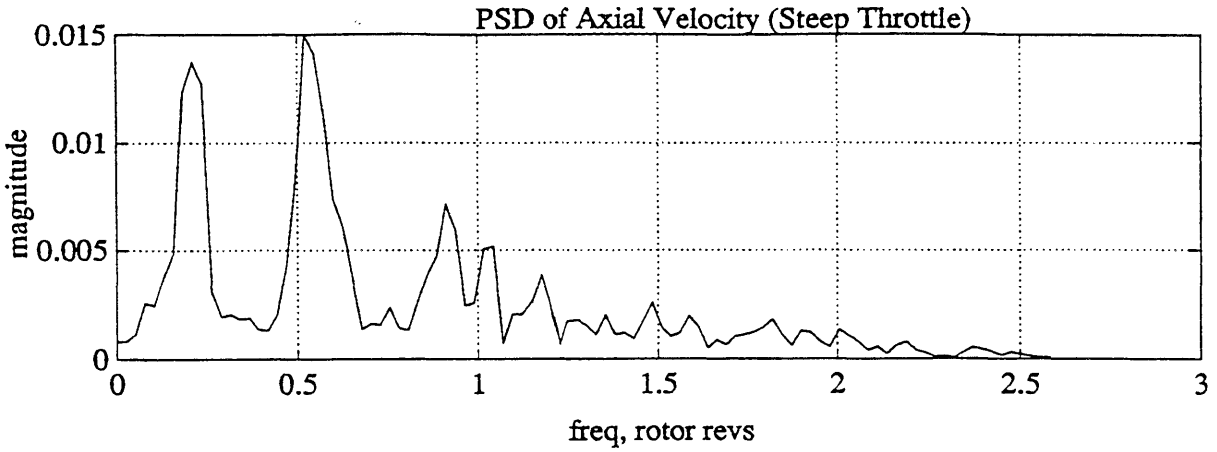

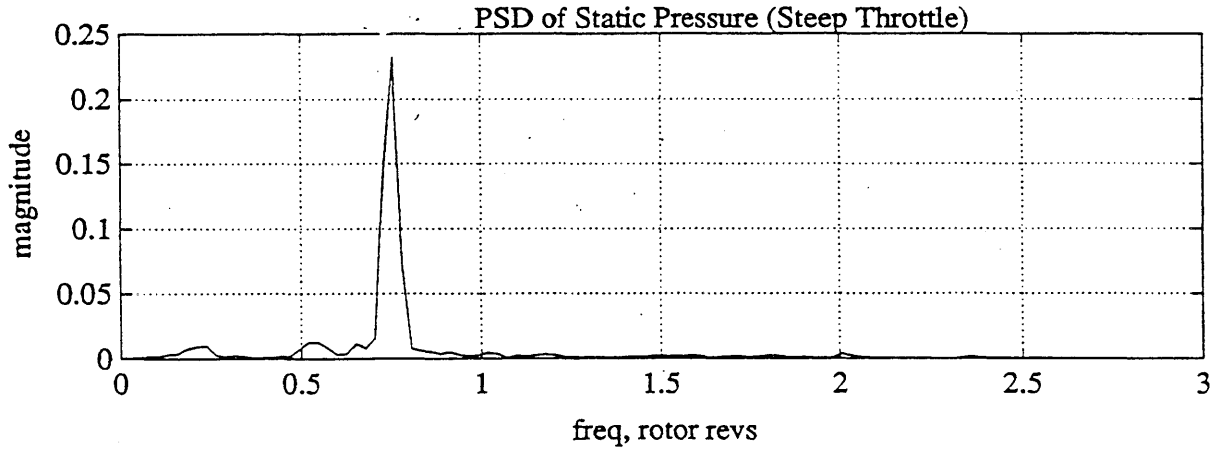

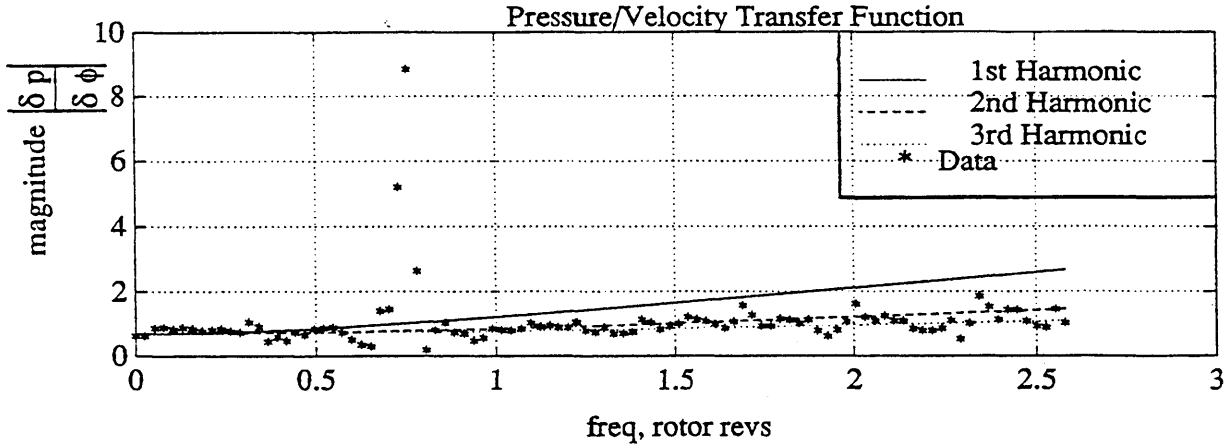

Figure 5.1 PSD's of the Axial Velocity $(\delta C_x / U_R)$ and Static Pressure $\left(\delta P / \frac{1}{2}\rho U_R^2\right)$ Perturbations at Entrance to Compressor with Magnitude of Transfer Function $(\delta P / \delta \phi)$ for the Original Compression System Configuration Operating Near Stall with Aeromechanical Feedback

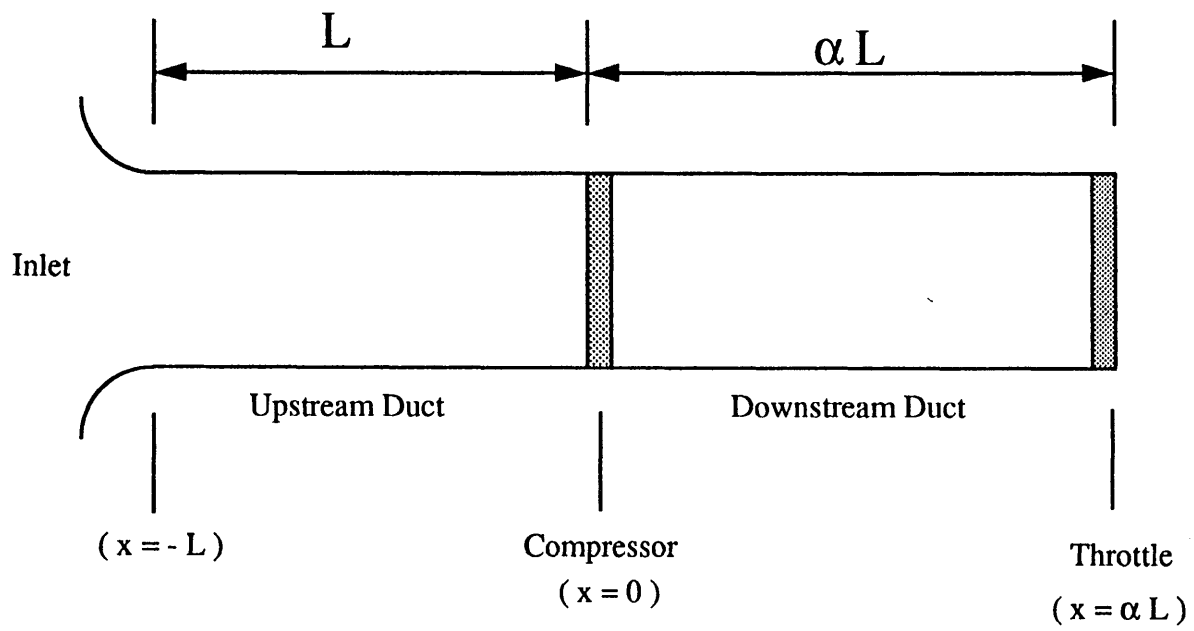

Figure 5.2: Schematic of One-Dimensional Acoustic Model of Compression System

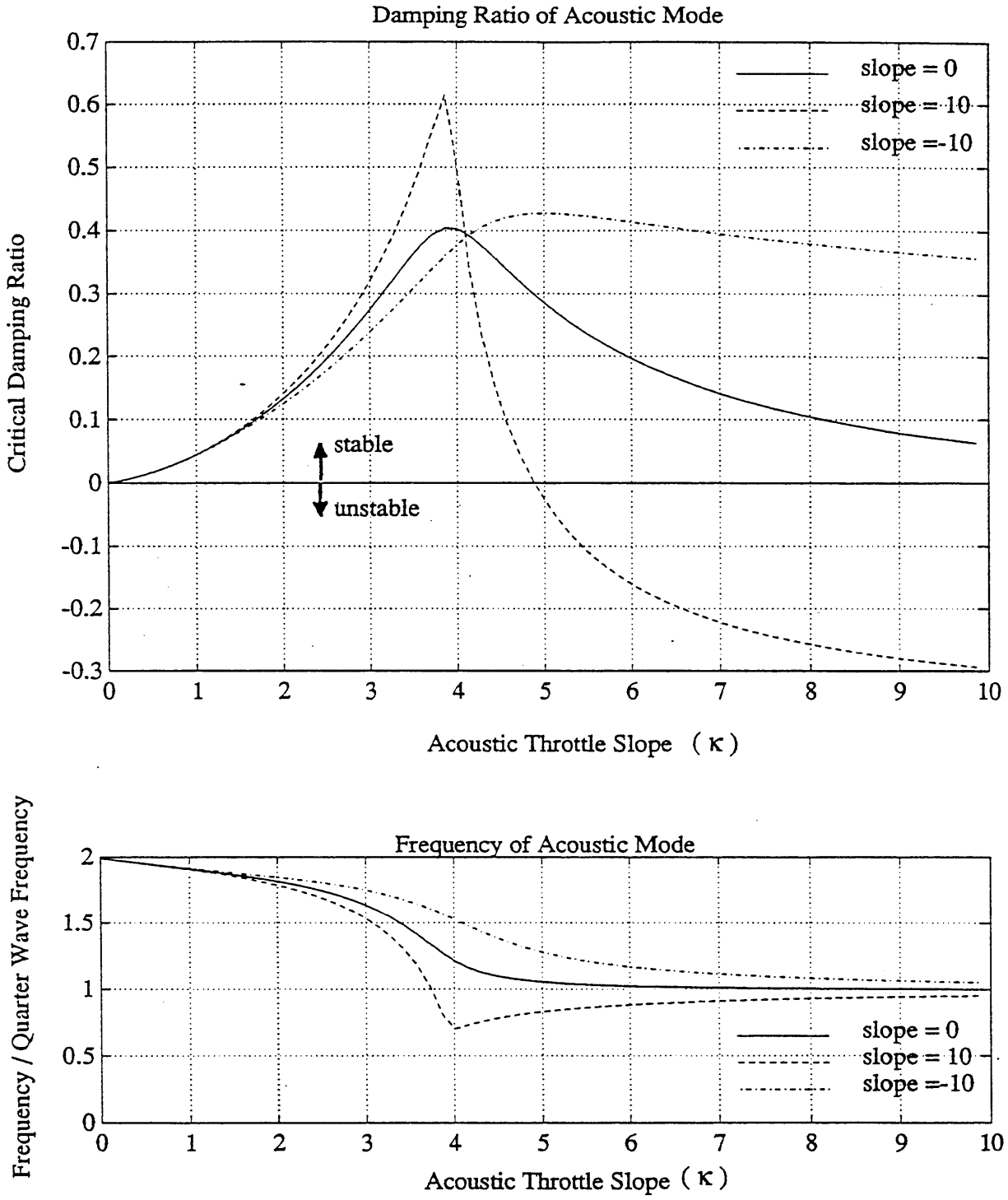

Figure 5.3 One-Dimensional Acoustic Modes of the Compression System as a Function of Acoustic Throttle Slope for Three Compressor Slopes $\frac{\partial \Psi}{\partial \Phi}$

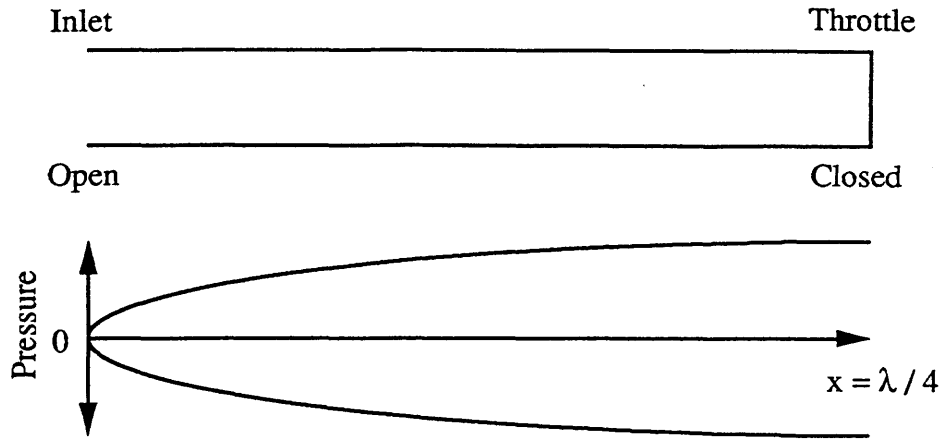

Open / Closed Organ Pipe Acoustic Mode
(Limit of Steep Acoustic Throttle Slope)

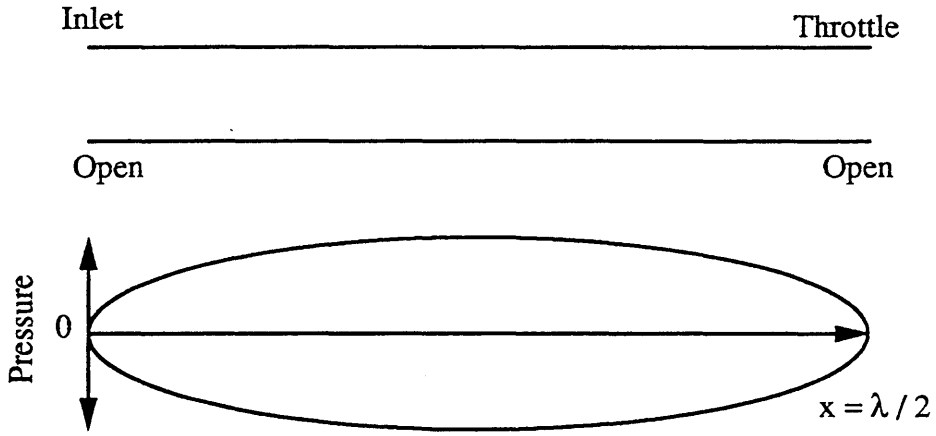

Open / Open Organ Pipe Mode
(Limit of Shallow Acoustic Throttle Slope)

Figure 5.4: Organ Pipe Analogy For Limiting Throttle Conditions

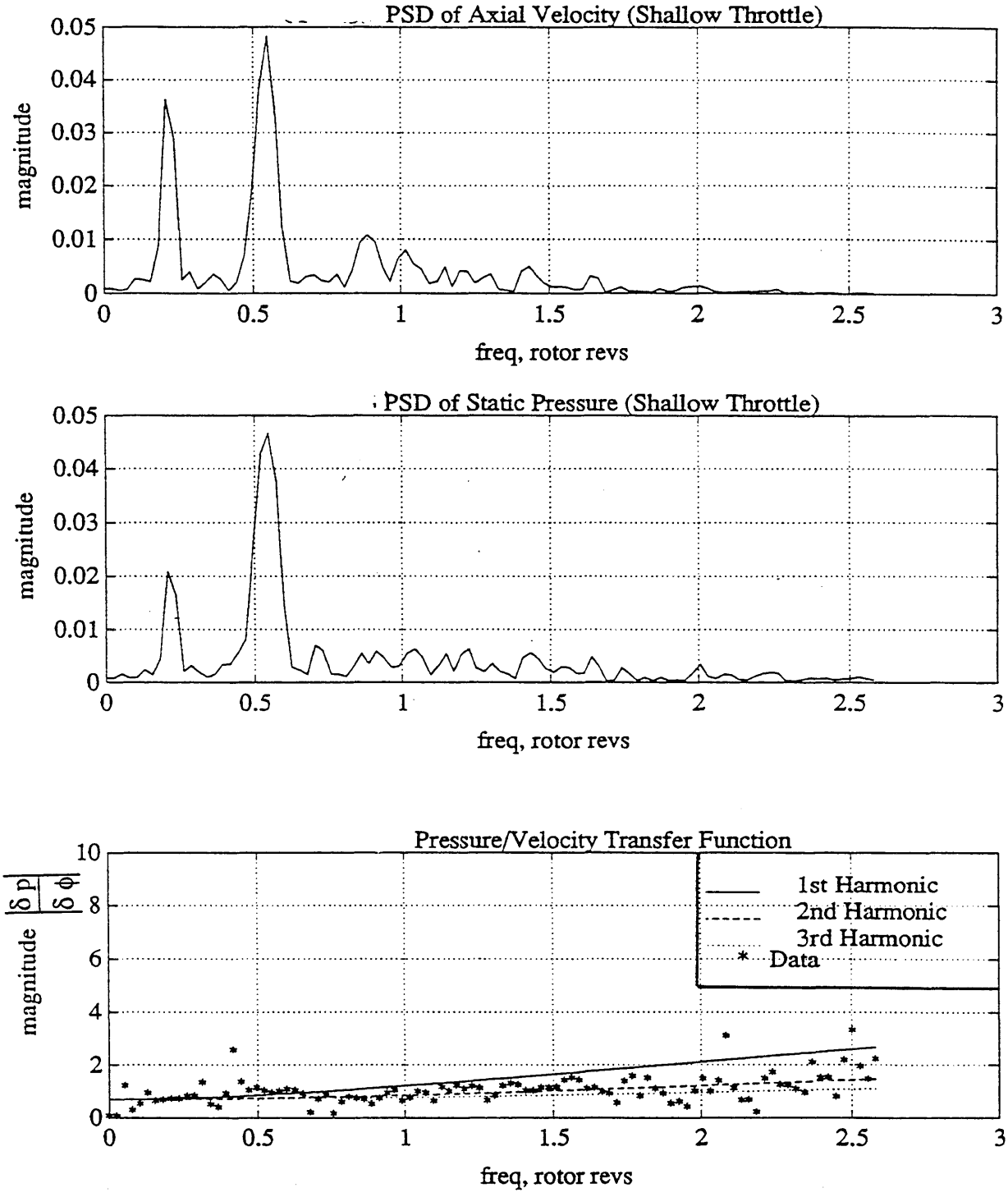

Figure 5.5 PSD's of the Axial Velocity $\left(\delta C_x / U_R\right)$ and Static Pressure $\left(\delta P / \frac{1}{2}\rho U_R^2\right)$ Perturbation at Entrance to Compressor for Compression System with Reduced Acoustic Throttle Slope Operating Near Stall with Aeromechanical Feedback

Chapter 6: Discussion

Aeromechanical feedback control was demonstrated to extend the stable flow range of an axial flow compressor by stabilizing the small amplitude, non-axisymmetric, compression system dynamics, thus achieving the primary objective of the research. However, there are several issues regarding interpretation and applicability of the results to the general objective of increasing compression system stable operating range using feedback control which warrant further discussion.

6.1 Implications of Non-Optimized Control Parameters

The theoretical model (of compression system dynamics with aeromechanical feedback introduced by the dynamic mass / momentum injection strategy) developed in this research predicts a greater degree of stabilization than achieved in the experimental phase of this research. The design optimized control strategy ($W=3.5$, $Q=0.9$, $\zeta=0.7$, $\Phi_i=1.0$), which was restricted to control parameters considered achievable with a simple mechanical design, was predicted to stabilize the first two spatial harmonics to a slope of $\frac{\partial \Psi}{\partial \Phi} = 1.2$. The control parameters achieved in the experiment ($W=3.5$, $Q=1.5$, $\zeta=0.3$, $\Phi_i=1.0$)were predicted to stabilize the compressor only to a slope of $\frac{\partial \Psi}{\partial \Phi} = 0.3$.

The failure to achieve the design control parameters is attributed to the specific mechanical implementation of the dynamic mass / momentum control strategy employed in this research and does not represent a fundamental limit on the performance of future control strategies. Using the experimentally determined control parameters in the model of the compression system with aeromechanical feedback, theoretical and predicted results for compression stability qualitatively agreed (Chapter 4). Therefore, although it yet remains

to be demonstrated, the control strategy developed in this research has the potential to achieve a substantially greater degree of stabilization.

6.2 Dynamic Compensation

In this section, the role of the structural dynamics in the control strategy linked to other (non-aeromechanical) forms of feedback stabilization of rotating stall. The conclusions from this interpretation offer some unifying comments concerning dynamic control of compressors and compression systems.

A number of potential sensing and actuating schemes for control of rotating stall in axial flow compressors have been investigated by Hendricks and Gysling [31] who considered several types of actuators, and three types of sensors: static pressure, total pressure, and axial velocity. Only proportional control was included in the study. The results indicated the most effective control strategies made use of axial velocity sensors and of actuators which modify the local pressure rise across the compression system. A further conclusion was that actuators with bandwidths at least three times the rotational frequency of the compressor were required for effective control.

These results should be contrasted with those from the optimized aeromechanical control system investigated in the present work. In this, static pressure was sensed and low bandwidth (roughly equivalent to the rotational frequency of the compressor) actuators were used to modify the pressure rise across the compressor. (The bandwidth of the aeromechanical actuators is defined as the natural frequency of the structural dynamic system.)

This apparent contradiction can be explained by considering the role of the reed dynamics in the feedback process. The reeds respond to (or sense) static pressure perturbations in

the upstream flow field. The reeds actuate the flow field by modifying the local pressure rise across the compression system as a function of reed displacement. The relationship between reed displacement and pressure perturbations is determined by the reed valve structural dynamics. The reed valves thus constitute a second order (rather than proportional) control law between the sensed variable (static pressure) and the actuation (injection regulated by reed valve displacement), and there is a temporal phase difference between the sensed variable and the actuation.

Let us now consider the motion of the reeds with respect to velocity perturbations in the upstream flow field. The analytical and measured reed deflection / axial velocity perturbation transfer functions were shown in Figure 4.43 for the compression system with optimized aeromechanical feedback. The specific point to note is that the reed dynamics are such as to compensate for the phase difference between the static pressure and axial velocity perturbations in the upstream flow field. Because of this, the reed deflection remains approximately 180 degrees out of phase with the velocity perturbations in the upstream flow field, for frequencies up to approximately two times the rotor frequency.

To the compression system flow field, therefore, the reeds appear as if they are being driven by high bandwidth actuators, commanded by a signal proportional to the velocity perturbations in the upstream flow field. Assuming that the primary effect of the reed displacement is to increase local pressure rise across the compressor, the feedback introduced by the optimized aeromechanical control scheme in the present study is essentially the same as the "best case" in the Hendricks and Gysling study [31].

Interpreting the role of the structural dynamics as providing dynamic compensation suggests that other types of feedback control strategies, namely electromechanical systems, can also use dynamic compensation to reduce sensing and actuation constraints.

6.3 Modeling the Injection Process

The effect of the jet actuation on the compression system was modeled by assuming that the high total pressure fluid was injected into a span-wise uniform flow field and that the injected flow mixed out in the span-wise direction before entering the compressor. As modeled, therefore, the compressor experienced a span-wise uniform flow field and the compressor performance remained purely a function of the local mass flow coefficient.

The experimental data, however, demonstrated that a different process occurred. For the experimentally optimized injection level, the high total pressure fluid basically filled in the axial momentum deficit in the casing boundary layer, changing the velocity profile entering the compressor. Viewing the injection process in this manner suggests that the local effect of the injection may be analogous to that of casing treatment.

To estimate the influence that the details of mixing process have on the stability of the compression system with feedback, the effect of the actuation can be modeled by assuming the compressor performance is a function of both the span-wise averaged mass flow and the shape of the axial velocity profile entering the compressor. The shape of the velocity profile can be parameterized as a function of the percentage of axial momentum injected into the upstream flow field.

$$\Psi = \Psi (\Phi, \alpha_i) \tag{6.1}$$

The percentage of momentum injected into the upstream flow field can be calculated as a function of the injection parameter and the nominal reed valve opening area:

$$\alpha_i = q \frac{\Phi_i^2}{\Phi_u^2} = \text{Non-dimensional Momentum Injected} \tag{6.2}$$

Thus, the quasi-steady, linearized change in pressure rise across the compressor (neglecting the inertial terms) is given by:

$$\delta \Psi = \frac{\partial \Psi}{\partial \Phi} \delta \phi + \frac{\partial \Psi}{\partial \alpha_i} \left(\frac{\Phi_i}{\Phi_c} \right)^2 \delta q \tag{6.3}$$

Comparing the total to static pressure rise coefficient recorded near stall ($\Phi = 0.42$) for two injection rates ($\Phi_i = 0.93$ ($\alpha_i = 0.07$) and $\Phi_i = 1.08$ ($\alpha_i = 0.14$)) shown in Figure 4.15, the change in compressor performance for a small change in momentum injected can be estimated:

$$\frac{\partial \Psi}{\partial \alpha_i} \approx \frac{\Delta \Psi}{\Delta \alpha_i} = \frac{0.373 - 0.366}{0.14 - 0.07} = 0.1$$

The expression for $\frac{\partial \Psi}{\partial \alpha_i}$ obtained by assuming that the injected flow mixes out is given by:

$$\frac{\partial \Psi}{\partial \alpha_i} = 2 \Phi_c^2 \left(1 - \frac{\Phi_c}{\Phi_i} \right) = 2 (0.42)^2 \left(1 - \frac{0.42}{1.0} \right) = 0.2 \tag{6.4}$$

Thus, the measured value of $\frac{\partial \Psi}{\partial \alpha_i}$ is of (very crudely) the same size as that estimated by assuming that the only effect of the injection was to transfer high momentum fluid into the core flow through the compressor. This suggests that the mechanism that changes the pressure rise across the compressor with the injection is reasonably modeled by assuming that the flow mixes out before entering the compressor. As developed in Chapter 3, the tip of the rotor is not highly loaded in the build used in this research, and, therefore, the pressure rise is not very sensitive to changes in the tip region. For compressors in which

the tip region of the rotor is highly loaded, the compressor performance could be expected to be much more sensitive to modifying the flow in the tip region [32].

As developed in Appendix C, modeling the effect of the injection on compressor performance assuming the flow does not mix out predicts the same qualitative results as the fully mixed out model. From a system stability context, the detailed mechanism that increases the local pressure rise across the compressor with increased injection area, is not the central issue. The important effect is that the pressure rise across the compression system increases with increasing amounts of high momentum fluid injected into the face of the compressor; the degree of mixing of the injected fluid is not critical to the success of injection based control schemes.

Whether complete mixing of the injected fluid is desirable is a compression system specific question. For example, Day [16] extended the stable flow range of an axial flow compressor using jets positioned to change the flow at the tip of the rotor. The jets used in his control scheme were located near the tip clearance region, a fraction of a chord upstream of the rotor. As such, the primary effect of the injection was to modify the detailed structure of the flow near the tip of the rotor. His work demonstrates that the rotating stall dynamics can be modifying employing a mechanism other than bulk momentum transfer into the flow field upstream of the compressor.

6.4 Simplified Interpretation of Stabilizing Mechanism

By making the simplifying assumptions that the injection serves to increase the local pressure rise across the compressor and that the reed valves respond proportionally, and opposite, to the local mass flow perturbations, the stabilizing mechanism of the dynamic control can be physically interpreted in a straightforward manner. The change in pressure

rise coefficient in phase with a given change in axial flow coefficient upstream of the compressor with feedback is given by:

$$\delta \Psi\ (\phi, q) = \frac{\partial \Psi}{\partial \Phi}\delta \phi_u + \frac{\partial \Psi}{\partial q}\delta q = \left(\frac{\partial \Psi}{\partial \Phi} + \frac{\partial \Psi}{\partial q}\frac{\partial q}{\partial \phi}\right)\delta \phi_u = \left\{\frac{\partial \Psi}{\partial \Phi} - K\right\}\delta \phi_u \tag{6.5}$$

In Equation (6.5), δq represents the actuation, $\frac{\partial \Psi}{\partial q}$ is the effect of actuation on the local pressure rise across the compressor, and $\left(\frac{\partial q}{\partial \phi} = -K\right)$ represents a proportional control law between the perturbation in axial velocity and the actuation.

The effective slope with feedback can be expressed in terms of the slope of the steady state compressor characteristic and the effect of the feedback.

$$\text{effective slope} = \left\{\frac{\partial \Psi}{\partial \Phi} - K\right\} \tag{6.6}$$

The arguments concerning unsteady energy production (Chapter 2) imply that the flow becomes unstable when the effective slope is becomes positive. For the compression system with feedback, Equation (6.6) shows that this occurs at a lower flow coefficient than the original compression system.

6.5 Acoustic Oscillations

For the compression system configuration originally investigated in this research, acoustic oscillations were observed when operating in the region where the rotating stall dynamics were stabilized with aeromechanical feedback. The analysis developed in this thesis offers an explanation as to why the acoustic modes of compression systems are generally not observed. The analysis predicts that the acoustic modes become progressively less damped as the acoustic compressor slope is increased, as is the case as the mass flow is reduced.

The analysis also predicts that the acoustic compressor slope must be positive for the acoustic mode to become unstable.

In compression systems without dynamic feedback, rotating stall, or surge, is generally encountered before the acoustic modes become under-damped or unstable. Dynamic feedback allows the compressor to operate with axisymmetric flow in regions with positive compressor slopes. The acoustic modes can thus become under-damped, and possibly unstable. Although the acoustic behavior of compression systems is dependent on the acoustic parameters of the system, the mechanism for an acoustic instability exists for any compression system operating with positive acoustic compressor slope. The model developed for the one-dimensional acoustic oscillations of the compression system shows that the stability of the organ pipe-type acoustic oscillations differs from the classical surge dynamics of the compression system. Therefore, the stability of acoustic oscillations should be considered for systems in which the rotating stall dynamics are stabilized using feedback control.

Chapter 7: Summary, Conclusions, and Recommendations

7.1 Summary and Conclusions

1) The onset of rotating stall in a low speed, single stage, axial flow compressor has been suppressed using aeromechanical feedback. The aeromechanical feedback was provided by an array of flexible reed valves that responded to static pressure perturbations in the upstream flow field. The reeds, which were modeled as mass-spring-dampers, regulated the amount of high pressure air injected into the face of the compressor. This research appears to be the first demonstration of dynamic control of rotating stall in an axial flow compressor using aeromechanical feedback.

2) Using a small amount of injection mass flow (4% of the mass flow through compressor) with a total pressure of approximately one dynamic head based on compressor wheel speed, the aeromechanical feedback reduced the stalling flow coefficient of the compression system by 10% from the stalling flow coefficient with the same amount of (steady state) injection without feedback.

3) The experimental apparatus designed and constructed for this research appears to be the first scheme to employ a locally reacting feedback strategy to suppress rotating stall. Locally reacting control schemes differ from the modal based control schemes, which have been used by previous researchers to stabilize rotating stall. The latter require arrays of sensors and actuators, as well as extensive real time computations, to stabilize the individual modes of the compression system independently. Locally reacting control strategies offer an alternative approach.

4) The control system design was based on a two-dimensional, linearized model of the compression system which included the effect of aeromechanical feedback. The model

predicted that the stability of the compression system is a function of several control parameters in addition to the compression system parameters. The experimental facility was designed to achieve values of the control parameters that were determined from a parametric study.

5) The model was successful in predicting the overall features of the compression system dynamics and the influence of the aeromechanical feedback.

6) The experimentally obtained control parameters differed from the optimal parameters called out by the linear model. Specifically, the reed frequency parameter obtained experimentally (Q=1.5) was 67% above the optimal value (Q=0.9) predicted by the model. Using the experimentally determined control parameters as inputs, the linear model predicted the experimentally observed trends in stalling flow coefficient as functions of damping ratio and injection parameter. Further, the model predicts that significant additional stabilization could be achieved for an optimized set of control parameters.

7) The basic linearized model was extended to include the effect of non-linear compressor characteristics and the effect of noise. The numerical simulation, based on a Galerkin approximation for the two lowest harmonics, yielded reasonable prediction of the compression system performance with aeromechanical feedback.

8) A physical interpretation was given for the role of the structural dynamics in the aeromechanical control strategy. The reed dynamics were found to serve as a dynamic compensators; the reed displacement, although driven by pressure perturbations, remained roughly 180 degrees out of phase with velocity perturbations in the upstream flow field over a large frequency range. This phase relation is similar to that found in the most effective active control strategies investigated to date [31].

9) Large amplitude acoustic oscillations were observed in the compression system in the region of the compressor map where rotating stall was suppressed with aeromechanical feedback. A one-dimensional acoustic analysis predicted that compressors operating on the positively sloped portion of their characteristic can drive acoustic oscillation unstable. The mechanism for the acoustic instability is similar to the mechanism responsible for surge and rotating stall, namely, that the compressor feeds energy into unsteady disturbances.

10) The acoustic analysis predicted that the frequency and critical damping ratio of acoustic disturbances was a function of several compression system parameters. Specifically, the acoustic throttle slope had a large effect on the behavior of the acoustic oscillations in the compression system studied. Based on the analysis, the acoustic oscillations were essentially eliminated by changing the acoustic throttle slope.

7.2 Recommendations for Future Work

Dynamic control of aerodynamic instabilities in compression systems has been demonstrated, by this work and other previous work, to be a valid concept. However, work is required to develop more effective and robust dynamic control strategies and to implement dynamic control in practical situations. Based on the results of this research, several specific issues warrant further study.

1) Develop a comprehensive fluid dynamic model of instabilities in compression systems. The feedback control scheme used in this work was shown to be effective for stabilizing two-dimensional, long wave length, rotating stall dynamics. However, much is still unknown about compression system instabilities. For axial flow compressors, instability is typically encountered near the peak of the compressor characteristic. The form of the instability is generally initially rotating stall, although surge can be "triggered" shortly

thereafter [5]. The fluid mechanics of rotating stall onset are not well understood. Some compressors exhibit short length scale disturbances with significant radial non-uniformity, which grow circumferentially and radially into full span stall [15]. Others, such as the compressor used in these experiments, develop small amplitude, full-span instabilities that lead to fully developed rotating stall. No adequate model presently exists for the three dimensional rotating stall inception process, and the parameters that determine the character of the stall inception process for a given compression system also remain unknown.

The author suggests a unified view of compression system stability, one which recognizes that a compression system contains many possible paths to performance limiting instabilities. The form of instability that occurs at the highest mass flow coefficient will be the one observed as the compression system is throttled. In some compressors, three dimensional disturbances appear to become unstable before the long wave length, two-dimensional waves, in other compressors, the converse is true. Moreover, as rotating stall control strategies become more effective in suppressing the full-span instabilities, different forms of instability may be encountered even for compressors that exhibit full-span stall inception in the absence of feedback stabilization. To fully exploit the benefits of dynamic control, understanding of the different forms of instability needs to be developed to define all the parameters that determine stability.

To motivate this type of study, an analysis that assesses the stability of an axisymmetric, span-wise non-uniform, velocity disturbance in an annular duct with uniform mean flow is presented in Appendix K. The model is presented mainly to demonstrate the plausibility of part-span disturbances influencing the breakdown of the uniform steady, axisymmetric flow through the compressor, but it also identifies possible parameters which influence the nature of the stall inception events. As shown in Appendix K, it is predicted that part-span, circumferentially uniform, disturbances are more stable than full-span disturbances in

compressors with span-wise uniform conditions. However, for some span-wise non-uniform loading distributions, part-span disturbances are predicted to become unstable at operating conditions where the full-span disturbances are stable. In compression systems in which such conditions are met, this implies that part-span disturbances would participate in the breakdown of the uniform, axisymmetric flow field. Disturbances of this type would therefore need to be considered in the development of control strategies for extending the stable flow range of the compression system.

2) Explore the use of dynamic compensation in other types of feedback control strategies. The use dynamic compensation, via the reed dynamics, demonstrated that actuators with bandwidths of roughly the rotation frequency of the compressor can stabilize compressor rotating stall dynamics. This is of particular importance for control schemes designed for high speed compressors, where actuator bandwidth has been predicted to be a significant obstacle to developing effective control strategies based on proportional control laws [11, 31].

The use of dynamic compensation in this research also allowed an effective control strategy to be developed based on sensing static pressure. Control strategies in which pressure is the sensed variable are viewed as easier to implement in high speed machines than control which require sensing of mass flow perturbations.

3) Consider locally reacting control strategies as possible alternatives to the modal based control schemes used by previous researchers. Locally reacting control schemes may be easier to implement, either aeromechanically or electromechanically, and these schemes may also offer advantages in compression systems operating in distorted flow fields, where the individual spatial harmonics no longer represent eigenmodes of the compression system [20].

Locally reacting control strategies offer the possibility of eliminating the mechanism for instability in compression systems, independent of the structure of the disturbance. By changing the real part of the local pressure rise versus mass flow transfer function across the compressor, locally reacting control strategies can theoretically stabilize rotating stall, surge, and acoustic instabilities with the same control strategy.

4) Explore the use of jet actuation in control strategies. The development of actuators that effectively manipulate the flow field is critical to the continuing development of dynamic control strategies. The analytical studies conducted to date show that high pressure injection is a promising candidate. These studies, however, took a simplified view of the injection process in which the jets are assumed to mix out over the span-wise direction before entering the compressor [11, 31], and a more in-depth look at the fluid dynamics should be carried out.

Span-wise locally acting jets, similar to those used by Day [16], which are concentrated on specific span-wise regions of the compressor flow through also warrant further study. By using injection to modify regions known to have a major influence on near stall performance of some compressors, such as the hub and tip regions, (instead of mixing the injection over the span), dynamic injection may be made more effective. Injecting fluid into the tip regions is similar, in principle, to casing treatment which has had marked success in increasing compressor stable flow range [32]. Using feedback to modulate the injection could offer improved performance over conventional casing treatment. Therefore, the effect of injection in specific span-wise regions (such as near the tip) on the fluid mechanics of the flow through compressors warrants further study. These studies could be carried out experimentally or computationally; it would seem that useful insight could be gained from the use of some three-dimensional computation procedures that now exist.

5) Investigate control strategies similar to the dynamic mass / momentum injection strategy to further optimize performance. The theoretically predicted optimal configuration has not been tested for this control scheme. The design configuration represents an optimization carried out under mechanical constraints. These constraints are not fundamental to the control strategy, but rather, to the specific experiment. Despite the mechanical constraints, the design configuration was predicted to be significantly more effective than the experimentally achieved system tested in this research. Although the theory predicts additional stabilization, extrapolation of the experimental results to those theoretically achievable with the design configuration would be unjustified at this point due to the issue raised above. An experimental device that could achieve a more optimized set of control parameters would be useful in evaluating the applicability of dynamic mass / momentum injection in other compression systems.

A variation of the present control strategy, in which the mass flow injected is drawn from downstream of the compression, is presented in Appendix J. In this control strategy, termed dynamic mass / momentum recirculation, injection upstream of the compressor is close-coupled to suction downstream of the compressor. The close-coupled suction downstream of the compressor is predicted to augment the stabilizing effect of the dynamic injection. Further development of the control strategy investigated in this research should consider this variation.

References

1. Greitzer, E. M., "Review: Axial Compressor Stall Phenomena," Journal of Fluid Engineering, Vol. 102, June 1980, pp. 134-151.

2. Greitzer, E. M., "Surge and Rotating Stall in Axial Flow Compressors; Part I: Theoretical Compression System Model," Journal of Engineering for Power, Vol. 98, 1976, pp. 190-198.

3 Greitzer, E. M., "Surge and Rotating Stall in Axial Flow Compressors; Part II: Experimental Results and Comparison with Theory," Journal of Engineering for Power, Vol. 98, 1976, pp. 199-217.

4. Day, I. J., Greitzer, E. M., and Cumpsty, N. A., "Prediction of Compressor Performance in Rotating Stall," Journal of Engineering for Power, Vol. 100, pp. 1-14, January, 1978.

5. Greitzer, E. M., " The Stability of Pumping Systems - The 1980 Freeman Scholar Lecture," Journal of Fluids Engineering, Vol. 103, June 1981, pp.193-242.

6. Moore, F. K., and Greitzer, E. M., "A Theory of Post Stall Transients in Axial Compression Systems Part I - Development of Equations," Journal of Engineering for Gas Turbines and Power, Vol. 108, January 1986, pp.68-76.

7. Moore, F. K., and Greitzer, E. M., "A Theory of Post Stall Transients in Axial Compression Systems Part II - Application," Journal of Engineering for Gas Turbines and Power, Vol. 108, January 1986, pp.68-76.

8. Epstein, A. H., Ffowcs-Williams, J. E., and Greitzer, E. M., "Active Suppression of Compressor Instabilities," Journal of Propulsion for Power, Vol. 5, pp.204-211, 1989.

9. Ffowcs-Williams, J. E., Huang, X. Y., "Active Stabilization of Compressor Surge," Journal of Fluid Mechanics, Vol. 204, 1989, pp. 245-269.

10. Gysling, D. L., Dugundji, J., Greitzer, E. M., and Epstein, A. H., "Dynamic Control of Centrifugal Compressor Surge Using Tailored Structures," Journal of Turbomachinery, Vol. 113, pp. 710-722, April 1991.

11. Simon, J. S., Valavani, L., Epstein, A. H., and Greitzer, E. M., "Evaluations of Approaches to Active Compressor Surge Stabilization," Journal of Turbomachinery, Vol. 115, pp. 57-67, January, 1993.

12. MacDougall, N. M., "Stall Inception in Axial Compressors," Ph.D. Thesis, Cambridge University, 1988.

13. Garnier, V. H., Epstein, A. H., and Greitzer, E. M., "Rotating Waves as a Stall Inception Indication in Axial Compressors," J. of Turbomachinery, Vol. 113, April 1991.

14. Longley, J. P.," Inlet Distortion and Compressor Stability," Ph.D. Thesis, Cambridge University, 1988.

15. Day, I. J., "Stall Inception in Axial Flow Compressors," Journal of Turbomachinery, Vol. 115, January 1993, pp.1-9.

16. Day, I. J., "Active Suppression of Rotating Stall and Surge in Axial Compressors," Journal of Turbomachinery, Vol. 115, January 1993, pp. 40-47.

17. Paduano, J. P., Epstein, A. H., Valavani, L., Longely, J. P., Greitzer, E. M., and Guennette, G. R., "Active Control of Rotating Stall in a Low Speed Compressor," Journal of Turbomachinery, Vol. 115, January 1993, pp.48-56.

18. Haynes, J. M., Hendricks, G. J., and Epstein, A. H., "Active Stabilization of Rotating Stall in a Three-Stage Axial Compressor," Presented at The IGTI Gas Turbine Conference, Cincinnati, OH, June 1993.

19. Moore, F. K., "A Theory of Rotating Stall of Multistage Axial Compressors Parts I - III ," Journal of Engineering for Power, Vol. 106, 1984, pp. 313-336.

20. Hynes, T. P., and Greitzer, E. M., "A Method for Assessing Effects of Circumferential Flow Distortion on Compressor Stability," Journal of Turbomachinery, July 1987, Vol. 109, pp.371-379.

21. Den Hartog, J. P., Mechanical Vibrations, McGraw-Hill, New York, 1956.

22. Morse, P. M., and Ingard, K. U., Theoretical Acoustics, Princeton University Press, Princeton, N.J., 1968.

23. White, F. M., Viscous Fluid Flow, McGraw-Hill, New York, 1974.

24. Magnus, K., Vibrations, Blackie and Sons, London, 1965, p.112.

25. Paduano, J. D., "Active Control of Rotating Stall in Axial Compressors," Gas Turbine Laboratory Report No. 208, Massachusetts Institute of Technology, March 1992.

26. Paduano, J. D., and Gysling, D. L., "Modeling Axial Compressor Nonlinear Rotating Stall Phenomena for Control," Presented at the SIAM Conference on Control and Its Applications, Minneapolis, MN, 1992.

27. Gopalakrishnan, S., " An Unconventional Blade Design for Axial Compressors," Gas Turbine Laboratory Report No. 98, Massachusetts Institute of Technology, May 1969.

28. Wellstead, P. E., "Non-Parametric Methods of System Indentification," Automatica, Vol. 17, No. 1, pp.55-69, 1981.

29. Patrick, W. P., "Sound Transmission Through Lined Ducts in Parallel," Ph.D. Thesis, Department of Aeronautics and Astronautics, Massachusetts Institute of Technology, 1979.

30. Wylie, E. B., and Streeter, V. L., Fluid Transients, McGraw-Hill, New York, 1978.

31. Hendricks, G. J., and Gysling, D. L., "A Theoretical Study of Sensor_Actuator Schemes for Rotating Stall Control," AIAA Paper 92-3486, presented at the 28th

Joint Propulsion Conference, Nashville, TN, 1992. To appear in the Journal of Propulsion.

32. Greitzer, E. M., Nikkanen, J. P., Haddad, D. E., Mazzay, R. S., and Joslyn, H. D., "A Fundamental Criterion for the Application of Rotor Casing Treatment," Journal of Fluids Engineering, June, 1979, Vol. 101, pp. 237-243.

33. Meirovitch, L., Elements of Vibration Analysis, McGraw-Hill, New York, 1986.

34. Millsaps, K. T., Jr., " The Impact of Unsteady Swirling Flow in a Single Gland Labyrinth Seal on Rotordynamic Stability: Theory and Experiment', Ph.D. Thesis, Department of Aeronautics and Astronautics, M. I. T., May 1992.

35. Thwaites, B., Editor, Incompressible Aerodynamics, Oxford University Press, 1960.

APPENDIX A: Rotating Stall Analysis

The following derivation of the stability model is based the work of other authors. The assumptions have been developed in Chapter 2. The linearized analysis describes incompressible, two-dimensional, small amplitude, non-axisymmetric disturbances about a uniform flow field. The structure of the model consists of descriptions of the flow fields upstream and downstream of the compressor, which are matched across the compressor, modeled as a semi-actuator disk. A schematic of the flow field is shown in Figure 2.1 in Chapter 2.

Description of the Upstream Disturbance Flow Field:

The perturbation flow field in the upstream region is assumed to be two-dimensional, incompressible and irrotational, and it is convenient to use a streamfunction for its description. The non-dimensional perturbation streamfunction is defined by:

$$\delta v \equiv -\frac{\partial \Psi}{\partial x} \qquad \delta \phi \equiv \frac{\partial \Psi}{\partial \theta} \qquad \text{(A.1) and (A.2)}$$

where: $\delta\phi$ = axial velocity perturbation normalized by the compressor wheel speed

δv = circumferential velocity perturbation normalized by the compressor wheel speed

The streamfunction for the upstream flow field satisfies the two dimensional Laplace equation.

$$\nabla^2 \Psi_u = 0 \qquad \text{(A.3)}$$

Since the flow field is in an annular region, the disturbances must be spatially periodic around the annulus of the compressor. Therefore, the circumferential dependence of the disturbance can be expressed in terms of spatial Fourier components.

$$\Psi_u \approx \sum_{n=-\infty}^{+\infty} A_n e^{in\theta} \tag{A.4}$$

Allowing for the disturbances to rotate, or travel around the annulus, with an amplitude that is time varying, i.e. growing or decaying, leads to the following form for the circumferential and temporal dependence of the upstream streamfunction:

$$\Psi_u \approx e^{in(\theta-\sigma\tau)} g(x) \tag{A.5}$$

The axial dependence is found from solving the Laplace equation using separation of variables. There are two solutions for the axial dependence, one that grows and one that decays exponentially upstream of the compressor.

$$g(x) \approx e^{+nx}; e^{-nx} \tag{A.6}$$

Applying the condition that the disturbances must vanish far upstream of the compressor, i.e. the flow is uniform far upstream of the compressor, leads to the following general form for the disturbance stream function for the upstream flow field:

$$\Psi_u = \sum_{n=1}^{+\infty} A_n e^{in(\theta-\sigma\tau)+nx} \tag{A.7}$$

Description of the Downstream Flow Field:

The downstream flow field may be rotational due to vorticity shed into the flow from the compressor. However, to match the boundary conditions across the compressor, the circumferential and time dependence of the downstream flow field must have the same form as the upstream flow field at the actuator disk (x = 0). Therefore, the downstream flow field must have the form:

$$\Psi_d \approx e^{i n (\theta - \sigma \tau)} \, h (x) \tag{A.8}$$

Since the flow is rotational, the streamfunction is governed by the 2-dimensional Poisson equation:

$$\nabla^2 \Psi_d = - \omega \tag{A.9}$$

where $\omega \equiv \frac{\partial v}{\partial x} - \frac{\partial \phi}{\partial \theta}$ is the non-dimensional vorticity

Because the flow field is inviscid and two dimensional, the vorticity convects with the flow.

$$\frac{D \omega}{D \tau} = \frac{\partial \omega}{\partial \tau} + \Phi \frac{\partial \omega}{\partial x} + \Phi \tan \beta_d \frac{\partial \omega}{\partial \theta} = 0 \tag{A.10}$$

where: β_d = the flow angle in the downstream flow field

Substituting the form of the circumferential and time dependence of the disturbances into the vorticity equation, yields the axial dependence of the vorticity:

$$\omega \approx e^{in(\theta-\sigma\tau)-inx(\tan\beta_d-\frac{\sigma}{\Phi})} \tag{A.11}$$

The homogeneous (potential) solution to the Poisson equation governing the downstream flow field is of the same form as the solution the upstream flow field. The condition that the disturbances be finite far downstream of the compressor restricts the homogeneous solutions to those that decay axially downstream of the compressor. Combining the homogeneous and particular solutions yields the following general form of the downstream flow field.

$$\Psi_d = \sum_{n=1}^{+\infty} B_n e^{in(\theta-\sigma\tau)-nx} + \sum_{n=1}^{+\infty} C_n e^{in(\theta-\sigma\tau)-inx(\tan\beta_d-\frac{\sigma}{\Phi})} \tag{A.12}$$

Boundary Conditions across Compressor:

The kinematic and dynamic boundary conditions which link the two flow fields are governed by the properties of the compressor.

Mass Flow Continuity:

Assuming the compressor is short in axial length and that the flow through the compressor is incompressible, mass continuity dictates:

$$\delta\phi_u = \delta\phi_d \tag{A.13}$$

Exit Flow Angle

Assuming the last blade row has sufficient solidity to fix the exit flow angle, the circumferential velocity perturbation at the exit of the stator is linked to the axial velocity perturbation through the follow relation:

$$\delta v_d = - \tan \beta_d \, \delta \phi_d \tag{A.14}$$

Pressure Rise across Compressor:

The total to static pressure rise across the compressor is given by the quasi-steady compressor performance as a function of mass flow coefficient.

$$\Psi = \Psi (\Phi) \tag{A.15}$$

For small perturbations, the compressor is assumed to respond quasi-steadily with the exception of the inertial of the fluid within the blade rows.

$$\delta \Psi = \delta p_{s_d} - \delta p_{t_u} = \frac{\partial \Psi}{\partial \Phi} \delta \phi - \mu \frac{\partial \phi}{\partial \tau} - \lambda \frac{\partial \phi}{\partial \theta} \tag{A.16}$$

In the above expression, $\left(\frac{\partial \Psi}{\partial \Phi}\right)$ is the slope of the total to static compressor characteristic, μ represents the inertia of the fluid in all the (stationary and rotating) blade rows, and λ represents the inertia of the fluid within the rotating blade rows only.

Eigenvalue Problem:

Substituting the assumed forms for the upstream and downstream flow fields into the matching conditions across the actuator disk, assuming axial mean flow in the upstream and downstream flow fields ($\tan \beta_d = 0$), and using the circumferential momentum equation to relate perturbations in static pressure to the stream function,

$$- \frac{\partial p}{\partial \theta} = 2 \left(\frac{\partial v}{\partial \tau} + \Phi \frac{\partial v}{\partial x} + \Phi \tan \beta_d \frac{\partial v}{\partial \theta} \right) = 2 \left(\frac{\partial v}{\partial \tau} + \Phi \frac{\partial v}{\partial x} \right) \tag{A.17}$$

or in terms of the perturbation streamfunction:

$$-\frac{\partial p}{\partial \theta} = 2\left(-\frac{\partial^2 \Psi}{\partial \tau\, \partial x} - \Phi\frac{\partial^2 \Psi}{\partial x^2} - \Phi \tan \beta_d \frac{\partial^2 \Psi}{\partial \theta\, \partial x}\right) = 2\left(-\frac{\partial^2 \Psi}{\partial \tau\, \partial x} - \Phi\frac{\partial^2 \Psi}{\partial x^2}\right) \tag{A.18}$$

yields the following expression for the pressure rise across the compressor in terms of the upstream perturbation streamfunction:

$$\left[i\,\sigma(4 + n\,\mu) + \frac{\partial \Psi}{\partial \Phi} - i\,n\,\lambda\right] A_n = 0 \tag{A.19}$$

Eq. A.19 is an eigenvalue problem to determine the time dependence of the disturbance in a compression system with no mean inlet or exit swirl:

$$\sigma = \frac{\left(\frac{\partial \Psi}{\partial \Phi}\right) i + (n\,\lambda)}{4 + n\,\mu} \tag{A.20}$$

The stability of each spatial harmonic is independent, and the slope of the compressor characteristic, $\left(\frac{\partial \Psi}{\partial \Phi}\right)$, solely determines the stability of the axisymmetric flow field. The inertial parameters determine the rotation rate of the disturbances.

Modification to Include Swirl Sensitivity of Compressor:

The above analysis assumes that the compressor performance is determined by the mass flow coefficient and the inertial parameters. However, for compressors operating without inlet guide vanes, the pressure rise across the compressor can also be affected by the inlet swirl. Thus, the quasi-steady compressor characteristic is assumed to be a function of the mass flow coefficient and the inlet flow angle.

$$\Psi = \Psi (\Phi, \alpha) \tag{A.21}$$

where: α is the swirl angle

For uniform axial mean flow in the upstream flow field, the swirl angle of the flow, defined as positive in the direction of the rotation, is related to the circumferential velocity perturbation

$$\alpha = \tan^{-1}\left(\frac{\delta v}{\Phi}\right) = \frac{1}{\Phi}\delta v \text{ (for small disturbances)} \tag{A.22}$$

Incorporating the swirl sensitivity in the dynamic boundary condition across the compressor yields the following expression:

$$\delta \Psi = \frac{\partial \Psi}{\partial \Phi}\delta \phi + \frac{\partial \Psi}{\partial \alpha}\frac{1}{\Phi}\delta v - \lambda \frac{\partial \phi}{\partial \theta} - \mu \frac{\partial \phi}{\partial \tau} \tag{A.23}$$

where: $\frac{\partial \Psi}{\partial \alpha}$ is the swirl sensitivity of the compressor

Solving for the eigenvalues of the compression system, as developed above, including swirl sensitivity yields the following eigenvalues:

$$\sigma = \frac{\left(\frac{\partial \Psi}{\partial \Phi}\right) i + \left(n\lambda - \frac{1}{\Phi}\frac{\partial \Psi}{\partial \alpha}\right)}{4 + n\mu} \tag{A.24}$$

Assuming that swirl in the direction of the rotor decreases the pressure rise across the compressor, the sign of $\frac{\partial \Psi}{\partial \alpha}$ is negative. Thus, the net effect of including swirl sensitivity is only to increase the rotation rate of the disturbances, while having no effect on stability.

Appendix B: Rotating Stall Model with Dynamic Mass / Momentum Injection

The basic structure of the model used to assess the effect of dynamic mass / momentum injection on the stability of the axisymmetric flow field through the compression system is similar to that used for the compression system without feedback. The description of the flow field consists of an irrotational upstream flow field and a vortical flow field downstream of the compressor, with the two matched across the compressor with feedback. The effect of the dynamic mass / momentum injection is thus incorporated into the boundary conditions across the compressor.

Several assumptions regarding the injection process are assumed in this model:

1) The high velocity fluid is injected axially, within a short distance upstream of the compressor. The short distance is assumed short compared to the circumferential length scale of the disturbances.

2) The high velocity fluid mixes out to a span-wise uniform state before entering the compressor.

3) The pressure rise of the compressor remains a pure function of the mass flow coefficient entering the compressor, with the inertia of the fluid with the blade rows of the compressor being modeled as in Appendix A.

A schematic of the dynamic mass / momentum injection strategy is shown in Figure 2.4 and a schematic of the model is shown in Figure 2.6. The mass flow and pressure rise boundary conditions are derived below.

Conservation of Mass:

The mass flow entering the compressor is given by the sum of the mass flow upstream of the injection region and the injected fluid:

$$\rho C_{x_u} H + \rho C_{x_i} \Delta = \rho C_{x_b} H \tag{B.1}$$

where: Δ = reed valve opening

H = annulus height

C_{x_i} = velocity of injected fluid

C_{x_u} = axial velocity of upstream flow field

Non-dimensionalizing Eq. B.1 leads to:

$$\Phi_u + \Phi_i q = \Phi_b \tag{B.2}$$

where: $q = \frac{\Delta}{H}$

$\Phi = \frac{C_x}{U_R}$

Conservation of Momentum:

The injection process is model in two parts. The first uses Bernoulli's Equation for the flow from immediately upstream of the injection region (axial station denoted by u) to the injection location (axial station denoted by a), where the injected fluid displaces the free stream flow field. Up to the injection location, the flow is assumed to remain axial and uniform in the span-wise direction.

$$P_{s_u} + \frac{1}{2}\rho C_{x_u}^2 = P_{s_a} + \frac{1}{2}\rho C_{x_a}^2 \tag{B.3}$$

Applying continuity from the span-wise uniform region immediately upstream of the injection location to the axial location of the injection leads to:

$$\rho H C_{x_u} = \rho (H - \Delta) C_{x_a} \tag{B.4}$$

The momentum balance between injection location (a) and the mixed out region downstream of the injection (axial station b) is obtained by assuming that the axial momentum of the injected fluid is transferred to the flow. Applying conservation of axial momentum within a control volume encompassing the injection region, extending from the injection location to the span-wise uniform, mixed-out state, immediately upstream of the compressor yields:

$$P_{s_a} H + \rho (H - \Delta) C_{x_a}^2 + \rho \Delta C_{x_i}^2 = P_{s_b} H + \rho H C_{x_b}^2 \tag{B.5}$$

Eliminating the flow variables at the injection location leads to an expression relating the static pressure and axial velocity of the span-wise uniform states immediately upstream and downstream of the injection region as a function of local valve area and time mean compression system parameters.

$$P_{s_u} + \frac{1}{2} \rho (C_{x_u}^2 + 2 C_{x_i}^2 q) + \frac{1}{2} \rho C_{x_u}^2 \frac{(1 - 2 q)}{(1 - q)^2} = P_{s_b} + \rho C_{x_b}^2 \tag{B.6}$$

Assuming that the reed valve opening area is a small percentage of the annulus height

$$q << 1$$

and, thus, that the injected mass flow is much smaller than the free stream mass flow

$$\Phi_i q << \Phi_u$$

and that the total pressure in the injection plenum is constant, the linearized relation between the span-wise uniform total pressure change across the injection region is given in non-

dimensional form as a function of the injection parameters and the local reed valve area opening:

$$\delta p_{t_b} - \delta p_{t_u} = 2\,\Phi_i\,(\Phi_i - \Phi_u)\,\delta q \tag{B.7}$$

$$\text{where: } \delta p_t = \delta p_s + 2\,\Phi\,\delta\phi$$

Boundary Conditions across Compressor with Feedback:

The span-wise uniform, perturbation axial velocity and total pressure across the injection region is given in terms of the mean flow parameters and the local perturbation in injection area. Combining these relations with the mass flow and pressure rise boundary conditions across the compressor leads to the mass flow and pressure rise boundary conditions across the compressor with dynamic mass / momentum injection.

Mass Flow:

$$\delta\phi_u + \Phi_i\,\delta q = \delta\phi_d \tag{B.8}$$

Pressure Rise:

$$\delta p_{s_d} - \delta p_{t_u} = \frac{\partial\Psi}{\partial\Phi}\,\delta\phi_u + \frac{\partial\Psi}{\partial\Phi}\,\Phi_i\,\delta q - \mu\frac{\partial\phi_u}{\partial\tau} - \mu\,\Phi_i\frac{\partial q}{\partial\tau} - \lambda\frac{\partial\phi_u}{\partial\theta} - \lambda\,\Phi_i\frac{\partial q}{\partial\theta} + 2\,\Phi_i\,(\Phi_i - \Phi_u)\,\delta q \tag{B.9}$$

Exit Flow Angle:

The exit flow angle boundary conditions remains unchanged from the basic compression system analysis, i.e. the flow in the downstream duct is axial and the flow angle is fixed by the exit blade angle.

$$\delta v_d = 0 \qquad \text{(B.10)}$$

Expressing the boundary conditions across the actuator disk in terms of the solution forms for the upstream and downstream flow fields leads to an expression relating the complex amplitude of the upstream perturbation streamfunction to the local reed valve displacement.

$$\left[i\,(4 + \mu n)\,\sigma + \frac{\partial \Psi}{\partial \Phi} - i\,\lambda\, n \right] A_n + \left[\Phi_i \left(\frac{2}{n} + \mu \right) \sigma - \lambda\, \Phi_i - \frac{\partial \Psi}{\partial \Phi} \Phi_i + 2\, \Phi_i\, (\Phi_i - \Phi_u) \right] q_n = 0 \qquad \text{(B.11)}$$

where $$\Psi_u = \sum_{n=1}^{+\infty} A_n\, e^{i n (\theta - \sigma \tau) + n x}$$

and $$q = \sum_{n=1}^{+\infty} q_n\, e^{i n (\theta - \sigma \tau)}$$

Structural Feedback

The structural dynamics of the reed valves relate reed valve displacement to the static pressure perturbations in the upstream flow field, thus providing the dynamic feedback. The reed valves are modeled as second order, locally reacting mass-spring-damper systems in the first cantilever bending mode, and are assumed to be continuous in the circumferential direction.

The dynamics of the reed valves were calculated by choosing a mode shape for the first cantilevered bending mode.

$$\Delta \left(\frac{x}{L}, t\right) = \Delta\,(t)\, \xi\left(\frac{x}{L}\right) \qquad \xi\left(\frac{x}{L}\right) \equiv \left(\frac{x}{L}\right)^2 \qquad \text{(B.12 and B.13))}$$

The equation of motion for the reed valves, expressed in terms of the tip deflection, based on the one mode approximation is given by:

$$M\ddot{\Delta} + B\dot{\Delta} + K\Delta = \Xi(t) \tag{B.14}$$

Where:

$$\Xi(t) \equiv \text{Modal Forcing Function} = \int_0^1 \xi\left(\frac{X}{L}\right) \delta P_{s_u} \, d\left(\frac{X}{L}\right) . \tag{B.15}$$

Assuming that the static pressure perturbation is constant over the axial extent of the reed valve, i.e. n L / R << 1,:

$$\Xi(t) = \frac{1}{3} L \, \delta P_{s_u} \tag{B.16}$$

and:

$$M \equiv \text{Modal Mass} = \int_0^1 \xi\left(\frac{X}{L}\right)^2 m\left(\frac{X}{L}\right) \, d\left(\frac{X}{L}\right) \tag{B.17}$$

where m = the mass per unit circumference per unit axial length of the reed valves

$$B \equiv \text{Modal Damping} = \int_0^1 \xi\left(\frac{X}{L}\right)^2 b\left(\frac{X}{L}\right) \, d\left(\frac{X}{L}\right) \tag{B.18}$$

$$K \equiv \text{Modal Stiffness} = \int_0^1 \xi\left(\frac{X}{L}\right)^2 k\left(\frac{X}{L}\right) \, d\left(\frac{X}{L}\right) \tag{B.19}$$

Defining the following non-dimensional parameters:

$$\tau \equiv \frac{t \, U_R}{R} \qquad q \equiv \frac{\Delta}{H} \qquad \tilde{L} \equiv \frac{L}{H} \tag{B.18), (B.20) and (B.21)}$$

and using the standard expressions for the natural frequency and critical damping ratio for second order, damped, harmonic oscillators:

$$\omega_n \equiv \sqrt{\frac{K}{M}} \qquad \zeta \equiv \frac{B}{2\,M\,\omega_n} \qquad \text{(B.22) and (B.23)}$$

and defining non-dimensional mass and frequency parameters:

$$W \equiv \frac{\rho_0\,R^2}{M}\,\tilde{L} \qquad Q \equiv \frac{\omega_n\,R}{U_R} \qquad \text{(B.24) and (B.25)}$$

leads to the following non-dimensional expression for the locally reacting reed valve dynamics:

$$\frac{\partial^2 q}{\partial \tau^2} + 2\,Q\,\zeta\,\frac{\partial q}{\partial \tau} + Q^2\,\delta q = \frac{1}{6}\,W\,\delta p_{s_u} \qquad \text{(B.26)}$$

Using Eq. B.26, the transfer function between reed displacement and static pressure is given by:

$$\frac{\delta q\,(\omega)}{\delta p_u\,(\omega)} = \frac{\frac{1}{6}\,W}{\left(Q^2 - \omega^2\right) + 2\,Q\,\zeta\,i\,\omega} \qquad \text{(B.27)}$$

where ω is the temporal frequency normalized by the rotor frequency.

The static pressure perturbations in the upstream flow field can be related to the perturbation streamfunction, Ψ_u, in the upstream flow field via the circumferential momentum equation.

$$\frac{\partial p_{s_u}}{\partial \theta} = 2 \left(\frac{\partial^2 \Psi_u}{\partial x \, \partial \tau} + \Phi_u \frac{\partial^2 \Psi_u}{\partial x^2} \right) \tag{B.28}$$

Thus, the reed valve dynamics and the upstream streamfunction are related by:

$$\frac{\partial^3 q}{\partial \theta \, \partial \tau^2} + 2\,Q\,\zeta \frac{\partial^2 q}{\partial \theta \, \partial \tau} + Q^2 \frac{\partial q}{\partial \theta} = \frac{1}{3} W \left(\frac{\partial^2 \Psi_u}{\partial x \, \partial \tau} + \Phi \frac{\partial^2 \Psi_u}{\partial x^2} \right) \tag{B.29}$$

Expanding the second order (in time) expression for the reed valve dynamics into two first order equations, the reed valve dynamics can be expressed as follows:

$$\frac{\partial^2 z}{\partial \theta \, \partial \tau} + 2\,Q\,\zeta \frac{\partial z}{\partial \theta} + Q^2 \frac{\partial q}{\partial \theta} = \frac{1}{3} W \left(\frac{\partial^2 \Psi_u}{\partial x \, \partial \tau} + \Phi \frac{\partial^2 \Psi_u}{\partial x^2} \right) \tag{B.30}$$

where the time rate of change of the reed valve displacement is given by z:

$$\frac{\partial q}{\partial \tau} = z \tag{B.31}$$

Substituting the solution forms for the perturbation variables leads to the following expressions relating the reed valve displacement and velocity to the upstream flow field:

$$\frac{1}{3} W n^2 \, (i \sigma - \Phi_u) \, A_n + i n Q^2 \, q_n + (n^2 \sigma + 2 Q \zeta i n) \, z_n = 0 \tag{B.32}$$

$$i n \sigma q_n + z_n = 0 \tag{B.33}$$

Eigenvalue Problem:

Combining Eq. B.32 and Eq. B.33 leads to a third order, generalized, complex eigenvalue problem governing the stability of the uniform, axisymmetric flow field through the compressor with aeromechanical feedback.

$$[\mathbf{A} - \sigma \mathbf{B}] \begin{Bmatrix} \delta A_n \\ \delta q_n \\ \delta z_n \end{Bmatrix} = 0 \tag{B.34}$$

The matrix **A** is defined as:

$$A = \begin{bmatrix} \frac{\partial \Psi}{\partial \Phi} - i n \lambda & A_{12} & 0 \\ -\frac{1}{3} W n^2 \Phi_u & i n Q^2 & i n 2 Q \zeta \\ 0 & 0 & 1 \end{bmatrix} \tag{B.35}$$

with $$A_{12} \equiv -\lambda \Phi_i - i \frac{\Phi_i}{n} \left(\frac{\partial \Psi}{\partial \Phi} + 2 (\Phi_i - \Phi_u) \right)$$

The Matrix **B** is defined as:

$$B = \begin{bmatrix} -i(4 + n\mu) & -(\frac{2}{n} + \mu)\Phi_i & 0 \\ -i\frac{1}{3} W n^2 & 0 & -n^2 \\ 0 & -in & 0 \end{bmatrix} \tag{B.34}$$

Appendix C: Rotating Stall Model with Dynamic Mass / Momentum Injection with Alternative Actuation Model

The detailed fluid mechanics of the in mixing process of the injection with the upstream flow field is a complex problem. In Appendix B, the injection process was modeled assuming the flow mixed out before entering the compressor. In this appendix, a model for the effect of the dynamic mass / momentum injection is presented assuming that the injection fluid does not mix out. The model assumes that the compressor performance is modified by changing the velocity profile entering the compressor. Thus, the injected fluid is assumed to remain within the region close to the tip of the compressor.

The basic structure of the model is similar to the structure of the models used through out this thesis. The model consists of an irrotational upstream flow field and a vortical flow field downstream of the compressor, and the two flow fields are matched across the compressor. The effect of the dynamic mass / momentum injection on the flow fields is incorporating into the boundary conditions across the compressor.

Several assumptions regarding the injection process are assumed in this model:

1) The high velocity fluid is injected axially, within a short distance upstream of the compressor. The short distance is assumed to be short compared to the circumferential length scale of the disturbances.

2) The high velocity fluid remains in the boundary layer region, close to the tip of the compressor, and thus has no kinematic effect on the core flow of the upstream flow field.

3) The pressure rise of the compressor is a function of the mass flow coefficient of the core flow entering the compressor and the shape of the axial boundary layer entering the compressor. The effect of the fluid inertia within the blade rows of the compressor on the pressure rise is modeled as in Appendix A.

4) The shape of the axial velocity profile is parameterized by the amount of axial momentum injected into the compressor, normalized by the span-wise averaged momentum of the mean core flow.

The model for the two-dimensional, incompressible, inviscid flow field is the same as that for the basic compression system shown in Figure 2.1.

Boundary Conditions across the Compressor

Conservation of Mass:

Since the injected fluid is assumed to remain in the tip region, primarily modifying the axial velocity profile in that region, the injection is assumed to not directly influence the mass flow of the core flow. Thus, the mass flow through the compressor is assumed to be continuous:

$$\Phi_u = \Phi_d \tag{C.1}$$

Conservation of Momentum:

The mean pressure rise across the compressor is assumed to be a function of the mass flow coefficient and the amount of momentum (normalized by the momentum of the free stream) injected into the upstream tip region.

$$\Psi = \Psi (\Phi, \alpha_i) \tag{C.2}$$

$$\alpha_i \equiv \left(\frac{\Phi_i}{\Phi_u}\right)^2 q$$

where (C.3)

Assuming the compressor responds to small perturbations in a quasi-steady manner, yet accounting for the inertia of the fluid within the compressor, the perturbation in pressure rise across the compressor is given by:

$$\delta p_{s_d} - \delta p_{t_u} = \frac{\partial \Psi}{\partial \Phi} \delta \phi_u + \frac{\partial \Psi}{\partial \alpha_i} \delta \alpha_i - \mu \frac{\partial \phi_u}{\partial \tau} - \lambda \frac{\partial \phi_u}{\partial \theta} \tag{C.4}$$

where $\frac{\partial \Psi}{\partial \alpha_i}$ is the change in pressure rise for a small change in momentum injected

Expressing the normalized perturbation in axial momentum injected in terms of the reed valve area opening (assuming that the mean reed valve opening is small compared to annulus height) yields:

$$\delta \alpha_i \equiv \left(\frac{\Phi_i}{\Phi_u}\right)^2 \delta q \tag{C.5}$$

Substituting Eq. C.5 into Eq. C.4 leads to the following expression for the pressure rise across the compressor:

$$\delta p_{s_d} - \delta p_{t_u} = \frac{\partial \Psi}{\partial \Phi} \delta \phi_u + \frac{\partial \Psi}{\partial \alpha_i} \left(\frac{\Phi_i}{\Phi_u}\right)^2 \delta q - \mu \frac{\partial \phi_u}{\partial \tau} - \lambda \frac{\partial \phi_u}{\partial \theta} \tag{C.6}$$

Exit Flow Angle:

The exit flow angle boundary condition remains the same as in the basic compression system analysis, i.e. the flow in the downstream duct is axial and the flow angle is fixed by the exit blade angle.

$$\delta v_d = 0 \tag{C.7}$$

Expressing the boundary conditions across the actuator disk in terms of solutions for the upstream and downstream flow fields leads to an expression relating the complex amplitude of the upstream perturbation streamfunction to the local reed valve displacement.

$$\left[i\,(4+\mu n)\,\sigma + \frac{\partial \Psi}{\partial \Phi} - i\,\lambda\, n \right] A_n + \left[\frac{\partial \Psi}{\partial \alpha_i} \left(\frac{\Phi_i}{\Phi_u} \right)^2 \right] q_n = 0 \tag{C.8}$$

where $$\Psi_u = \sum_{n=1}^{+\infty} A_n\, e^{i n (\theta - \sigma\tau) + n x}$$

and $$q = \sum_{n=1}^{+\infty} q_n\, e^{i n (\theta - \sigma\tau)}$$

Structural Feedback

The structural dynamics of the reed valves which relate the reed valve displacement to the static pressure perturbations in the upstream flow field are the same as the original model as developed in Appendix B. The reed valves are modeled as second order, locally reacting mass-spring-damper systems in the first cantilever bending mode. The reed valves are assumed to be continuous in the circumferential direction.

$$\frac{\partial^2 q}{\partial \tau^2} + 2\,Q\,\zeta \frac{\partial q}{\partial \tau} + Q^2\,\delta\, q = \frac{1}{6}\,W\,\delta P_{s_u} \tag{C.9}$$

As shown in Appendix B, expressing the static pressure perturbations in the upstream flow field in terms of the perturbation streamfunction and expressing the reed valve dynamics as

two first order (in time) equations leads to the following expressions relating nth spatial harmonics of the reed valve displacement and velocity, and upstream streamfunction:

$$\frac{1}{3} W n^2 (i \sigma - \Phi_u) A_n + i n Q^2 q_n + (n^2 \sigma + 2 Q \zeta i n) z_n = 0 \qquad \text{(C.10)}$$

Where the nth spatial harmonics of the reed valve displacement and reed valve velocity is given by:

$$i n \sigma q_n + z_n = 0 \qquad \text{(C.11)}$$

Eigenvalue Problem:

Combining Eq. C.11 and Eq. C.12 leads to a third order, generalized, complex eigenvalue problem governing the stability of the uniform, axisymmetric flow field through the compressor with aeromechanical feedback.

$$[A - \sigma B] \begin{Bmatrix} \delta A_n \\ \delta q_n \\ \delta z_n \end{Bmatrix} = 0 \qquad \text{(C.12)}$$

where the matrix **A** is given by:

$$A = \begin{bmatrix} \frac{\partial \Psi}{\partial \Phi} - i n \lambda & -\frac{i}{n} \frac{\partial \Psi}{\partial \alpha_i} \left(\frac{\Phi_i}{\Phi_u} \right)^2 & 0 \\ -\frac{1}{3} W n^2 \Phi_u & i n Q^2 & i n 2 Q \zeta \\ 0 & 0 & 1 \end{bmatrix}$$

where the matrix **B** is given by:

$$\mathbf{B} = \begin{bmatrix} -i(4+n\mu) & 0 & 0 \\ -i\frac{1}{3}W n^2 & 0 & -n^2 \\ 0 & -in & 0 \end{bmatrix}$$

The stability derivative, $\frac{\partial \Psi}{\partial \alpha_i}$, can be estimated from the steady state performance of the compressor for several injection rates operating near the stalling flow coefficient. An estimate of $\frac{\partial \Psi}{\partial \alpha_i}$ for the optimal injection rate, $\Phi_i = 1.0$, was determined to be on the order of $\frac{\partial \Psi}{\partial \alpha_i} = 0.1$.

The model developed in this appendix assuming that the flow does not mix out can be compared to the model developed in Appendix B assuming that the flow mixes out by comparing the expression for the pressure rise across the compressor, Eq. C.6 and Eq. B.9, respectively. The perturbation in total to static pressure rise for a given, static and spatially uniform, reed valve displacement is given by:

$$\delta p_{s_d} - \delta p_{t_u} = 2\,\Phi_i\left(\Phi_i - \Phi_u\right)\delta q + \frac{\partial \Psi}{\partial \Phi}\Phi_i\,\delta q \qquad \text{(for the mixed out model)}$$

and

$$\delta p_{s_d} - \delta p_{t_u} = \frac{\partial \Psi}{\partial \alpha_i}\left(\frac{\Phi_i}{\Phi_u}\right)^2 \delta q \qquad \text{(for the not mixed out model)}$$

Using estimated values for the following parameters for the optimized configuration operating near stall,

$$\Phi_i = 1.0$$

$$\Phi_u = 0.4$$

$$\frac{\partial \Psi}{\partial \alpha_i} = 0.1$$

$$\frac{\partial \Psi}{\partial \Phi} = 0.0$$

The change in total to static pressure rise is given by:

$$\delta p_{s_d} - \delta p_{t_u} = (1.2)\,\delta q \qquad \text{for the mixed out model}$$

and

$$\delta p_{s_d} - \delta p_{t_u} = (0.63)\,\delta q \qquad \text{for the not mixed out model}$$

Thus, although not identical, the effect of the injection on the total to static pressure rise across the compressor as a function of steady, circumferentially uniform, reed valve displacement for the two limiting cases of the flow mixing out and not mixing out is similar.

Appendix D: Conservation Equation for 2-Dimensional, Incompressible, Inviscid Flow

In this appendix, a conservation equation is derived that is applicable to 2-dimensional, incompressible, inviscid flow fields such as those examined in the rotating stall analysis used in this thesis. The conservation equation provides a rigorous definition for the conserved quantities in the flow fields. The approach taken is similar to the approach used in acoustics to define the principle of conservation of the flux of acoustic intensity.

The conservation equation is derived using the linearized continuity and momentum equations. The 2-D, incompressible, inviscid momentum equation is given, in dimensional form, by:

$$\frac{\partial \vec{U}}{\partial t} + \vec{U} \cdot \nabla \vec{U} + \frac{1}{\rho} \nabla P = 0 \tag{D.1}$$

The velocity field is assumed to be given by a uniform, mean flow quantity and a small perturbation,

$$\vec{U} = (\overline{U} + u)\hat{i} + (\overline{V} + v)\hat{j} \tag{D.2}$$

where $\hat{i}$ and $\hat{j}$ are unit vectors in an orthogonal coordinate system.

The pressure field is given by a uniform, mean pressure and a small perturbation:

$$P = \overline{P} + p \tag{D.3}$$

Linearizing the momentum equation, neglecting terms on the order of the small perturbations squared:

$$\frac{\partial \vec{u}}{\partial t} + \vec{\vec{U}} \cdot \nabla \vec{u} + \frac{1}{\rho} \nabla p = 0 \tag{D.4}$$

Taking the dot product of the linearized momentum equation and the perturbation velocity vector yields a scalar equation:

$$\vec{u} \cdot \left[\frac{\partial \vec{u}}{\partial t} + \vec{\vec{U}} \cdot \nabla \vec{u} + \frac{1}{\rho} \nabla p \right] = 0 \tag{D.5}$$

Eq. D.5 can be expressed in terms of a time rate of change of a scalar quantity and the divergence of a vector field by expanding the above expression (Eq. D.5) in terms of scalar quantities for a 2-D flow field yields:

$$\left\langle u \frac{\partial u}{\partial t} + v \frac{\partial v}{\partial t} \right\rangle + \left[\overline{U} u \frac{\partial u}{\partial x} + \overline{V} u \frac{\partial u}{\partial y} + \overline{U} v \frac{\partial v}{\partial x} + \overline{V} v \frac{\partial v}{\partial y} \right] + \left\{ \frac{1}{\rho} u \frac{\partial p}{\partial x} + \frac{1}{\rho} v \frac{\partial p}{\partial y} \right\} = 0 \tag{D.6}$$

and noting that the terms in the brackets in Eq. D.6 can by expressed as follows:

$$\left\langle u \frac{\partial u}{\partial t} + v \frac{\partial v}{\partial t} \right\rangle = \frac{\partial}{\partial t} \left(\frac{u^2 + v^2}{2} \right) \tag{D.7}$$

$$\left[\overline{U} u \frac{\partial u}{\partial x} + \overline{V} u \frac{\partial u}{\partial y} + \overline{U} v \frac{\partial v}{\partial x} + \overline{V} v \frac{\partial v}{\partial y} \right] = \nabla \cdot \left(\frac{u^2 + v^2}{2} \vec{\vec{U}} \right) - \left(\frac{u^2 + v^2}{2} \right) \left(\nabla \cdot \vec{\vec{U}} \right) \tag{D.8}$$

$$\left\{ u \frac{\partial p}{\partial x} + v \frac{\partial p}{\partial y} \right\} = \nabla \cdot (p \vec{u}) - p (\nabla \cdot \vec{u}) \tag{D.9}$$

Thus, using Eqs. D.7 through D.9, and using the continuity equation for incompressible flow,

$$\nabla \cdot \vec{U} = 0 \Rightarrow \nabla \cdot \vec{u} = 0 \text{ and } \nabla \cdot \vec{\vec{U}} = 0 \tag{D.10}$$

the dot product of the perturbation velocity field and the linearized momentum equation can be expressed in the form of a conservation equation for 2-dimensional, incompressible, inviscid flow:

$$\frac{\partial}{\partial t}\left[\rho \frac{(u^2 + v^2)}{2}\right] + \nabla \cdot \left[\rho \frac{(u^2 + v^2)}{2} \vec{\vec{U}} + p\,\vec{u}\right] = 0 \tag{D.11}$$

Integrating the conservation equation over a volume of fluid in which the linearized momentum and continuity equations apply yields:

$$\int_{Volume} \frac{\partial}{\partial t}\left[\rho \frac{(u^2 + v^2)}{2}\right] dV + \int_{Volume} \nabla \cdot \left[\rho \left(\frac{u^2 + v^2}{2}\right) \vec{\vec{U}} + p\,\vec{u}\right] dV = 0 \tag{D.12}$$

For steady state conditions with oscillatory disturbances, the temporal average of the first integral is zero, and thus, for oscillatory disturbances, the time averaged conservation equation (Eq. D.12), evaluated over a volume of fluid, reduces to

$$\int_{Volume} \nabla \cdot \left[\rho \left(\frac{u^2 + v^2}{2}\right) \vec{\vec{U}} + p\,\vec{u}\right] dV = 0 \tag{D.12a}$$

Defining the perturbation intensity,

$$\vec{F} \equiv \left[\rho \left(\frac{u^2 + v^2}{2}\right) \vec{\vec{U}} + p\,\vec{u}\right] \tag{D.13}$$

and using the Divergence Theorem,

$$\int_{Volume} \nabla \cdot \vec{F}\, dV = \int_{Surface} \vec{F} \cdot \vec{n}\, dS \tag{D.14}$$

the time averaged conservation equation can be expressed as a conservation of flux over a closed surface.

$$\int_{Surface} \left[p\,\vec{u} + \frac{1}{2}\rho\left(u^2 + v^2\right)\vec{\overline{U}} \right] \cdot \vec{n}\, dS = 0 \tag{D.15}$$

If the control volume contains regions of the flow field in which the linearized momentum and / or continuity equations do not apply, the flux of the perturbation intensity through a closed surface surrounding the region can be defined as a source term.

$$\int_{Surface} \left[p\,\vec{u} + \frac{1}{2}\rho\left(u^2 + v^2\right)\vec{\overline{U}} \right] \cdot \vec{n}\, dS = \text{Source Term} \tag{D.16}$$

Application of the Conservation Equation to the Rotating Stall Analysis:
Equation D.16 can be applied to the stability analysis of the compressor flow field at neutral stability in order to interpret the role of the individual components of the flow field in terms of perturbation intensity. Consider the control volumes shown in Figure D.1. One control volume surrounds the upstream flow field and the other surrounds the downstream flow field. By evaluating the flux of the perturbation intensity through the control volumes, an audit of the sources of perturbation intensity can be performed.

The flux of the quantity defined above through an axial plane of an unit area is a scalar quantity given by:

$$\left[p\,u + \frac{1}{2}\rho\left(u^2 + v^2\right)\overline{U} \right] \tag{D.17}$$

For the rotating stall analysis, the perturbations far upstream are zero, and the flux of perturbation intensity through surface I is, therefore, zero. Since the there are no source regions in the upstream flow field, the perturbation intensity is conserved in the upstream flow field. Therefore, by Eq. D.15, the flux of perturbation intensity at surface II is also zero.

The production of perturbation intensity across the compressor can be determined by calculating the change in flux across the compressor using the compressor boundary conditions which relate pressure and velocity perturbations across the compressor. The change in flux of perturbation intensity across the compressor is given by the difference in perturbation intensity flux through surface III (immediately downstream of the compressor) and the flux through surface II (immediately upstream of the compressor):

$$\int_{\text{annulus}} \left[p_{s_d} u_d + \frac{1}{2} \rho \left(u_d^2 + v_d^2 \right) \overline{U} \right] - \left[p_{s_u} u_u + \frac{1}{2} \rho \left(u_u^2 + v_u^2 \right) \overline{U} \right] = \text{Source Term} \tag{D.18}$$

Using the dimensional form of the boundary conditions across the compressor developed in Appendix A:

$$u_u = u_d \tag{D.19}$$

$$v_d = 0 \tag{D.20}$$

$$p_{s_d} - p_{t_u} = p_{s_d} - \left(p_{s_u} + \rho \, \overline{U} \, u \right) = \left(\frac{\partial \Psi}{\partial \Phi} - \mu \frac{\partial}{\partial \tau} - \lambda \frac{\partial}{\partial \theta} \right) \left(\frac{1}{2} \rho \, U_R \right) u \tag{D.21}$$

The change in perturbation flux across the compressor can be written as:

$$\int_{annulus} \left[(p_{s_d} - p_{s_u})\, u + \frac{1}{2} \rho\, v_{\tilde{u}}^2\, \overline{U} \right] = \text{Source Term} \tag{D.22}$$

Using the result from the stability analysis, at neutral stability the slope of the total to static compressor characteristic is zero and the static pressure across the compressor is given by:

$$(p_{s_d} - p_{s_u}) = \rho\, \overline{U}\, u - \left(\mu \frac{\partial u}{\partial \tau} + \lambda \frac{\partial u}{\partial \theta} \right) \left(\frac{1}{2} \rho\, U_R \right) \tag{D.23}$$

At neutral stability the perturbations through the compressor are harmonic in time and in circumferential position. Therefore, the product of the axial velocity perturbation and the derivatives in time and circumferential position of the axial velocity integrate to zero over the annulus. Thus, the annulus averaged change in flux of perturbation intensity, or perturbation intensity production, across the compressor is given by:

$$\int_{annulus} \left[\rho\, \overline{U}\, u^2 - \frac{1}{2} \rho\, v_{\tilde{u}}^2\, \overline{U} \right] = \text{Source Term} \tag{D.24}$$

The production of perturbation intensity across the compressor must balance the flux of perturbation intensity through surface IV, far downstream of the compressor. Since the potential mode in the downstream flow field decays exponentially with axial distance downstream of the compressor, only the vortical mode is present at this location. For the vortical mode, the first order perturbation in static pressure is zero, and the flux of perturbation intensity through surface IV is given by:

$$\int_{annulus} \left[\frac{1}{2} \rho \left(u_{d_v}^2 + v_{d_v}^2 \right) \overline{U} \right] \tag{D.25}$$

Where u_{d_v} and v_{d_v} are the axial and circumferential velocity perturbations associated with the downstream vortical mode.

The balance between perturbation intensity produced across the compressor and the flux of perturbation intensity far downstream of the compressor is therefore given by equating (D.24) and (D.25):

$$\int_{annulus} \left[\rho \, \overline{U} \, u_{\tilde{u}_p}^2 - \frac{1}{2} \rho \, v_{\tilde{u}_p}^2 \, \overline{U} \right] \doteq \int_{annulus} \left[\frac{1}{2} \rho \left(u_{\tilde{d}_v}^2 + v_{\tilde{d}_v}^2 \right) \overline{U} \right] \tag{D.26}$$

Where u_{u_p} and v_{u_p} are the axial and circumferential velocity perturbations associated with the upstream potential mode.

Since the mean axial flow field is constant throughout the flow field and the flow is incompressible, showing that Eq. D.26 is valid reduces to showing that the two expressions below are equivalent:

$$\left(2 \, u_{\tilde{u}_p}^2 - v_{\tilde{u}_p}^2 \right)_{\substack{annulus \\ averaged}} \doteq \left(u_{\tilde{d}_v}^2 + v_{\tilde{d}_v}^2 \right)_{\substack{annulus \\ averaged}} \tag{D.27}$$

In a potential flow, axial and circumferential velocity perturbations are equal in magnitude and in quadrature, i.e. 90 degrees out of phase. Therefore, the following relation holds for the annulus average of the perturbation velocities in the upstream flow field:

$$\left(2 \, u_{\tilde{u}_p}^2 - v_{\tilde{u}_p}^2 \right)_{\substack{annulus \\ averaged}} = \left(u_{\tilde{u}_p}^2 \right)_{\substack{annulus \\ averaged}} \tag{D.28}$$

Using Eq. D.28, Eq. D.27 can be expressed as:

$$\left(u_{\tilde{u}_p}^2 \right)_{\substack{annulus \\ averaged}} \doteq \left(u_{\tilde{d}_v}^2 + v_{\tilde{d}_v}^2 \right)_{\substack{annulus \\ averaged}} \tag{D.29}$$

Decomposing the upstream and downstream flow field in terms of potential and vortical modes, the continuity equation across the compressor can be written as:

$$u_{u_p} = u_{d_p} + u_{d_v} \tag{D.30}$$

Similarly, the exit flow angle condition on the downstream flow field can be written as:

$$v_{d_p} = - v_{d_v} \tag{D.31}$$

Using mass flow continuity (Eq. D.30):

$$(u_{u_p})^2 = (u_{d_p})^2 + (2\, u_{d_p} u_{d_v}) + (u_{d_v})^2 \tag{D.32}$$

From the relation between the axial and circumferential velocities associated with a vortical disturbance, the downstream axial and circumferential vortical perturbations are in phase at neutral stability and are related by:

$$(u_{d_v}) = \frac{\overline{U}\, R}{\omega_{rs}} (v_{d_v}) \tag{D.33}$$

Where ω_{rs} is the frequency of the rotating disturbance and R is the mean radius of the compression system.

Using the exit flow angle condition (Eq. D.31), one can show that the downstream circumferential velocity associated with the vortical perturbation is in phase with the downstream circumferential velocity associated with the potential perturbation. Therefore, the downstream axial velocity associated with the vortical perturbation and the downstream axial velocity associated with the potential perturbation are in quadrature, and do not

contribute to the annulus averaged perturbation flux. Therefore, Eq. D.32 can be expressed as:

$$\left(u_{u_p}\right)^2 = \left(u_{d_p}\right)^2 + \left(u_{d_v}\right)^2 \underset{\text{averaged}}{\text{annulus}} \tag{D.34}$$

The annulus averaged square of the axial and circumferential velocities associated with the downstream potential perturbations are equivalent.

$$\left(u_{d_p}\right)^2 = \left(v_{d_p}\right)^2 \underset{\text{averaged}}{\text{annulus}} \tag{D.35}$$

Substituting Eq. D.35 and the exit flow angle boundary condition (Eq. D.31), into Eq. D.34, the annulus average of the square of the perturbation velocities can be written:

$$\left(u_{u_p}\right)^2 = \left(u_{d_v}\right)^2 + \left(v_{d_v}\right)^2 \underset{\text{averaged}}{\text{annulus}} \tag{D.36}$$

Eq. D.36 is the same as Eq. D.29, and thus, the results from the linear stability analysis for the compressor flow field at neutral stability confirm that perturbation intensity is conserved with in the upstream and downstream flow fields and that the production of perturbation intensity across the compressor at neutral stability is balanced by the flux of perturbation intensity in the downstream vortical flow field.

Although applying the conservation analysis to the rotating stall flow field yields no additional information not contained in the linear stability analysis, it is a rigorous application of the conservation principle of a quantity (perturbation intensity) that scales with the perturbation quantities squared and lends credence to the simplified, and therefore, intuitively useful, (although non rigorous) unsteady energy arguments presented in Chapter 2.

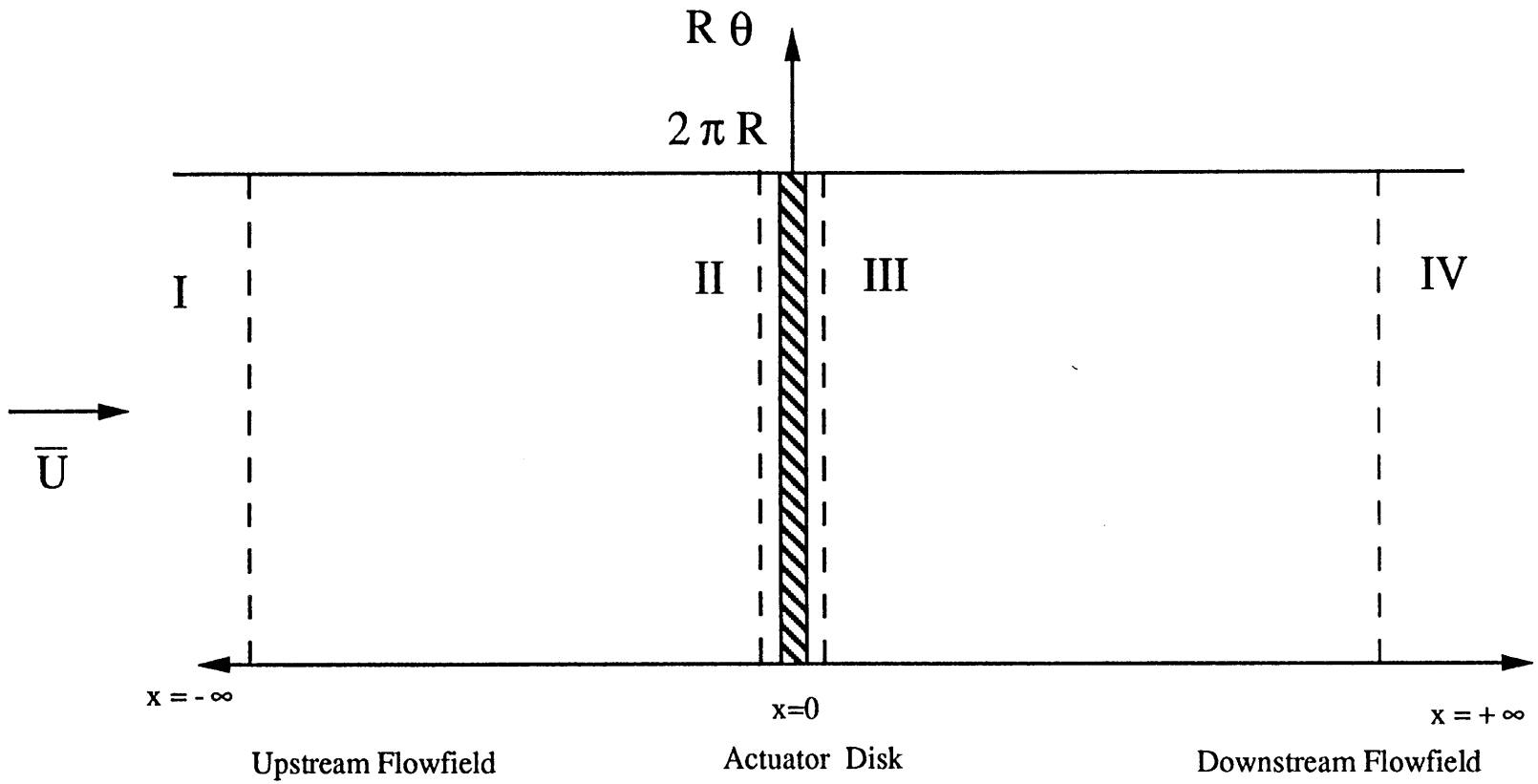

Figure D.1: Control Volume for Application of Conservation of Perturbation Intensity

Appendix E: Galerkin Based Non-Linear Simulation

In order to assess the effect of finite amplitude disturbances on the compression system, a Galerkin procedure was applied to numerically simulate finite amplitude, non-axisymmetric compression system dynamics. The non-linear simulation developed in this appendix retains a linearized description of the upstream and downstream flow fields. The only non-linearity included is the non-linearity of the compressor pressure rise versus mass flow pressure rise. The Galerkin procedure includes the two lowest spatial harmonics for the compression system with dynamic mass / momentum injection. The annulus averaged mass flow coefficient is assumed to be constant in the simulation.

The small amplitude rotating stall dynamics of the compression system are governed by the three first order in time, partial differential equations.

Pressure Rise PDE:

Based on the model developed in Appendix B, the pressure balance across the compressor with feedback can be expressed in terms of the upstream flow field (evaluated at x=0) and reed valve deflection:

$$\frac{\partial \Psi}{\partial \Phi}\frac{\partial^2 \Psi_u}{\partial \theta^2} + 4\frac{\partial^2 \Psi_u}{\partial \tau\, \partial x} - \mu\frac{\partial^3 \Psi_u}{\partial \tau\, \partial \theta^2} - \lambda\frac{\partial^3 \Psi_u}{\partial \theta^3}$$

$$+\left[\frac{\partial \Psi}{\partial \Phi}\Phi_i + 2\,\Phi_i\left(\Phi_i - \Phi_u\right)\right]\frac{\partial q}{\partial \theta} - \left[\mu\,\Phi_i + \frac{2\,\Phi_i}{n}\right]\frac{\partial^2 q}{\partial \theta\, \partial \tau} - \lambda\,\Phi_i\frac{\partial^2 q}{\partial \theta^2} = 0 \qquad \text{(E.1)}$$

Reed Valve Dynamics:

The reed valves are modeled as locally reacting, mass-spring-dashpots which respond to pressure perturbations in the upstream flow field, as developed in Appendix B.

$$\frac{\partial^2 z}{\partial\theta\,\partial\tau} + 2\,Q\,\zeta\,\frac{\partial z}{\partial\theta} + Q^2\,\frac{\partial q}{\partial\theta} - \frac{1}{3}\,W\,\frac{\partial^2\Psi_u}{\partial x\,\partial\tau} - \frac{1}{3}\,W\,\Phi_u\,\frac{\partial^2\Psi_u}{\partial x^2} = 0 \tag{E.2}$$

and

$$\frac{\partial q}{\partial\tau} - z = 0 \tag{E.3}$$

Thus, the above system of equations contains three complex equations in terms of three complex variables for each spatial harmonic. For the Galerkin procedure, the circumferential and axial forms of the solutions will be assumed to be represented by the circumferential and axial forms of the first and second spatial harmonics of the solutions to the linearized analysis:

$$\Psi_u\,(x,\theta) = A_1\,e^{i\,\theta + x} + A_2\,e^{i\,2\theta + 2x} \tag{E.4}$$

$$z\,(x,\theta) = Z_1\,e^{i\,\theta} + Z_2\,e^{i\,2\theta} \tag{E.5}$$

$$q\,(x,\theta) = q_1\,e^{i\,\theta} + q_2\,e^{i\,2\theta} \tag{E.6}$$

where $A_1, A_2, Z_1, Z_2, q_1, q_2$ are complex coefficients.

Taking the real part of the solutions:

$$\text{real}\left(\Psi_u\right) = \left(A_{R_1}\cos(\theta) - A_{I_1}\sin(\theta)\right)e^{x} + \left(A_{R_2}\cos(2\theta) - A_{I_2}\sin(2\theta)\right)e^{2x} \tag{E.7}$$

$$\text{real}\,(z) = \left(z_{R_1}\cos(\theta) - z_{I_1}\sin(\theta)\right) + \left(z_{R_2}\cos(2\theta) - z_{I_2}\sin(2\theta)\right) \tag{E.8}$$

$$\text{real}\,(q) = \left(q_{R_1}\cos(\theta) - q_{I_1}\sin(\theta)\right) + \left(q_{R_2}\cos(2\theta) - q_{I_2}\sin(2\theta)\right) \tag{E.9}$$

where A_{R_1}, A_{I_1}, A_{R_2}, A_{I_2}, z_{R_1}, z_{I_1}, z_{R_2}, z_{I_2}, q_{R_1}, q_{I_1}, q_{R_2}, q_{I_2} are real coefficients.

The system now consists of twelve real variables. To reduce the partial differential equations into a system of twelve real, first order, ordinary differential equations, the approximate Galerkin method will be used. In this method, the circumferential and axial derivatives are expressed in terms of the assumed mode shapes and substituted into the governing partial differential equations. Substituting the approximate solutions into the PDE's results in an a residual for each of the three PDE's. The expression for the residual is then orthogonalized with respect to each of the four assumed mode shapes by integrating the product of the residual and the assumed mode over the annulus.

$$\int_0^{2\pi} (\text{Residual})\,(\text{assumed mode})\,d\theta = 0 \qquad \text{(E.10)}$$

Evaluating equation (E.10) for the three residuals for the four assumed modes results in twelve first order, ordinary differential equations.

Pressure Rise PDE orthogonalized with respect to cos(θ):

$$- A_{R_1} FCC + A_{I_1} FSC - 4 A_{R_2} FCC2 + 4 A_{I_2} FS2C + (4 + \mu) \dot{A}_{R_1} - \lambda A_{I_1}$$

$$- q_{R_1} \Phi_i FSC - q_{I_1} \Phi_i FCC - 2 q_{R_2} \Phi_i FS2C - 2 q_{I_2} \Phi_i FCC2$$

$$- 2 \Phi_i (\Phi_i - \Phi_u) q_{I_1} + \left[\mu \Phi_i + \frac{2 \Phi_i}{n}\right] \dot{q}_{I_1} + \lambda \Phi_i q_{R_1} = 0 \qquad \text{(E.11)}$$

Pressure Rise PDE orthogonalized with respect to sin(θ):

$$- A_{R_1} FSC + A_{I_1} FSS - 4 A_{R_2} FSC2 + 4 A_{I_2} FSS2 - (4 + \mu) \dot{A}_{I_1} - \lambda A_{R_1}$$

$$- q_{R_1} \Phi_i \, FSS - q_{I_1} \Phi_i \, FSC - 2 \, q_{R_2} \Phi_i \, FSS2 - 2 \, q_{I_2} \Phi_i \, FSC2$$

$$- 2 \, \Phi_i \, (\Phi_i - \Phi_u) \, q_{R_1} + \left[\mu \, \Phi_i + \frac{2 \, \Phi_i}{n} \right] \dot{q_{R_1}} - \lambda \, \Phi_i \, q_{I_1} = 0 \qquad \text{(E.12)}$$

Pressure Rise PDE orthogonalized with respect to cos(2θ):

$$- A_{R_1} \, FCC2 + A_{I_1} \, FSC2 - 4 \, A_{R_2} \, FC2C2 + 4 \, A_{I_2} \, FS2C2 + (8 + 4 \, \mu) \, \dot{A_{R_2}} - 8 \, \lambda \, A_{I_2}$$

$$- q_{R_1} \Phi_i \, FSC2 - q_{I_1} \Phi_i \, FCC2 - 2 \, q_{R_2} \Phi_i \, FS2C2 - 2 \, q_{I_2} \Phi_i \, FC2C2$$

$$- 4 \, \Phi_i \, (\Phi_i - \Phi_u) \, q_{I_2} + 2 \left[\mu \, \Phi_i + \frac{2 \, \Phi_i}{n} \right] \dot{q_{I_2}} - 4 \, \lambda \, \Phi_i \, q_{R_2} = 0 \qquad \text{(E.13)}$$

Pressure Rise PDE orthogonalized with respect to sin(2θ):

$$- A_{R_1} \, FS2C + A_{I_1} \, FSS2 - 4 \, A_{R_2} \, FS2C2 + 4 \, A_{I_2} \, FS2S2 - (8 + 4 \, \mu) \, \dot{A_{I_2}} - 8 \, \lambda \, A_{R_2}$$

$$- q_{R_1} \Phi_i \, FSS2 - q_{I_1} \Phi_i \, FS2C - 2 \, q_{R_2} \Phi_i \, FS2S2 - 2 \, q_{I_2} \Phi_i \, FS2C2$$

$$- 4 \, \Phi_i \, (\Phi_i - \Phi_u) \, q_{R_2} + 2 \left[\mu \, \Phi_i + \frac{2 \, \Phi_i}{n} \right] \dot{q_{R_2}} - 4 \, \lambda \, \Phi_i \, q_{I_2} = 0 \qquad \text{(E.14)}$$

where FCC, FCC2, FC2C2, FSS, FSS2, FS2S2, FSC, FS2C, FSC2, FS2C2 represent the integrals of the slope of the compressor characteristic, expressed as a function of circumferential position, integrated over the annulus and weighted by the assumed mode shapes.

$$FCC \equiv \frac{1}{\Pi} \int_0^{2\Pi} \frac{\partial \Psi}{\partial \Phi} (\theta) \cos(\theta) \cos(\theta) \, d\theta$$

$$FS2C \equiv \frac{1}{\Pi} \int_0^{2\Pi} \frac{\partial \Psi}{\partial \Phi}(\theta)\, \sin(2\theta)\, \cos(\theta)\, d\theta \qquad \text{etc.} \qquad \text{(E.15)}$$

$\frac{\partial \Psi}{\partial \Phi}$ The slope of the compressor characteristic is given as a function of local mass flow coefficient through the compressor defined by:

$$\frac{\partial \Psi}{\partial \Phi}(\theta) = F\,(\phi_u + \Phi_i\, q) \qquad \text{(E.16)}$$

and noting the definition of the streamfunction: $\delta\, \phi_u \equiv \frac{\partial \Psi_u}{\partial \theta}$,

$$\frac{\partial \Psi}{\partial \Phi}(\theta) = F\,(\Phi_d - A_{R_1} \sin(\theta) - A_{I_1} \cos(\theta) - 2A_{R_2} \sin(2\theta) - 2A_{I_2} \cos(2\theta) +$$

$$+ \Phi_i\, q_{R_1} \cos(\theta) - \Phi_i\, q_{I_1} \sin(\theta) + \Phi_i\, q_{R_2} \cos(2\theta) - \Phi_i\, q_{I_2} \sin(2\theta)\,) \qquad \text{(E.17)}$$

$F(\Phi)$ is a function describing the quasi-steady slope of the compressor characteristic as a function of local compressor mass flow coefficient.

Reed Valve Dynamics PDE with respect to cos(θ):

$$-\dot{z_{I_1}} - 2\,Q\,\zeta\, z_{I_1} - Q^2\, q_{I_1} - \frac{1}{3} W\, \dot{A_{R_1}} - \frac{1}{3} W\, \Phi_u\, A_{R_1} = 0 \qquad \text{(E.18)}$$

Reed Valve Dynamics PDE with respect to sin(θ):

$$-\dot{z_{R_1}} - 2\,Q\,\zeta\, z_{R_1} - Q^2\, q_{R_1} - \frac{1}{3} W\, \dot{A_{I_1}} - \frac{1}{3} W\, \Phi_u\, A_{I_1} = 0 \qquad \text{(E.19)}$$

Reed Valve Dynamics PDE with respect to cos(2θ):

$$- 2\dot{z_{I_2}} - 4\,Q\,\zeta\,z_{I_2} - 2\,Q^2\,q_{I_2} - \frac{2}{3}\,W\,\dot{A_{R_2}} - \frac{4}{3}\,W\,\Phi_u\,A_{R_2} = 0 \qquad \text{(E.20)}$$

Reed Valve Dynamics PDE with respect to sin(2θ):

$$- 2\dot{z_{R_2}} - 4\,Q\,\zeta\,z_{R_2} - 2\,Q^2\,q_{R_2} - \frac{2}{3}\,W\,\dot{A_{I_2}} - \frac{4}{3}\,W\,\Phi_u\,A_{I_2} = 0 \qquad \text{(E.21)}$$

Definition of reed valve velocity with respect to cos(θ):

$$\dot{q_{R_1}} - z_{R_1} = 0 \qquad \text{(E.22)}$$

Definition of reed valve velocity with respect to sin(θ):

$$\dot{q_{I_1}} - z_{I_1} = 0 \qquad \text{(E.23)}$$

Definition of reed valve velocity with respect to cos(2θ):

$$\dot{q_{R_2}} - z_{R_2} = 0 \qquad \text{(E.24)}$$

Definition of reed valve velocity with respect to sin(2θ):

$$\dot{q_{I_2}} - z_{I_2} = 0 \qquad \text{(E.25)}$$

The resulting system of twelve, ordinary differential equations in time can then be numerically integrated in time. At each time step, the non-linear terms are updated with the previous time step value for the perturbation values. Expressing the system of equations in state space formulation leads to:

$$[C]\{\dot{x}\} = [B]\{x\}$$
$$\{\dot{x}\} = [C^{-1}\,B]\{x\} = [A]\{x\} \tag{E.26}$$

A 4th order Runge-Kutta numerical integration technique was used to simulate the time resolved, non-linear behavior of the compression system.

$$\begin{aligned} k_1 &= \Delta t\, \dot{x}(x_{old}) \\ k_2 &= \Delta t\, \dot{x}\left(x_{old} + \frac{k_1}{2}\right) \\ k_3 &= \Delta t\, \dot{x}\left(x_{old} + \frac{k_2}{2}\right) \\ k_4 &= \Delta t\, \dot{x}(x_{old} + k_3) \\ x_{new} &= x_{old} + \frac{k_1}{6} + \frac{k_2}{3} + \frac{k_3}{3} + \frac{k_4}{6} \end{aligned} \tag{E.27}$$

Noise Model:

To simulate the effect of noise on the compression system, a random static pressure perturbation at the face of the compressor was added to the simulation. The pressure balance PDE (Eq. E.1) with noise is given by:

$$\frac{\partial \Psi}{\partial \Phi}\frac{\partial^2 \Psi_u}{\partial \theta^2} + 4\frac{\partial^2 \Psi_u}{\partial \tau\, \partial x} - \mu\frac{\partial^3 \Psi_u}{\partial \tau\, \partial \theta^2} - \lambda\frac{\partial^3 \Psi_u}{\partial \theta^3}$$

$$+\left[\frac{\partial \Psi}{\partial \Phi}\Phi_i + 2\,\Phi_i(\Phi_i - \Phi_u)\right]\frac{\partial q}{\partial \theta} - \left[\mu\,\Phi_i + \frac{2\,\Phi_i}{n}\right]\frac{\partial^2 q}{\partial \theta\, \partial \tau} - \lambda\,\Phi_i\frac{\partial^2 q}{\partial \theta^2} = \left\{-\frac{\partial p_{noise}}{\partial \theta}\right\} \tag{E.28}$$

The reed dynamics PDE (Eq. E.2) with noise is given by:

$$\frac{\partial^2 z}{\partial \theta\, \partial \tau} + 2\,Q\,\zeta\frac{\partial z}{\partial \theta} + Q^2\frac{\partial q}{\partial \theta} - \frac{1}{3}W\frac{\partial^2 \Psi_u}{\partial x\, \partial \tau} - \frac{1}{3}W\,\Phi_u\frac{\partial^2 \Psi_u}{\partial x^2} = \left\{\frac{1}{3}W\frac{\partial p_{noise}}{\partial \theta}\right\}$$

(E.29)

Where the random noise is given by:

$$p_{noise} = p_1 \cos(\theta) + p_2 \sin(\theta) + p_3 \cos(2\theta) + p_4 \sin(2\theta)$$
$$\text{where } p_{n=1\text{-}4} = p_{max}\, 2\{RND_{n=1\text{-}4} - 0.5\} \qquad \text{(E.30)}$$

The random number (RND) is a value with uniform distribution between 0 and 1. The noise was applied to each spatial assumed mode shape independently. The magnitude of the random noise applied to each spatial assumed mode shape was bounded by a maximum noise level given by:

$$|p_{max}| = \sqrt{2}\, p_{rms} \qquad \text{(E.31)}$$

With this formulation, the noise source approximates a noise source with rms amplitude of P_{rms} with a flat power spectra density between 0 Hz and 1 / (2 ΔT) Hz where ΔT is the time step. For the simulations used in this thesis, the time step was 1000 Hz, and thus the noise was distributed between 0 Hz and 500 Hz.

Applying the Galerkin method to the system of equations with noise, results in a state space model of the rotating stall dynamics with an excitation term.

$$[C]\{\dot{x}\} = [B]\{x\} + \{D\}_{noise}$$
$$\{\dot{x}\} = [C^{-1} B]\{x\} + [C]^{-1}\{D\}_{noise} \qquad \text{(E.32)}$$

where the noise excitation matrix is given by:

$$\{D\} = \begin{Bmatrix} -p_1 \\ -p_2 \\ -2p_3 \\ -2p_4 \\ \frac{1}{3}W p_1 \\ \frac{1}{3}W p_2 \\ \frac{2}{3}W p_3 \\ \frac{2}{3}W p_4 \\ 0 \\ 0 \\ 0 \\ 0 \end{Bmatrix} \qquad \text{(E.33)}$$

The noise input at each time step was held constant over that step for the non-linear integration.

Features of the Non-linear Simulation

In addition to providing a method to account for random excitation of the compression system, the non-linear simulation allows non-linearities resulting from the compressor characteristic to influence the compression system dynamics.

One feature that the non-linear simulation contains which is absent from the linearized analysis is the ability to predict small amplitude limit cycles. The nonlinear simulation predicts that small amplitude limit cycles can develop in the simulation for certain

compressor characteristics. Figure E.1 shows two compressor characteristics, (A) and (B). The primary difference between the two characteristics is the shape of the characteristics in the positively slope region, with (A) being steeper than (B). Figure E.2 shows initial condition responses of the two compression systems operating at similar, linearly unstable, operating points denoted on Figure E.1. The Figure shows the normalized axial velocity perturbations through the compressors at a single circumferential position. Although the linearized dynamics of the compression systems are similar, ($\frac{\partial \Psi}{\partial \Phi}$ = 0.03), the resultant finite amplitude oscillations are very different. For the compression system with characteristic (A), the oscillations grow with time and the simulation predicts that the flow transitions into large amplitude rotating stall. However, for characteristic (B), the oscillations grow initially, but, eventually stabilize into a small amplitude limit cycle. The oscillations shown are self-excited, no external excitation was incorporated in the simulation. The small amplitude limit cycle behavior for characteristic B is similar to the limit cycles predicted by Moore-Greitzer[7].

One Spatial Harmonic Non-linear Simulation of the Basic Compression System:

The mechanism behind the limit cycle oscillations can be interpreted by applying the Galerkin method to the basic compression system using a single spatial harmonic. For the basic compression system, i.e. without dynamic mass / momentum injection, Eq. E.1 reduces to:

$$\frac{\partial \Psi}{\partial \Phi}\frac{\partial^2 \Psi_u}{\partial \theta^2} + 4\frac{\partial^2 \Psi_u}{\partial \tau \partial x} - \mu\frac{\partial^3 \Psi_u}{\partial \tau \partial \theta^2} - \lambda\frac{\partial^3 \Psi_u}{\partial \theta^3} = 0 \qquad \text{(E.34)}$$

Assuming solutions of the form:

$$\text{real}\left(\Psi_u\right) = \left(A_R \cos(\theta) - A_I \sin(\theta)\right) e^x \qquad \text{(E.35)}$$

and applying the Galerkin procedure as developed above, leads to the following state space representation:

$$\begin{Bmatrix} \dot{A}_R \\ \dot{A}_I \end{Bmatrix} = \frac{1}{(4+\mu)} \begin{bmatrix} FCC & -FSC+\lambda \\ -FSC-\lambda & FSS \end{bmatrix} \begin{Bmatrix} A_R \\ A_I \end{Bmatrix} \tag{E.36}$$

Where FCC, FSC, FSS contain the non-linear terms in the compressor characteristic and are defined in Equation E.15.

If the non-linearity in the compressor characteristic is removed, the Galerkin formulation reduces to an exact solution for the linearized PDE. The state space representation for the linearized system is given by:

$$\begin{Bmatrix} \dot{A}_R \\ \dot{A}_I \end{Bmatrix} = \frac{1}{(4+\mu)} \begin{bmatrix} \frac{\partial \Psi}{\partial \Phi} & \lambda \\ -\lambda & \frac{\partial \Psi}{\partial \Phi} \end{bmatrix} \begin{Bmatrix} A_R \\ A_I \end{Bmatrix} \tag{E.37}$$

Comparing Eq. E.37 with Eq. E.36, we see that the role of the slope of the compressor characteristic, $\frac{\partial \Psi}{\partial \Phi}$, in the linear analysis is analogous to that of a weighted average (over the annulus) of the local slope of the compressor characteristic in the non-linear analysis.

$$\frac{\partial \Psi}{\partial \Phi_{linear}} \rightarrow \frac{1}{\pi} \int_0^{2\pi} F\left[\Phi_u - A_R \sin(\theta) - A_I \cos(\theta)\right] \cos^2(\theta)\, d\theta \tag{E.38}$$

and

$$\frac{\partial \Psi}{\partial \Phi_{linear}} \rightarrow \frac{1}{\pi} \int_0^{2\pi} F\left[\Phi_u - A_R \sin(\theta) - A_I \cos(\theta)\right] \sin^2(\theta)\, d\theta \tag{E.39}$$

For a compression system with infinitesimal disturbances , both the non-linear and linear simulations predict an initially exponentially growing disturbance for positive compressor slopes. However, for the non-linear simulation, the weighted, annulus averaged, slope is a function of the disturbance amplitude. If the shape of the compressor characteristic is such that the weighted annulus averaged compressor slope decreases with increasing disturbance amplitude in the neighborhood of the linearly unstable operating point, a mechanism for a limit cycles exists. The limit cycle oscillation will stabilize to a finite amplitude oscillation when the annulus averaged slope, defined in equations (E.38) and / or (E.39), is zero.

The possibility for small amplitude limit cycles can be quantified for compressor characteristics expressed as a cubic function of compressor mass flow coefficient.

$$\Psi(\Phi) = A\,\Phi^3 + B\,\Phi^2 + C\,\Phi + D \tag{E.40}$$

For this compressor characteristic, the slope is given by:

$$\frac{\partial \Psi}{\partial \Phi}(\Phi) = 3A\,\Phi^2 + 2B\,\Phi + C \tag{E.41}$$

The form of the limit cycle will be a constant amplitude, first harmonic disturbance rotating around the annulus at a constant speed. The Galerkin analysis expresses the constant amplitude rotating wave as the summation of two standing waves of oscillating amplitude. As the wave rotates around the compressor, an instant in time will exist when A_R has a maximum and $A_I = 0$. The time rate of change of A_R is zero at this instant, and thus,

$$FCC = \int_0^{2\Pi} F\left[\Phi_u - A_R \sin(\theta)\right] \cos^2(\theta)\, d\theta = 0 \tag{E.42}$$

Substituting the expression for the slope of the compressor (Eq. E.41) derived from the cubic characteristic yields:

$$FCC = \int_0^{2\Pi} \left[3\,A\left\langle \Phi_u - A_R \sin(\theta)\right\rangle^2 + 2\,B\left\langle \Phi_u - A_R \sin(\theta)\right\rangle + C\right] \cos^2(\theta)\, d\theta = 0 \tag{E.43}$$

Solving for the amplitude of the disturbance that satisfies Eq. E.43, yields the amplitude of the limit cycle oscillations as a function of the linearized slope at the mean operating mass flow coefficient and the cubic term in the compressor characteristic:

$$\left|\delta\phi\right| = \left|A_R\right| = \frac{2}{\sqrt{3}} \sqrt{\frac{\partial\Psi}{\partial\Phi_{linear}}} \over (-A) \tag{E.44}$$

For small amplitude limit cycles to exist, the cubic term of the compressor characteristic must be negative. A physical interpretation of the requirement is that the compressor characteristic must be more steeply sloped approaching its peak from the high flow region than from the low flow region.

The non-linearity associated with the shape of the compressor characteristic can also have an influence in the stall inception process and the compression system dynamics prior to stall inception. Non-linearity in the compressor characteristic allows for coupling between axisymmetric and non-axisymmetric oscillations in the compression system. For a more detailed assessment of the influence of the shape of the characteristic on the stall inception process, the reader is referred to Paduano and Gysling [26].

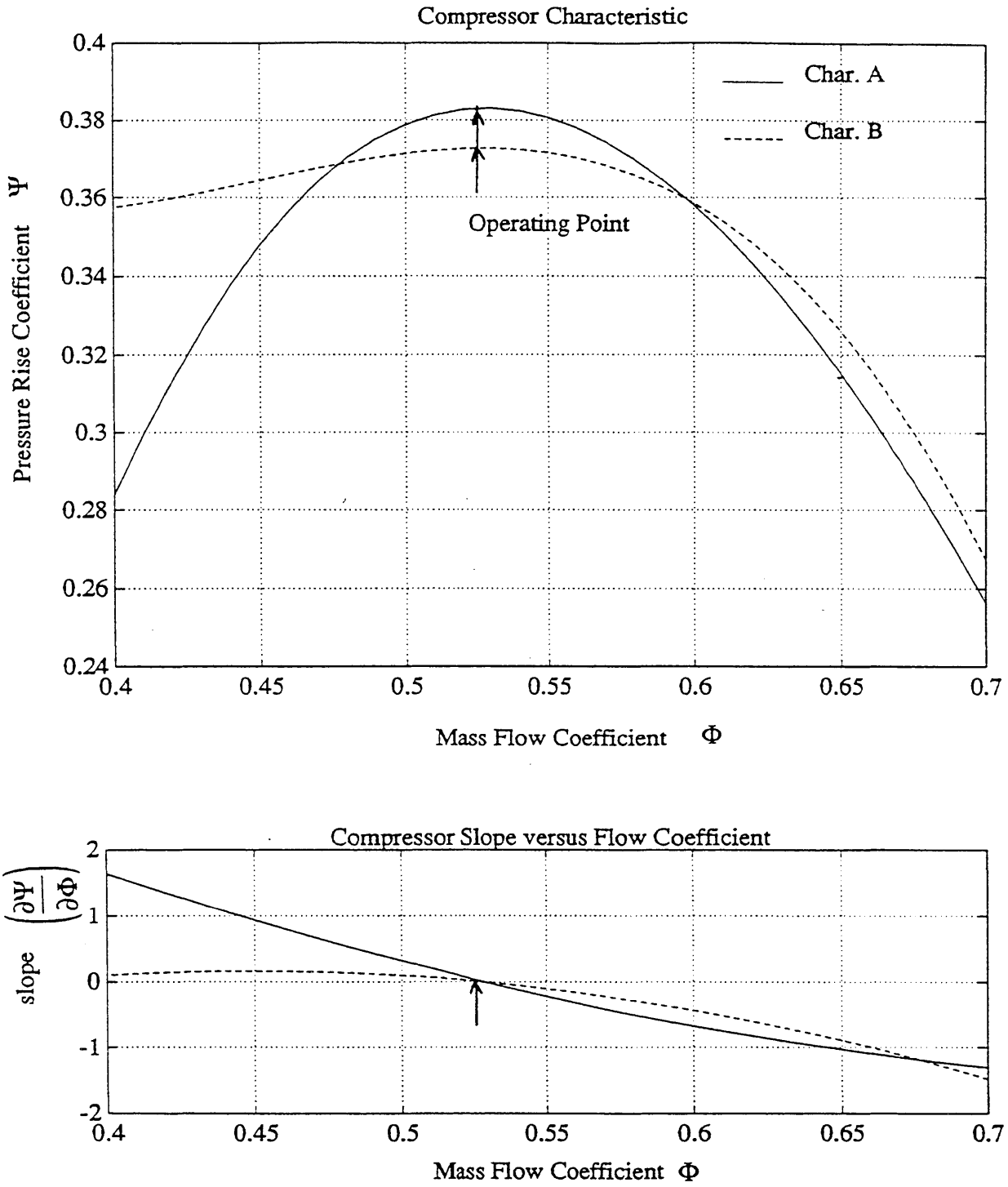

Figure E.1: Two Compressor Characteristics used to Demonstrate Effect of Non-Linearities on Compression System Dynamics with Slope of Characteristics versus Flow Coefficient also Shown

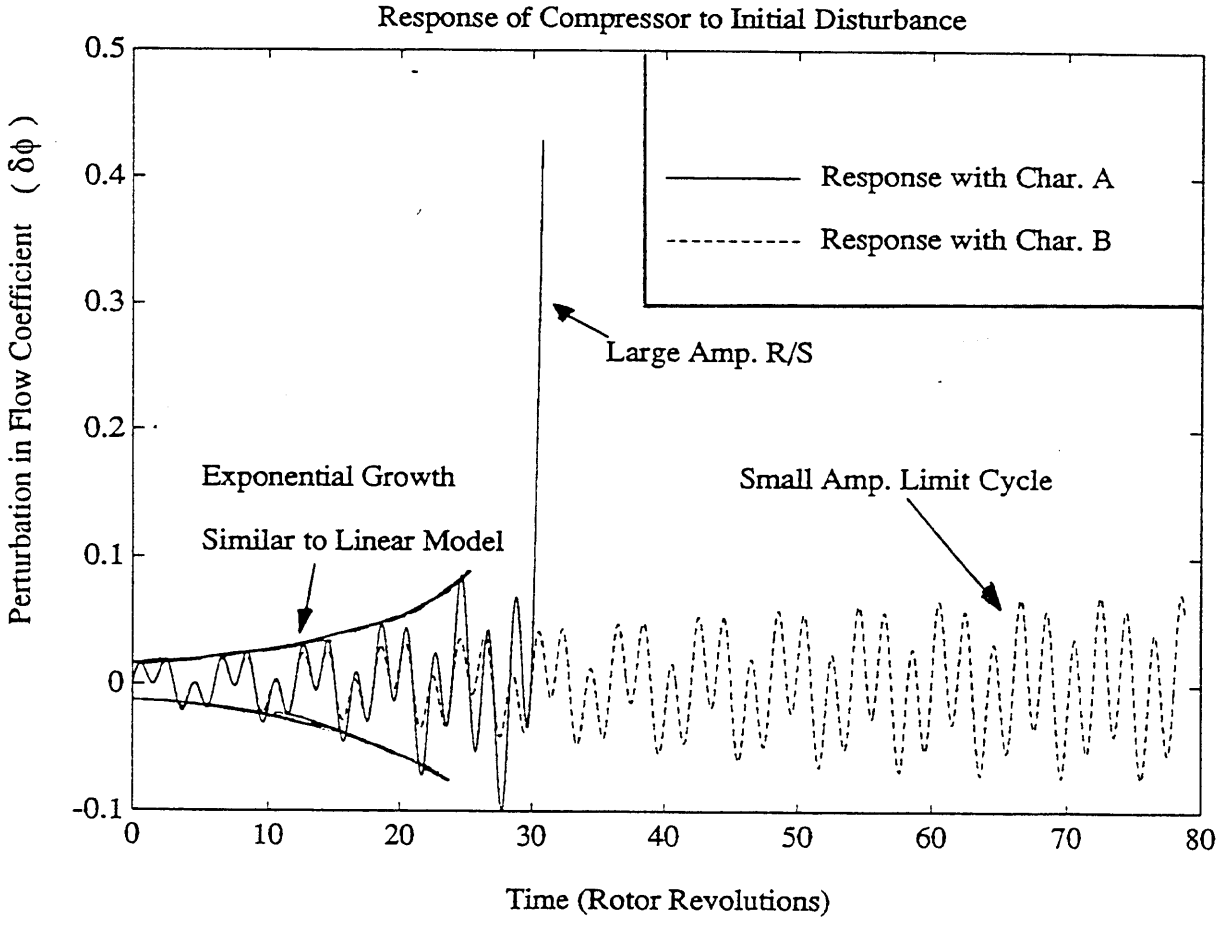

Figure E.2: Perturbation in Flow Coefficient at a Fixed Circumferential Position for Initial Condition Response Predicted by Non-linear Simulation for for Characteristics A and B Operating with the Same Linear Slope $\left(\frac{\partial \Psi}{\partial \Phi} = 0.03\right)$

Appendix F: Digital Signal Processing

Several digital signal processing techniques are employed in this research. The software package MATLAB was used for the signal processing. The algorithms are outlined in this appendix:

Discrete Fourier Coefficients:

The fast Fourier transform is applied to transform discrete time resolved data into the frequency domain. The fast Fourier transform for a discrete time resolved data set, x(n), containing N samples, sampled at a frequency of f_S, is given by:

$$X(k+1) = \sum_{n=0}^{N-1} x(n+1)\, e^{-i\frac{2\pi k n}{N}} \qquad \text{(F.1)}$$

where: x is a discrete time resolved signal

X is the discrete Fourier transform

The index k ranges from 0 to N-1 and specifies the harmonic frequency as multiples of the sampling frequency. The actual frequencies corresponding to the elements in the discrete Fourier transform given, (up to the Nyquist frequency = $f_S / 2$), by:

$$f(k) = \frac{k}{N} f_s \quad \text{for } k = 0 \text{ to } k = \frac{N}{2} \qquad \text{(F.2)}$$

Power Spectral Density

The power spectral density function P_{XX} (termed "PSD" in text) of a discrete time resolved signal of length N is defined in terms of the discrete Fourier transform by the following expression:

$$P_{xx}(k) = X(k)\,X^{*}(k) \qquad \text{for } k = 0 \text{ to } N/2 \tag{F.3}$$

The magnitude of the PSD's presented in this thesis are normalized as defined below:

$$\frac{1}{N}\sum_{n=1}^{N} x(n)^2 = \frac{1}{N/2}\sum_{n=1}^{N/2} P_{xx}(n) \tag{F.4}$$

Cross Power Spectral Density:

The cross power spectral density [28] between two discrete time resolved signals x (n) and y (n), both of length N, is defined in terms of the discrete Fourier transform of the individual signals:

$$P_{xy}(k) = Y(k)\,X^{*}(k) \qquad \text{for } k = 0 \text{ to } N/2 \tag{F.5}$$

Welch Method

MATLAB employs the Welch method to obtain an estimate of the power spectral density and cross power spectral density by averaging the power specta over several intervals of length N for samples containing more that N samples.

The averaged power spectral density for a discrete time resolved signal containing m windows of length n is given by:

$$S_{xx}(k) = \frac{1}{m}\sum_{i=1}^{m} P_{xx}(k)_i \tag{F.6}$$

The cross power spectra density averaged over m windows of length n is given by:

$$S_{xy}(k) = \frac{1}{m}\sum_{i=1}^{m} P_{xy}(k)_i \tag{F.7}$$

Estimate of Transfer Function:

The frequency domain transfer function, magnitude and phase, of two discrete time resolved signals can be estimated using the ratio of the averaged values of the power spectral density and the cross power spectral density [28]

$$H(k) = \frac{S_{xy}(k)}{S_{xx}(k)} \tag{F.8}$$

Coherence

The coherence of the two signals gives an estimate of the accuracy of the transfer function estimate. The coherence function is given by [28],

$$\gamma^2_{xy}(k) = \frac{|S_{xy}(k)|^2}{S_{xx}(k)\, S_{yy}(k)} \tag{F.9}$$

Spatial Fourier Decomposition

The time resolved axial velocity measurement from a circumferential array of 8 equally spaced hot-wires placed at mid span approximately 1/3 chord upstream of the rotor were used to obtain information about the spatial structure of the disturbances within the compressor. At each point in time, the axial velocity measurements recorded around the annulus can be decomposed into complex spatial Fourier coefficients. The spatial Fourier decomposition method used in this research was developed by Garnier [13] and further refined by Paduano[25] and has been used by several other researchers at the Gas Turbine Lab for studying the small amplitude disturbances in axial flow compression systems prior to stall.

The complex Spatial Fourier Coefficients are given by the following expressions:

$$V(n) = \frac{2}{\pi}\int_0^{2\pi} v(\theta)\cos(n\theta)\,d\theta + i\frac{2}{\pi}\int_0^{2\pi} v(\theta)\sin(n\theta)\,d\theta \qquad \text{(F.10)}$$

Using this definition [25], a sinusoidal disturbance, v(θ), with harmonic number (n) has a magnitude of $|V_n|$ and an angular position given by $\angle V_n$.

Using the above definition, the non-axisymmetric perturbation in axial flow coefficient ($\delta\phi$) can be represented as a summation of its Spatial Fourier Coefficients (SFC):

$$\delta\phi(\theta) = \sum_{n=1}^{\infty} \left|\tilde{\phi}_n\right| \cos\left(n\theta + \angle\tilde{\phi}_n\right)$$

where $\left|\tilde{\phi}_n\right|$ is the magnitude of the nth Spatial Fourier Coefficient and $\angle\tilde{\phi}_n$ is the phase angle of the nth Spatial Fourier Coefficient. For the array of 8 hot-wires this decomposition can resolve the magnitude and phase of the first three spatial harmonics (n=1,2, and 3).

Appendix G: Measurement of Injection Quantities

The annulus averaged, temporal mean, injection mass flow was measured using a Venturi flow meter. The pressure in the injection plenum was measured referenced to the static pressure in the free stream immediately upstream of the compressor. The momentum of the injected mass flow was determined using the mass flow measurement and the pressure in the injection plenum, .

Injected Mass Flow Measurement:

The Venturi flow meter contained a 2.0 inch diameter inlet and a 1.2 inch diameter throat. A schematic of the B.I.F. Inc. UVT-PI-0182-022231 Venturi flow meter is shown in Figure G.1. Two pressure measurements were recorded using a Magnehelic 0-5 psi differential pressure gauge for the differential pressure measurement and a Marshalltown 0-100 psig pressure gauge for the gauge pressure at the inlet to the flow meter. An Omega thermocouple recorded the temperature in the distribution plenum.

The actual mass flow through the Venturi flow meter is calculated by the product of the ideal mass flow and an empirically determined discharge coefficient:

$$\dot{m}_i = \mu \dot{m}_{ideal} \qquad \text{(G.1)}$$

For range of mass flow measured, using an empirical discharge coefficient of $\mu = 0.98$ results in a error of less than 1% from the manufacture's tabulated discharge coefficient versus Reynolds number [34].

The ideal mass flow through the flow meter can be derived using 1-D, adiabatic, compressible flow relations [34].

$$\dot{m}_{ideal} = \beta_{comp}\, A_t \sqrt{\frac{2\,\rho_1\,(p_1 - p_t)}{1 - \sigma^2}} \qquad \text{(G.2)}$$

where A_t = throat area, $\sigma \equiv \frac{A_t}{A_1}$ = area ratio, and

$$\beta_{comp} = \sqrt{\frac{(1-\sigma^2)\frac{\gamma}{\gamma-1}\frac{1}{1-\pi}\left(1-\pi^{\frac{\gamma-1}{\gamma}}\right)\pi^{\frac{2}{\gamma}}}{1-\sigma^2\,\pi^{\frac{2}{\gamma}}}} = \text{compressibility factor}$$

$$\pi \equiv \frac{p_1}{p_t} = \text{pressure ratio}$$

$$\gamma = \text{ratio of specific heats} = 1.4 \text{ for air}$$

Defining the injection parameter, $\Phi_i \equiv \frac{C_{x_i}}{U_R}$, and the normalized reed opening, $q \equiv \frac{\Delta}{H}$, where Δ is the reed valve opening and H is the annulus height, injected mass flow coefficient is given by:

$$\frac{\dot{m}_i}{\rho\, A\, U_R} = \frac{\rho\, C_{x_i} \frac{\Delta}{H} A}{\rho\, A\, U_R} = \Phi_i\, q \qquad \text{(G.3)}$$

where, ρ is the ambient density, A is the annulus area, and U_R is the mid-span wheel speed of the rotor

Given the injected mass flow coefficient, the mass flow coefficient through the compressor can be determined using the sum of the injected mass flow and the mass flow measured upstream of the injection location:

$$\Phi_c = \Phi_u + \Phi_i \, q \tag{G.4}$$

Axial Momentum of Injected Fluid Measurement:

The axial momentum of the injected fluid is given by the product of the mass flow and the velocity of the injected fluid.

$$\dot{m}_i \, C_{x_i} = \text{momentum injected} \tag{G.5}$$

The velocity of the injected fluid was determined by measuring the pressure differential between the injection plenum and the free-stream static pressure and assuming that the injected fluid expands to the free-stream static pressure in an ideal manner.

$$C_{x_i} = \sqrt{\frac{p_{\text{inj plenum}} - p_{\text{freestream}}}{\frac{1}{2}\rho}} \tag{G.6}$$

The non-dimensional momentum injected, normalized by the axial momentum entering the compressor is given by:

$$\alpha_i \equiv \frac{\dot{m}_i \, C_{x_i}}{\rho \, A \left(\Phi_c \, U_R\right)^2} = \frac{\Phi_i^2 \, q}{\Phi_c^2} \tag{G.7}$$

Appendix H: Rotating Stall Model with Visco-Elastic Dynamic Mass / Momentum Injection

The basic structure of the model used to assess the effect of dynamic mass / momentum injection with a visco-elastic dashpot is similar to the model used for the compression system with the dynamic mass / momentum injection modeled in Appendix B.

The boundary conditions across the compressor are identical to those derived in Appendix B:

Mass Flow Across Modified Compressor:

$$\delta\phi_u + \Phi_i\,\delta q = \delta\phi_d \tag{H.1}$$

Pressure Rise Across Modified Compressor:

$$\delta p_{s_d} - \delta p_{t_u} = \frac{\partial \Psi}{\partial \Phi}\,\delta\phi_u + \frac{\partial \Psi}{\partial \Phi}\,\Phi_i\,\delta q - \mu\frac{\partial \phi_u}{\partial \tau} - \mu\,\Phi_i\frac{\partial q}{\partial \tau} - \lambda\frac{\partial \phi_u}{\partial \theta} - \lambda\,\Phi_i\frac{\partial q}{\partial \theta} + 2\,\Phi_i\,(\,\Phi_i - \Phi_u)\,\delta q \tag{H.2}$$

Exit Flow Angle:

The exit flow angle boundary conditions remains unchanged form the basic compression system analysis:

$$\delta v_d = 0 \tag{H.3}$$

Expressing the boundary conditions across the actuator disk in terms of the solutions forms for the upstream and downstream flow fields leads to an expression relating the complex

spatial Fourier component of the nth spatial harmonic of the upstream perturbation streamfunction to that of the local reed valve displacement.

$$\left[i (4 + \mu n) \sigma + \frac{\partial \Psi}{\partial \Phi} - i \lambda n \right] A_n + \left[\Phi_i \left(\frac{2}{n} + \mu \right) \sigma - \lambda \Phi_i - \frac{\partial \Psi}{\partial \Phi} \Phi_i + 2 \Phi_i (\Phi_i - \Phi_u) \right] q_n = 0 \tag{H.4}$$

where
$$\Psi_u = \sum_{n=1}^{+\infty} A_n e^{i n (\theta - \sigma \tau) + n x} \tag{H.5}$$

and
$$q = \sum_{n=-\infty}^{+\infty} q_n e^{i n (\theta - \sigma \tau)} \tag{H.6}$$

Structural Feedback:

The only difference from the model developed in Appendix B is the feedback provided by the reed valves. In the reed dynamics with a visco-elastic dashpot, the reed valves are modeled as a third order, locally reacting mass-spring-(visco-elastic)-damper systems in the first cantilever bending mode. The dynamics of the reed valves were calculated by assuming a mode shape for the first cantilevered bending mode. Thus, the reed displacement as a function of time and position is given by:

$$\Delta \left(\frac{x}{L}, t \right) = \Delta(t) \, \xi \left(\frac{x}{L} \right) \quad \text{where} \quad \xi \left(\frac{x}{L} \right) \equiv \left(\frac{x}{L} \right)^2 = \text{assumed mode shape} \tag{H.7}$$

The equation of motions for the reed valves, expressed in terms of the tip deflection (Δ) and the position of the junction of the spring and dashpot in the visco-elastic dashpot (ε) shown in Figure X, is given by:

$$M \ddot{\Delta} + K \Delta + \alpha K (\Delta - \varepsilon) = \Xi (t) \tag{H.8}$$

and

$$B\,\dot{\varepsilon} = \alpha\,K\,(\Delta - \varepsilon) \tag{H.9}$$

Where the quantity, $\alpha \equiv \frac{K_{ve}}{K}$,is the ratio of the spring constant in the visco-elastic dashpot to the spring constant of the reed and the other variables are as defined in Appendix B:

$$\Xi\,(t) \equiv \text{Modal Forcing Function} = \int_0^1 \xi(\tfrac{x}{L})\,\delta P_{s_u}\,L\,d(\tfrac{x}{L}) = \frac{1}{3}\,L\,\delta P_{s_u} \tag{H.10}$$

and:

$$M \equiv \text{Modal Mass} = \int_0^1 \xi(\tfrac{x}{L})^2\,m(\tfrac{x}{L})\;d(\tfrac{x}{L}) \tag{H.11}$$

$$B \equiv \text{Modal Damping} = \int_0^1 \xi(\tfrac{x}{L})^2\,b(\tfrac{x}{L})\;d(\tfrac{x}{L}) \tag{H.12}$$

$$K \equiv \text{Modal Stiffness} = \int_0^1 \xi(\tfrac{x}{L})^2\,k(\tfrac{x}{L})\;d(\tfrac{x}{L}) \tag{H.13}$$

Defining the following non-dimensional parameters:

$$\tau \equiv \frac{t\,U_R}{R} \qquad q \equiv \frac{\Delta}{H} \quad y \equiv \frac{\varepsilon}{H} \quad \tilde{L} \equiv \frac{L}{H} \tag{H.14}$$

and retaining the standard expressions for the natural frequency and critical damping ratios for second order, damped, harmonic oscillators:

$$\omega_n \equiv \sqrt{\frac{K}{M}} \qquad \zeta \equiv \frac{B}{2\,M\,\omega_n} \tag{H.15}$$

and the non-dimensional mass and frequency parameters:

$$W \equiv \frac{\rho_0\,R^2}{M}\,\tilde{L} \qquad Q \equiv \frac{\omega_n\,R}{U_R} \tag{H.16}$$

leads to the following non-dimensional expression for the locally reacting reed valve dynamics:

$$\frac{\partial^2 q}{\partial \tau^2} + (1+\alpha)\,Q^2\,\delta q - \alpha\,Q^2\,\delta y = \frac{1}{6}\,W\,\delta p_{s_v} \tag{H.17}$$

$$\frac{\partial y}{\partial \tau} + \frac{\alpha\,Q}{2\,\zeta}\,\delta y - \frac{\alpha\,Q}{2\,\zeta}\,\delta q = 0 \tag{H.18}$$

Using Eq. H.17 and Eq. H.18, the transfer function between reed displacement and static pressure is given by:

$$\frac{\delta q\,(\omega)}{\delta p_u\,(\omega)} = \frac{\frac{1}{6}W}{\left(Q^2 - \omega^2\right) + \frac{2\,Q\,\zeta\,\omega\,(i + \chi\,\omega)}{1 + (\chi\,\omega)^2}} \tag{H.19}$$

where $\chi \equiv \frac{2\,\zeta}{\alpha\,Q}$ and ω = temporal frequency non-dimensionalized by rotor frequency.

As in the other models, the static pressure perturbations in the upstream flow field can be related to the perturbation streamfunction in the upstream flow field via the circumferential momentum equation.

$$\frac{\partial \delta P_{s_u}}{\partial \theta} = 2\left(\frac{\partial^2 \Psi_u}{\partial x\, \partial \tau} + \Phi_u \frac{\partial^2 \Psi_u}{\partial x^2}\right) \tag{H.20}$$

Defining the velocity of the reed motion as a state variable leads to three first order equations for the compression system dynamics in terms of reed displacement, reed velocity, the additional state variable introduced by the visco-elastic dashpot model, and the upstream streamfunction:

$$\frac{1}{3} W n^2 (i\sigma - \Phi_u) A_n + i n (1+\alpha) Q^2 q_n + (n^2 \sigma) z_n - i n \alpha Q^2 y_n = 0 \tag{H.21}$$

$$i n \sigma q_n + z_n = 0 \tag{H.22}$$

$$\frac{\alpha Q}{2\zeta} q_n + \left(-\frac{\alpha Q}{2\zeta} + i n \sigma\right) y_n = 0 \tag{H.23}$$

Eigenvalue Problem:

Combining Equations H.21, H.22, and H.23, leads to a fourth order, generalized, complex eigenvalue problem governing the stability of each spatial harmonic of the uniform, axisymmetric flow field through the compressor with aeromechanical feedback.

$$[\mathbf{A} - \sigma \mathbf{B}] \begin{Bmatrix} \delta A_n \\ \delta q_n \\ \delta z_n \\ \delta y_n \end{Bmatrix} = 0 \tag{H.24}$$

The matrix **A** in Eq. H.24 is given by:

$$A = \begin{bmatrix} \frac{\partial \Psi}{\partial \Phi} - i\lambda n & A_{12} & 0 & 0 \\ -\frac{1}{3} W n^2 \Phi & i n (1+\alpha) Q^2 & 0 & -i n \alpha Q^2 \\ 0 & 0 & 1 & 0 \\ 0 & \frac{\alpha Q}{2\zeta} & 0 & -\frac{\alpha Q}{2\zeta} \end{bmatrix}$$

where $A_{12} \equiv -\lambda \Phi_i - i \frac{\Phi_i}{n} \left(\frac{\partial \Psi}{\partial \Phi} + 2 (\Phi_i - \Phi_u) \right)$, and the matrix **B** in Eq. H.24 is given by:

$$B = \begin{bmatrix} -i(4+\mu n) & -(\frac{2}{n}+\mu)\Phi_i & 0 & 0 \\ -\frac{1}{3} W n^2 & 0 & -n^2 & 0 \\ 0 & -in & 0 & 0 \\ 0 & 0 & 0 & -in \end{bmatrix}$$

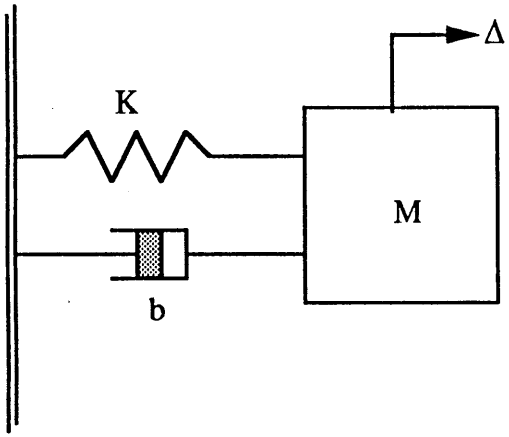

Model of Reed Dynamics with Viscous Dashpot

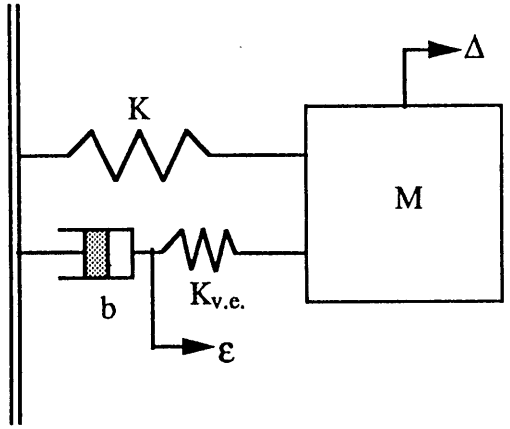

Model for Reed Dynamics with Visco-Elastic Dashpot

Figure H.1: Schematics of Reed Valve Dynamics Showing Viscous and Visco-Elastic Dashpot Models

Appendix I: One Dimensional Acoustic Analysis of Compression System

To determine the influence of compression system parameters on acoustic oscillations in the compression system, a one-dimensional acoustic analysis was applied to the compression system. The analysis was developed using acoustic transmission matrices, which are a compact and convenient method to relate the acoustic state variables upstream of an acoustic element to the acoustic state variables downstream of the flow element. The format of the transmission matrices used in this thesis is given below:

$$\begin{Bmatrix} p_1 \\ \rho c u_1 \end{Bmatrix} = \begin{bmatrix} T_{11} & T_{12} \\ T_{21} & T_{22} \end{bmatrix} \begin{Bmatrix} p_2 \\ \rho c u_2 \end{Bmatrix} \tag{I.1}$$

where p is the acoustic pressure perturbation, u is the acoustic axial velocity perturbation and T_{ij} is an element in the transmission matrix.

The one-dimensional, acoustic model of the compression system contained four acoustic elements: the upstream duct, the compressor, the downstream duct, and the throttle. Using the acoustic transmission matrices for the individual components, the transmission matrix for the entire compression system can be readily assembled. A schematic of the model is shown in Figure 5.2.

The transmission matrices for the flow elements are given below.

The Upstream Duct:

The flow in the upstream duct was assumed to be a subsonic, one-dimensional flow with a small amplitude acoustic disturbance. The one-dimensional, compressible, linearized continuity and axial momentum equations are given below:

$$\frac{\partial \rho}{\partial t} + U\frac{\partial \rho}{\partial x} + \bar{\rho}\frac{\partial u}{\partial x} = 0 \tag{I.2}$$

$$\bar{\rho}\frac{\partial u}{\partial t} + \bar{\rho}U\frac{\partial u}{\partial x} = -\nabla p \tag{I.3}$$

where:

$$\rho = \bar{\rho} + \delta\rho \tag{I.4}$$

$$u = \bar{U} + \delta u \tag{I.5}$$

Manipulation of the continuity and momentum equations, and assuming isentropic compression, i. e.,

$$\frac{\partial p}{\partial \rho} = c^2 \tag{I.6}$$

where c is the speed of sound, leads to the one-dimensional convective wave equation:

$$\frac{1}{c^2}\left[\frac{\partial}{\partial t} + \bar{U}\frac{\partial}{\partial x}\right]^2 p = \frac{\partial^2 p}{\partial x^2} \tag{I.7}$$

The one-dimensional, convective wave equation describes the acoustic oscillations within the duct. Assuming traveling wave solutions of the form,

$$e^{i(\omega t - k x)}$$

leads to a dispersion relation,

$$k = \frac{\omega}{c} \frac{1}{1 - M_x^2} [\pm 1 - M_x] \tag{I.8}$$

where M_X is the axial Mach number of the flow

The general form for a one-dimensional, acoustic pressure disturbance in the duct consists of a wave traveling with the mean flow and a wave traveling against the mean flow and is given by:

$$p(x, t) = A e^{i(\omega t - k_1 x)} + B e^{i(\omega t + k_2 x)} \tag{I.9}$$

where $$k_1 \equiv \frac{\omega}{c} \frac{1}{1 + M_x} \quad ; \quad k_2 \equiv \frac{\omega}{c} \frac{1}{1 - M_x}$$

Using the general expression for the acoustic pressure perturbations in the duct and the axial momentum equation, the acoustic state variables at the ends of a duct of length L can be related. At the entrance to the duct, x= - L, the acoustic pressure and axial velocity perturbations are given by:

$$p_{x=-L} = A e^{i \omega t + i k_1 L} + B e^{i \omega t - i k_2 L} \tag{I.10}$$

$$\rho c u_{x=-L} = A e^{i \omega t + i k_1 L} - B e^{i \omega t - i k_2 L} \tag{I.11}$$

At the exit of the duct, x = 0, the acoustic pressure and axial velocity perturbations are given by:

$$p_{x=0} = A e^{i \omega t} + B e^{i \omega t} \tag{I.12}$$

$$\rho c u_{x=0} = A e^{i \omega t} - B e^{i \omega t} \tag{I.13}$$

Expressing Equations I.10 through I.13 in the form of an acoustic transmission matrix yields:

$$\begin{Bmatrix} p \\ \rho c u \end{Bmatrix}_{x=-L} = \begin{bmatrix} \frac{1}{2}\left(e^{i k_1 L} + e^{-i k_2 L}\right) & \frac{1}{2}\left(e^{i k_1 L} - e^{-i k_2 L}\right) \\ \frac{1}{2}\left(e^{i k_1 L} - e^{-i k_2 L}\right) & \frac{1}{2}\left(e^{i k_1 L} + e^{-i k_2 L}\right) \end{bmatrix} \begin{Bmatrix} p \\ \rho c u \end{Bmatrix}_{x=0} \tag{I.14}$$

Acoustic Transmission Matrix for the Compressor:

The compressor is modeled as a one-dimensional actuator disk. For simplicity, the flow through the compressor is assumed to be incompressible. Neglecting the compressibility of the flow through the compressor results in errors on the order of the compressor Mach number squared. The compressor is assumed to be quasi-steadily, following it steady state performance characteristic for the acoustic oscillations. Also, the inertia of the fluid within the compressor was considered to be negligible compared to the inertial of the fluid within the ducts associated with the acoustic oscillations.

The quasi-steady model for the performance of the compressor is given by:

$$p_{s_d} - p_{t_u} = p_{s_d} - \left(p_{s_u} + \rho \overline{U} u\right) = \frac{1}{2} \rho U_R^2 \frac{\partial \Psi}{\partial \Phi} \delta\phi = \frac{1}{2} \rho U_R \frac{\partial \Psi}{\partial \Phi} u \tag{I.15}$$

where

$$\Psi = \Psi(\Phi) = \frac{P_{s_d} - P_{t_u}}{\frac{1}{2} \rho U_R^2} \tag{I.16}$$

Assuming that the flow through the compressor is incompressible requires that the axial velocity is continuous across the compressor:

$$u_u = u_d \tag{I.17}$$

Assembling Equations I.15 and I.17 in form of an acoustic transmission matrix yields:

$$\begin{Bmatrix} p \\ \rho c u \end{Bmatrix}_u = \begin{bmatrix} 1 & -\beta \\ 0 & 1 \end{bmatrix} \begin{Bmatrix} p \\ \rho c u \end{Bmatrix}_d \tag{I.18}$$

$$\text{where: } \beta \equiv \text{acoustic compressor slope} \equiv \left(\frac{1}{2} M_R \frac{\partial \Psi}{\partial \Phi} + M_x \right) \tag{I.19}$$

Alternatively, the acoustic compressor slope can be expressed in terms of the total to total compressor characteristic:

$$\beta \equiv \frac{1}{2} M_R \frac{\partial \Psi_{tt}}{\partial \Phi} \tag{I.20}$$

Acoustic Transmission Matrix for the Downstream Duct:

The acoustic transmission matrix for the downstream duct is similar to that of the upstream duct, however, the downstream duct is of length αL.

$$\begin{Bmatrix} p \\ \rho c u \end{Bmatrix}_{x=0^+} = \begin{bmatrix} \frac{1}{2}\left(e^{i k_1 \alpha L} + e^{-i k_2 \alpha L}\right) & \frac{1}{2}\left(e^{i k_1 \alpha L} - e^{-i k_2 \alpha L}\right) \\ \frac{1}{2}\left(e^{i k_1 \alpha L} - e^{-i k_2 \alpha L}\right) & \frac{1}{2}\left(e^{i k_1 \alpha L} + e^{-i k_2 \alpha L}\right) \end{bmatrix} \begin{Bmatrix} p \\ \rho c u \end{Bmatrix}_{x=\alpha L} \tag{I.21}$$

Acoustic Transmission Matrix for the Throttle:

The throttle is assumed to be an orifice plate, modeled as a one-dimensional actuator disk. The transmission matrix for an orifice plate, assuming quasi-steady flow is given by:

$$\begin{Bmatrix} p \\ \rho c u \end{Bmatrix}_u = \begin{bmatrix} 1 & \kappa \\ 0 & 1 \end{bmatrix} \begin{Bmatrix} p \\ \rho c u \end{Bmatrix}_d \tag{I.22}$$

where:

$$\kappa \equiv \frac{1-\sigma}{\sigma} M_{x_{th}} \equiv \text{Acoustic Throttle Slope}$$

$$\sigma \equiv \frac{A_{orifice}}{A_{duct}} \equiv \text{Area Ratio of Orifice}$$

$$M_{x_{th}} = \text{Axial Mach Number of Flow through Orifice}$$

Acoustic Transmission Matrix For Entire Compression System:

A model for the acoustic behavior of the entire compression system can be constructed by assembling the transmission matrices of the individual components:

$$\begin{Bmatrix} p \\ \rho c u \end{Bmatrix}_{x=-L} = \begin{bmatrix} \frac{1}{2}\left(e^{i k_1 L} + e^{-i k_2 L}\right) & \frac{1}{2}\left(e^{i k_1 L} - e^{-i k_2 L}\right) \\ \frac{1}{2}\left(e^{i k_1 L} - e^{-i k_2 L}\right) & \frac{1}{2}\left(e^{i k_1 L} + e^{-i k_2 L}\right) \end{bmatrix} \begin{bmatrix} 1 & -\beta \\ 0 & 1 \end{bmatrix}$$

$$\begin{bmatrix} \frac{1}{2}\left(e^{i k_1 \alpha L} + e^{-i k_2 \alpha L}\right) & \frac{1}{2}\left(e^{i k_1 \alpha L} - e^{-i k_2 \alpha L}\right) \\ \frac{1}{2}\left(e^{i k_1 \alpha L} - e^{-i k_2 \alpha L}\right) & \frac{1}{2}\left(e^{i k_1 \alpha L} + e^{-i k_2 \alpha L}\right) \end{bmatrix}$$

$$\begin{bmatrix} 1 & \kappa \\ 0 & 1 \end{bmatrix} \begin{Bmatrix} p \\ \rho c u \end{Bmatrix}_{x=+\alpha L} \tag{I.23}$$

The acoustic transmission matrix of the entire compression system can thus be written as:

$$\begin{Bmatrix} p_1 \\ \rho c u_1 \end{Bmatrix}_{x=-L} = \begin{bmatrix} Z_1 & Z_2 \\ Z_2 & Z_1 \end{bmatrix} \begin{bmatrix} 1 & Z_3 \\ 0 & 1 \end{bmatrix} \begin{bmatrix} Z_4 & Z_5 \\ Z_5 & Z_4 \end{bmatrix} \begin{bmatrix} 1 & Z_6 \\ 0 & 1 \end{bmatrix} \begin{Bmatrix} p_2 \\ \rho c u_2 \end{Bmatrix}_{x=\alpha L} \tag{I.24}$$

where the Z's are defined by the elements of transmission matrices for the individual components in equation (I.23). Carrying out the matrix multiplication in equation (I.24), the transmission matrix for the entire compression system is expressed as:

$$\begin{Bmatrix} p \\ \rho c u \end{Bmatrix}_{x=-L} = \begin{bmatrix} \xi_{11} & \xi_{12} \\ \xi_{21} & \xi_{22} \end{bmatrix} \begin{Bmatrix} p \\ \rho c u \end{Bmatrix}_{x=+\alpha L} \tag{I.25}$$

Eigenvalue Analysis:

The boundary conditions at the entrance to the inlet duct and the exit of the throttle define the eigenvalue problem for the acoustic behavior of the compression system. The regions upstream of the inlet and downstream of the throttle are assumed to be free fields, and thus, behave as pressure release boundary conditions. Expanding transmission matrix for the expression for the pressure upstream of the inlet in terms of the conditions downstream of the throttle yields:

$$p(x=-L) = \xi_{1\,1}\; p(x=+\alpha L) + \xi_{1\,2}\; \rho\, c\, u(x=+\alpha L) \tag{I.26}$$

Applying the pressure release boundary conditions, i.e. p = 0 at (x= -L) and at (x=+αL), requires that $\xi_{12} = 0$ for non-trivial solutions to exist. The eigenvalues for the acoustic oscillations are solutions to the complex, non-linear equation below, expressed in terms of the elements of the transmission matrices for the individual components as defined in equation (I.24):

$$\xi_{1\,2} = Z_6\,(Z_1\,Z_4 + Z_5(Z_1\,Z_3 + Z_2)) + Z_1\,Z_5 + Z_4\,(Z_1\,Z_3 + Z_2) = 0 \tag{I.27}$$

Solving Eq. I.27 for the complex time dependence of the acoustic oscillations yields the growth (or damping) rate and natural frequency of the acoustic oscillations in the compression system. The time dependence of the acoustic oscillations is given by:

$$e^{i\,\omega t} = e^{\mathrm{Real}(i\,k\,L)\,\frac{c}{L}t + i\,\mathrm{Imag}(i\,k\,L)\,\frac{c}{L}t} \tag{I.28}$$

$$\text{where} \quad k \equiv \frac{\omega}{c}$$

For complex frequencies with a positive imaginary component, the system is stable. For complex frequencies with a negative imaginary component, the solutions grow exponentially with time, and the system is unstable.

Equivalent Critical Damping Ratio:

Relating the growth rates of the acoustic oscillations to an equivalent critical damping ratio of a second order, mass-spring-damper system, gives a useful physical interpretation of the growth (or decay) rates of the eigenvalues. For a second order, damped oscillatory system, the time dependence of the oscillations is given by:

$$e^{\left(\zeta + i\sqrt{1+\zeta^2}\right)\omega_n t} \tag{I.29}$$

where: $\zeta \equiv \frac{b}{2\,m\,\omega_n}$ = critical damping ratio and $\omega_n \equiv \sqrt{\frac{k}{m}}$ = Natural Frequency

Thus, the equivalent critical damping ratio of the acoustic oscillations is given in terms of the eigenvalues of the system by:

$$\zeta = \frac{-\,\text{Real}\,(i\,k\,L)}{\sqrt{(\text{Real}(i\,k\,L))^2 + (\text{Imag}(i\,k\,L))^2}} \tag{I.30}$$

Response to External Excitation:

The eigenvalue analysis assess the stability of the compression system to acoustic disturbances, however, it is also useful to predict the system response to excitation. In the compression system, the main noise source was assumed to be an unsteady pressure fluctuation across the compressor. Modeling this noise source as an external forcing function allows the response of the acoustic oscillations within the system to be predicted. When calculating the steady state system response to purely oscillatory excitation, a simpler form of the transmission matrices can be used than was used in the eigenvalue analysis. Also for simplicity, the axial Mach number in the duct was assumed to be negligible for the force response analysis.

For purely oscillatory solutions, the frequencies and wave numbers of the acoustic oscillations are purely real. Thus, the transmission matrix for a duct of length L reduces to:

$$\begin{Bmatrix} p \\ \rho\, c\, u \end{Bmatrix}_{x=-L} = \begin{bmatrix} \cos(kL) & i\sin(kL) \\ i\sin(kL) & \cos(kL) \end{bmatrix} \begin{Bmatrix} p \\ \rho\, c\, u \end{Bmatrix}_{u} \tag{I.31}$$

Using Eq. I.31 and applying the pressure release boundary condition upstream of the compressor ($p = 0$ at $x = -L$), the acoustic state variables at the entrance to the compressor can be related:

$$p_u = \frac{-i\sin(kL)}{\cos(kL)} \rho\, c\, u_u \equiv Z_7\, \rho\, c\, u_u \tag{I.32}$$

The Compressor with excitation is modeled as follows:

$$\begin{Bmatrix} p \\ \rho\, c\, u \end{Bmatrix}_{u} = \begin{bmatrix} 1 & -\beta \\ 0 & 1 \end{bmatrix} \begin{Bmatrix} p \\ \rho\, c\, u \end{Bmatrix}_{d} + \begin{Bmatrix} -F(t) \\ 0 \end{Bmatrix} \tag{I.33}$$

where F(t) is the excitation, represented as a variation in the static pressure rise across the compressor. Expressing the acoustic state variables upstream of the compressor to the acoustic state variables downstream of the throttle yields:

$$\begin{Bmatrix} p \\ \rho\, c\, u \end{Bmatrix}_{u} = \begin{bmatrix} 1 & -\beta \\ 0 & 1 \end{bmatrix} \begin{bmatrix} \cos(\alpha kL) & i\sin(\alpha kL) \\ i\sin(\alpha kL) & \cos(\alpha kL) \end{bmatrix} \begin{bmatrix} 1 & \kappa \\ 0 & 1 \end{bmatrix} \begin{Bmatrix} p \\ \rho\, c\, u \end{Bmatrix}_{x=\alpha L} + \begin{Bmatrix} -F(t) \\ 0 \end{Bmatrix} \tag{I.34}$$

Applying the pressure release boundary condition at the exit to the throttle, ($p = 0$ at $x = \alpha L$), and expanding Eq. I.34 leads to the following expression for 1)the pressure upstream of the compressor.

$$p_u = \left[\kappa (\cos (k \alpha L) - i \beta \sin (k \alpha L) + (i \sin (k \alpha L) - \beta \cos (k \alpha L)\right] \rho c u_{\alpha L} - F (t) \tag{I.35}$$

Defining Z_8 as the terms in the square bracket in Eq. I.35, the pressure upstream of the compressor can be expressed as:

$$p_u = Z_8 \rho c u_{\alpha L} - F (t) \tag{I.36}$$

and 2) the acoustic velocity upstream of the compressor:

$$\rho c u_u = [\kappa i \sin (k \alpha L) + \cos(k \alpha L)] \rho c u_{\alpha L} \tag{I.37}$$

Defining Z_9 as the terms in the square bracket in Eq. I.37, the velocity upstream of the compressor can be expressed as:

$$\rho c u_u = Z_9 \rho c u_{\alpha L} \tag{I.38}$$

Using Equations I.36 and I.38 and the relation between the acoustic state variables upstream of the compressor (Eq. I.32), the transfer function between the disturbances in pressure rise across the compressor and the acoustic pressure at the entrance of the compressor is given by:

$$\frac{p_u(\omega)}{F (\omega)} = \frac{1}{\frac{Z_8}{Z_9 Z_7} - 1} \tag{I.39}$$

Figure I.1 shows the predicted frequency response of the pressure upstream of the compressor to white noise for the compression system operating at the peak of it

characteristic, $\frac{\partial \Psi}{\partial \Phi} = 0$,with a steep and a shallow throttle slope. As shown, the acoustic pressure oscillations near the frequency of the quarter wave length organ pipe mode are predicted to be amplified for the system with the steep throttle slope. However, no such amplification is predicted to occur at that frequency with the shallow throttle slope.

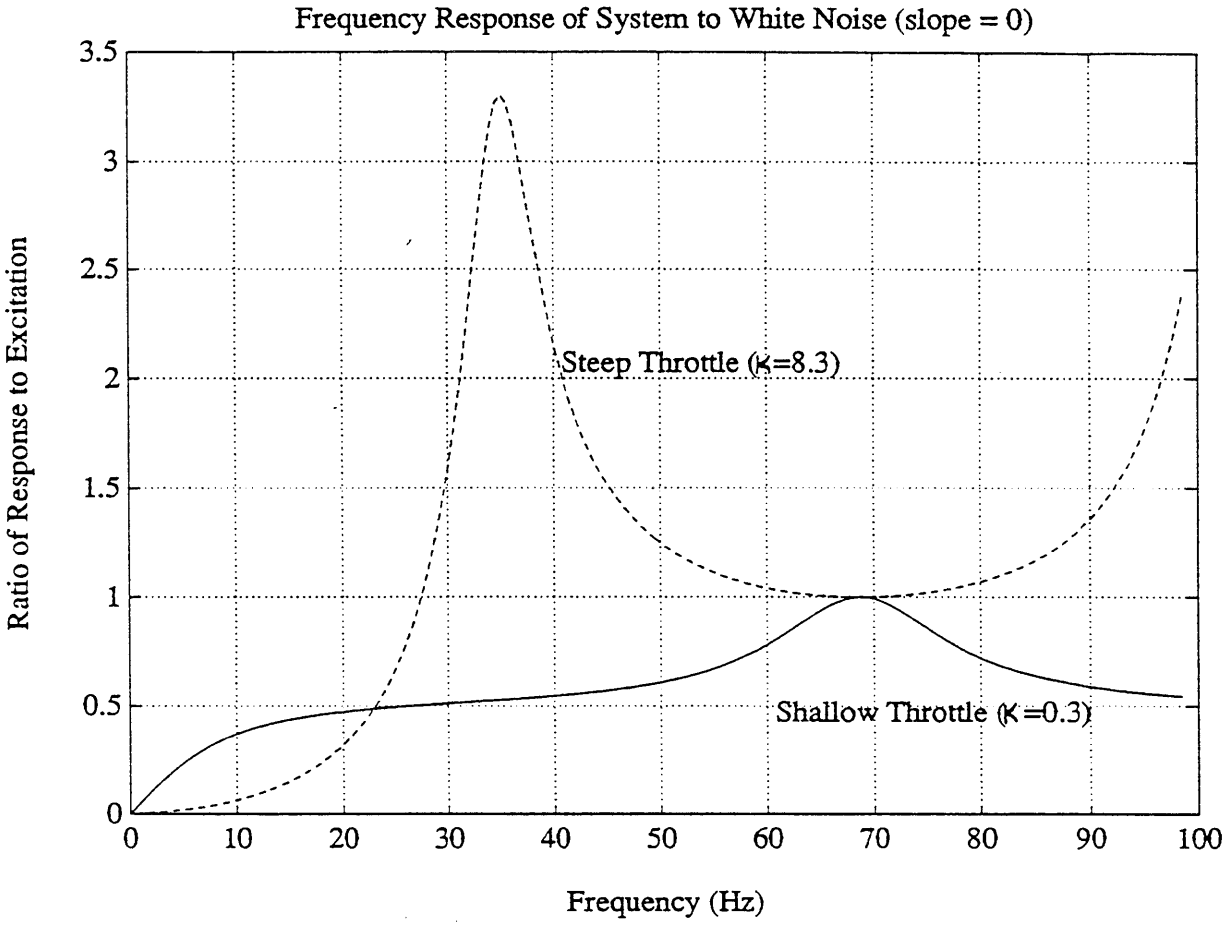

Figure I.1 Static Pressure Perturbations at Entrance to Compressor Normalized by Magnitude of White Noise Excitation at Face of Compressor for Compression System Operating at Peak of Characteristic with a Steep Acoustic Throttle Slope ($\kappa = 8.3$) and a Shallow Acoustic Throttle Slope ($\kappa = 0.3$)

Appendix J: Rotating Stall Model with Dynamic Mass / Momentum Recirculation

In this appendix, a variation of the dynamic mass / momentum injection strategy used in this research is presented. In this variation, termed dynamic mass / momentum recirculation, the high pressure injection source is bled from downstream of the compressor. The recirculation is assumed to be close coupled and locally reacting, i.e., the fluid injected at a given circumferential location is removed from immediately downstream of the compressor at the same circumferential location. As will be shown, this modification serves to augment the stabilizing effect of the strategy developed in this thesis.

The basic model structure is similar to the basic structure of the models used through out this thesis. The effect of the dynamic mass / momentum recirculation on the flow field is incorporated into the boundary conditions across the actuator disk.

Several assumptions regarding the recirculation process are inherent in this model:

1) The high velocity fluid is injected axially, within a short distance upstream of the compressor compared to the circumferential length scale of the disturbances.

2) The high velocity fluid injected upstream of the compressor mixes out to a span-wise uniform state before entering the compressor.

3) The fluid injected upstream at a given circumferential location is removed from immediately downstream of the compressor, at the same circumferential position. Thus, the recirculation is close-coupled.

4) The pressure rise of the compressor remains a pure function of the mass flow coefficient entering the compressor, with the inertia of the fluid within the blade rows being modeled as in Appendix A.

A schematic of the mass / momentum recirculation model is shown in Figure J.1. The effect of the injection upstream of the compressor, the compressor, and the mass removal downstream of the compressor will be lumped into one semi-actuator disk.

Modeling the Injection Region

The injection process is modeled as developed in Appendix B.

Conservation of Mass:

The mass flow entering the compressor is given by the sum of the mass flow upstream of the injection and the injected fluid:

$$\Phi_u + \Phi_i \, q = \Phi_b \tag{J.1}$$

where Φ_i is the injection parameter, q is the normalized reed valve opening area.

Conservation of Momentum:

As developed in Appendix B, the linearized relation between the span-wise uniform total pressure change across the injection location is given by the following expression relating the change in total pressure to the injection parameters and the local reed valve area opening:

$$\delta p_{t_b} - \delta p_{t_u} = 2 \, \Phi_i \, (\Phi_i - \Phi_u) \, \delta q \tag{J.2}$$

Modeling the Mass / Momentum Removal Region

The mass removal process is assumed to create an axially discontinuous change in mass flow and static pressure downstream of the compressor.

Conservation of Mass

The mass flow in the flow field downstream of the removal location is given by the mass flow through the compressor minus the mass flow recirculated Noting that the mass flow injected upstream is equal to the mass flow removed downstream, mass continuity requires:

$$\rho\, C_{x_c} H - \rho\, C_{x_i} \Delta = \rho\, C_{x_d} H \tag{J.3}$$

where C_X is the axial velocity, H is the annulus height, Δ is the reed valve opening, and ρ is the density.

Non-dimensionalizing leads to:

$$\Phi_c - \Phi_i\, q = \Phi_d \tag{J.4}$$

Conservation of Momentum

The effect of the removal of mass and momentum downstream of the compressor on the momentum balance is given by:

$$P_{s_c} H + \rho H C_{x_c}^2 = \rho \Delta C_{x_i} C_{x_c} + P_{s_d} H + \rho H C_{x_d}^2 \tag{J.5}$$

Using Equations J.1 and J.4 to simplify the above expression, the change in static pressure downstream of the compressor due to the mass and momentum removal is given by:

$$P_{s_d} - P_{s_c} = \rho\, q\, C_{x_i} C_{x_d} \tag{J.6}$$

Linearizing and non-dimensionalizing, assuming the steady state mass flow recirculated is small, yields:

$$\delta p_{s_d} - \delta p_{s_c} = 2 \Phi_i \Phi_d \delta q \tag{J.7}$$

Combining these relations with the mass flow and pressure rise boundary conditions across the compressor developed in Appendix A, leads to the mass flow and pressure rise boundary conditions across the compressor with dynamic mass / momentum recirculation.

Mass Flow Across Modified Compressor:

$$\delta\phi_u = \delta\phi_d \tag{J.8}$$

Pressure Rise Across Modified Compressor:

$$\delta p_{s_d} - \delta p_{t_u} = \frac{\partial \Psi}{\partial \Phi} \delta\phi_u + \frac{\partial \Psi}{\partial \Phi} \Phi_i \delta q - \mu \frac{\partial \phi_u}{\partial \tau} - \mu \Phi_i \frac{\partial q}{\partial \tau} - \lambda \frac{\partial \phi_u}{\partial \theta} - \lambda \Phi_i \frac{\partial q}{\partial \theta} + 2 \Phi_i^2 \delta q \tag{J.9}$$

Exit Flow Angle:

The exit flow angle boundary conditions remains unchanged from the basic compression system analysis:

$$\delta v_d = 0 \tag{J.10}$$

Eigenvalue Problem

Expressing the boundary conditions across the actuator disk in terms of solutions for the upstream and downstream flow fields leads to an expression relating the complex amplitude of the upstream perturbation streamfunction to the local reed valve displacement.

$$\left[i (4 + \mu n) \sigma + \frac{\partial \Psi}{\partial \Phi} - i \lambda n \right] A_n + \left[(\Phi_i \ \mu) \sigma - \lambda \Phi_i - \frac{\partial \Psi}{\partial \Phi} \Phi_i + 2 \Phi_i^2 \right] q_n = 0 \qquad \text{(J.11)}$$

where $\Psi_u = \sum_{n=1}^{\infty} A_n e^{i n (\theta - \sigma \tau) + n x}$ and $q = \sum_{n=1}^{\infty} q_n e^{i n (\theta - \sigma \tau)}$

The structural dynamics of the reed valves are identical to the model in dynamic mass / momentum injection.

$$\frac{\partial^2 q}{\partial \tau^2} + 2 Q \zeta \frac{\partial q}{\partial \tau} + Q^2 \delta q = \frac{1}{6} W \delta p_{s_u} \qquad \text{(J.12)}$$

The static pressure perturbations in the upstream flow field can be related to the perturbation streamfunction in the upstream flow field via the circumferential momentum equation.

$$\frac{\partial p_{s_u}}{\partial \theta} = 2 \left(\frac{\partial^2 \Psi_u}{\partial x \, \partial \tau} + \Phi_u \frac{\partial^2 \Psi_u}{\partial x^2} \right) \qquad \text{(J.13)}$$

Writing the expression for the reed valve dynamics as two first order equations leads to the following expression relating the reed valve displacement and velocity to the upstream flow field:

$$\frac{1}{3} W n^2 (i \sigma - \Phi_u) A_n + i n Q^2 q_n + (n^2 \sigma + 2 Q \zeta i n) z_n = 0 \qquad \text{(J.14)}$$

where the time rate of change of the reed valve displacement is given by:

$$i\,n\,\sigma q_n + z_n = 0 \tag{J.15}$$

Combining Equations J.11, J.14 and J.15 leads to a third order, generalized, complex eigenvalue problem governing the stability of each spatial harmonic.

$$[\mathbf{A} - \sigma\,\mathbf{B}] \begin{Bmatrix} \delta A_n \\ \delta q_n \\ \delta z_n \end{Bmatrix} = 0 \tag{J.16}$$

The matrix **A** is defined as:

$$\mathbf{A} = \begin{bmatrix} \frac{\partial \Psi}{\partial \Phi} - i\,n\,\lambda & A_{12} & 0 \\ -\frac{1}{3} W\,n^2\,\Phi_u & i\,n\,Q^2 & i\,n\,2\,Q\,\zeta \\ 0 & 0 & 1 \end{bmatrix}$$

where $$A_{12} \equiv -\lambda\,\Phi_i - i\frac{\Phi_i}{n}\left(\frac{\partial \Psi}{\partial \Phi} + 2\,\Phi_i\right)$$

and the matrix **B** is defined as:

$$\mathbf{B} = \begin{bmatrix} -i\,(4 + n\,\mu) & -\mu\,\Phi_i & 0 \\ -i\frac{1}{3} W n^2 & 0 & -n^2 \\ 0 & -i\,n & 0 \end{bmatrix}$$

Comparing the stability matrices above for dynamic mass / momentum recirculation with the stability matrices for dynamic mass / momentum injection (see Appendix B), the two

are found to be similar in structure. Although the two control strategies constitute different dynamic systems with different stability characteristics, the main difference between the two systems is that the former (the recirculation strategy) has a larger effect on the pressure rise across the actuator disk for a given reed valve deflection than the latter.

The pressure rise for a given, spatially uniform, static change in reed deflection for the two system is given by:

$$\delta p_{s_d} - \delta p_{t_u} = \left(\frac{\partial \Psi}{\partial \Phi} \Phi_i + 2 \Phi_i^2 \right) \delta q \quad \text{for recirculation} \tag{J.17}$$

and

$$\delta p_{s_d} - \delta p_{t_u} = \left(\frac{\partial \Psi}{\partial \Phi} \Phi_i + 2 \Phi_i \left(\Phi_i - \Phi_u \right) \right) \delta q \quad \text{for injection} \tag{J.18}$$

Although the results of a parameter optimization study are not presented in this thesis, it is reasonable to assume that the dynamic mass / momentum recirculation strategy developed in this appendix has the potential to be more effective in stabilizing rotating stall than the strategy that was implemented.

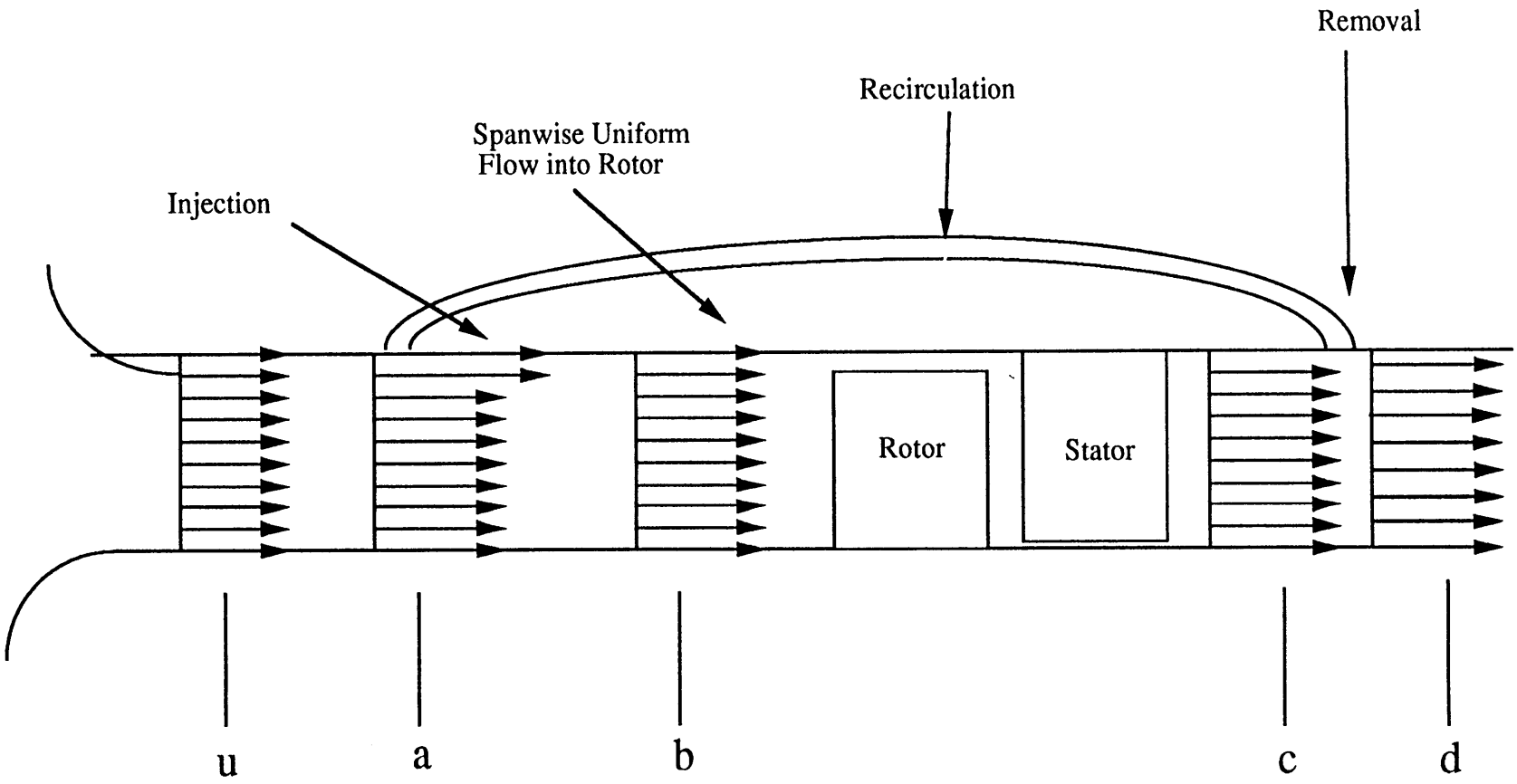

Figure J.1: Schematic of Dynamic Mass / Momentum Recirculation

Appendix K: Radial Stability Model

In this Appendix, a model is presented to demonstrate the plausibility of radial modes of a compression system influencing the process through which the uniform flow field transitions into some form of non-uniform unsteady flow. The model is viewed as a simplified first step in determining the parameters that influence the role of radial disturbances. The model assesses the stability of a two dimensional flow field in the axial and radial directions. A schematic of the flow field is shown in Figure K.1.

Considering only the axial and radial components assumes that the circumferential disturbances are decoupled from the radial disturbances. This seems realistic for compressors with high hub to tip ratios, in which the circumferential variations of any circumferential disturbance are insignificant over the length scale of the span of the annulus. A similar analysis, although applied to the steady state redistribution of the axial and radial components of flow through a compressor, is developed in [35].

Assumptions:

The model contains the following basic assumptions:

1) The flow field is essentially two-dimensional in the axial and span-wise directions.
2) The circumferential variations are negligible.
3) The upstream flow field is irrotational.
4) The downstream flow field is rotational.
5) The steady state flow field is uniform and axial.
6) The mean pressure rise is uniform in the span-wise direction.
7) The flow is incompressible and inviscid.

Boundary Conditions:

The flow field is required to satisfy the following boundary conditions:

1) no normal velocity at the walls, i.e., $v = 0$ at $h = 0$ and $h = H$

2) mass flow at a given span-wise location is continuous across the compressor

3) radial flow angle at a given span-wise location is continuous across compressor

4) pressure rise across compressor is function of span-wise local mass flow coefficient and span-wise local compressor performance

5) disturbances are bounded far upstream and downstream of the compressor

Stability Analysis:

As with the rotating stall analysis, the stability of the flow field will be determined using a perturbation streamfunction (Ψ). In dimensional form, the perturbation streamfunction is defined by:

$$u = \frac{\partial \Psi}{\partial h} \quad ; \quad v = -\frac{\partial \Psi}{\partial x} \qquad \text{(K.1) and (K.2)}$$

where, h is the span-wise coordinate, x is the axial coordinate, u is the axial velocity perturbation, and v is the radial velocity perturbation.

The perturbation streamfunction for the upstream flow field must satisfy the Laplace equation:

$$\nabla^2 \Psi_u = \frac{\partial^2 \Psi_u}{\partial x^2} + \frac{\partial^2 \Psi_u}{\partial h^2} = 0 \qquad \text{(K.3)}$$

The solution, consistent with the boundary conditions is given by:

$$\Psi_u = \sum_{n=1}^{\infty} A_n \sin(\frac{n\pi h}{H}) e^{\frac{n\pi x}{H}} e^{s t} \tag{K.4}$$

The axial and radial velocity perturbations associated with perturbation streamfunction given in Eq. K.4 as shown in Figure K.2 for the first harmonic, (n = 1).

The downstream flow field must satisfy the Poisson equation:

$$\nabla^2 \Psi_d = \frac{\partial^2 \Psi_d}{\partial x^2} + \frac{\partial^2 \Psi_d}{\partial h^2} = - \omega_\theta \tag{K.5}$$

where ω_θ = the normal vorticity

The vorticity convects with the downstream flow field:

$$\frac{D\,\omega}{D\,t} = \frac{\partial \omega}{\partial t} + (\overline{U} + \delta u)\frac{\partial \omega}{\partial x} + \delta v \frac{\partial \omega}{\partial h} = 0 \tag{K.6}$$

Linearizing Eq. K.6 yields:

$$\frac{D\,\omega}{D\,t} = \frac{\partial \omega}{\partial t} + \overline{U}\frac{\partial \omega}{\partial x} = 0 \tag{K.7}$$

At x = 0, the downstream disturbance must have the same form, in time and span-wise direction, as the upstream flow field:

$$\omega = G(x) \sin(\frac{n\pi h}{H}) e^{s t} \tag{K.8}$$

Therefore, the general disturbance streamfunction form the downstream flow field is given by:

$$\Psi_d = \sum_{n=1}^{\infty} B_n \sin(\frac{n\pi h}{H}) e^{\frac{-n\pi x}{H}} e^{st} + \sum_{n=1}^{\infty} C_n \sin(\frac{n\pi h}{H}) e^{-\frac{s}{\overline{U}}x} e^{st} \qquad (K.9)$$

Boundary Conditions across Actuator Disk:

The compressor is modeled as a two-dimensional actuator disk with the boundary conditions across the disk expressed in terms of the perturbation streamfunctions.

Mass Flow Continuity across Compressor:

$$u_u = u_d \Rightarrow \frac{\partial \Psi_u}{\partial h}(\frac{h}{H}) = \frac{\partial \Psi_d}{\partial h}(\frac{h}{H}) \qquad (K.10)$$

Continuous Radial Flow Angle

$$v_u = v_d \Rightarrow \frac{\partial \Psi_u}{\partial x}(\frac{h}{H}) = \frac{\partial \Psi_d}{\partial x}(\frac{h}{H}) \qquad (K.11)$$

Pressure Rise across Compressor:

The pressure rise associated with the perturbations is assumed to given by:

$$\delta P_{s_d}(\frac{h}{H}) - \left(\delta P_{s_d}(\frac{h}{H}) + \rho \overline{U} \delta u(\frac{h}{H})\right) = \frac{1}{2}\rho U_R \frac{\partial \Psi}{\partial \Phi}(\frac{h}{H}) \delta u(\frac{h}{H}) \qquad (K.12)$$

Using the Radial Momentum equation:

$$\frac{Dv}{Dt} = -\frac{\partial^2 \Psi}{\partial t \partial x} - \overline{U}\frac{\partial^2 \Psi}{\partial x^2} = -\frac{1}{\rho}\frac{\partial P_s}{\partial h} \qquad (K.13)$$

The pressure rise boundary condition (Eq. K.12) can be expressed in terms of the perturbation streamfunctions:

$$\frac{\partial^2\Psi_d}{\partial t\,\partial x} + \overline{U}\frac{\partial^2\Psi_d}{\partial x^2} - \frac{\partial^2\Psi_u}{\partial t\,\partial x} - \overline{U}\frac{\partial^2\Psi_u}{\partial x^2} - \overline{U}\frac{\partial^2\Psi_u}{\partial h^2} - \frac{1}{2}U_R\left(\frac{\partial\Psi}{\partial\Phi}\frac{\partial^2\Psi_u}{\partial h^2} + \frac{\partial}{\partial h}\left(\frac{\partial\Psi}{\partial\Phi}\right)\frac{\partial\Psi_u}{\partial h}\right) = 0 \tag{K.14}$$

Simplifying, and using the constant radial flow angle boundary condition, the pressure rise across the compressor can be expressed in terms of the upstream perturbation streamfunction.

$$\overline{U}\frac{\partial^2\Psi_u}{\partial h^2} - 2\frac{\partial^2\Psi_u}{\partial t\,\partial x} - \frac{1}{2}U_R\frac{\partial\Psi}{\partial\Phi}\frac{\partial^2\Psi_u}{\partial h^2} - \frac{1}{2}\rho\frac{\partial}{\partial h}\left(\frac{\partial\Psi}{\partial\Phi}\right)\frac{\partial\Psi_u}{\partial h} = 0 \tag{K.15}$$

Eigenvalue Problem for Uniform Span-wise Loading Case:

The homogeneous differential equation (Eq. K.15) can be solved in a straight forward manner for the case where the span-wise loading is uniform, with loading defined here as the local slope of the compressor (unsteady) total to static pressure rise performance, as a function of span. For constant span-wise loading, the homogeneous differential equation reduces to:

$$\overline{U}\frac{\partial^2\Psi_u}{\partial h^2} - 2\frac{\partial^2\Psi_u}{\partial t\,\partial x} - \frac{1}{2}U_R\frac{\partial\Psi}{\partial\Phi}\frac{\partial^2\Psi_u}{\partial h^2} = 0 \tag{K.16}$$

Substituting the upstream streamfunction:

$$\Psi_u = \sum_{n=1}^{\infty} A_n \sin\left(\frac{n\pi h}{H}\right) e^{\frac{n\pi x}{H}} e^{s t} \tag{K.17}$$

yields an eigenvalue problem that determines the following expression for the time dependence of the lowest spatial mode, i.e. n=1,

$$e^{s\,t} = e^{U_R \frac{\pi}{4\,H}\left(\frac{\partial \Psi}{\partial \Phi} - 2\,\Phi\right) t} \tag{K.18}$$

The form of the instability corresponds to a divergence of the initially, span-wise uniform, flow field when the span-wise uniform, (and hence span-wise averaged), slope of the compressor characteristic satisfies:

$$\frac{\partial \Psi}{\partial \Phi} > 2\,\Phi \tag{K.19}$$

Comparing the above stability condition for uniform span-wise loading to that from the stability model presented in Appendix A, where the 2-D, rotating stall modes become unstable when,

$$\frac{\partial \Psi}{\partial \Phi} > 0 \tag{K.20}$$

one finds that the rotating stall instability condition from the full-span rotating stall model would be reached first for a compression system being throttled down to lower flow coefficients from an initially stable flow region. Thus, the full-span rotating stall instability would develop first, and the conditions for the part-span instability described above would never develop as modeled. For different span-wise loading conditions, however, the analysis developed in this appendix, predicts that instability of the part-span mode can occur at operating conditions in which the full-span rotating stall is stable. This is shown below.

Eigenvalue Problem for Non-Uniform Span-wise Loading Case:

The non-uniform span-wise loading stability analysis will be performed using the Galerkin procedure [24] for an assumed mode shape corresponding the solution to the uniform loading solution. Thus, the perturbation streamfunction is assumed to be of the form:

$$\Psi_u = A(t)\sin(\frac{\pi h}{H})\, e^{\frac{\pi x}{H}} \tag{K.21}$$

Substituting the assumed mode shape into the PDE describing the linearized flow field (Eq. K.15) yields an expression for the residual resulting from the approximation:

$$-\overline{U}\frac{\pi^2}{H^2}A\sin(\frac{\pi h}{H}) - 2\frac{\pi}{H}\dot{A}\sin(\frac{\pi h}{H}) + \frac{1}{2}U_R\frac{\partial\Psi}{\partial\Phi}(h)\frac{\pi^2}{H^2}A\sin(\frac{\pi h}{H})$$

$$-\frac{1}{2}U_R\frac{\partial}{\partial h}\left(\frac{\partial\Psi}{\partial\Phi}(h)\right)\frac{\pi}{H}A\cos(\frac{\pi h}{H}) = \text{residual} \tag{K.22}$$

Orthogonalizing the residual with respect to the assumed mode by integrating the product of the error and the assumed mode shape over the span yields a governing ordinary differential equation:

$$2\dot{A}\int_0^H \sin^2(\frac{\pi h}{H})\,dh = \frac{1}{2}U_R\left(\frac{\pi}{H}\right)A\int_0^H\left[\frac{\partial\Psi}{\partial\Phi}(h) - 2\Phi\right]\sin^2(\frac{\pi h}{H})\,dh$$

$$-\frac{1}{2}U_R A\int_0^H\frac{\partial}{\partial h}\left(\frac{\partial\Psi}{\partial\Phi}(h)\right)\cos(\frac{\pi h}{H})\sin(\frac{\pi h}{H})\,dh \tag{K.23}$$

The functional dependence of the stability of the system on the span-wise loading in represented as spatial integral of the local slope over the span of the annulus. In an attempt to parameterize the relative stability of the part span divergence mode modeled in this appendix with the stability of the full span, rotating stall instability mode modeled in Appendix A, the following approach will be taken.

The stability of the full span rotating stall model is a function of the span-wise averaged slope of the compressor characteristic. The full span model predicts instability when the span-wise averaged slope is positive, independent of the detailed span-wise loading. Therefore, stability of the part span stall will be assessed for various loading distributions with a zero span-wise averaged slope.

The span-wise loading distributions will be expressed as a zero mean linear distribution and a zero mean quadratic distribution:

$$\frac{\partial \Psi}{\partial \Phi}(h) = B\left(\frac{h}{H} - \frac{1}{2}\right) + C\left[\left(\frac{h}{H} - \frac{1}{2}\right)^2 - \frac{1}{12}\right] \tag{K.24}$$

Expressing the loading distribution in Eq. K.24 as a polynomial in span-wise coordinate yields:

$$\frac{\partial \Psi}{\partial \Phi}(h) = \left(-\frac{B}{2} + \frac{C}{6}\right) + (B - C)\frac{h}{H} + (C)\left(\frac{h}{H}\right)^2 \tag{K.25}$$

Substituting the expression for the span-wise loading (Eq. K.25) into Eq. K.23 and assuming solutions of the form e^{st}, yields an expression for the growth rate, s, of the disturbances and, hence, the stability of the system:

$$2\,s\int_{o}^{H}\sin^2\left(\frac{\pi\,h}{H}\right)d\,h=\frac{1}{2}U_R\left(\frac{\pi}{H}\right)\int_{0}^{H}\left[\left(-\frac{B}{2}+\frac{C}{6}-2\,\Phi\right)+(B-C)\frac{h}{H}+(C)\left(\frac{h}{H}\right)^2\right]\sin^2\left(\frac{\pi\,h}{H}\right)d\,h$$

$$-\frac{1}{2}U_R\int_{0}^{H}\left[\frac{(B-C)}{H}+\frac{(2\,C)}{H}\left(\frac{h}{H}\right)\right]\cos\left(\frac{\pi\,h}{H}\right)\sin\left(\frac{\pi\,h}{H}\right)d\,h \qquad \text{(K.26)}$$

Evaluating the integrals in Eq K.26 yields:

$$s=\frac{1}{2}U_R\frac{\pi}{H}\left(\frac{C}{4\,\pi^2}-\Phi\right) \qquad \text{(K.27)}$$

Noting that the above stability criteria is given for a zero, span-wise averaged compressor slope, the part-span, axisymmetric mode modeled in this appendix is predicted to become unstable at a higher flow coefficient than the full-span rotating stall model if:

$$C>4\,\pi^2\,\Phi \qquad \text{(K.28)}$$

The magnitude of the quadratic component of span-wise loading is therefore predicted to be a parameter in determining whether a given compression system will exhibit part-span stall or full-span stall inception. The model predicts that the linear component of span wise loading distribution does not influence the relative stability of the part-span and full-span modes considered.

The above result can be made more specific by determining the span-wise loading distribution required for which the full-span and part-span modes are predicted to become unstable simultaneously at the peak of the total to static, span-wise averaged pressure rise characteristic. Assuming a mass flow coefficient of $\Phi = 0.5$, the span-wise variations in slope required for the above stability condition is given by:

$$\frac{\partial \Psi}{\partial \Phi}\left(\frac{h}{H}\right) = 4\pi^2\,\Phi\left[\left(\frac{h}{H}-\frac{1}{2}\right)^2-\frac{1}{12}\right] = 2\pi^2\left[\left(\frac{h}{H}-\frac{1}{2}\right)^2-\frac{1}{12}\right] \qquad \text{(K.29)}$$

The span-wise loading distribution required for this condition to be met is shown in Figure K.3. As shown, the slope is required to vary from roughly $\frac{\partial \Psi}{\partial \Phi} = +3.0$ at the hub and at the tip to roughly $\frac{\partial \Psi}{\partial \Phi} = -2.0$ at mid-span for this condition to be met. This span-wise loading distribution appears to be a physically realistic span-wise loading for compressors operating with end-wall boundary layers which tend to load the end-wall regions more heavily with respect to the core flow.

A qualitative interpretation of the above stability criteria is that compressors in which the hub and tip regions are highly loaded relative to the core flow are more susceptible to part-span stall inception than compressors with uniform span-wise loading Thus, this simplified analysis identifies a compressor parameter that is predicted to influence the nature of the stall inception process.

The analysis presented in this appendix is viewed as a first step in developing a comprehensive fluid dynamic stability model of compression systems. The results are intended to provide qualitative, physical interpretation of the parameters that determining the nature of the stall inception process. A stability analysis that incorporates the coupling between the radial and circumferential modes of a compression system would be a useful next step in this process.

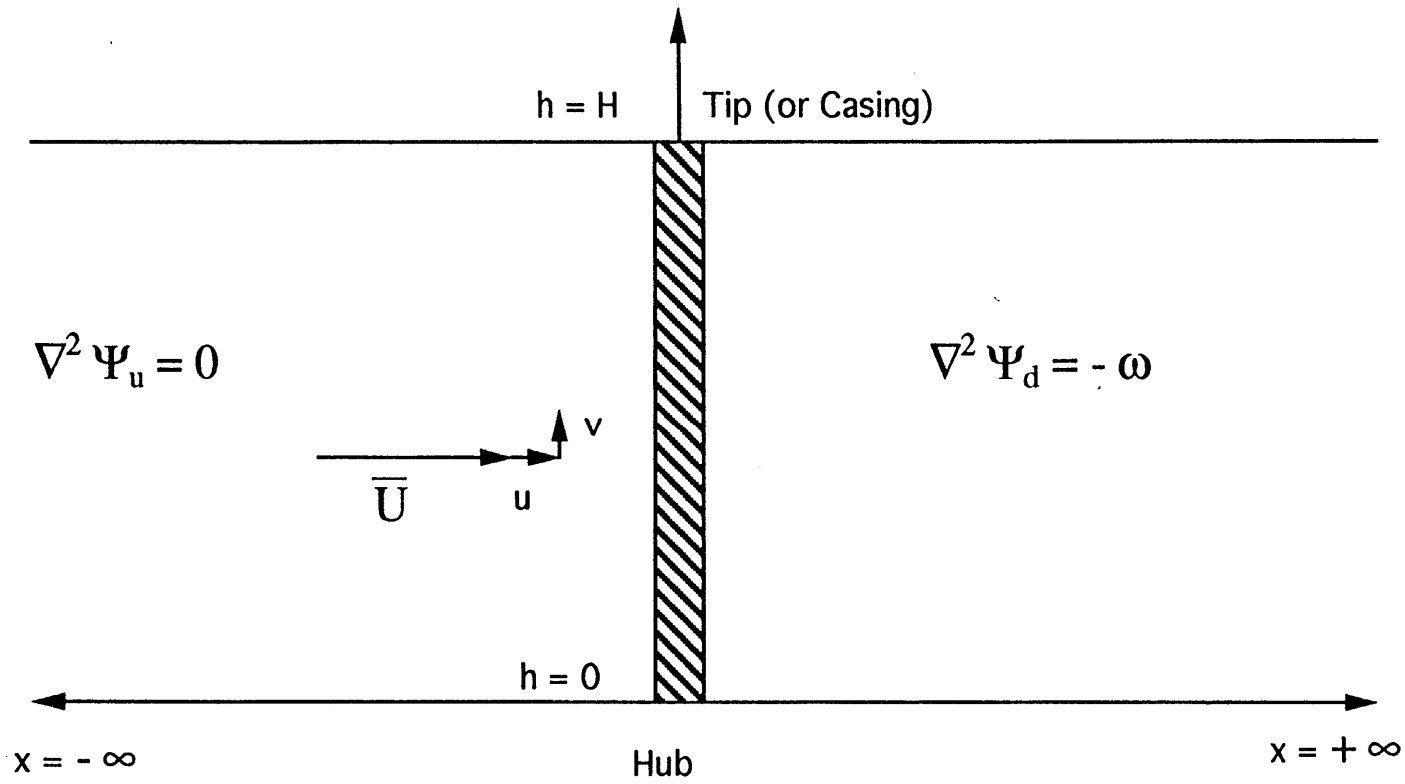

Figure K1: Schematic of 2 - D Radial Stability Model

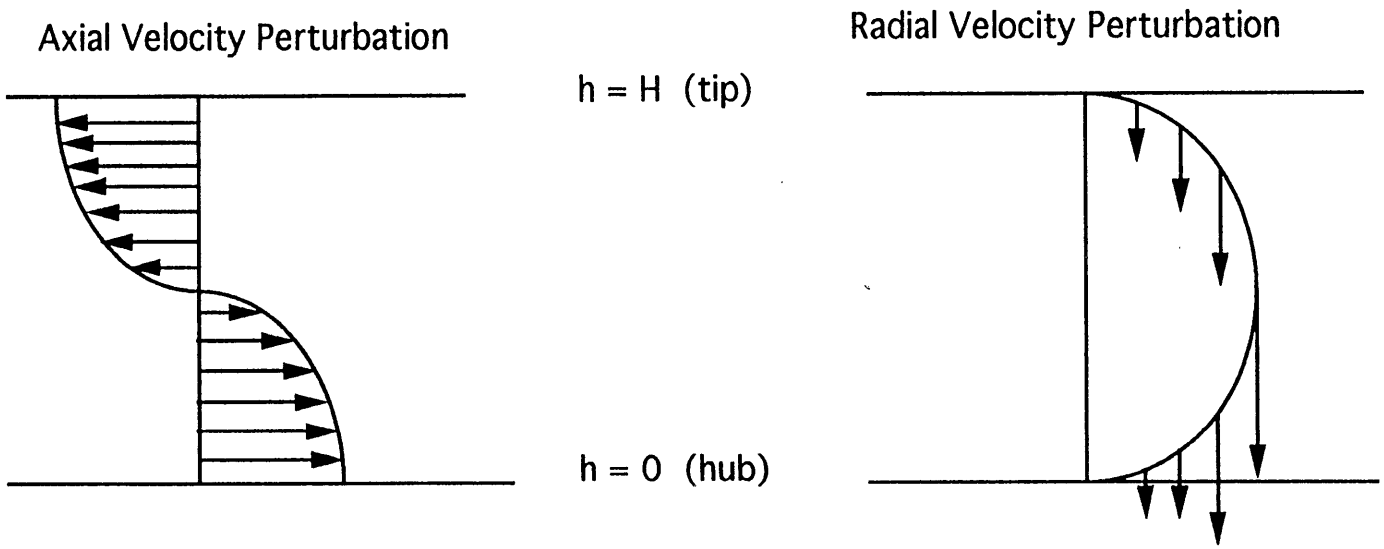

$$u_u\left(\frac{h}{H}\right) = \frac{\pi}{H} A \cos\left(\frac{\pi h}{H}\right)$$

$$v_u\left(\frac{h}{H}\right) = -\frac{\pi}{H} A \sin\left(\frac{\pi h}{H}\right)$$

Figure K.2: Schematic of Velocity Pertubations in Radial Mode

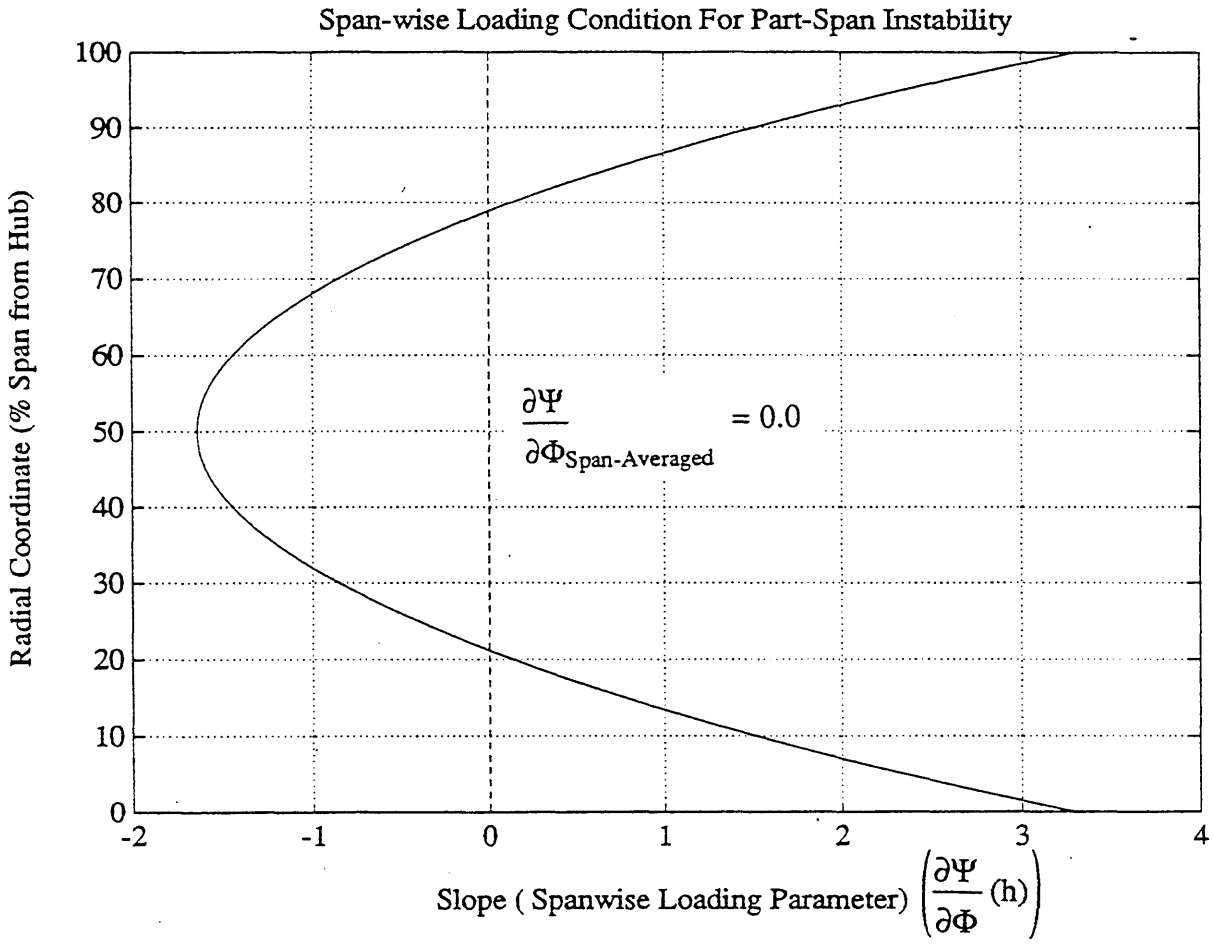

Figure K.3: Span-wise Loading Distribution (slope) for which Part-span Disturbances are Predicted to Become Unstable at Peak of Span-wise Averaged Inlet Total to Exit Static Pressure Rise Versus Mass Flow Characteristic